Étude de la sublimation du chrome lors de l'oxydation haute température de l'alliage AISI 441 et recherche de solutions de protection

Wichitra Wongpromrat

THÈSE

Pour obtenir le grade de

DOCTEUR DE L'UNIVERSITÉ GRENOBLE ALPES

préparée dans le cadre d'une cotutelle entre l'*Université Grenoble Alpes*

Spécialité : **Matériaux, Mécanique, Génie Civil, Electrochimie**

Arrêté ministériel : le 6 janvier 2005 - 7 août 2006

Et

l'Institut de Technologie de King Mongkut de Ladkrabang

Spécialité : **Chemical Engineering**

Présentée par

Wichitra WONGPROMRAT

Thèse dirigée par **Yves WOUTERS** et **Walairat CHANDRA-AMBHORN**
codirigée par **Valérie PARRY et Somrerk CHANDRA-AMBHORN**
préparée au sein des **Laboratoire SIMaP**
dans **l'École Doctorale I-MEP2** de Grenoble
et département **Chemical Engineering** de Bangkok

ÉTUDE DE LA SUBLIMATION DU CHROME LORS DE L'OXYDATION HAUTE TEMPÉRATURE DE L'ALLIAGE AISI 441 ET RECHERCHE DE SOLUTIONS DE PROTECTION

Thèse soutenue publiquement le **8 octobre 2015**
devant le jury composé de :

M. Sébastien CHEVALIER
Professeur, Université de Bourgogne, Président et Rapporteur
Mme. Pornwasa WONGPANYA
Associate Professor, Suranaree University of Technology, Rapporteur
Mme. Teeraporn SUTEEWONG
Lecturer, KMITL, Examinateur
M. Somrerk CHANDRA-AMBHORN
Associate Professor, KMUTNB, Co-directeur de thèse en Thaïlande
Mme. Valérie PARRY
Maître de conférences, Grenoble INP, Co-directeur de thèse en France
Mme. Walairat CHANDRA-AMBHORN
Assistant Professor, KMITL, Directeur de thèse en Thaïlande
M. Yves WOUTERS
Professeur, Université Joseph Fourier, Directeur de thèse en France

ACKNOWLEDGEMENTS

First, I would like to gratefully acknowledge Franco-Thai scholarship supported by French government for giving me the greatest opportunity in my life that is study in France. Furthermore, Franco-Thai scholarship as well as Grenoble Institute of Technology (INPG) and Faculty of Engineering, King Mongkut's Institute of Technology Ladkrabang (KMITL) financially support my education fees, my living cost in France, assurances and research resourcing costs. I also would like to thank Dr. Moncef Meddeb, Dr. Stéphane Roy and Ms. Wanpen Sirapat and Ms. Salisa Limsakul who have taken care of me and given advice and helps during my Ph.D. study.

I cannot express enough thanks to my thesis directors; Prof. Yves Wouters and Asst. Prof. Walairat Chandra-ambhorn, my thesis co-directors; Assoc. Prof. Valérie Parry and Assoc. Prof. Somrerk Chandra-ambhorn, and Prof. Alain Galerie who always patiently and kindly advised, suggested and took care of me. Not only about my academic problems have you attended but also my living and sentiment.

I would like to sincerely thank to my defense president and reveiwer, Prof. Sébastien Chevalier, another reviewer, Assoc. Prof. Pornwasa Wongpanya, and examiners, Assoc. Prof. Prakob Kijchaiya, Assoc. Prof. Duangkamol Na-Ranong and Dr. Teetaporn Suteewong for accepting to be the jury in my thesis defense.

My completion of this project is much more difficult to accomplish without the helps and supports of the members of SIMaP Laboratory, CMTC, LEPMI and Phelma ; Grégory Berthomé, Laurence Latu-Romain, Frédéric Charlot, Thierry Encinas, Stéphane Coindeau, Alexandre Crisci, Raphael Boichot, Marc Mantel and Richard Bressoux. Also, I would like to thank Jacqueline Cuoq, Jean-Pierre Petit, Céline Pascal, Jean-Jacques Franciosi, Alain Domain, Anusara Srisrual, Abdelhahim Loucif, Milan Skocic, Isamaël Guillotte, Nàthalia De Castro Pissolati, Vanessa Raponi, Youcef Madi, Audrey Col, Jingxian Wang, Diego Pinheiro Aun, Elise Gardin, Yannick Le Port, Adrien Le Gentil and anyone who used to contact me and gave me the helps in any chances for their occasionally helps and a good working atmosphere in the group.

I also have to thank Prof. Suchatvee Suwansawat, president of KMITL, the lecturers and staffs of School of Chemical Engineering, KMITL for merciful helps, especially for Dr. Santi Wattananusorn who gave me the knowledge of transport phenomena and boundary layer calculation.

For the living in France where the culture, language, tradition and climate are completely different from Thailand, I must acknowledge Thai student community in Grenoble for the supports, joyful, helps and taking care each other like a family. I gave a special thanks to Anusara Srisrual, Jiravan Mongkoltanatas, Siridhorn Soonthornthum, Priew Eiamlamai, Nittaya Samati, Patpong Amonwat, Ratchaneekorn Kamchan, Sakson Promkesa Kanaparin Ariyawong and Jarukan Jitwongnan for sincere helps and attentions. I am very happy to know all of you.

Finally, to my caring, loving, and supportive family and my best friends; Prateep Lueprasert, Winatta Sakdasri and Warangkhana Yanphaisan, when times got rough I am very appreciated that you have always been by my side. I am very lucky to be a part of our family and be your friend.

Wichitra Wongpromrat

Contents

Chapter 1

Introduction

1.1 Background

High temperature corrosion is an important problem obstructing the development in many fields. For example, the degradation of materials due to high temperature corrosion in high temperature units of the industry leads to not only increasing the operating costs but may also affects the safety. The violent level depends on the chemicals and operating conditions. Another important application involving with high temperature corrosion problem is power generation process. In this research, high temperature corrosion in this application was focused.

According to the drastic increase in petroleum prices and environmental problems such as global warming, the alternative clean and sustainable energy sources are needed in order to supply the ever-growing demand. H_2 is one of the attractive choices that can be used as a fuel for the future. H_2 can be generated by various processes such as hydrocarbon reforming, biomass gasification, electrolysis of water etc. Among these processes, electrolysis of water seems to be the most interesting choice since it needs just only water which is a clean and renewable resource as a reactant [1]. Electrolysis is an electrochemical process that supplies electric energy to separate water into H_2 and O_2 [2]. Electricity can be produced by supplying H_2 and O_2 obtained from the electrolyser to the power generators that are fuel cells (FCs). The FCs can be classified into 6 categories: polymer electrolyte membrane fuel cells (PEMFCs), direct methanol fuel cells (DEFCs), alkaline fuel cells (AFCs), phosphoric acid fuel cells (PAFCs), molten carbonate fuel cells (MCFCs) and solid oxide fuel cells (SOFCs). Among these, SOFC is the most attractive FC because its efficiency can be reached up to 60% which is the highest efficiency that FCs could produce.

Due to high temperature operation more than 1000°C of conventional SOFCs, the traditional materials used in SOFCs must be ceramic materials. The problems of this SOFC are the complicated fabrication of electrolyte and the expensive ceramic capital costs. Since the molding process of the electrolyte has been improved, its ohmic resistance was reduced, so, the operating temperature of SOFC can be reduced to intermediate temperature around 800°C. Thus, metallic materials, especially ferritic stainless steels, have been tried to use as interconnect [3]–[5] due to their oxidation resistance, electrical conductivity, thermal expansion match with other cell components, cheaper cost, etc.

However, high temperature corrosion can occur in the metallic interconnect part of SOFCs. Normally, Cr in the steels would be reacted with O_2 and forms chromium oxide or chromia scale (Cr_2O_3) covering the steels. This is protective layer preventing the contact of O_2 and the steel components. Thus, the rust cannot be formed. Nevertheless, at high temperature operation containing O_2 and/or H_2O like cathodic SOFC condition, Cr_2O_3 is volatilised by reacting with O_2 (especially with wet O_2), then, the steel loses its protective layer resulting in the deterioration of materials and their properties.

For many decades, researchers and developers have been trying to solve this problem. Some alloys are specially developed for using as a metallic interconnect such as Ducrolloy.

However, the expensive cost of Ducrolloy leads to an economic problem. Moreover, due to the Cr-based composition of Ducrolloy, Cr species volatilisation is promoted in higher rate than ferritic stainless steel [6]. Therefore, various coating materials and methods have been tried to coat on ferritic stainless steels for protecting Cr species volatilisation. Unfortunately, there is no method which is able to supply, at least, 40,000 h service lifetime.

In this study, Cr species volatilisation from metallic materials, AISI 441 ferritic stainless steel, was studied and tried to solve by different methods. The simple coating method was used to protect Cr species volatilisation while the new method, surface heat treatment or preoxidation, was also studied. In addition, the specimens, before and after experiment, were characterised by many analysis tools.

1.2 Research scopes

1). Study of Cr species volatilisation from bare AISI 441 ferritic stainless steel. Effect of gas linear velocity, oxidation time and surface roughness on Cr species volatilisation were determined. The condition studied was simulated cathodic condition of SOFC.

2). Characterisations and 3D reconstructions of the nodules developed during short time thermal oxidation of as-received AISI 441.

3). Performance improvement of AISI 441 used as a metallic interconnect in SOFC by the following methods.

- Coating on the specimen surface with Mn-Co spinel by an electroplating method.
- Preoxidation of AISI 441 in Ar at 250 °C for 3 h.
- Preoxidation of AISI 441 in Ar at 850 °C for 3 h.
- Preoxidation of AISI 441 in CO/CO_2 at 250 °C for 3 h.
- Preoxidation of AISI 441 in CO/CO_2 at 850 °C for 3 h.

After coating and preoxidation, Cr species volatilisation from the coated and preoxidised specimens were determined. The results were compared with that of the bare ones.

4). Inductively coupled plasma spectrometry (ICP), scanning electron microscope (SEM), energy-dispersive X-ray spectroscopy (EDX), X-ray photoelectron spectroscopy (XPS), X-ray diffractometer (XRD), Raman spectroscopy and focused ion beam coupled with scanning electron microscope (FIB-SEM) were used for observing the specimens.

References

[1] J. D. Hooladay, J. Hu, D. L. King, and Y. Wang, “An overview of hydrogen production technologies,” Catal. Today, vol. 139, pp. 244–260, 2009.

[2] D. Marcelo and A. Dell’Era, “Economical electrolyser solution,” Int. J. Hydrogen Energy, vol. 33, pp. 3041–3044, 2008.

[3] Z. Yang, M. S. Walker, P. Singh, and J. W. Stevenson, “Anomalous corrosion behavior of stainless steels under SOFC interconnect exposure conditions,” Electrochem. Solid-State Lett., vol. 6, no. 10, p. B35, 2003.

[4] N. Shaigan, W. Qu, D. G. Ivey, and W. Chen, “A review of recent progress in coatings, surface modifications and alloy developments for solid oxide fuel cell ferritic stainless steel interconnects,” J. Power Sources, vol. 195, no. 6, pp. 1529–1542, Mar. 2010.

[5] R. Sachitanand, M. Sattari, J.-E. Svensson, and J. Froitzheim, “Evaluation of the oxidation and Cr evaporation properties of selected FeCr alloys used as SOFC interconnects,” Int. J. Hydrogen Energy, vol. 38, no. 35, pp. 15328–15334, Nov. 2013.

[6] M. Stanislowski, E. Wessel, K. Hilpert, T. Markus, and L. Singheiser, “Chromium vaporization from high-temperature alloys,” J. Electrochem. Soc., vol. 154, no. 4, p. A295, 2007.

Chapter 2

Bibliography

2.1 Fuel cells

Fuel cells are the electrochemical devices converting chemical energy to electrical energy. Fuel cells are composed of electrodes, that are negative and positive electrodes called anode and cathode respectively, and electrolyte sitting between the two electrodes [1]. Figure 2.1 shows the schematic of fuel cells.

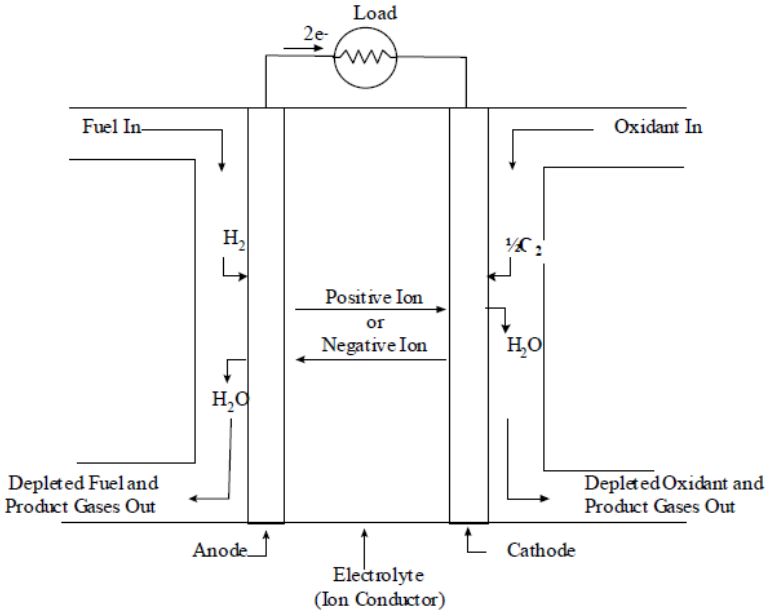

Figure 2.1 The schematic of fuel cells [1].

Fuel and oxidant would be continuously fed to anode and cathode respectively. The electrochemical reactions occur at the electrodes and the electricity is produced. Eqs. 2.1-2.2 show the reactions occurring at anode and cathode sides respectively for oxygen and hydrogen reactants [2].

Anode: $H_2(g) + O^{2-}(g) \rightarrow H_2O(g) + 2e^-$ (Eq. 2.1)

Cathode: $0.5O_2(g) + 2e^- \rightarrow O^{2-}(g)$ (Eq. 2.2)

2.1.1 Classification of fuel cells

Fuel cells are classified into 6 categories by the type of electrolyte : polymer electrolyte membrane fuel cells (PMEMFCs), direct methanol fuel cells (DEFCs), alkaline fuel cells (AFCs), phosphoric acid fuel cells (PAFCs), molten carbonate fuel cells (MCFCs) and solid oxide fuel cells (SOFCs) [1], [3]-[5].

Among these categories, SOFCs are the most efficient one which is able to produce electricity reaching up to 65% efficiency. In addition, various fuel gases can be used i.e. H_2, CH_4 and CO_2 that are able to be obtained from several sources [6]. Thus, in this research, the condition study is SOFC conditions.

2.1.2 Classification of SOFCs

2.1.2.1 Tubular SOFC

The components of a tubular SOFC are assembled in the form of a hollow tube. The cell is constructed in layers around a tubular cathode. Air is flowed in the tube while fuel is flowed around the exterior as shown in Figure 2.2. The advantage of tubular SOFC is that the air and the fuel are naturally isolated because the tubes are closed at one end, so the high temperature seal is not required to separate the fuel from the oxidant. This makes the performance of tubular SOFC very stable over several years. However, the disadvantages are not only the complicated construction and high investment costs, but also the power density produced by tubular SOFC is much lower than that of planar SOFC [7], [8].

2.1.2.2 Planar SOFC

Planar SOFC has been developed from tubular SOFC by increasing operating area while decreasing the cell size. Thus, the current density of planar SOFC is higher than that of tubular SOFC. Due to higher specific current path of planar SOFC, planar SOFC has higher efficiency than tubular SOFC. Furthermore, the construction of planar SOFC is less complicated leading to cheaper investment cost than the tubular one. Figure 2.3 shows a schematic of planar SOFC.

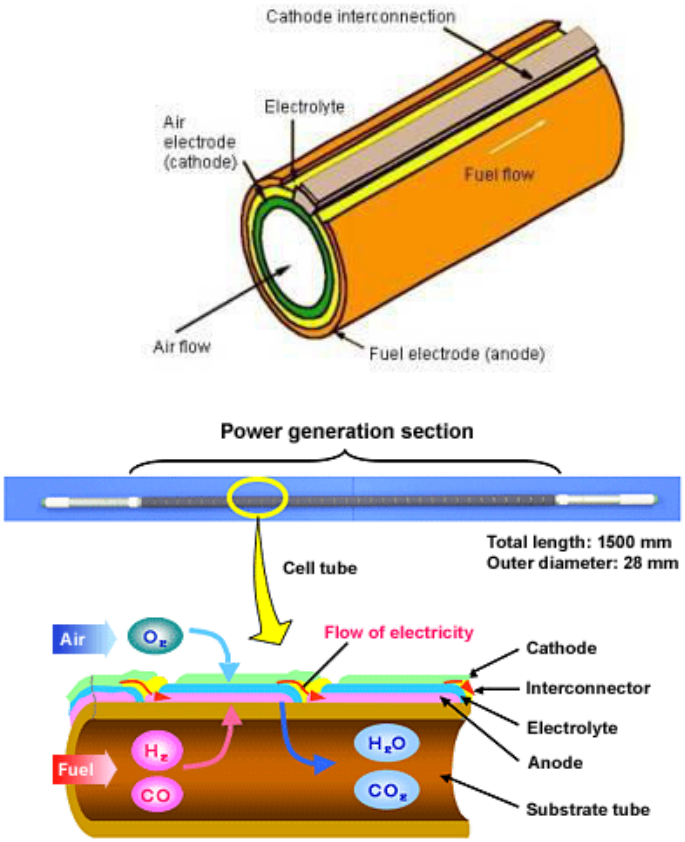

Figure 2.2 Tubular SOFC [7], [9].

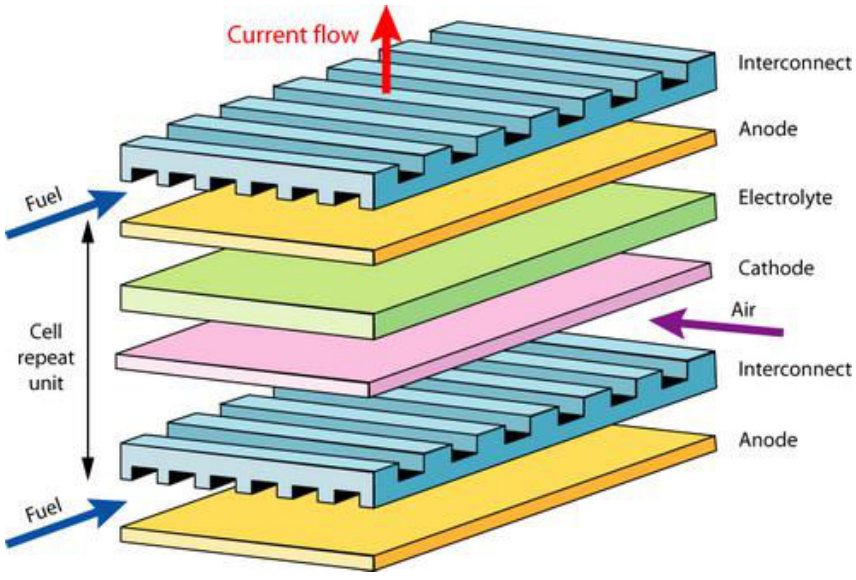

Figure 2.3 Planar SOFC [10].

2.1.3 Interconnect of SOFC

SOFCs comprise anode, electrolyte and cathode. The combination of these components is called single cell. Several single cells are connected in series with interconnect material which is responsible as follows [11]:

1). For separating the fuel flow of one cell and the oxidant flow of the neighbouring cell.

2). For carrying the electricity generated from each single cell to the external circuit.

As mentioned above, the fuel cells are classified by the type of electrolyte materials. For SOFC, the electrolyte is solid oxide material that is ceramic, so other components of SOFC are traditionally made of ceramic materials because of compatibility with the electrolyte. The traditional interconnect is also made of costly ceramic. Therefore, the operating condition of SOFC must be higher than 1000 °C in order to maintain high electrical conductivity of the interconnect and ionic conductivity of the electrolyte. Since the molding process has been improved, the operating temperature of SOFCs can be reduced to an intermediate temperature around 800 °C, and metals could be tried to be used as interconnect of SOFCs. The attractive reasons that metals are applied instead of ceramics are shown in the following [12].

1). Lower material and fabrication costs comparing with the ceramic one.

2). Easier to fabricate.

3). Better electrical and thermal conductivities.

4). No deformation due to different gas atmospheres across the interconnect.

However, the materials applied as interconnect must be able to fulfil the following requirements [3], [11], [13], [14]:

1). Be stable at high temperatures.

2). High temperature oxidation and corrosion resistances in both anodic and cathodic atmospheres.

3). Excellent electrical conductivity with preferably nearly 100% electronic conduction.

4). Thermal expansion match with other cell components.

5). Low permeabilities of H_2 and O_2 to minimise the direct combination reaction.

6). Chemical compatibility in both fuel and oxidant.

7). No reaction or inter-diffusion between interconnect and its adjacent components, in particular for anode and cathode.

8). Easy to fabricate.

9). Adequate high temperature strength and creep resistance.

2.2 Stainless steels [15], [16]

The metallic materials which have been applied for using as an interconnect are stainless steels because of their high oxidation and corrosion resistances.

Generally, corrosion of the metals can easily occur in humidified atmosphere leading to the formation of rust and degradation of materials. The rust would be continuously formed via electrochemical reaction because of high anodic property of the metals against oxygen.

Stainless steels are the Fe-based alloys with a combination of Cr at least 11-12%, so stainless steels have more special property than the common ones. This property is the corrosion resistance that means anti-rust formation even though stainless steels are in humidified and/or the acidic atmosphere. Therefore, in summary, the addition of Cr in the metals affects the decreasing of anodic property of the metals (the increasing of cathodic properties of the metals).

Cr is an important component in the stainless steels. The anodic property of Cr element is higher than that of H (electropotential = 0). However, if Cr is put in nitric acid (HNO_3) or chromic acid (H_2CrO_4), at the beginning, its anodic property still remains (negative electropotential) but it becomes cathodic element after holding for a while. Its electropotential increases to about 0.8-0.9 V. Thus, Cr is not corroded anymore. This property is called "passivity" or "passive state". This passivity is a result of the reaction of Cr with O leading to the formation of Cr_2O_3 on the surface. This Cr_2O_3 is a film protecting the movement of electron or reducing the motion ability of electron. Therefore, the electrochemical reaction is even more difficult, so corrosion is suppressed.

For the passivity property, Cr in the alloy needs to be higher than 11-12%. According to the experiment determining the anodic and cathodic properties of Cr-containing alloys with different percentages of Cr in diluted sulfuric acid (H_2SO_4), the results are shown in Figure 2.4.

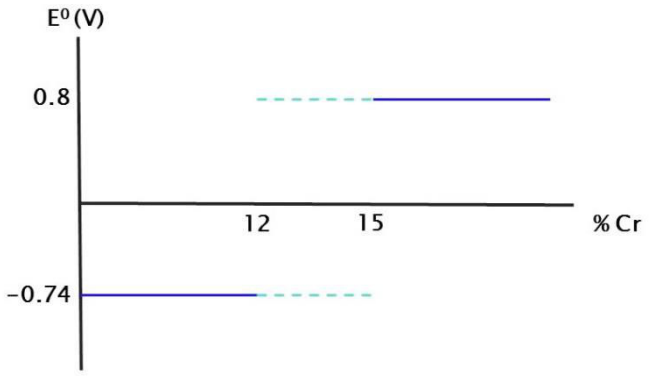

Figure 2.4 The correlation of electropotential and Cr contents in the alloy [16].

C is an element normally introduced in the alloy for increasing the mechanical strength. It can be well reacted with Cr and forms chromium carbide (Cr_xC_y) leading to the decreasing of Cr in the alloy to be lower than 12% (in case of 12% addition of Cr in the alloy). Thus, the rust can still form (electropotential < 0). Normally, 15-18% Cr is necessary in the alloy for preventing the decreasing of Cr to be less than 12% after reacting with C.

Cr_xC_y is mostly formed along the metallic grain boundaries. Hence, in Fe-15%Cr, Cr along the metallic grain boundaries is probably less than 12% (depends on the amount of C in

the alloys). The alloys would be corroded along the metallic grain boundaries, a phenomenon which is called “intergranular corrosion” shown in Figure 2.5.

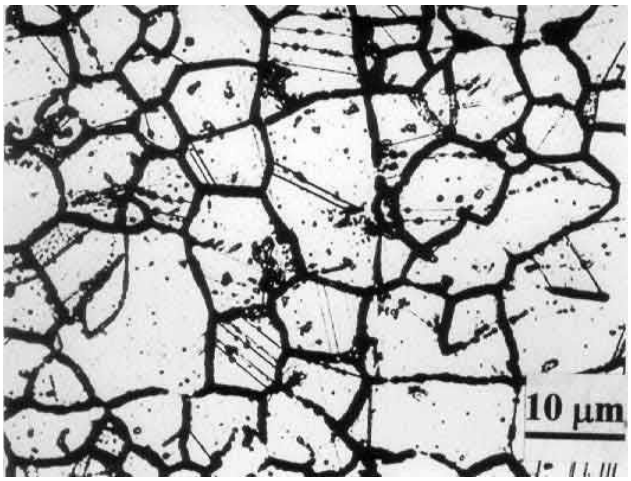

Figure 2.5 Intergranular corrosion [16].

2.2.1 Classification of stainless steels [15], [17]

The stainless steels can be classified into 5 groups. These 4 of 5 groups are classified by their crystallographic structures/microstructures of the alloy that are ferritic stainless steels, martensitic stainless steels, austenitic stainless steels and duplex stainless steels. For the other group called “precipitation-hardenable stainless steels”, these alloys can be hardened by heat treatment.

2.2.1.1 Ferritic stainless steels

Ferritic stainless steels are the simplest stainless steels which are mainly composed of Fe and Cr. Cr is the stabiliser, so the increasing of Cr increases the stabilisation of the steels [16]. The microstructure of the alloys in this family is body-centred-cubic (BCC) that is the same as Fe at room temperature. These alloys are magnetic and cannot be hardened by heat treatment. Typically, the strength of ferritic stainless steels is not high. After annealing, their yield strengths are in the range of 275-350 MPa, poor toughness and high fabricability. The advantages of ferritic stainless steels are the resistance of chloride stress-corrosion cracking, atmospheric corrosion and low cost comparing with other similar oxidation property alloys.

Ferritic stainless steels are composed of 11-30% Cr. The amounts of other elements such as C, N and Ni which are able to compound with Fe to become austenitic are low. In general, the application of ferritic stainless steels depends on the amount of Cr in the steels.

The ferritic stainless steels with low amount of Cr as around 11% such as AISI 405 and AISI 409 have moderate corrosion and oxidation resistances and good fabricability. They can be used in automotive exhaust systems.

The intermediate-Cr (16-18%) alloys such as AISI 430 and AISI 434 are used for automotive trim and cooking utensils. Because of their poor toughness and weldability, these alloys are not readily fabricated as the lower Cr alloys.

The high-Cr (19-30%) alloys such as AISI 442 and AISI 446, which are often referred to the superferritic steels, are used in the high corrosion and oxidation applications. These alloys contain very low C with usual addition of either Mo or Al. The special melting techniques are used for their fabrication leading to very low C and N contents in the alloys. Furthermore, their stabilisation and weldability can be improved by adding the stabilising elements such as Ti and Nb.

2.2.1.2 Austenitic stainless steels

This group is the largest family in terms of number of alloys and usage. These alloys cannot be hardened by heat treatment like ferritic stainless steels. Nevertheless, other properties are not the same as ferritic stainless steels. Austenitic stainless steels are non-magnetic alloys. Their microstructure is face-centre-cubic (FCC) like Fe at high temperatures around 900-1400°C. They possess excellent ductility, formability and toughness even at cryogenic conditions. In addition, they can be substantially hardened by cold work.

Although, Ni is a major element used for stabilising austenitic structure, C and N are additionally used because C and N are readily soluble in FCC structure. Their corrosion resistance depends on the amount of Cr and Mo in the alloys.

Austenitic stainless steels can be subdivided into 2 categories that are Cr-Ni alloys such as AISI 304 and AISI 316 and Cr-Mn-N alloys such as AISI 201 and 18-2Mn. For Cr-Mn-N alloys, Ni amount is normally lower than that in Cr-Ni alloys while N amount is higher in order to maintain the stability of the structure. Mn (5-20%) needs to be added in low Ni alloys to improve solubility of N in the austenite and prevent martensitic transformation. Moreover, the addition of N increases the strength of austenitic alloys. The tensile yield strength of Cr-Ni alloys after annealing is typically around 200-275 MPa. On the contrary, the tensile yield strength of high N alloys is up to 500 MPa.

Figures 2.6a and b show the effect of cold working on the strengths of AISI 301 (7% Ni) and AISI 305 (11.5% Ni) respectively. In addition, work hardening rate depends on composition of the alloys. Comparing Figures 2.6a and b, it can be seen that, at the same %cold work, work hardening rate of AISI 305 (higher Ni) is less than the other one. That means work hardening is inversely proportional to composition of the alloys.

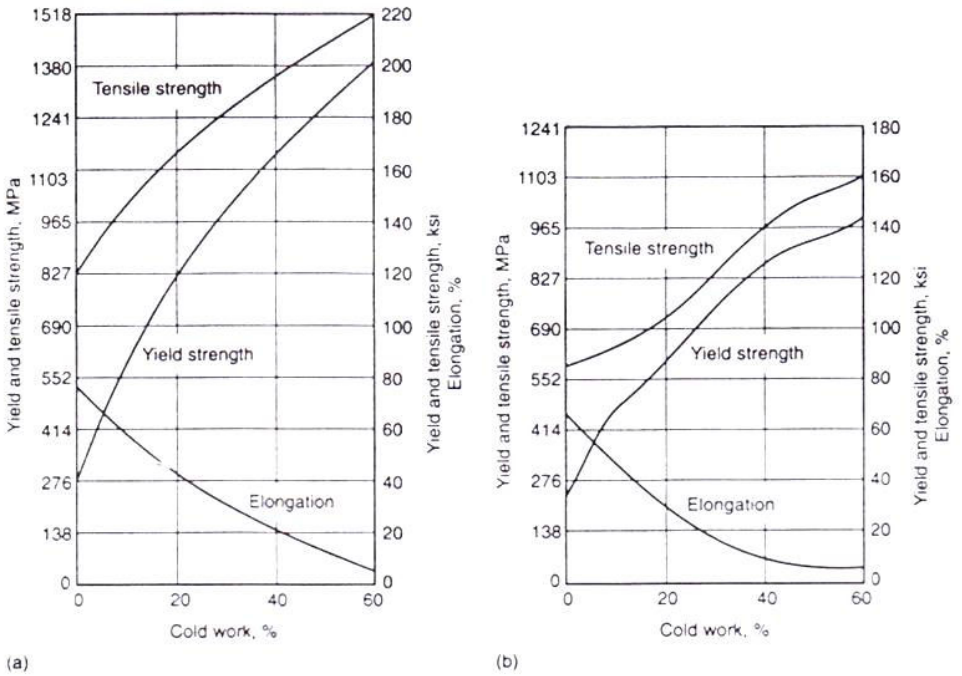

Figure 2.6 Effect of cold working on strength of the alloys a) AISI 301 and b) AISI 305 [15].

Another property depending on composition of the alloys is corrosion resistance. Mo is added to austenitic stainless steels for improving corrosion resistance in chloride atmosphere. For high temperature oxidation conditions, high Cr-containing alloys such as AISI 309 and AISI 316 are used whereas high Ni-containing alloys are used in severe reducing acid environments. For preventing intergranular corrosion when using in high temperature application, Ti or Nb is added to stabilise C. Also, lower C alloys (AISI L or S designations), such as AISI 304L, have been established to prevent intergranular corrosion. Furthermore, Ni-based alloys (32-34% Ni) possess high corrosion resistivity.

2.2.1.3 Martensitic stainless steels

This category is similar to Fe-C alloys that are austenite, hardened by quenching and then tempered for increasing ductility and toughness. These alloys are magnetic. Their heat-treated structure is body-centred-tetragonal (BCT). In the annealed condition, the tensile yield strength of these alloys is about 275 MPa that is appropriate for machining, cold forming and cold working.

Hardening by heat treatment is dependent on C content in the alloys. Increasing of C content increases strength but decreases ductility and toughness. Wear resistance of martensitic stainless steels is also proportional to C content in the alloys.

Ductility and corrosion resistance can be improved by adding Mo and Ni to martensitic stainless steels. Ni also serves to maintain the desired microstructure, preventing excessive free ferrite when higher Cr contents are used for improving corrosion resistance. However, the addition of these elements is somewhat restricted because higher amounts of additional elements affect a microstructure that is not fully martensitic.

2.2.1.4 Duplex stainless steels

This family is Cr-Ni-Mo alloys that are balanced to contain a mixture of austenite and ferrite. They are magnetic. The duplex structure leads to improve stress-corrosion cracking resistance comparing with austenite while their ductility and toughness are improved comparing with ferrite. In annealed condition, tensile yield strengths of duplex stainless steels are in the range of 550-690 MPa that are around 2 times of tensile yield strength of each phase alone.

The original alloy in this group was obtained by the addition of N in the ferritic stainless steel grade AISI 329 for increasing the amount of austenite to nearly 50%. In addition, N also improves as-welded corrosion properties, chloride corrosion resistance and toughness. The toughness of the alloys is proportional to the amount of austenite in the structure.

2.2.1.5 Precipitation-hardenable (PH) stainless steels

This category is Cr-Ni alloys that can be hardened by aging treatment. These alloys can be subdivided into 3 groups by their solution-annealed condition microstructures that are austenitic (such as A286), semi-austenitic (such as PH 17-7) and martensitic (such as 17-4PH). If the semi-austenitic is heat treated, the austenite structure transforms to martensite. In order to facilitate the aging treatment in cold work, some elements are compounded such as Al, Ti Nb or Cu.

Similar to martensitic stainless steels, PH alloys can attain high tensile yield strength up to 1700 MPa. They also have good toughness and ductility with moderate-to-good corrosion resistance. A combination of strength and corrosion resistance is better achieved than martensitic stainless steels because PH alloys contain higher Cr, Ni and Mo while C content is very low. Due to very low C content of the martensitic PH stainless steels, these alloys have good toughness and ductility while the wear resistance is reduced.

The most well-known PH stainless steel is 17-4PH that is composed of Cr and Ni with Cu for age hardening and Nb for stabilising C. The age hardening agents used in other alloys include Ti (Custom 455), Al (PH13-8Mo) and Nb (Custom 450). Mo and Cu are added to improve corrosion resistance. C content is normally restricted except in semi-austenitic such as 634 which C is required to provide the desired phase transformation.

2.2.2 Appropriate stainless steels used as a metallic interconnect

According to the required properties of interconnect as described above, the properties of stainless steel candidates must also be considered. Table 2.1 shows the physical properties of some stainless steel grades.

Table 2.1 Physical properties of stainless steels [15].

AISI grade	CTE* (μm/m°C) from 0°C to			Thermal conductivity	Electrical resistivity	Melting range (°C)
	315°C	538°C	850°C**	(W/mK) at 500°C	(nΩ m)	
Ferritic						
430	11.0	11.4	11.96	26.3	600	1425-1510
430F	11.0	11.4	11.96	26.3	600	1425-1510
434	11.0	11.4	11.96	26.3	600	1425-1510
444	10.6	11.4	12.52	-	620	-
446	10.8	11.2	11.76	24.4	670	1425-1510
Austenitic						
201	17.5	18.4	19.66	21.5	690	1400-1450
301	17.2	18.2	19.60	21.5	720	1400-1420
302	17.8	18.4	19.24	21.5	720	1400-1420
303	17.8	18.4	19.24	21.5	720	1400-1420
304	17.8	18.4	19.24	21.5	720	1400-1450
305	17.8	18.4	19.24	21.5	720	1400-1450
316	16.2	17.5	19.32	21.5	740	1375-1400
317	16.2	17.5	19.32	21.5	740	1375-1400
321	17.2	18.6	20.56	22.2	720	1400-1425
Martensitic						
410	11.4	11.6	11.88	28.7	570	1480-1530
414	11.0	12.1	13.64	28.7	700	1425-1480
416	11.0	11.6	12.44	28.7	570	1480-1530
420	10.8	10.8	10.80	-	550	1450-1510
431	12.1	-	-	-	720	-
PH						
PH13-8Mo	11.2	11.9	12.88	22.0	1020	1400-1440
15-5 PH	11.4	-	-	23.0	770	1400-1440
17-4 PH	11.6	-	-	23.0	800	1400-1440
17-7 PH	11.6	-	-	21.8	830	1400-1440

*CTE = Coefficient of thermal expansion

** Estimated value obtained from extrapolation of CTE from 0 °C to 315°C and 538°C

All stainless steels have good melting point ranges. They would not be melted during modern SOFC operation at temperatures lower than 1000°C. Electrical resistivity of austenitic and PH stainless steels is higher than that of ferritic and martensitic stainless steels while their thermal conductivity is lower. Therefore, ferritic and martensitic are proper than other stainless steel families for SOFC. CTE is another important property that must be considered. As mentioned before, it should match with the other SOFC components. Taking into account lanthanum strontium manganite (LSM) commonly used as a cathode in SOFC, its CTE is 12×10^{-6} /K at 850°C [14]. The CTEs of ferritic stainless steels and martensitic stainless steels are very close to the CTE of LSM. Another important properties of interconnect are corrosion and oxidation resistances that must be high. Ferritic stainless steels have better corrosion resistance comparing with martensitic ones [18]. Thus, the best stainless steel candidate used as metallic interconnect is ferritic stainless steels.

2.3 High temperature oxidation of stainless steel in SOFC condition

Before explaining about high temperature oxidation of ferritic stainless steels, it is necessary to understand the reactions occurring during high temperature operation. There are 2 reactions occurring in series: chromia scale formation, Eq. 2.3, and Cr volatilisation. For Cr species volatilisation, many reactions are possible depending on the oxidation atmospheres. The major Cr species volatilisation reactions in O_2 and wet O_2 are shown in Eqs. 2.4-2.6 [19], [20].

$$Cr(s) + O_2(g) \rightarrow Cr_2O_3(s) \quad \text{(Eq. 2.3)}$$

$$Cr_2O_3(s) + 1.5O_2(g) \rightarrow 2CrO_3(g) \quad \text{(Eq. 2.4)}$$

$$Cr_2O_3(s) + O_2(g) + H_2O(g) \rightarrow 2CrO_2(OH)(g) \quad \text{(Eq. 2.5)}$$

$$Cr_2O_3(s) + 1.5O_2(g) + 2H_2O(g) \rightarrow 2CrO_2(OH)_2(g) \quad \text{(Eq. 2.6)}$$

Even though Cr species volatilisation is focused in this study, the oxide formation is also important. Therefore, in this section, overall high temperature oxidation is firstly elucidated and Cr species volatilisation would be explained in the next section (Section 2.4).

2.3.1 Mechanism of metal-oxygen reaction

The simplest chemical reaction of a metal (M) and O_2 is written as Eq. 2.7. The mechanism path of this reaction contains many steps that are illustrated in Figure 2.7.

$$xM + \frac{y}{2}O_2 = M_xO_y \quad \text{(Eq. 2.7)}$$

The initial step of the metal-oxide reaction is the adsorption of atomic O on the metal surface. O dissolves in the metal. The oxide nucleates and grows on the surface either as a film or as separate oxide nuclei. These steps, the adsorption and initial oxide formation, depend on surface orientation, crystal defects at the surface, surface preparation and the impurities in the metal and gas [21]. After that, the oxide grows and covers the surface as a film acting as a diffusion barrier protecting the metal from the gas, so the following reactions can proceed only through the solid-state diffusion of the reactants through the film. During growing up of the scale (a thick film), cavities and microcracks may be created as the result of stress generation in the scale. This could lead to cracking, spallation, and failure of the oxide scale.

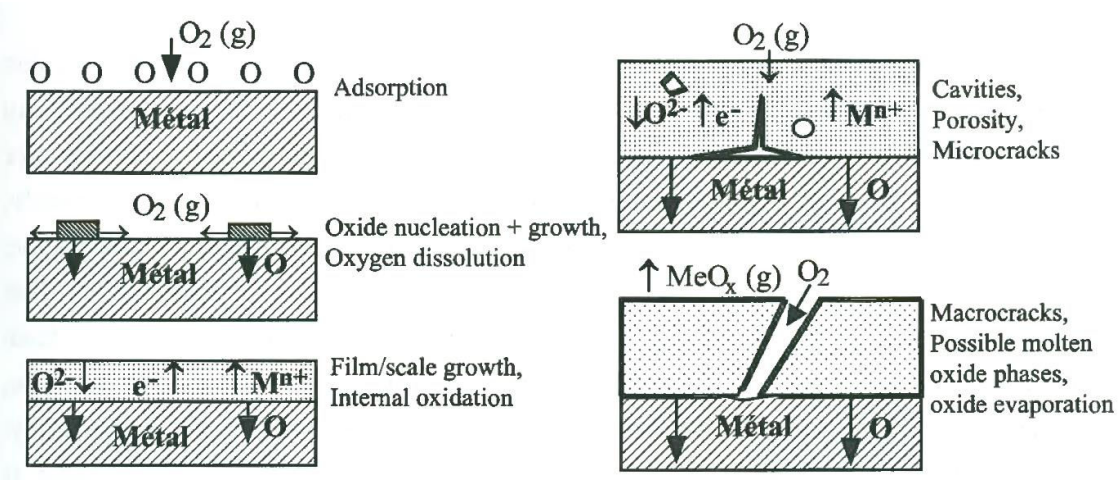

Figure 2.7 Schematic illustration of some main metal-oxygen reactions [22].

2.3.2 Thermodynamics of high temperature oxidation

Considering the example of the metal-oxide, M_xO_y, formation in Eq. 2.7, this chemical reaction is driven by the Gibbs free energy change (ΔG) shown in Eq. 2.8.

$$\Delta G = \Delta G^\circ + RT\ln K \qquad \text{(Eq. 2.8)}$$

where ΔG° = Standard Gibbs free energy change
R = Gas constant
T = Absolute temperature
K = Equilibrium constant

K can be expressed in terms of the activity (a) as in Eq. 2.9.

$$K = \frac{a_{product}}{a_{reactant}}$$

$$K = \frac{a_{M_xO_y}}{(a_M)^x \cdot (a_{O_2})^{y/2}} \qquad \text{(Eq. 2.9)}$$

At high temperatures and low pressures, the activity of O_2 can be approximately estimated by its partial pressure (P_{O_2}). The activities of solids are constant (a = 1). Therefore, at the equilibrium stage where $\Delta G = 0$, the standard Gibbs free energy change of the oxide can be expressed in Eq. 2.10.

$$\Delta G°(M_xO_y) \cong RT \ln\left(\frac{1}{(P_{O_2})^{y/2}}\right) \quad \text{(Eq. 2.10)}$$

The chemical reaction can spontaneously occur when $\Delta G°(M_xO_y)$ is negative value or at the equilibrium stage. Thus, the oxide can be formed if the Eq. 2.11 is actualised [21].

$$\Delta G°(M_xO_y) \leq RT \ln(P_{O_2})^{-y/2}$$
$$\Delta G°(M_xO_y) \leq -\frac{yRT}{2}\ln(P_{O_2})$$
$$-\frac{2\Delta G°(M_xO_y)}{yRT} \leq \ln(P_{O_2})$$
$$P_{O_2} \geq \exp\left(-\frac{2\Delta G°(M_xO_y)}{yRT}\right) \quad \text{(Eq. 2.11)}$$

2.3.3 Defects

As mentioned above, defects are one of the factors affect the oxidation process. Hence, before moving to the next sections, some explanations about defects are described.

Defects are an imperfection in the crystalline structure. They may affect the diffusion of species (cations and anions) and the growth of oxide scale. Defects can be classified into 3 groups by the crystallographic structures: point defects, line defects and plane defects.

2.3.3.1 Point defects

These defects disturb the crystal pattern at an isolated site. They can be distinguished as intrinsic and extrinsic defects [23].

Intrinsic defects appear in material sites when atoms are missing from their positions leading to vacancy creation. In addition, it can also occur when particles occupy the interstices between the regular lattice sites (interstitials). The point defects are also composed of heteroparticles (such as S on O site) and theoretically of misplaced atoms i.e. a cation on an anion site (energetically not favourable). Generally, the mole fraction of point defects in inorganic compounds does not exceed 10^{-3}-10^{-2}. If this value is exceeded, point defects may cluster or associate and the aggregation of point defects probably occurs leading to the formation of extended defects such as the planar defect [21], [22]. The intrinsic defects are shown in Figure 2.8.

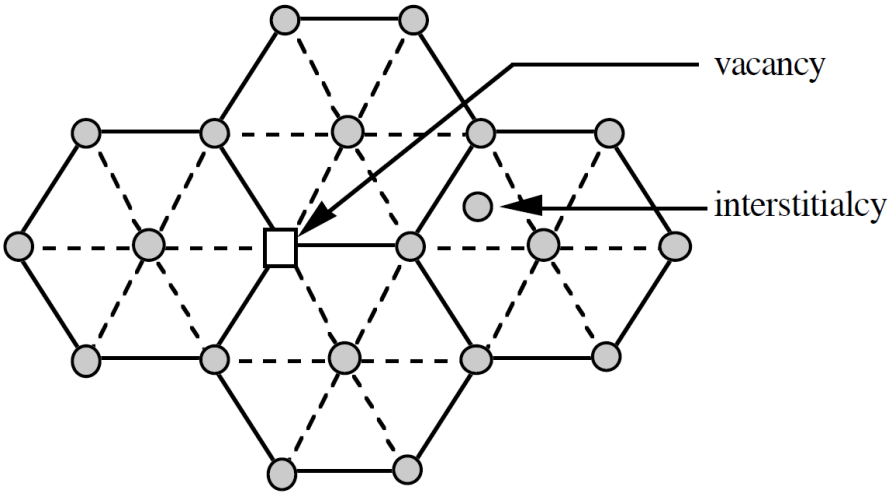

Figure 2.8 The intrinsic defects caused by the missing of atom and interstitial atom [23].

Extrinsic defects occur because of the addition of foreign atoms in materials. The foreign atoms are called solutes in case that they are intentionally added. On the other hand, they are called impurities if they are not intentionally added. The solutes or impurities may occupy the lattice sites (substitutional sites) or may fill interstitial sites. The extrinsic defects affect almost all engineering properties, in particular for electronic properties in a semiconducting crystal.

2.3.3.2 Line defects

Line defects or dislocations occur by displacement in the periodic structure of the crystal in the certain line. Dislocations can be separated into screw dislocation and edge dislocation as shown in Figure 2.9. Screw dislocations exist because of the distortion of the structure by shear stress. Edge dislocations are caused by the termination of atomic connections within the crystal structure.

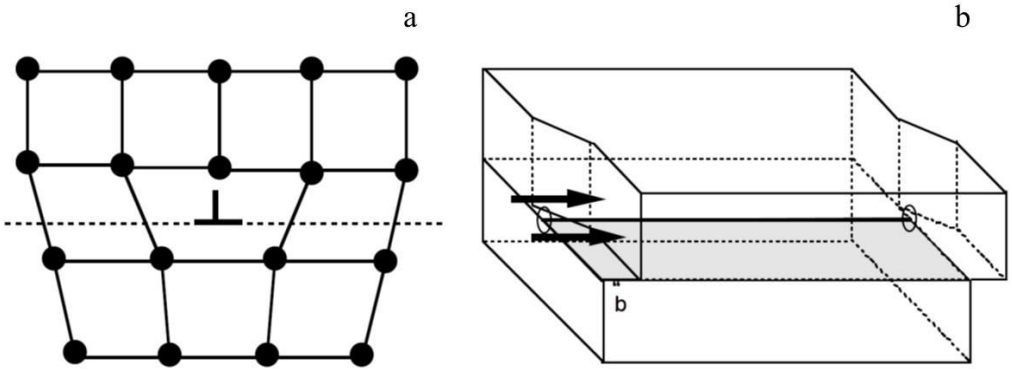

Figure 2.9 a). Edge dislocation and b). screw dislocation. The dotted planes show the slip planes [23].

2.3.3.3 Plane defects

Plane defects are located at the interfaces of homogeneous regions. These defects comprise the stacking faults, internal surfaces (grain boundaries) and external surfaces.

2.3.3.4 Electronic defects

There is one more type of defects caused by electronic imperfection i.e. electrons and holes. If electrons and/or holes are localised at atoms or regular sites in the structure, the electronic defects occur. Electronic defects commonly provide the point defects in the structure. These defects are divided into 2 types that are Frenkel defect and Schottky defect which are shown in Figure 2.10.

Frenkel defect occurs when the smaller ion, definitely cation, is displaced from its position to an interstitial site. Thus, the point defect of cation interstitial is found in the new location of cation while cation vacancy is created at its original location.

Schottky defect occurs when one ion, negative or positive, is missing at its position in its lattice site leading to the presence of vacancy. The opposite ion must diffuse to the appropriate adjacent sink to maintain the electronic neutrality of the structure and leaves also a vacancy.

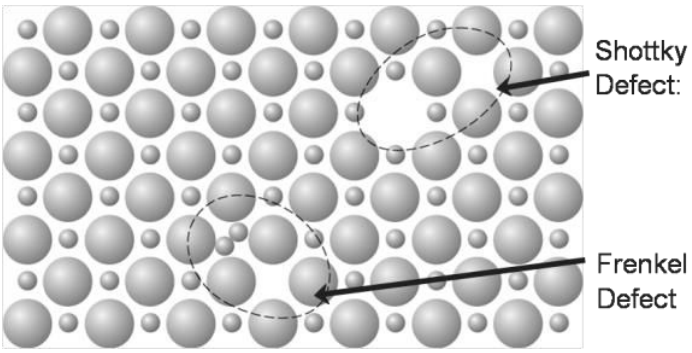

Figure 2.10 Electronic defects in a crystallographic structure [24].

2.3.4 Diffusion

Diffusion is a random movement of particles by using their own energy, no bulk motion (convection) is required. The diffusion rate depends on temperature and particle size. In solid-state diffusion, the particles refer to atoms, ions, vacancies and interstitials. The diffusion occurs from high to low particle chemical potential regions [25]. At steady state, the diffusion of the particles follows Fick's first law shown in Eq. 2.12.

$$J = -D\frac{\partial \phi}{\partial x} \qquad \text{(Eq. 2.12)}$$

where J = Diffusion flux

D = Diffusion coefficient

$\frac{\partial \phi}{\partial x}$ = Concentration gradient of the diffusing species

However, the most particles diffuse at non-steady state. This results in the accumulation or depletion of the diffusing species. Fick's second law, Eq. 2.13, is used for describing this phenomenon.

$$\frac{\partial \phi}{\partial t} = D\frac{\partial^2 \phi}{\partial x^2} \qquad \text{(Eq. 2.13)}$$

Diffusivity of the particles can be affect by various factors: impurities, temperature and short-circuit diffusion. Impurities of the metals can change the defect concentration through their effect on charge balance [25]. For temperature, the diffusion coefficient is dependent directly on temperature described by Arrhenius equation in Eq. 2.14.

$$D = D_0 \exp\left(-\frac{Q_d}{RT}\right) \qquad \text{(Eq. 2.14)}$$

where D = Diffusion coefficient

D_0 = temperature-independent pre-exponential factor

Q_d = Activation energy of diffusion

R = gas constant

T = Temperature

Short-circuit diffusion is the diffusion along the high diffusivity paths that are dislocations and plane defects where the regions provide activation energy of diffusion lower than that in the lattice. This diffusion is an important transport pattern through protective scales.

2.3.5 Oxidation kinetics

Even though, the kinetics of oxidation reaction in terms of reaction rate cannot interpretate oxidation mechanism, the reaction rate is able to use to classify the oxidation behaviour of the metals. Rate equations are classified as logarithmic, linear and parabolic.

2.3.5.1 Logarithmic rate equation

This rate equation is the characteristic of the oxidation of a metal at low temperature (generally below 300-400 °C). It is initially quite rapid and then drops off to low or negligible rate. This behaviour can be described by the logarithmic and inverse logarithmic equations as shown in Eq. 2.15-2.16 and Figure 2.11.

Logarithmic: $x = k_l \log(t+t_0) + A$ (Eq. 2.15)

Inverse logarithmic: $\frac{1}{x} = B - k_{il} \log t$ (Eq. 2.16)

where x may alternatively represents the thickness of the scale, the amount of O consumed per unit area of the metal, etc. t denotes the time, k_l and k_{il} represent the rate constants, A and B are constant.

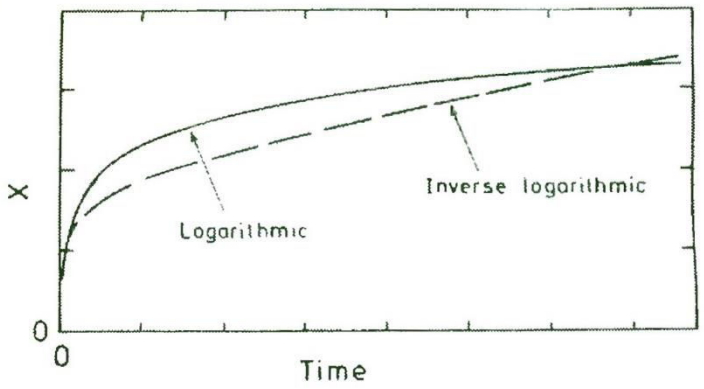

Figure 2.11 Logarithmic and inverse logarithmic oxidation behaviours [21].

2.3.5.2 Linear rate equation

The rate of linear oxidation, Figure 2.12, is constant with time and follows Eq. 2.17.

$$x = kt \qquad \text{(Eq. 2.17)}$$

where k is linear rate constant.

If the oxidation behaviour of the metal is linear that means kinetics may be limited by a reaction step. This possibly includes a steady-state reaction i.e. adsorption at the surface or oxide formation at metal/oxide interface. Thus, this oxidation behaviour cannot found in materials covered by protective layer (except when part of the scale is protective and keeps a constant thickness).

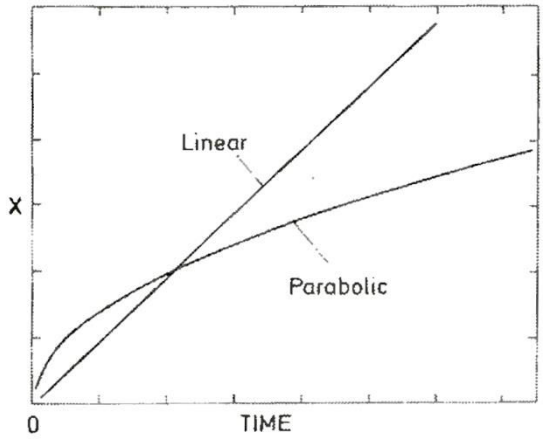

Figure 2.12 Linear and parabolic oxidation behaviours [21].

2.3.5.3 Parabolic rate equation

At high temperatures, the oxidation behaviour of many metals follows a parabolic rate equation as shown in Figure 2.12. This parabolic oxidation can be observed when diffusion of ions through the barrier compact layer is rate determining. According to the growing oxide scale, thicker scale, the diffusion distance is longer, so the reaction rate is continuously decreasing. This behaviour is corresponding to Eq. 2.18.

$$x^2 = k_p t \qquad \text{(Eq. 2.18)}$$

where k_p is parabolic rate constant.

In summary, linear rate equation represents non-protective stage of metal oxidation. Parabolic and logarithmic rate equations imply the protective oxidation of the metals.

In case of porous layer formation, various oxidation patterns can be observed as shown in Figures 2.13-2.14. The behaviour as in Figure 2.13 occurred when the fissure growth rate is sufficiently low. The protective oxide can rebuilt until reaching a critical thickness when the cracking occurs again. For Figure 2.14, the protective stage can be seen as a parabolic oxidation at the initial stage. When the scale thickness reaches a critical thickness, the scale becomes non-protective because of high cracking rate. This catastrophic process is termed “breakaway oxidation.

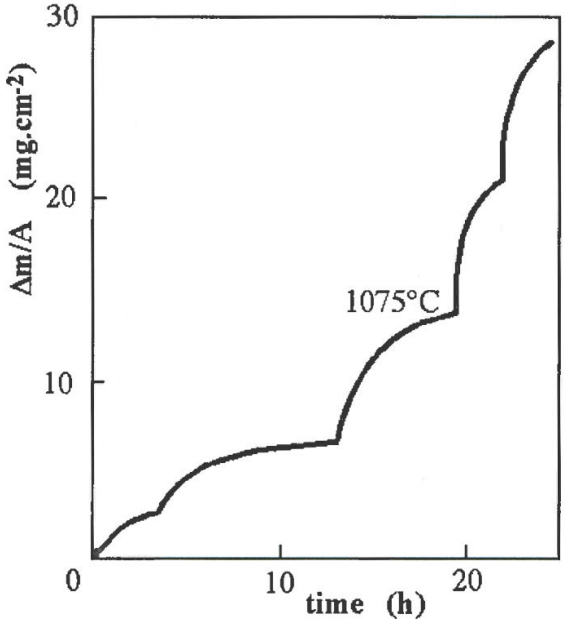

Figure 2.13 Cr oxidation in 1 bar partial pressure of O_2 at 1075°C [22].

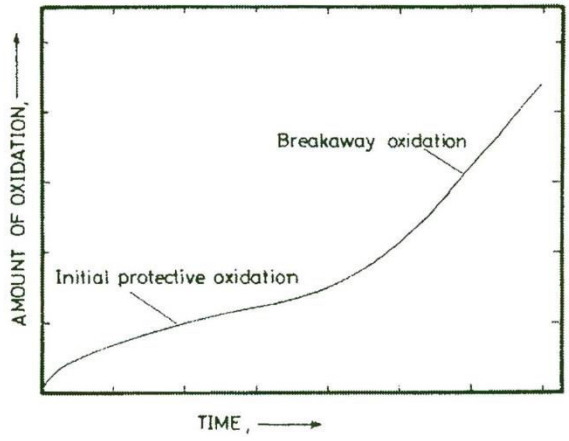

Figure 2.14 Schematic illustration of breakaway oxidation kinetics [21].

In case of the formation of multi-layer scales, a continuous variation of oxidation may be observed. It is explained by the Loriers-Haycock model which considers that, at an initial stage, oxidation behaviour is parabolic oxidation, then, it follows linear kinetics at a critical thickness of the protective sub-scale.

2.4 Cr volatilisation from stainless steels

The failure of stainless steels occurs not only from the cracking of oxide layer, as described in the last section, but also from Cr species volatilisation from the steels. In the condition containing O_2 or wet O_2 at high temperature like SOFC condition, Cr from Cr_2O_3 protective layer is reacted with O_2 and wet O_2 and forms Cr volatile species.

There are 2 steps of Cr species volatilisation occurring in series. Firstly, Cr_2O_3 reacts with O_2 (and possibly H_2O) and forms Cr volatile species. This is the reaction step. Then, these volatile species diffuse through the boundary gas layer to the heart of the gas vein. This is the diffusion step. If the rate of the first step, reaction step, is slower than the other one, the volatilisation reaction is rate determining. Here, Cr species volatilisation is independent on gas flow rate. On the contrary, if the diffusion rate is slower than the reaction rate, Cr species volatilisation is limited by diffusion. In this case, Cr species volatilisation can be accelerated by increasing the flow rate of the gas.

The study of Cr species volatilisation has been begun by Caplan et al. [26]. They studied the phenomenon of Cr species volatilisation from Cr_2O_3 pellets by heating them at 1000-1200°C in various atmospheres. It was found that the oxidation of Cr led to Cr species volatilisation. Cr species volatilisation occurred in O_2, more in wet O_2, but did not occur in Ar or wet Ar. After this first study, Cr species volatilisation has been studied in wider and deeper points of view.

Hilpert et al. [27] modelled thermodynamics data using Chemsage program to thermodynamically study the formation of Cr volatile species in dry and humid air. The results are shown in Figures 2.15-2.16. They found that several Cr volatile species were demonstrated in both, dry and wet, atmospheres. Increasing operating temperature and/or moisture content led to the increased all Cr volatile species contents. The main species volatilised in dry and wet condition are CrO_3 and $CrO_2(OH)_2$ respectively. These results are in good agreement with the study of Gindorf et al. [19]. They also presented the thermodynamic computation using IVTANTHERMO [28] and Ebbinghaus [29], [30]. They found that the Cr species volatilisation reactions should be as shown in Eq. 2.4-2.6 and the main species in low and high humidity condition were CrO_3 and $CrO_2(OH)_2$ respectively.

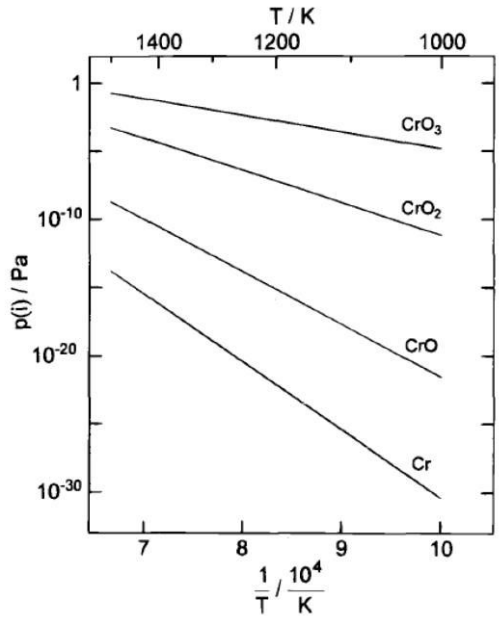

Figure 2.15 Effect of temperature on the formation of Cr volatile species on chromia scale in dry air at partial pressure of O_2 (P_{O_2}) = 2.13×10^4 Pa [27].

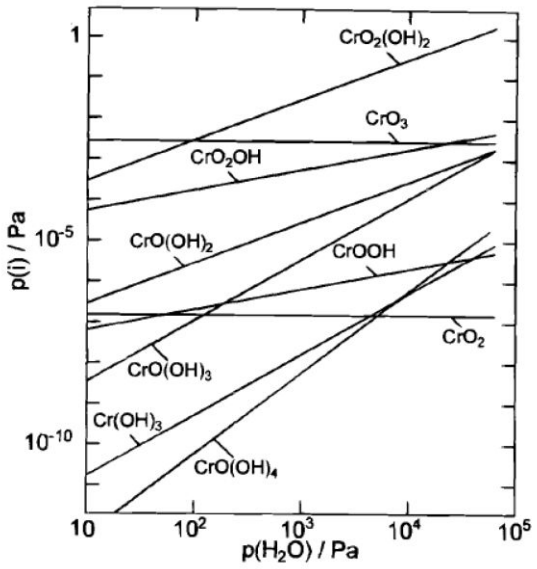

Figure 2.16 Effect of partial pressure of water (P_{H_2O}) on the formation of Cr volatile species on chromia scale in humid air at P_{O_2} = 2.13×10^4 Pa [27].

The effect of temperature, P_{O_2} and P_{H_2O} on Cr species volatilisation were investigated by many researchers [19], [31]-[33]. All results were in consistent that increasing of these factors led to the acceleration of Cr volatilisation rate reaction and deterioration of chromia oxide protective scale.

Another interesting factor on Cr species volatilisation is the gas velocity along the specimen. Gindorf et al. [20] also demonstrated Cr volatilisation from Cr_2O_3 powder in different flow rates of 10% humid air at 1223 K. The results are shown in Figure 2.17. It was found that, at low gas flow rate, Cr volatilisation rate was increased with increasing gas flow rate. At the flow rate higher than 400 ml/min, Cr volatilisation was independent on the gas flow rate. These results are similar to the results of Stanislowski et al. [34] which observed Cr species volatilisation from Ducrolloy (Cr-based alloy). However, Stanislowski et al. observed 3 zones of Cr volatilisation phenomenon as shown in Figure 2.18. The first zone was an equilibrium state between chromia scale formation and volatilisation of Cr. At Zone II, non-equilibrium took place. The diffusion of Cr volatile species in air was not high enough to maintain equilibrium within the reaction tube. A Cr concentration gradient was formed between the gas and the sample. It was called boundary layer which limits the distance of vapour diffusion in the gas. The increase in the gas flow rate leads to decreasing in the boundary layer thickness and increasing in the diffusion rate and Cr volatilisation rate. Finally, in the last zone, Zone III, Cr species volatilisation was limited by surface reaction because the boundary layer thickness was thin enough. The diffusion rate of Cr vapour was higher than the surface reaction rate. The maximum Cr volatilisation rate was reached in this zone.

Moreover, Stanislowski et al. studied Cr species volatilisation from various steels in cathodic SOFCs condition. They revealed that the different contents of Mn, Ti, Al, Si and W in alloys led to different types of outer oxide scales which led to different Cr volatilisation rates. They found that, under the same experimental conditions, Cr species volatilisation from Cr_2O_3 outer layer of Ducrolloy was higher than from $(Mn,Cr)_3O_4$ spinel (Mn-Cr spinel) outer layer of Fe-based alloys by about 61-75%. In anodic SOFC condition, Cr species volatilisation was significantly much lower than in cathodic condition and can be considered as negligible.

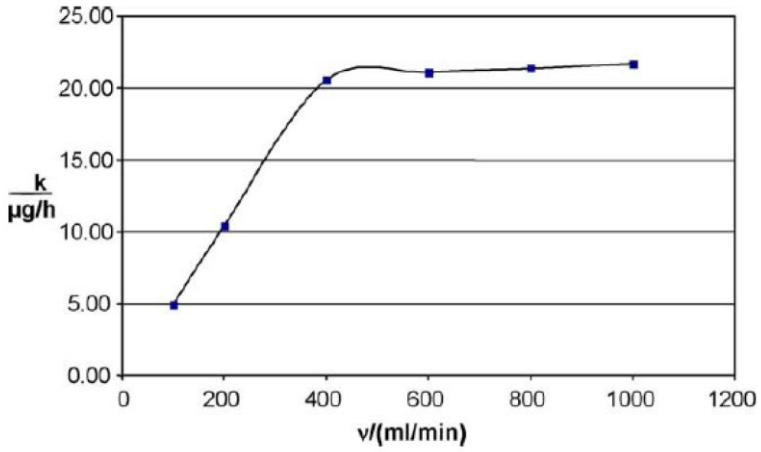

Figure 2.17 Cr volatilisation rate from Cr_2O_3 powder in 10% humid air at 950°C [20].

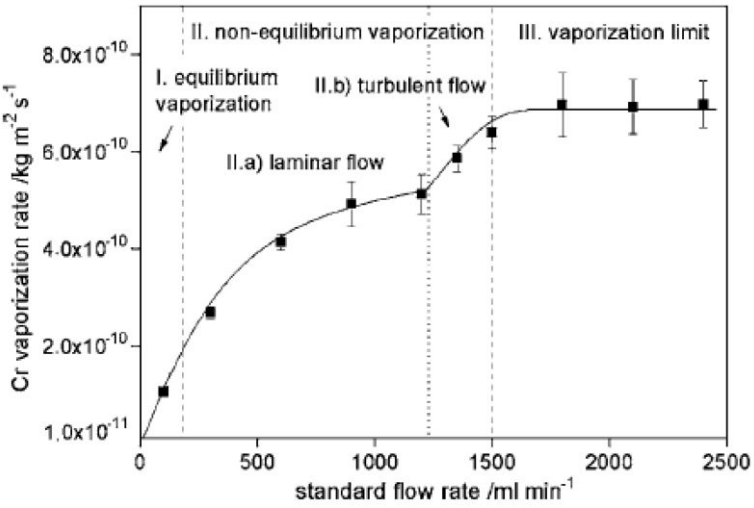

Figure 2.18 Effect of air flow rate on Cr volatilisation rate from Ducrolloy in 1.88% humid air at 800°C [34].

Another important factor is oxidation temperature. Many research have already reported this effect on Cr species volatilisation from various materials e.g. Crofer 22H and Sanergy HT by Falk-Wibdusch et al. [35], [36] from High Temperature Corrosion Center (HTC) of Chalmers University of Technology and AISI 441 reported by Wongpromrat et al. [37]. All results are in good agreement with the observation of higher Cr species volatilisation when oxidation temperature increases. From the paper of Falk-Wibdusch et al. [36], Cr species volatilisation and global oxidation were studied simultaneously in 3%H_2O-air. The results show that the oxidation rate was higher than Cr volatilisation rate. Crofer 22F and Sanergy HT which formed the same oxide consisting of chromia and Mn-Cr spinel provided similar Cr species volatilisation.

The recent publication about this area was published by Sachitanand et al. [38] from Chalmers University of Technology. They simultaneously studied oxidation and Cr species volatilisation from 5 different alloys; E-brite, ZMG232 Ga10, Sanergy HT, Crofer 22 H (Fe-22.7Cr-1.4W-0.55Nb-0.2Si) and Crofer 22 APU. The experiments were carried out under 3%H_2O in air at 850°C up to 1000 h. The results show that the oxide formed on all specimens was double layers consisting of Mn-Cr spinel top-layer and chromia sub-layer. High Mn content affected the thicker spinel layer and higher Mn/Cr ratio in spinel that better reduced Cr activity on the top surface resulting in lowering Cr species volatilisation. In addition, Mn content was also influent mass gain of the alloys because of spinel formation. Taking into account mass gain and Cr species volatilisation instantaneously, it can be seen that they were inversely proportional. Among these alloys, E-brite was the worst specimen due to the highest Cr species volatilisation and spallation of the oxide resulting from the formation of Si-continuous layer. However, none of the tested alloys can be applied as interconnect of SOFC without protective coating even for Crofer 22 APU which was the best material in this study.

In summary, during high temperature oxidation, Cr and Fe-Cr alloys are oxidised. The oxidation behaviour can be divided into 2 steps. The first step is the solid-state diffusion of ionic species in the Cr_2O_3 protective scale with parabolic kinetics. If the thickness of the scale

overpasses the critical thickness, cracks and spallation are observed. Breakaway oxidation occurs when the cracking rate is high. The second step is the volatilisation of Cr from Cr_2O_3 to Cr volatile species with linear kinetics. Thus, the growth kinetics of the chromia scale could be evaluated by a parabolic rate constant and a surface-reaction rate constant [39]. For interconnect application, the degradation rate of material in terms of oxidation and Cr volatilisation rates must be low while maintaining the stability of the material. Electrical conductivity, thermal conductivity, mechanical properties and thermal expansion compatibility with other cell components must be acceptable over the application duration. Nevertheless, no bare material can be applicable, so the interconnect must be protected before the application.

2.4.1 Influence of Cr volatilisation in SOFC

In SOFC, Cr species volatilisation from metallic interconnect not only affects its own properties but also the efficiency and lifetime of SOFC. The degradation of the metallic interconnect resulting from Cr species volatilisation leads to lowering its electrical and thermal conductivities and oxidation resistance. Thus, the efficiency of SOFC is lower. Furthermore, Cr species volatilisation results in the deterioration of cathode materials. In particularly of humidified air or O_2 atmosphere, the most volatile species, $CrO_2(OH)_2$, transports with the oxidant through cathode to cathode/electrolyte interface and competes with O_2 to electrochemically react and blocks the interface with Cr(III) called “Cr-poisoning” as shown in Figure 2.19.

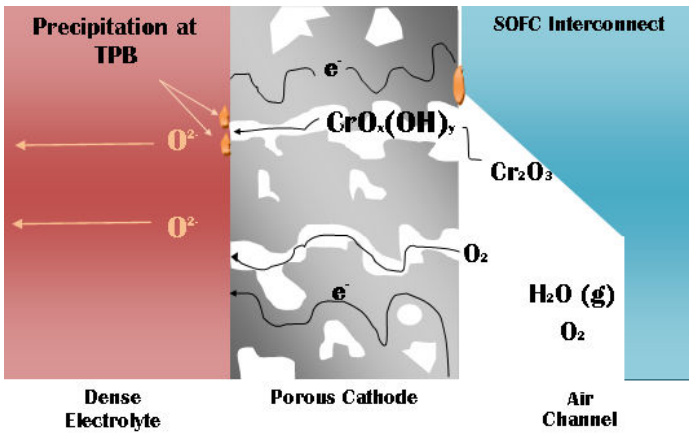

Figure 2.19 Cr-poisoning caused by Cr species volatilisation from metallic interconnect. TPB stands for triple phase boundary [40].

It is very well known that Cr-poisoning occurred because of the decomposition the perovskite structure of cathode and the formation of spinel leading to poorer electrical properties of SOFCs. However, Yokokawa et al. [41] investigated that there are 3 possibilities occurred due to Cr species volatilisation.

1). The change of cathode perovskite lattice to spinel form as described above.

2). The reaction of Cr volatile species with cathode material, commonly LSM (Lanthanum-Strontium Manganite). Strontium chromate, $SrCrO_4$ is thermodynamically formed as shown in Eq. 2.19. Nevertheless, this reaction does not lead to rapid degradation but significantly affects the stability of materials.

$$La_{0.8}Sr_{0.2}MnO_3(s) + 0.1CrO_3(g) + 0.05O_2(g) \rightarrow$$

$$La_{0.8}Sr_{0.1}MnO_3(s) + 0.1SrCrO_4(g) \quad \text{(Eq. 2.19)}$$

3). The Cr_2O_3 deposition or chromium manganite, $CrMn_2O_4$ formation on TPB. These are the direct reason for Cr-poisoning taking place under the O_2 potential gradient caused by the strong Mn^{4+} stability and resulting in slow oxide ion diffusivity in LSM.

2.4.2 Cr volatilisation protection

For the better applicability of metallic interconnect in SOFC, the interconnect materials have been attempted to coat by several coating materials and methods. The properties of coating are also important. Its thermal expansion must also be compatible with interconnect material and other cell components in order to avoid cracking. Its electrical conductivity needs to be high over the long application and it must be able to increase oxidation resistance and Cr species volatilisation from the interconnect. Generally, the coating applied on the metallic interconnect is classified into 3 families; metallic coating, ceramic coating (perovskite and spinel) and other complex depositions.

2.4.2.1 Metallic coating

One of the most popular metallic coating at the present time is Co as well as its co-depositions. It is promising element being able to reduce Cr species volatilisation and oxidation rate. Co_xO_y was rapidly formed during early oxidation stage and blocked Cr diffusion to the top surface while provided good electrical conductivity and adherence on the steels [42], [43]. After long term of oxidation, $(Co,Mn,Fe)_3O_4$ was formed with very low Cr content in the outer surface and blocked Cr species volatilisation for at least 3000 h [44]. Furthermore, it was found that Co-coated on metallic interconnect acting as Cr migration inhibitor leading to anti-Cr-poisoning and an improvement and more stability of cathode than uncoated interconnect [42], [45].

Co coated material was also investigated compared to other metallic depositions. Magrasò et al. [46] oxidised uncoated Sanergy HT comparing with Co coated and Ce/Co coated by physical vapour deposition (PVD) method on the same material in humidified air at 850°C for up to 4200 h and found similar oxidation behaviours and area specific resistances (ASRs) of uncoated and Co coated Sanergy HT. On the contrary, Ce/Co coated specimen improved oxidation resistance and reduced ASR that means it improved SOFC interconnect performance. In addition, Cr species volatilisations from both coated specimen were reduced comparing with that of uncoated one. These results were similar with the results of Canovic et al. [47] and Falk-

Winisch et al. [48] reporting that Co coated on Sanergy HT had only minor effects on oxidation rate comparing with uncoated sample even it strongly inhibited Cr species volatilisation from the specimen. Moreover, they also studied oxidation and Cr species volatilisation from Ce coated Sanergy HT and found that the results were conversely with that of Co coated one. Ce coated specimen improved oxidation rate but it did not significantly affect Cr volatilisation. Combining these two coatings can reduce both Cr species volatilisation and oxidation rates.

Kim et al. [49] coated Y, Co and Y/Co on AISI 444 by electron beam evaporation method. Then, these specimens were oxidised in 3%H_2O+air at 800°C for 1000 h. They found that scale growth on Y coated specimen was slower than that of uncoated one leading to lower ASR. Co coated specimen was also able to reduce ASR but its scale growth rate was higher than Y coated specimen, so Y was the most effective for SOFC interconnect application in this work.

Molin et al. [50] observed oxide formations and electrical conductivities of Y coated, Co coated and uncoated Crofer 22 APU. The cyclic thermogravimetric oxidation of these specimens were exposed in air at 800°C. Mn-Cr spinel and chromia were formed on uncoated and Co coated specimens while $YCrO_3$ perovskite was developed on Y coated specimen resulting in deceleration of oxide scale formation comparing with other specimens. However, electrical conductivity of Co coated specimen was higher than that of Y coated specimen which had an equivalent electrical conductivity with uncoated specimen.

Stanislowski et al. [51] coated Co, Ni and Cu by sputtering on Crofer 22 APU and E-brite and tested Cr species volatilisation in humidified air ($P(H_2O)$ = 1.88 kPa) at 800°C. They revealed that metallic coating can reduce 99% of Cr species volatilisation comparing to uncoated one while self-evaporations could be neglected. Furthermore, these coating were able to reduce substrate oxidation and long term degradation of materials. Their stabilities, adherences and electrical conductivities were still observed even up to 1200 h of oxidation time at 800°C.

Grolig et al. [52] studied oxidation and Cr species volatilisation from uncoated AISI 441 comparing with reactive elements coated (RE), Ce and La, and RE/Co coated specimens in 3%H_2O+air at 850°C for 500 h. Severe spallation was observed from uncoated specimen which did not observe on RE coated specimens. RE/Co coated specimens exhibited better oxidation rate and decreased Cr species volatilisation for about 90%.

The recent very interesting paper presenting about Cr species volatilisation from Co coated on Crofer 22 APU by PVD method was published by Falk-Windisch et al. [53]. Four different specimen preparations (uncoated, Co-coated, post-coated and pre-coated specimens) as shown in Figure 2.20 were oxidised in their work. For post-coated and pre-coated specimens, the materials were mechanically deformed, in order to press into interconnect shape, after and before coating respectively. Cracks consisting of Fe and Cr-rich were observed on pre-coated specimen at the tensile deformation position while post-coated specimen was well covered by Co. However, oxidation and Cr species volatilisation results of all 3 coated specimens were similar and better than that of uncoated one. It was surprised that pre-coated could also improve oxidation and Cr species volatilisation resistances although the oxide was cracked during material deformation. SEM and EDX showed that, Co oxide was formed during first 6 min of

oxidation and expanded in volume leading to small crack healing. Mn was observed at the large crack position that was possibly due to Mn-Cr spinel formation. After 24 h of oxidation, oxide scale became thicker at the crack positions. Co could be observed within some crack areas and the distribution of Co, Mn and Cr were more homogeneously on the top layer which could contain $(Co,Cr,Mn)_3O_4$ spinel. After 168 h of oxidation, Mn-Co spinel was thicker and preventing the increasing of Cr species volatilisation from the specimen, so pre-coated specimen was as effective as coated (undeformed) and post-coated specimens in terms of oxidation and Cr species volatilisation considerations.

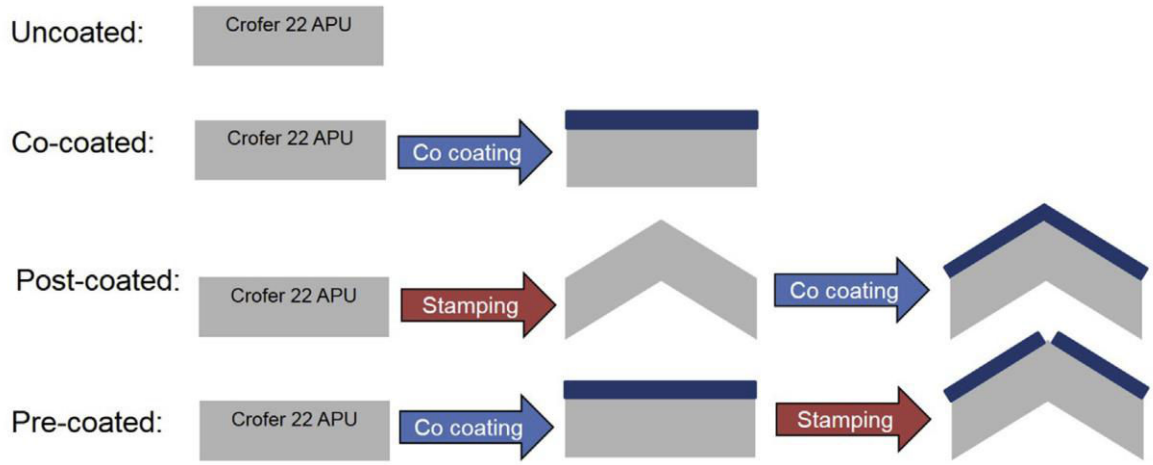

Figure 2.19 Schematic drawing of the 4 different materials investigated [53].

2.4.2.2 Ceramic coating

There are 2 types of ceramic usually used as coating materials on metallic interconnect that are perovskite and spinel. Several ceramic coating phases were developed on metallic interconnect by various methods as the following illustrations.

1). Perovskite coating

Lanthanum strontium manganite ($La_xSr_{1-x}MnO_3$: LSM) is the most popular perovskite structure coated on metallic interconnect since it is usually used as cathode materials. Thus, the crack problem occurring due to thermal expansion mismatch would not be happened. In the case that other materials ($La_xSr_{1-x}CrO_3$; LSC, $LaCrO_3$, $LaMnO_3$) are used as cathode instead of LSM, their thermal expansion coefficients are still compatible (LSM: 12×10^{-6} K^{-1} [3], [14], [54], LSC-80: 11.1×10^{-6} K^{-1} [3], $LaCrO_3$: 9.5×10^{-6} K^{-1} [3], $LaMnO_3$: 12.5×10^{-6} K^{-1} [3]) and also match with the thermal expansion coefficients of a YSZ electrolyte (10×10^{-6} K^{-1}) [3], [54]. The electrical resistivity of LSM coated on metallic materials was determined for evaluating the interconnect properties suitability. It was found that its electrical resistivity was low. Kim et al. [55] examined area specific resistance (ASR) of LSM dipped-coated AISI 430 steel. After oxidation in air at 750°C for 2600 h, ASR maintained almost constant at 74 $m\Omega\cdot cm^2$. ASRs of LSM coated on AISI 439, AISI 444 and AISI 430 AISI were also measured by Conceição

et al. [5] during oxidation in air at 800°C up to 200 h. After oxidation for 200 h, ASRs of LSM-AISI 439, LSM-AISI 444 and LSM-AISI 430 were 8.0, 0.6 and 63 $m\Omega \cdot cm^2$ respectively while the acceptable upper limit of ASR of metallic interconnect is 100 $m\Omega \cdot cm^2$ [56], [57]. These results showed better electrical conductive properties of materials comparing with uncoated ones. In addition, no cracking area was observed, so, LSM is interesting to coat on metallic interconnect. However, Lee et al. [58] showed that (La,Sr),(Co,Fe)O_3 (LSCF) coated on Crofer 22 APU by screen printing. The coated specimen had better ASR value than that of LSM coated specimen after high temperature oxidation in air at 800°C for 300 h. In the following, the protective materials with perovskite structure coatings, LSM and others, are presented.

Above publication presented by Stanislowski et al. [51] also reported Cr species volatilisation suppression by coating with ceramic materials that were $La_{0.8}Sr_{0.2}CrO_3$ (LSC-80), $La_{0.99}(Cr_{0.77}Mg_{0.05}Al_{0.18})O_3$ (LMAC) and $La_xSr_{1-x}MnO_3$ (LSM-80and LSM-65). However, their Cr species volatilisation reduction performances were poorer than the metallic coatings and did not reach the desire level.

Kurokawa et al. [59] applied perovskite coatings; LSM-65 and LSCF on AISI 430 ferritic steel by spray or dip coating. Then, uncoated and coated specimens were oxidised in humidified air ($P(H_2O)$ = 10 kPa) at 800°C. The results showed that Cr species volatilisation significantly decreased after coating with these materials up to a factor of 40. Cr volatilities from LSM and LSCF (both coating methods) specimens decreased because of the obstruction of Cr diffusion by LSM and LSCF. Corresponding to the work of Chu et al. [60], after long term high temperature oxidation of LSM coated metallic materials, dense LSM film exposed on the specimen surface and obstructed the diffusion of Cr through coating layer to the outer surface. Hence, chromia was only produced at metal/coating interface and cannot react with oxidants, O_2 and H_2O, in the atmosphere resulting in suppression of Cr species volatilisation. On the other hand, Palcut et al. [61] explained that LSM was a barrier inhibiting the diffusion of O and reduce partial pressure of O at chromia/coating interface leading to the improvement of corrosion resistance of the materials.

There were many other coating perovskite materials deposited on metallic interconnect such as coated $La_xSr_{1-x}CoO_3$ (LSC), $La_{0.6}Sr_{0.4}Co_{0.2}Fe_{0.8}O_3$ (LSCF) and $LaNi_xFe_{1-x}O_3$ (LNF) on Crofer 22 APU, AISI 430 and E-brite by PVD method by Lacey et al. [43], $LaCrO_3$ depositing on Haynes 230, Ni-based alloy by Guillou et al. [62] LSM-80 and LNF coated on AISI 441 by Ardigo et al. [63] and (La,Sr)CrO_3 screen printed on a DIN 50049 ferritic steel by Brylewski et al. [64]. All results are in good agreement that is these coatings greatly improved corrosion and Cr species volatilisation resistances by limiting outward Cr diffusion from the substrate during high temperature oxidation process.

2). Spinel coating

Even though it is very well known that both perovskite and spinel oxides can improve oxidation resistance of alloy while reducing Cr species volatilisation from the alloy specimen [65], spinel oxides were proven that their properties were better than those of perovskite ones. Sauchuk et al. [66] proved that, a perovskite phase of (La,Sr),(Mn,Co,)O_3 (LSMC) coated on Crofer 22 APU, ITMLC and ZMG232L ferritic stainless steels was determined comparing with

2 spinels, $MnCo_xFe_{2-x}O_4$ (MCF) and $Cu_{1-x}Ni_xMn_2O_4$ (CNM), coated on the same entire specimens. The results showed that the spinel coated alloys were more suitable to apply as metallic interconnect than perovskite coated due to lower the electrical resistances at alloy/coating interface and denser coating layers (less porosity) resulting in lowering degradation rates as shown in Figure 2.21. Furthermore, spinel structures can be sintered faster and the sintering temperature was lower than that of perovskite oxide, so, in the recent papers, spinel coatings, especially for Mn-Co spinel ($Mn_xCo_{3-x}O_4$), have been studied more than perovskite.

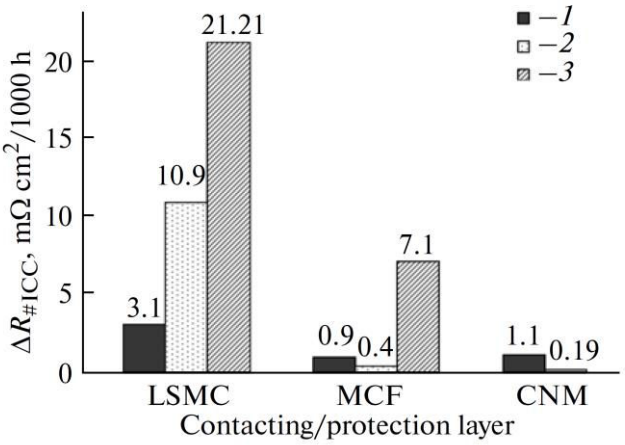

Figure 2.21 Calculated degradation rates ($\Delta R_{\#ICC}$) of the ASR resistance between interconnect and contact layer for Crofer 22 APU (1), ITMLC (2) and ZMG232L (3) in combination with different contact materials [66].

Fang et al. [67] oxidised $MnCo_2O_4$ coated on Fe-21Cr alloy and found that this coating not only acted as a Cr transport barrier but also improved electrical conductivity of specimen. After oxidation in air at 750°C for 1000 h, ASR was reduced about 75% comparing to uncoated one resulting by the migration of Cr into the coating layer and, then, Mn-Co-Cr spinel was generated which had lower ASR than that of chromia scale. Furthermore, Mn-Co spinel also improved oxidation resistance, inhibited outward diffusion of Cr and decelerated scale growth rate [68]-[72] (it could be further improved by preoxidation in air at 900°C for 8 h [67]) and suppressed Cr species volatilisation even Cr could migrate to the coating layer [59], [68], [73], [74]. Wang et al. [75] elucidated that there was a reactive layer consisting of 2 layers developed during oxidation of Mn-Co spinel coated specimen. The first one was the layer in contact with chromia grew by diffusion of Co and Mn from the coating toward chromia. Meanwhile, Cr diffused into the coating layer and formed a second reactive layer. The first layer formed by the diffusion of Mn and Co to chromia should be beneficial for reducing Cr species volatilisation.

Moreover, Ni-containing spinel oxides were tried to coat on metallic interconnect such as $NiCo_2O_4$ and Fe-doped Ni-Co spinel reported by Jalivand et al. [76] and $NiMn_2O_4$ of Zhang et al. [77]. From both publications, it was ensured that these coatings were protective coatings

improving oxidation resistance of the specimen and preventing Cr species volatilisation. Also, their ASRs were excellent especially for the Fe-doped Ni-Co spinel coating.

2.4.2.3 Other complex coatings

Since the efficiencies of coating metallic interconnects were not good enough, more complex coatings were attempted to use for the better applicability in SOFC. The examples of some complex coatings are as follows.

Choi et al. [78] deposited LSM-YSZ coating film on AISI 444 by aerosol deposition. The ratio of YSZ in LSM was varied from 0-100%. After oxidation of all specimens in air at 800°C for 250 h, lower Cr content was observed on the surface which contained higher amount of YSZ, but pure YSZ coated specimen showed the highest electronic resistivity comparing with other coated specimens. Thus, these results revealed that the most appropriate coating in this study was composite LSM-YSZ.

Gorokhovsky et al. [79] coated TiCrAlYO on ferritic stainless steel by the large area filtered arc deposition (LAFAD) process. Oxidation, Cr species volatilisation and ASR were studied in this work. It was demonstrated that this coating possessed high temperature oxidation resistance with an excellent Cr species volatilisation suppression. Since its poor electronic conductivity, it could not be applied as a protective layer of metallic interconnect. Anyway, Mn and Co could additionally be doped into this coating structure to form electronically conductive spinel phase which was thermodynamically stable and applicable with the long term operation of SOFC.

Balland et al. [80] performed high temperature oxidation experiments of Crofer 22 APU coated with 3 coatings; La_2O_3, Mn-Co spinel and combination of La_2O_3 and Mn-Co spinel in air and dual atmosphere (air+3%H_2O/H_2+3%H_2O) at 800°C. It was shown that the chromia formation on combination coating specimen was slower than that formed on single Mn-Co spinel layer. Considering in dual atmosphere experiments, the combination coating also inhibited the formation of Fe oxide compared to the single La_2O_3 coating. However, the further study of this coating was needed for evaluating its performance.

Liu et al. [81] coated (Ti,Al)N on Fe-25Cr and Crofer 22 APU by filtered-arc method. Then, the coated specimens were high temperature oxidised for short time. The results showed that (Ti,Al)N remained stable at the temperature up to 700°C. Increasing of Al content promoted higher stability of TiN coating. At 900°C (Ti-30Al)N was completely oxidised while some of (Ti-50Al)N still remained as nitride. All coatings were the effective inhibitors preventing the migration of Cr. Nevertheless, the stabilities of these coatings should be further improved.

2.5 Conclusions

This study is focused on interconnect of SOFC. According to the SOFC operating condition which is at high temperature around 800°C and contains H_2, O_2 and H_2O, therefore, interconnect must have high oxidation and corrosion resistances while maintaining electrical conductivity and thermal expansion compatibility with other cell components. The most

attractive material is ferritic stainless steels. During the operation, oxidation reaction between Cr in the steels and O_2 occurs leading to the formation of chromia scale protective layer as the following equation.

$$Cr(s) + O_2(g) \rightarrow Cr_2O_3(s)$$

The oxidation patterns during high temperature process can be divided into 2 types that are linear oxidation and parabolic oxidation. Linear oxidation is a sign of breakaway oxidation while parabolic oxidation implies a protective scale. Typically, oxidation behaviour of stainless steels is of parabolic type. However, parabolic oxidation can be transformed to linear oxidation due to the failure of oxide scale. The protective scale failure may result in cracking of oxide layer and Cr species volatilisation from the protective chromia layer. The major Cr species volatilisation reactions in dry and wet atmospheres containing O_2 are shown in the following equations.

$$Cr_2O_3(s) + 1.5O_2(g) \rightarrow 2CrO_3(g)$$

$$Cr_2O_3(s) + 1.5O_2(g) + 2H_2O(g) \rightarrow 2CrO_2(OH)_2(g)$$

Cr species volatilisation from the steels leads to the deteriorations of interconnect and cathode materials (by Cr-poisoning), Electrical conductivities of interconnect and cathode are lower leading to poorer performance of SOFC. Moreover, the service lifetime of SOFC would be shorter. Therefore, it needs to be suppressed by protective coating with an effective materials that may be metallic, ceramic or other complex coating.

References

[1] Fuel cell handbook, 5th ed. West Virginia: U.S. Department of Energy, Office of Fossil Energy, National Energy Technology Laboratory, 2000.

[2] V. Ramani, “Fuel Cells,” Electrochem. Soc., pp. 41–44, 2006.

[3] S. C. Singhal and K. Kendall, High temperature solid oxide fuel cells: Fundamentals, design and applications. Elsivier, 2007.

[4] “Technical advances improve the potential for fuel cell which eliminates the need to store or generate hydrogen: direct methanol fuel cell,” 2001. [Online]. Available: http://www1.eere.energy.gov/vehiclesandfuels/pdfs/success/dmfuelcell3_23_01.pdf. [Accessed: 25-Jun-2015].

[5] L. Conceição, L. Dessemond, E. Djurado and M. Souza, “Thin films of $La_{0.7}Sr_{0.3}MnO_{3-\delta}$ dip-coated on Fe–Cr alloys for SOFC metallic interconnect,” Int. J. Hydrogen Energy, vol. 38, pp. 15335-15347, 2013.

[6] O. Yamamoto, “Solid oxide fuel cells : fundamental aspects and prospects,” Electrochimica Acta, vol. 45, pp. 2423–2435, 2000.

[7] E. Guire, “Solid oxide fuel cells,” 2003. [Online]. Available: http://www.csa.com/discoveryguides/fuecel/overview.php. [Accessed: 05-Jul-2011].

[8] S. C. Singhal, “Solid oxide fuel cells,” The Electrochemical Society Interface. 2007. [Online]. Available: http://www.electrochem.org/dl/interface/wtr/wtr07/wtr07_p41-44.pdf. [Accessed: 27-Jun-2015].

[9] “Development status of SOFC,” 2012. [Online]. Available: http://www.mhi.co.jp/en/technology/business/power/sofc/development_situation.html. [Accessed: 05-Jul-2011].

[10] Á. Varga and S. Mounse, “Fuel cells,” 2006. [Online]. Available: http://www.doitpoms.ac.uk/tlplib/fuel-cells/printall.php. [Accessed: 25-Mar-2015].

[11] W. Z. Zhu and S. C. Deevi, “Development of interconnect materials for solid oxide fuel cells,” Mater. Sci. Eng. A, vol. 348, no. 1–2, pp. 227–243, 2003.

[12] J. Wu and X. Liu, “Recent development of SOFC metallic interconnect,” J. Mater. Sci. Technol., vol. 26, no. 4, pp. 293–305, 2010.

[13] J. W. Fergus, “Metallic interconnects for solid oxide fuel cells,” Mater. Sci. Eng. A, vol. 397, no. 1–2, pp. 271–283, 2005.

[14] X. Chen, P. Hou, C. Jacobson, S. Visco, and L. Dejonghe, “Protective coating on stainless steel interconnect for SOFCs: oxidation kinetics and electrical properties,” Solid State Ionics, vol. 176, no. 5–6, pp. 425–433, Feb. 2005.

[15] J. R. Davis, Ed., ASM specialty handbook: Stainless steels, 1st ed. Ohio: ASM international, 1994.

[16] M. Sathitrajinda, Steels, 1st ed. Bangkok: The Engineering Institute of Thailand Under H.M. The King’s Patronage, 1986.

[17] S. D. Cramer and B. S. Covino, Eds., *ASM handbook Corrosion : Materials*, 1st ed., vol. 13B. Ohio: ASM international, 2005.

[18] ASM handbook Properties and Selection: Irons, steels, and high-performance alloys, 2nd ed. ASM international, 1993.

[19] A. Yamauchi, K. Kurokawa, and H. Takahashi, “Evaporation of Cr_2O_3 in atmospheres containing H_2O,” Oxid. Met., vol. 59, no. June, pp. 517–527, 2003.

[20] C. Gindorf, L. Singheiser, and K. Hilpert, “Vaporisation of chromia in humid air,” J. Phys. Chem. Solids., vol. 66, pp. 384–387, 2005.

[21] P. Kofstad, High temperature corrosion. Elsevier Applied Science Publisher LTD, 1988.

[22] P. Sarrazin, A. Galerie, and J. Fouletier, Mechanisms of high temperature corrosion: A kinetics approch. Trans Tech Publ., Stafa-Zuerich, CH, 2008.

[23] J. W. Morris, “Defects in Crystals,” Materials Science, 2007, pp. 76–107.

[24] R. M. Saburaphael, “Imperfections in solids – Stoichiometric and impurity defects.” 2013. [Online]. Available: https://amazingsolids.wordpress.com/2013/06/15/imperfections-in-solids-stoichiometric-and-impurity-defects/**.** [Accessed: 26-Mar-2015].

[25] D. J. Young, High temperature oxidation and corrosion of metals, 1st ed. Elsevier, 2008.

[26] D. Caplan and M. Cohen, “The Volatilization of chromium oxide,” J. Electrochem. Soc., vol. 108, pp. 438–442, 1961.

[27] K. Hilpert, D. Das, M. Miller, D. H. Peck, and R. Wei, “Chromium vapor species over solid oxide fuel cell interconnect materials and their potential for degradation processes,” J. Electrochem. Soc., vol. 143, no. 11, pp. 3642–3647, 1996

[28] IVTANTHERMO-A Thermodynamic Database and Software System for the Personal Computer, V. S. Yungman, V. A. Medvedev, I. V. Veits, and G. A. Bergman, Editors, CRC Press and Begell House, Boca Raton, FL (1993).

[29] B. B. Ebbinghaus, Combus. Flame, 93, 119, (1993).

[30] B. B. Ebbinghaus, Report of the Lawrence Livermore National Laboratory, TJCRL-JC-1 15742 (1993).

[31] H. Asteman, J. E. Svensson, and L. G. Johansson, “Evidence for chromium evaporation influencing the oxidation of 304L: The effect of temperature and flow rate,” Oxid. Met., vol. 57, no. 3–4, pp. 193–216, 2002.

[32] H. Asteman, J. Svensson, M. Norell, and L. Johansson, “Influence of Water Vapor and Flow Rate on the High-Temperature Oxidation of 304L ; Effect of Chromium Oxide Hydroxide Evaporation,” Oxid. Met., vol. 54, no. 1–2, pp. 11–26, 2000.

[33] E. J. Opila, D. L. Myers, N. S. Jacobson, I. M. B. Nielsen, D. F. Johnson, J. K. Olminsky, and M. D. Allendorf, “Theoretical and experimental investigation of the thermochemistry of $CrO_2(OH)_2(g)$,” J. Phys. Chem., vol. 111, pp. 1971–1980, 2007.

[34] M. Stanislowski, E. Wessel, K. Hilpert, T. Markus, and L. Singheiser, “Chromium vaporization from high-temperature alloys: I. Chromia-forming steels and the influence of outer oxide layers,” J. Electrochem. Soc., vol. 154, no. 4, pp. A295, 2007.

[35] H. Falk-Windisch, J. E. Svensson and J. Froitzheim, “The effect of temperature on chromium vaporization and oxide scale growth on interconnect steels for solid oxide fuel cells,” J. Power Sources., vol. 287, pp. 25-35, 2015.

[36] H. Falk Windisch, J. Froitzheim and J. E. Svensson, “Influence of chromium evaporation and oxidation on interconnect steels at 650-850°C,” J. Electrochem. Soc., vol. 57, no. 1, pp. 2225-2233, 2013

[37] W. Wongpromrat, H. Thaikan, W. Chandra-ambhorn, and S. Chandra-ambhorn, "Chromium vaporisation from AISI 441 stainless steel oxidised in humidified oxygen," Oxid. Met., vol. 79, no. 5–6, pp. 529–540, 2013.

[38] R. Sachitanand, M. Sattari, J. E. Svensson and J. Froitzheim, "Evaluation of the oxidation and Cr evaporation properties of selected FeCr alloys used as SOFC interconnects" Int. J. Hydrogen Energy, vol. 38, pp. 15328-15334, 2013.

[39] C. S. Tedmon, "The Effect of oxide volatilization on the oxidation kinetics of Cr and Fe-Cr alloys," J. Electrochem. Soc., vol. 113, no. 8, pp. 766, 1966.

[40] R. Bateni, University of Toronto. [Online]. Available: http://www.mie.utoronto.ca/labs/sofc/reza_bateni.html. [Accessed: 30-Mar-2015].

[41] H. Yokokawa, T. Horita, N. Sakai, K. Yamaji, M. E. Brito, Y. P. Xiong, and H. Kishimoto, "Thermodynamic considerations on Cr poisoning in SOFC cathodes," Solid State Ionics, vol. 177, pp. 3193–3198, 2006.

[42] Q.-X. Fu, D. Sebold, F. Tietz and H.-P. Buchkremer, "Electrodeposited cobalt coating on Crofer22APU steels for interconnect apllications in solid oxide fuel cells," Solid State Ionics, vol. 192, pp. 376-382, 2011.

[43] R. Lacey, A. Pramanick, J. C. Lee, J. I. Jung, B. Jiang, D. D. Edwards, R. Naum and S. T. Misture, "Evaluation of Co and Perovskite Cr-blocking thin films on SOFC interconnects," Solid State Ionics, vol. 181, pp. 1294-1302, 2010.

[44] J. Froitzheim, S. Canovic, M. Nikumaa, R. Sachitanand, L. G. Jahansson and J. E. Svensson, "Long term study Cr evaporation and high temperature corrosion behaviour of Co coated ferritic steel for solid oxide fuel cell interconnects," J. Power Sources., vol. 220, pp. 317-227, 2012.

[45] X. Li, J. W. Lee and B. N. Popov, "Performances studies of solid oxide fuel cell cathodes in the presence of bare and cobalt coated E-brite alloy interconnects," J. Power Sources., vol. 187, pp. 356-362, 2009.

[46] A. Magrasò, H. Falk-Windisch, J. Froitzheim, J. E. Svensson and R. Haugsrud, "Reduced long term electrical resistance in Ce/Co-coated ferritic steel for solid oxide fuel cell metallic interconnects," Int. J. Hydrogen Energy, vol. 40, pp. 8579-8585, 2015.

[47] S. Canovic, J. Froitzheim, R. Sachitanand, M. Nikumaa, M. Halvarsson, L. G. Johansson and J. E. Svensson, "Oxidation of Co- and Ce- nanocoated FeCr steels: A microstructure investigation," Surf. Coat. Tech., vol. 215, pp. 62-74, 2013.

[48] H. Falk-Windisch, J. Froitzheim and J. E. Svensson, "Influence of chromium evaporation and oxidation on interconnect steels at 650-850°C," J. Electrochem. Soc., vol. 57, no. 1, pp. 2225-2233, 2013.

[49] S. H. Kim, J. Y. Huh, J. H. Jun, J. H. Jun and J. Favergeon, "Thin element coatings of yttrium, cobalts, and yttrium/cobalt on ferritic stainless steel for SOFC interconnect applications," Curr. Appl. Phys., vol. 10, pp. S86-S90, 2010.

[50] S. Molin, B. Kusz, M. Gazda and P. Jasinski, “Protective coatings for stainless steel SOFC applications,” J. Solid State Electrochem, vol. 13, pp. 1695-1700, 2009.

[51] M. Stanislowski, J. Froitzheim, L. Niewolak, W. J. Quadakkers, K. Hilpert, T. Markus and L. Singheiser, “Reduction of chromium vaporization from SOFC interconnectors by highly effective coatings,” J. Power Sources., vol. 164, pp. 578-589, 2007.

[52] J. G. Grolig, J. Froitzheim and J. E. Svensson, “Coated stainless steel 441 as interconnect material for solid oxide fuel cells: Oxidation performance and chromium evaporation,” J. Power Sources., vol. 248, pp. 1007-1013, 2014.

[53] H. Falk-Windisch, M. Sattari, J. E. Svensson and J. Froitzheim, “Chromium vaporization from mechanically deformed pre-coated interconnects in Solid Oxide Fuel Cells,” J. Power Sources., vol. 297, pp. 217-223, 2015.

[54] S. C. Singhal and M. Dokiya, Solid oxide fuel cells (SOFC VI), Proceedings of The Sixth International Symposium, Proceedings Volume 99-19, The Electrochemical Society, INC., USA, 1999.

[55] J. H. Kim, R. H. Song and S. H. Hyun, “Effect of slurry-coated $LaSrMnO_3$ on the electrical property of Fe-Cr alloy for metallic interconnect of SOFC,” Solid State Ionics, vol. 174, pp. 185-191, 2004.

[56] B. Hua, J. Pu, F. Lu, J. Zhang, B. chi and L. Jian, “Development of a Fe-Cr alloy for interconnect application in intermediate temperature solid oxide fuel cells,” J. Power Sources., vol. 195, pp. 2782-2788, 2010.

[57] P. D. Jablonski and D. E. Alman, “Oxidation resistance of novel ferritic stainless steels alloyed with titanium for SOFC interconnect applications,” J. Power Sources., vol. 180, pp. 433-439, 2008.

[58] S. Lee, C. L. Chu, M. J. Tsai and J. Lee, “High temperature oxidation behavior of interconnect coated with LSCF and LSM for solid oxide fuel cell by screen printing,” Appl. Surf. Sci., vol. 256, pp. 1817-1824, 2010.

[59] H. Kurokawa, C. P. Jacobson, L. C. DeJonghe and S. J. Visco, “Chromium vaporization of bare and of coated iron-chromium alloys at 1073 K,” Solid State Ionics, vol. 178, pp. 287-296, 2007.

[60] C. L. Chu, J. Lee, T. H. Lee and Y. N. Cheng, “Oxidation behavior of metallic interconnect coated with La-Sr-Mn film by screen painting and plasma sputtering,” Int. J. Hydrogen Energy, vol. 34, pp. 422-434, 2009.

[61] M. Palcut, L. Mikkelsen, K. Neufeld, M. Chen, R. Knibbe and P. V. Hendriksen, “Improved oxidation resistance of ferritic steels with LSM coating for high temperature electrochemical apllications,” Int. J. Hydrogen Energy, vol. 37, pp. 8087-8094, 2012.

[62] S. Guillou, C. Desgranges and S. Chevalier, “Influence of a coating on oxidation resistance and resistivity of a chromia former alloy for high temperature vapor electrolysis application,” Oxid. Met., vol. 80, pp. 341-361, 2013.

[63] M. R. Ardigo, I. Popa, S. Chevalier, V. Parry, A. Galerie, P. Girardon, F. Perry, R. Laucournet, A. Brevet and E. Rigal, "Coated interconnects development for high temperature water vapour electrolysis: Study in anode atmosphere," Int. J. Hydrogen Energy, vol. 38, pp. 15910-15916, 2013.

[64] T. Brylewski, J. Dabek, K. Przybylski, J. Morgiel and M. Rekas, "Screen-printed (La,Sr)CrO_3 coatings on ferritic stainless steel interconnects for solid oxide fuel cells using nanopowders prepared by means of ultrasonic spray pyrolysis," J. Power Sources., vol. 208, pp. 86-95, 2012.

[65] K. Przybylski and T. Brylewski, "Interface Reactions between Conductive Ceramic Layers and Fe-Cr Steel Substrates in SOFC Operating Conditions," Materials Transactions, vol. 52, no. 3, pp. 345-351, 2011.

[66] V. Sauchuk, S. Megel, E. Girdauskaite, N. Trofimenko, M. Kusnezoff and A. Michaelis, "Influence of protective layers on SOFC operation," Russia Journal of Electrocheimistry, vol. 47, no. 5, pp. 522-530, 2011.

[67] Y. Fang, C. Wu , X. Duan, S. Wang and Y. Chen, "High-temperature oxidation process analysis of $MnCo_2O_4$ coating on Fe-21Cr alloy," Int. J. Hydrogen Energy, vol. 36, pp. 5611-5616, 2011.

[68] T. Uehara, N. Yasuda, M. Okamoto and Y. Baba, "Effect of Mn-Co spinel coating for Fe-Cr ferritic alloy ZMG232L and 232J3 for solid oxide fuel cell interconnects on oxidation behavior and Cr-evaporation," J. Power Sources., vol. 196, pp. 7251-7256, 2011.

[69] J. W. Stevenson, Z. G. Yang, G. G. Xia, Z. Nie and J. D. Templeton, "Long-term oxidation behavior of spinel-coated ferritic stainless steel for solid oxide fuel cell interconnect applications," J. Power Sources., vol. 231, pp. 256-263, 2013.

[70] L. Chen, E. Y. Sun, J. Yamanis and N. Magdefrau, "Oxidation kinetics of $Mn_{1.5}Co_{1.5}O_4$-coated Haynes 230 and Crofer 22 APU for solid oxide fuel cell intetconnects," J. Electrochem. Soc., vol. 157, no. 6, pp. B931-B942, 2010.

[71] W. Wei, W. Chen and D. G. Ivey, "Oxidation resistance and electrical properties of anodically electrodeposited Mn-Co oxide coatings for solid oxide fuel cell interconnect applications," J. Power Sources., vol. 186, pp. 428-434, 2009.

[72] M. R. Bateni, P. Wei, X. Deng and A. Petric, "Spinel coatings for UNS 430 stainless steel interconnects," Surf. Coat. Tech., vol. 201, pp. 4677-4684, 2007.

[73] M. R. Ardigo, I. Popa, S. Chevalier, V. Parry, A. Galerie, P. Girardon, F. Perry, R. Laucournet and A. Brevet, "Effect of coatings on a comercial stainless steel for SOFC interconnect application in anode atmosphere," ESC Trans., vol. 57, no. 1, pp. 4490-44952301-2311, 2013.

[74] A. Kruk, M. Stygar and T. Brylewski, "Mn-Co spinel protective-conductive coating on AL453 ferritic stainless steel for IT-SOFC interconnect applications," J. Solid State Electrochem, vol. 17, pp. 993-1003, 2013.

[75] K. Wang, Y. Liu and J. W. fergus, “Interaction between SOFC interconnect coating materials and chromia,” J. Am. Ceram. Soc., vol. 94, no. 12, pp. 4490-4495, 2011.

[76] G. Jalivand and M. A. Faghihi-Sani, “Fe doped Ni-Co spinel protective coating on ferritic stainless steel for SOFC interconnect application,” Int. J. Hydrogen Energy, vol. 38, pp. 12007-12014, 2011.

[77] W. Zhang, J. Pu, B. Chi and L. Jian, “NiMnO4 spinel as an alternative coating material for metallic interconnects of intermediate temperature solid oxide fuel cells,” J. Power Sources., vol. 196, pp. 5591-5594, 2011.

[78] J. J. Choi, J. Ryu, B. D. Hahn, W. H. Yoon, B. K. Lee, J. H. Choi and D. S. Park, “Oxidation behavior of ferritic steel alloy coated with LSM-YSZ composite ceramics by aerosol deposition,” J. Alloys and Compounds, vol. 492, pp. 488-495, 2010.

[79] V. I. Gorokhovsky, P. E. Gannon, J. Wallace, D. VanVorous, C. Bowman, M. C. Deibert and R. J. Smith, “Evaluation of SOFC interconnect made of ferritic steels with nano-structured oxi-ceramic protective coatings deposited by the LAFAD process,” J. Electrochem. Soc., vol. 158, no. 5, pp. B526-B535, 2011.

[80] A. Balland, P. Gannon, M. Deibert, S. Chevalier, G. Caboche and S. Fontana, “Investigation of La2O3 and/or (Co,Mn)3O4 deposits on Crofer22APU for the SOFC interconnect application,” Surf. Coat. Tech., vol. 203, pp. 3291-3296, 2009.

[81] X. Liu, C. Johnson, C. Li, J. Xu and C. Cross, “Developing TiAlN coatings for intermediat temperature solid oxide fuel cell interconnect applications,” Int. J. Hydrogen Energy, vol. 33, pp. 189-186, 2008.

Chapter 3

Materials, techniques and experiments

3.1 Specimen

AISI 441 is a ferritic stainless steel which is one of the most appropriate stainless steels used as a metallic interconnect of SOFC. In this study, AISI 441 was supplied by APERAM. Its chemical composition is shown in Table 3.1.

Table 3.1 Chemical composition of AISI 441 (given by the supplier).

Element	Cr	C	Mn	Si	Al	Ti	Nb	Mo	Fe
AISI 441	17.83	0.01	0.24	0.60	0.006	0.13	0.55	0.01	Balance

The difference between AISI 441 and other ferritic stainless steels is the addition of Ti and Nb in the alloy. The purpose of Ti and Nb addition is to stabilise the ferritic structure even at high temperatures [1], [2]. Ti and Nb addition increases the transition temperature preventing phase transformation from ferritic to martensitic phase [3]–[5]. Furthermore, Ti and Nb improve the other alloy properties as follows:

1). Cr volatilisation, oxidation and corrosion resistances [6], [7].

2). Mechanical properties ; Ti addition leads to the finer alloy structure while Laves phase (Fe_2Nb) directly affects the mechanical properties [3], [4], [8].

3). Electrical conductivity ; Fe_2Nb would capture Si preventing the formation of SiO_2 continuous layer (electrical resistivity of SiO_2 is 10^{18} $\Omega \cdot cm$ at room temperature [9]) leading to lowering electrical resistance [6], [7], [10].

3.2 Characterisation and techniques

3.2.1 Inductively coupled plasma-optical emission spectrometry (ICP-OES)

ICP-OES, called ICP in the following, is one of the most popular and powerful analytical tools for determining the trace elements. This technique is based on the spontaneous emission of photon from atoms and ions that have been excited in a radio frequency (RF) generator. The components of ICP system are shown in Figure 3.1. Gas, liquid and solid samples are able to be analysed by ICP. Gas and liquid samples can be directly injected to the instrument while solid sample must be extracted or acid digested in order to avoid blockage of the sample introduction system.

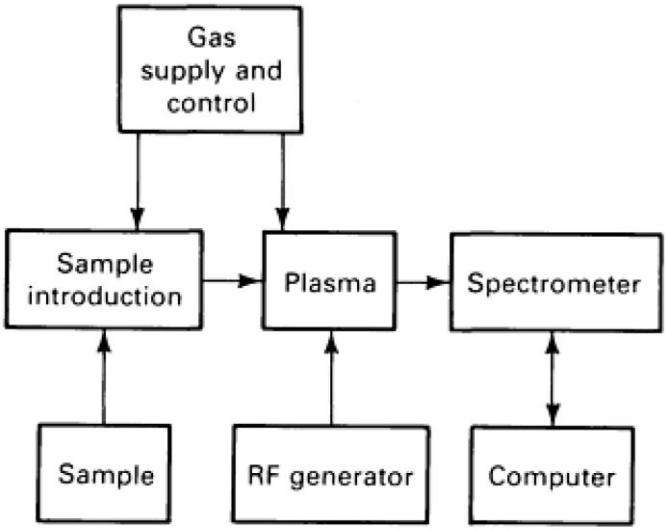

Figure 3.1 Components in an ICP analytical system [11].

The samples are converted to an aerosol, a very fine fog of droplets, by a nebuliser in order to introduce the analysed elements into the ICP. Then, the aerosol is flowed to the torch, Figure 3.2, which is composed of 3 concentric tubes. An induction Cu coil that is called load coil surrounds the top end of the torch and is connected to a RF generator.

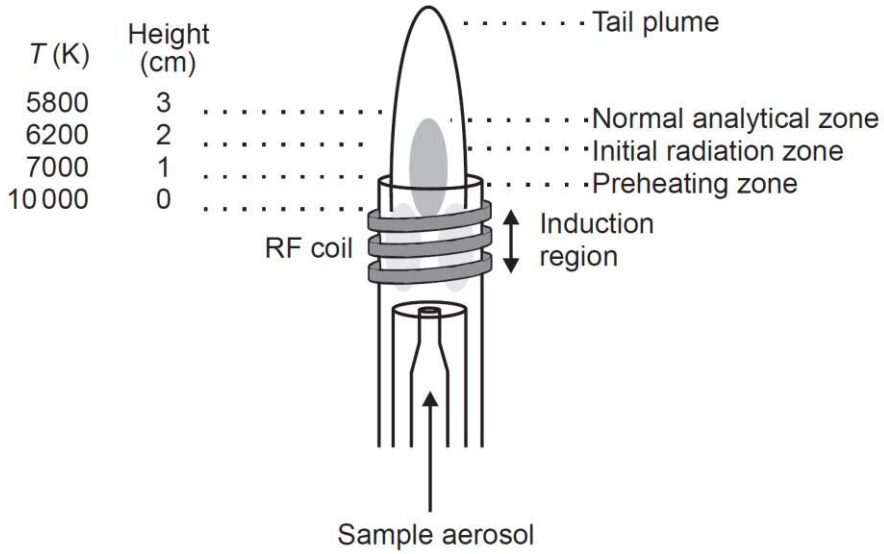

Figure 3.2 Schematic diagram of an ICP assembly showing the components of the ICP torch, the RF coil, the different plasma regions and the temperature as a function of height above the load coil [12].

The solvent in the aerosol is removed, or desolvated, and the remained aerosol becomes a salt material (solid particles). At the torch core where the temperature is 10,000 K, the salts are quickly vaporised (vaporisation) and liberated (atomisation) as free atoms in the gaseous

state. These steps occur at the preheating zone. The atoms collide each other, then, the additional energy is obtained. With this additional energy, the atoms are promoted to excited states. In case of sufficient energy, atoms can be converted to ions and these ions are also promoted to excited states. Then, both exciting atoms and ions would relax to the ground state via emission of photons. These photons have characteristic energies, so the wavelength of photons can be used to identify the elements. The number of photon emitted is directly proportional of the original element in the sample. The excitation and ionisation processes predominantly occur at the initial radiation zone while the normal analytical zone is the place measuring the emitted proton. All steps are summarised in Figure 3.3.

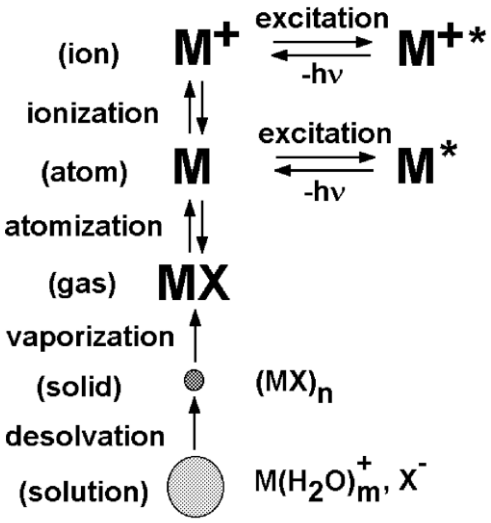

Figure 3.3 Processes that take place when a sample droplet is introduced into an ICP [13].

3.2.2 Scanning electron microscopy (SEM)

SEM is a tool using an electron beam to form a specimen image [14]. It is operated in the vacuum and focuses the electron beam and magnifies the images with the help of electromagnetic lenses. SEM provides the information of the specimen surface or near surface. The schematic of the main components of SEM is shown in Figure 3.4. The electron gun is the source of electrons. It is usually the tungsten filament thermionic emission type. Field emission gun (FEG) is used instead in case that the higher resolution of images is required. Electrons are accelerated to an energy which is usually between 1-30 keV. The condenser lenses (magnetic lenses) demagnify the electron beam until hitting the specimen. When electrons penetrate the surface, the interactions occur leading to an emission of electron or photon from, or through, the surface. Electrons emitted are collected with a detector and interpreted as an image.

The incident electrons or primary electrons lead to the secondary effects that can be categorised into 3 types: secondary electrons (SE), backscattering electrons (BSE) and relaxation of excited atoms (REA) [15], [16]. Normally, all SEMs have facilities for detecting SE and BSE.

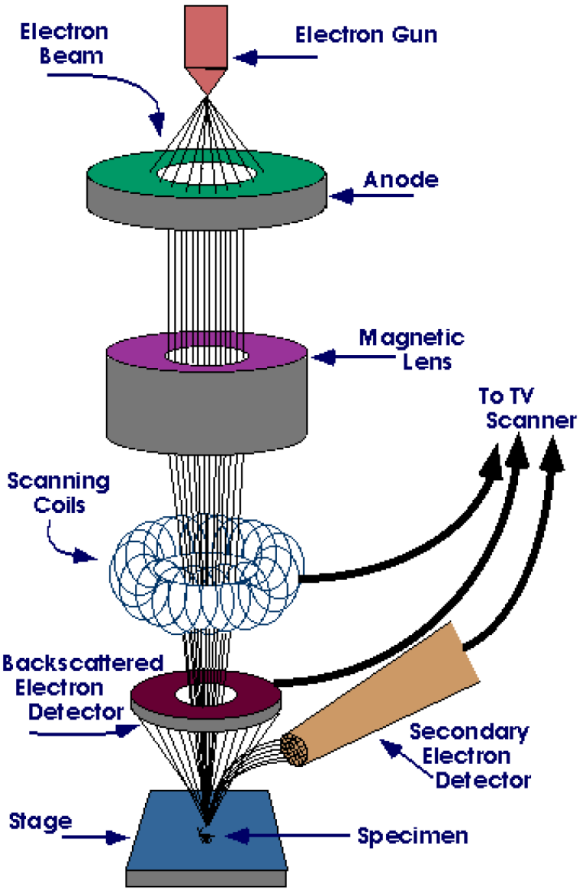

Figure 3.4 Schematic of main components of SEM [16].

3.2.2.1 Secondary electron (SE)

SE is most commonly used in SEM. When a primary electron penetrates the specimen surface, it can attack an electron of atoms at/near the surface leading to its emission. The emitted electron is called SE. Figure 3.5 shows the creation of SE.

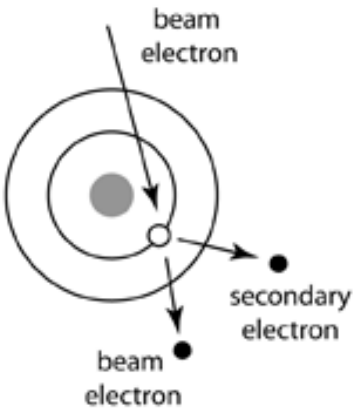

Figure 3.5 The collision of primary electron leading to the generation of SE [17].

3.2.2.2 Backscattering electron (BSE)

BSE occurs when the primary electrons goes back and leaves the surface without collision. Most of BSEs carry higher energy than SE. It is used for diffraction, imaging and analysis in SEM. Backscattering electron is shown in Figure 3.6. In addition, BSE can sometimes promote SE as shown in Figure 3.7.

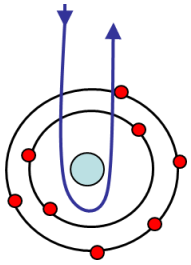

Figure 3.6 Backscattering electron [18].

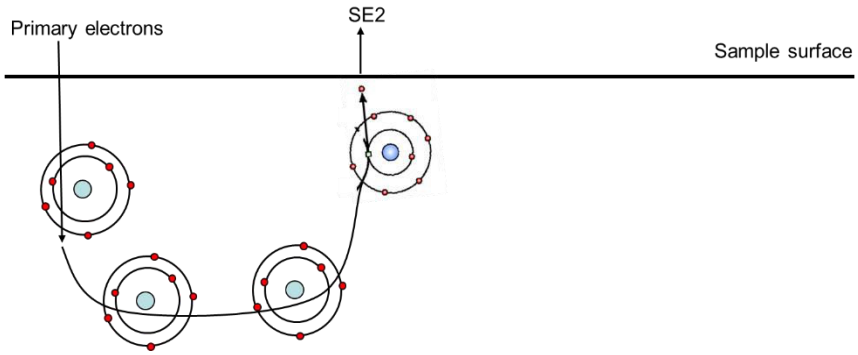

Figure 3.7 SE generation by colliding of BSE [18].

The images obtained from SE and BSE modes are rather different. SE provides topographic information and higher resolution images while BSE gives the information about the contrast resulting from the atomic number difference. Figure 3.8 shows the same analysed area by using SEM in the different processing modes, SE and BSE.

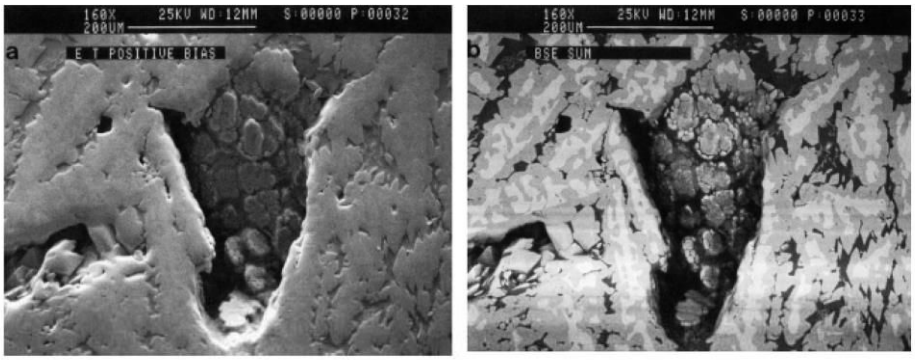

Figure 3.8 The comparison between a) a SE image and b) a BSE image for the same area of Ni alloy [19].

3.2.2.3 Relaxation of excited atoms (REA)

In case that electrons have been knocked out of an atom resulting in the creation of empty locations, these empty orbitals are filled with the electrons from the higher states (excited states). The excess energy is released because of the relaxation of electrons. There are 3 ways that are able to happen due to the electron relaxation.

Cathodoluminescence is the effect occurring when the vacant electron state is an outer state. Therefore, the energy released is small and is commonly emitted in the form of a photon which may be in the visible range.

On the contrary, if the vacant electron state is an inner state, higher energy is released. There are 2 possibilities of an energy emission that are a characteristic X-ray and a characteristic electron called Auger electron. The schematics of these effects are shown in Figure 3.9. For X-ray emission, when the inner shell electron is knocked out, the excited electron jumps into the inner shell vacancy. The energy released is the difference of energies of 2 electron shells and is a characteristic of atom species. The wavelength of X-ray (λ) can be calculated by Eq. 3.1 [15].

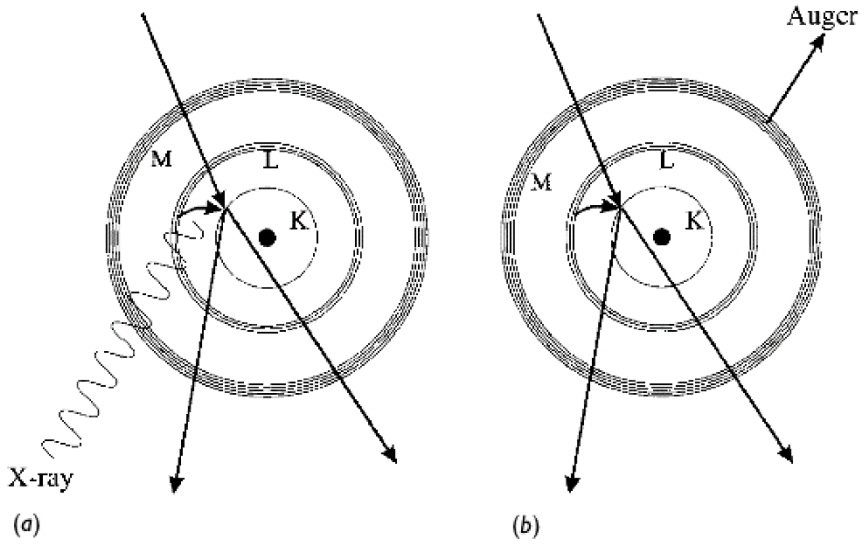

Figure 3.9 Two ways in which an inner-shell-excited atom can relax. In both cases, a K shell electron has been knocked out in a) a characteristic X-ray and b) an Auger electron [15].

$$\lambda = \frac{hc}{\Delta E} \qquad \text{(Eq. 3.1)}$$

where h = Planck's constant = 6.626×10^{-34} m^2kg/s
c = Celerity of light = 3×10^8 m/s
ΔE = The released energy

For Auger electron emission, an outer electron carrying the excess energy as kinetic energy is ejected. There are 3 electrons involving in this process: the original vacancy, the excited electron jumping into the vacancy and the outer electron leaving the atom.

3.2.3 Energy-dispersive X-ray spectrometer (EDX)

EDX is an additional tool installed in SEM. The objective of EDX is to analyse the chemical composition of the materials. The emitted X-ray photon enters to the detector where the results are interpreted in terms of the spectrum. One of the important limitation of EDX is the large interaction volume as shown in Figure 3.10.

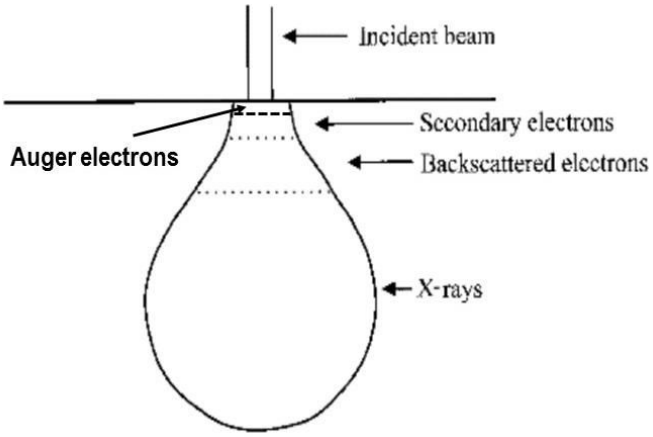

Figure 3.10 The interaction volume and the regions from which Auger electrons, secondary electrons, backscattering electrons and X-rays may be detected. The original figure is obtained from [15].

Due to the larger interaction volume, EDX is not an appropriate tool using for analysing the thin layer or specific place because the results could be disturbed by the surrounding elements. Thus, in this study, other tool used to analyse chemical compositions of the top surface was X-ray photoelectron spectroscopy (XPS).

3.2.4 X-ray photoelectron spectroscopy (XPS)

The 2 main objectives of this technique are (i) to provide the chemical compositions of the surfaces and the state of the detected elements and (ii) to use it for quantitative analysis [20]. By absorbing a photon, an atom gains an energy that would strike the electron in the inner shell. The inner shell electron (photoelectron) is ejected and a vacancy appears. The electron at the excited state would jump into this vacancy and emits the excess energy in terms of X-ray. Another possibility is the outer electron (Auger) emission. The differences of the energy at the initial state (before losing electron) and the energy after electron missing is called binding energy [11]. The binding energy is used to identify elements. The results of XPS are interpreted as a spectrum line. The example of XPS spectrum is shown in Figure 3.11. In this work, the X-ray of Mg was used to strike the photoelectron from the atom.

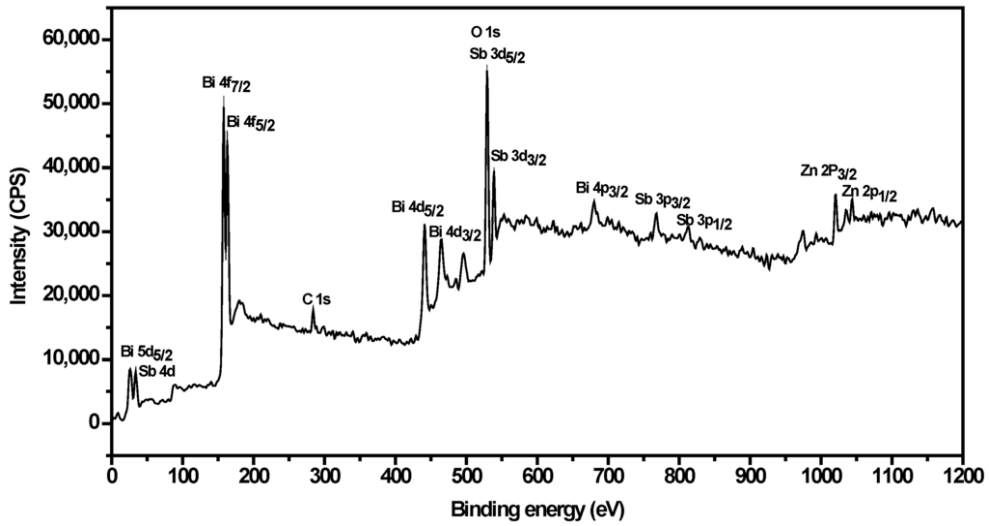

Figure 3.11 XPS spectrum of $ZnBiSbO_4$ photocatalyst [21].

3.2.5 X-Ray diffraction spectroscopy (XRD)

XRD is used for deducting crystalline information of the solid samples such as the crystalline structure and orientations. The principle of XRD is analysis of X-ray diffraction in sample by using Bragg's law presented in Eq. 3.2 [22] and Figure 3.12.

$$2d\sin\theta = n\lambda \qquad \text{(Eq. 3.2)}$$

where d = Lattice spacing
θ = The incident angle to specimen surface.
n = An integer (1, 2, 3,…)
λ = The wavelength of X-ray

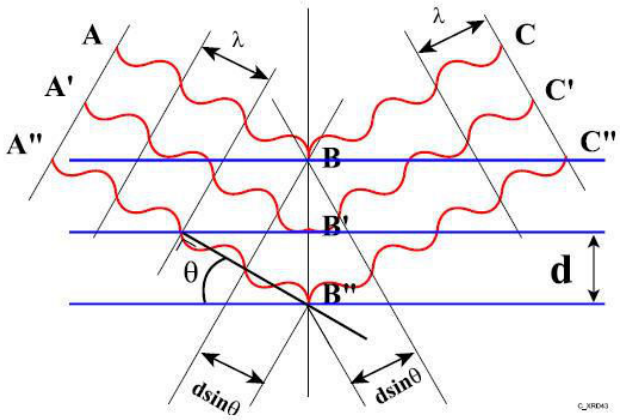

Figure 3.12 Diffraction of X-ray in crystalline structure at different incident angles [23].

According to characteristics of crystalline structure and lattice spacings of each compound, X-ray diffraction patterns are unique. The crystallized compounds can be observed by scanning X-rays with various incident angles and observing the intensities of diffracted X-rays at each angle. The measurement of X-ray diffracted intensities is achieved by the detector. The results of XRD can be interpreted by comparing with the standard database called « Joint Committee of Power Diffraction Standards (JCPDSs) ».

3.2.6 Raman spectroscopy

Raman spectroscopy is used to identify the molecular structures and phase compositions by using the molecular-scattering phenomena described by quantum theory and classical electromagnetic theory [11]. It investigates the vibrational, rotational and other low-frequencies modes of molecules by detecting light-scattering. The generic Raman system is shown in Figure 3.13. Raman has a very high performance for distinguishing the molecules which are composed of very similar chemical species [24]. The vibrations of each molecule contain several vibrational modes. Figure 3.14 shows the vibrational modes of CO_2. Each vibrational pattern leads to the different wavenumber (Raman shift) interpretation, so many peaks which represent a molecule can be observed as shown in Figure 3.15 [25].

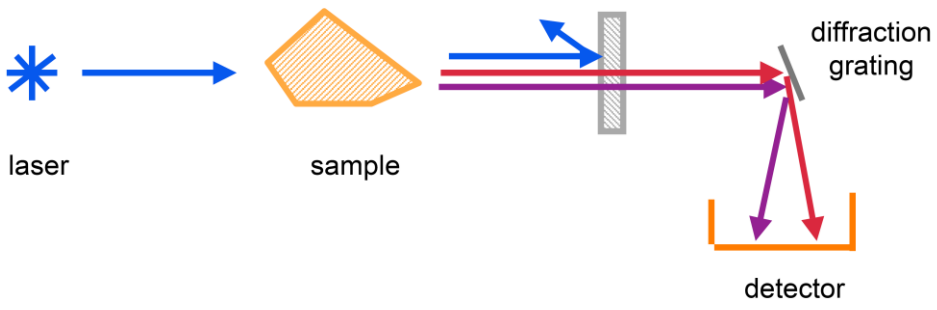

Figure 3.13 Generic Raman system flow diagram with a single light source.

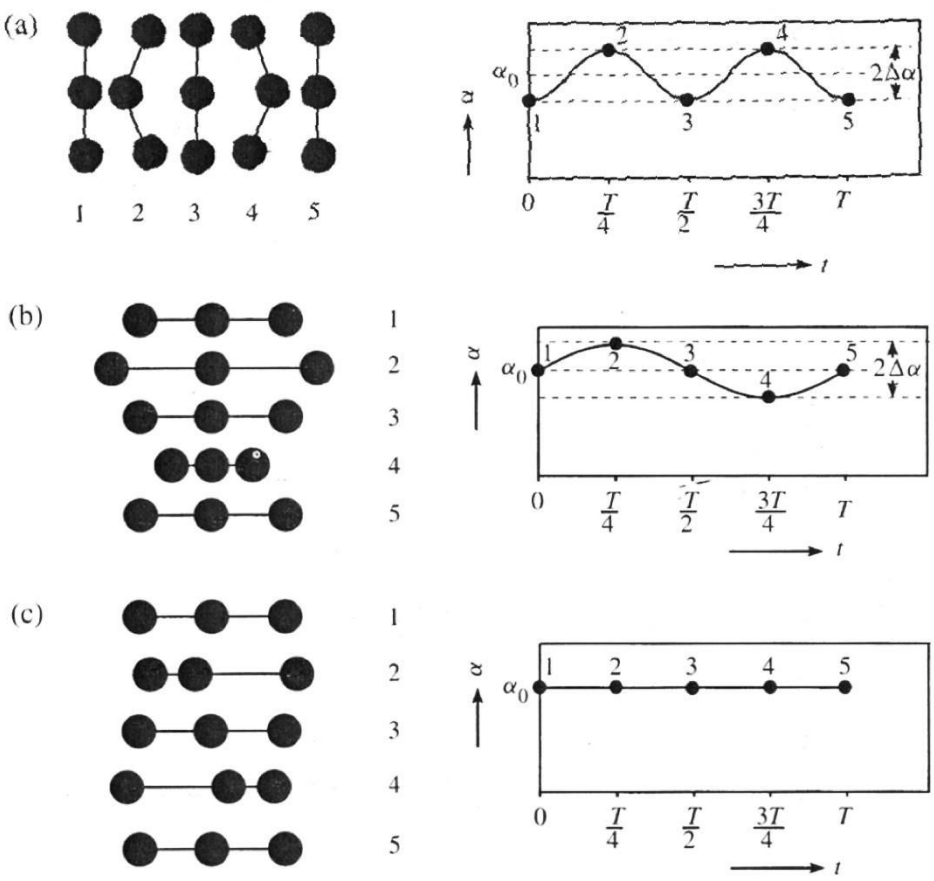

Figure 3.14 Vibrational modes of CO_2 [25].

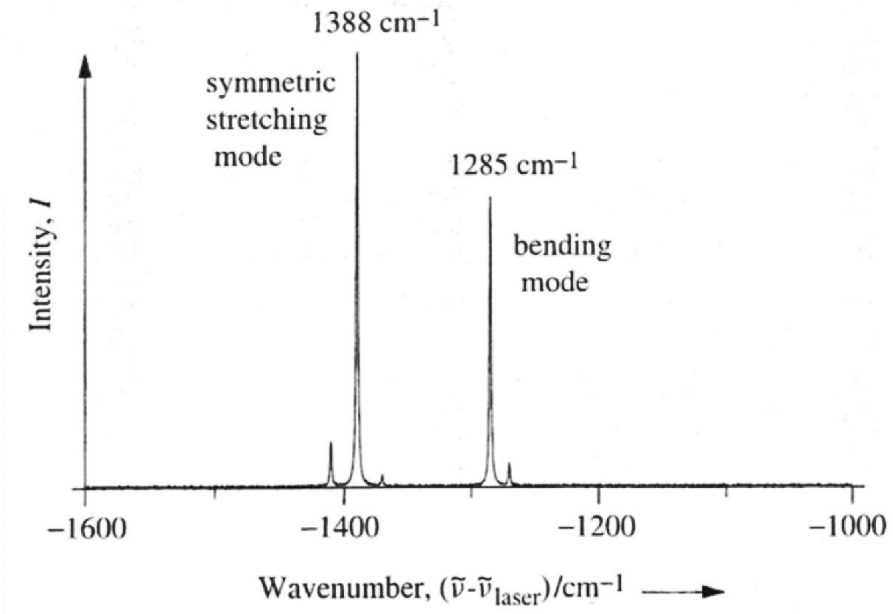

Figure 3.15 Raman spectrum of CO_2 [25].

3.2.7 Focused ion beam coupled with scanning electron microscope (FIB/SEM)

The FIB-SEM is composed of 2 columns: FIB column and SEM column as shown in Figure 3.16. The intercolumn angle is 54°. Ga^+ source is installed inside the FIB column for cutting, technically called milling, the interesting area while SEM records the cross sectional images. Before milling, the interesting area must be protected by C deposition in order to avoid the surface damage resulting from the milling process.

In this study, FIB-SEM was used to observe the cross section at precise positions of the nodules described in Chapter 5. Also, the evolution of nodules was observed by slicing the nodules every 20 nm. However, the results obtained from FIB-SEM are SEM images. Thus, an additional computer software named Fiji ImageJ must be used in order to analyse the results. From this useful program, the similarities, evolutions and 3D reconstructions of 2 types of nodules were investigated.

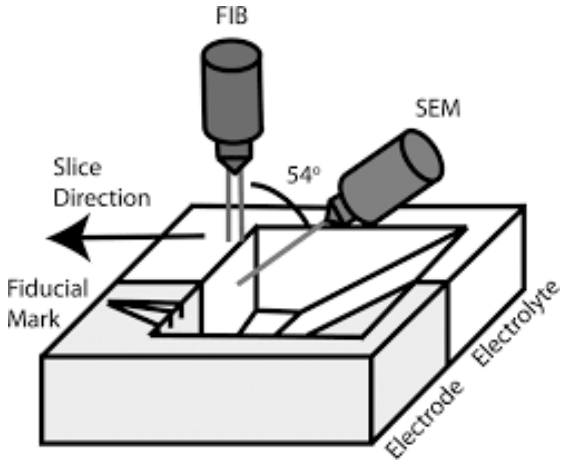

Figure 3.16 Schematic of FIB-SEM.

3.3 Experiments

In this work, the experimental procedures were divided into 2 steps: (i) specimen preparations and (ii) high temperature oxidation experiments.

3.3.1 Specimen preparations

AISI 441 sheet was cut into the dimensions of $15 \times 25 \times 1$ mm^3. Then, the specimens were polished up to #1200 grit SiC paper in order to control the surface roughness of each specimen and attain the smoother surface area that affects oxidation of the specimen. The polished specimens are called Bare 441 in the following. After that, Bare 441 specimens were ultrasonically cleaned for 5 min and tested high temperature oxidation experiments for measuring Cr volatilisation from the specimens.

In addition, Bare 441 was protected by developing the oxide layer covering the specimens. The methods used to form the oxide layers were electrodeposition coating method, so-called electroplating, and surface heat treatment or preoxidation.

3.3.1.1 Electroplating coating

Electrodeposition is the application of metallic coatings to metallic or other conductive surfaces by an electrochemical process. The schematic of electroplating method is shown in Figure 3.17.

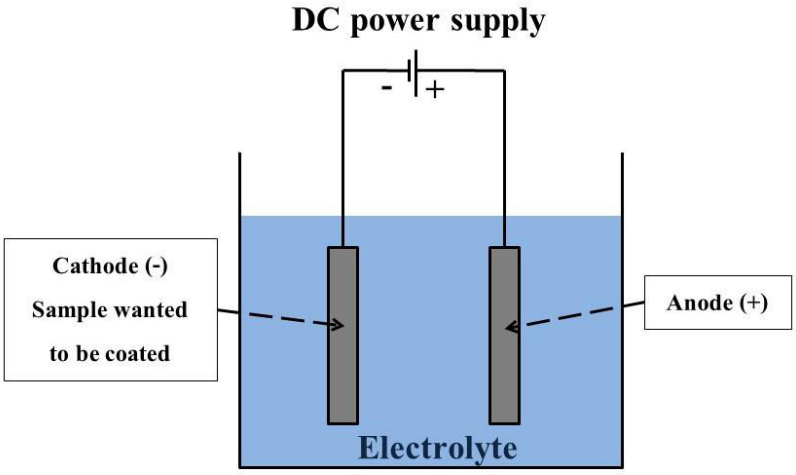

Figure 3.17 The schematic of the electroplating method.

The sample to be coated is plugged in cathode side while electrical conductive material is used as an anode in an electrolysis cell. Both electrodes are dipped into the electrolyte solution. The reactions are shown as following equations [26], [27].

Cathode: $M^{n+}(aq) + ne^- \rightarrow M(s)$ (Eq. 3.3)

Anode: $M(s) \rightarrow M^{n+}(aq) + ne^-$ (Eq. 3.4)

Every plating solution contains ingredients which serve one or more of the following functions [27].

1). To provide a source of coating metal.
2). To form complex with ions of the depositing metal.
3). To provide electrical conductivity.
4). To stabilise a solution e.g. against hydrolysis reaction.
5). To act as a pH buffer.
6). To modify or regulate the physical formation of the deposit.
7). To aid in dissolving the anode.
8). To modify other properties of, either the solution or the deposit.

The schematic of electroplating method is shown in Figure 3.18. The square box was used as a container in order to symmetrically distribute the charge movement. Before coating the Bare 441 specimen was pickled with 25%vol H_2SO_4 resulting in better adherence of the coating, then, it was put at the position of cathode. Anode was an inert material which did not participate in the reaction, but it has to be maintain for integrating the circuit. The bigger size of anode was used in order to reduce the current density. Too high current density leads to surface burnt. The distances between 2 electrodes and the electrodes to the edges of the container must be equal for the symmetric charge distribution.

The electrolyte was prepared from 0.1 M $CoSO_4$ (cobalt sulfate), 0.5 M $MnSO_4$ (manganese sulfate), 0.7 M $NaC_6H_{11}O_7$ (sodium gluconate), 1.0 M H_3BO_3 (boric acid), 0.1 M $(NH_4)_2SO_4$ ammonium sulfate and 20%vol H_2SO_4. All chemicals supplied by Ajax finechem pty Ltd.

The preparation electrolyte solution [28] was started from adding H_3BO_3 and $NaC_6H_{11}O_7$ into distilled water. Mixed solution was stirred by a magnetic stirrer until completely dissolved. Then, $CoSO_4$ was added with continue agitation for 30 min and kept standing for 24 h. After that, $MnSO_4$ was added with agitation. The pH of solution was measured and adjusted to 3.0 with ammonium sulfate or 20%vol H_2SO_4 [29]. The schematic of electrolyte preparation is shown in Figure 3.19.

Electrical current used for coating in this experiment was 0.2 A for 6 min. The thickness of Co and Mn assuming 100% yield can be calculated by Eq. 3.5 [30].

$$\delta = \frac{M_W}{nF\rho A} \int I\,dt \qquad \text{(Eq. 3.5)}$$

where δ = thickness of the deposited metal
M_W = atomic weight of the metal
n = valence charge = +2
F = Faraday's constant = 9.65×10^4 $C \cdot mol^{-1}$
ρ = density of the metal
A = deposition area
I = electrical current in Ampere (A)
t = depositing time in second (s)

Assuming that the depositing ratio of Mn:Co = 1:2. Thus, M_W and ρ were 57.60 g/mol and 8.34 $g \cdot cm^{-3}$ respectively. Finally, the theoritical thickness of this deposition was around 3 µm.

After metal deposition, the specimen was heated in ambient air at 800°C for 4 h in order to form the spinel structure of the depositing elements [31], [32].

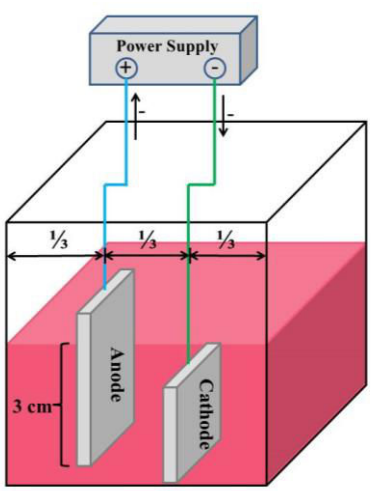

Figure 3.18 Schematic of electroplating coating used in this experiment (0.2 A, 6 min).

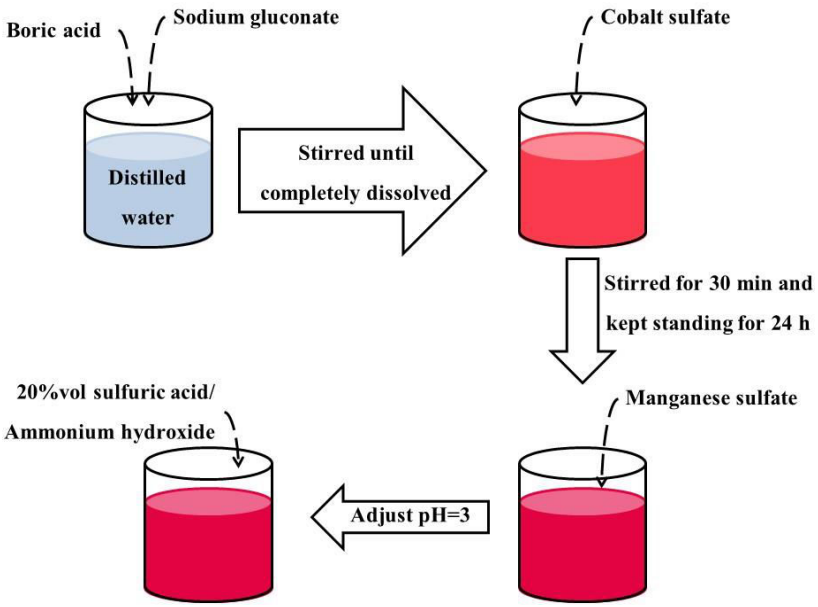

Figure 3.19 Schematic of electrolyte preparation.

3.3.1.2 Preoxidation

In the present work, Bare 441 specimens were preoxidised in 4 different conditions: Ar at 250°C, Ar at 850°C, CO/CO_2 at 250°C and CO/CO_2 at 850°C. The schematic of preoxidation experimental setup is shown in Figure 3.20. Ar, CO and CO_2 tanks were connected to the horizontal furnace. The cleaned Bare 441 specimen was put inside the column as a position of « S ». During preoxidation, the furnace was fed by 13.7 $L.h^{-1}$ (at room temperature) of high purity Ar contaminating with 2 ppm of O_2 (given by supplier) or by 11 $L.h^{-1}$ of equimolar CO_2/CO mixture (according to the stoichiometric ratio of CO_2:CO = 1:1, as shown in Eq. 3.6). The oxygen content of CO_2 gas is 10 ppm (given by the supplier). The oxygen partial pressures

(P_{O_2}) imposed by these peroxidising atmospheres are reported in Table 3.2. In the case of preoxidation in CO/CO_2 mixture, P_{O_2} during preoxidation were calculated by using the standard free energy of reaction reported by Young [33].

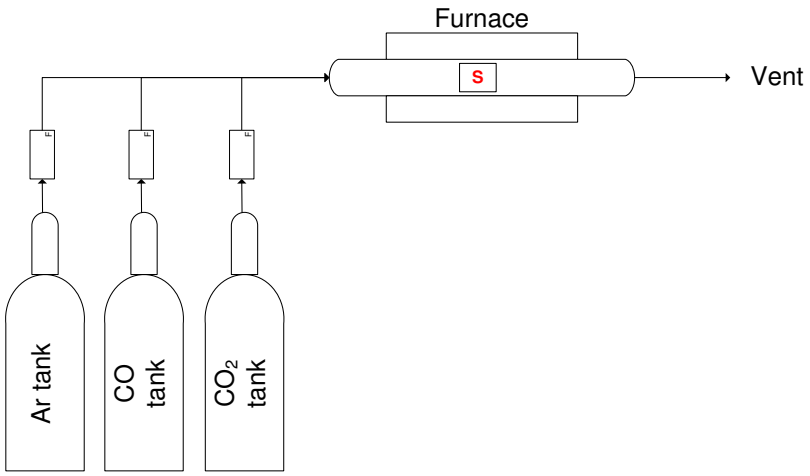

Figure 3.20 The schematic of preoxidation experimental setup.

$$CO(g) + \frac{1}{2}O_2(g) = CO_2(g) \qquad \text{(Eq. 3.6)}$$

Table 3.2 Specimen preparation methods (P. for preoxidised).

Specimens	Polished	Preoxidation gas		Preoxidation temperature		Partial pressure of O_2 during preoxidation, P_{O_2} (bar)	$\log P_{O_2}$
		Ar	CO_2/CO	250°C	850°C		
Bare 441	✓					-	-
P.Ar-250	✓	✓		✓		$2 \times 10^{-6*}$	– 5.7
P.Ar-850	✓	✓			✓	$2 \times 10^{-6*}$	– 5.7
P.CO_2/CO-250	✓		✓	✓		4.56×10^{-48}	– 47.5
P.CO_2/CO-850	✓		✓		✓	6.31×10^{-18}	– 17.2

*Specification from supplier

The specimens were preoxidised in each condition for 3 h after a temperature ramp increase of 20°C.min^{-1}. Then, they were subsequently characterised and used for volatilisation testing.

3.3.2 High temperature oxidation experiments

Before high temperature oxidation, the exact size and weight of specimens were measured with a precision of 0.02 mm and 10 µg respectively. Then, they were cleaned by ethanol (EtOH) in an ultrasonic bath for 5 min and dried with synthetic air.

Figure 3.21 shows the experimental setup used for determining Cr volatilisation. O_2 was flowed from the O_2 tank through the humidifier set in order to adjust humidity in the gas. The humidifier set consisted of the boiler, condenser and thermo cryostat for controlling the temperature of cooling water (set to 33°C for 5% humidity). After that, the humidified gas was flowed to the column installed inside the vertical furnace. The specimen was hung inside the column as the "S" position in Figure 3.21. At the outlet of the column, the condenser containing distilled water was installed in order to condense Cr volatile species in the gas. Before venting the gas to the atmosphere, the gas was flowed through the 2nd bubbler that was water-containing Erlenmeyer flask in order to make sure that all Cr volatile species from the specimen was condensed in the solution. After the experiment, the specimen was weighed again. The column was cleaned by 0.1 M HCl acid. Cleaning acid solution, condensate and the solution from the 2nd bubbler were collected and analysed by ICP in order to find the total amount of Cr volatile from the sample.

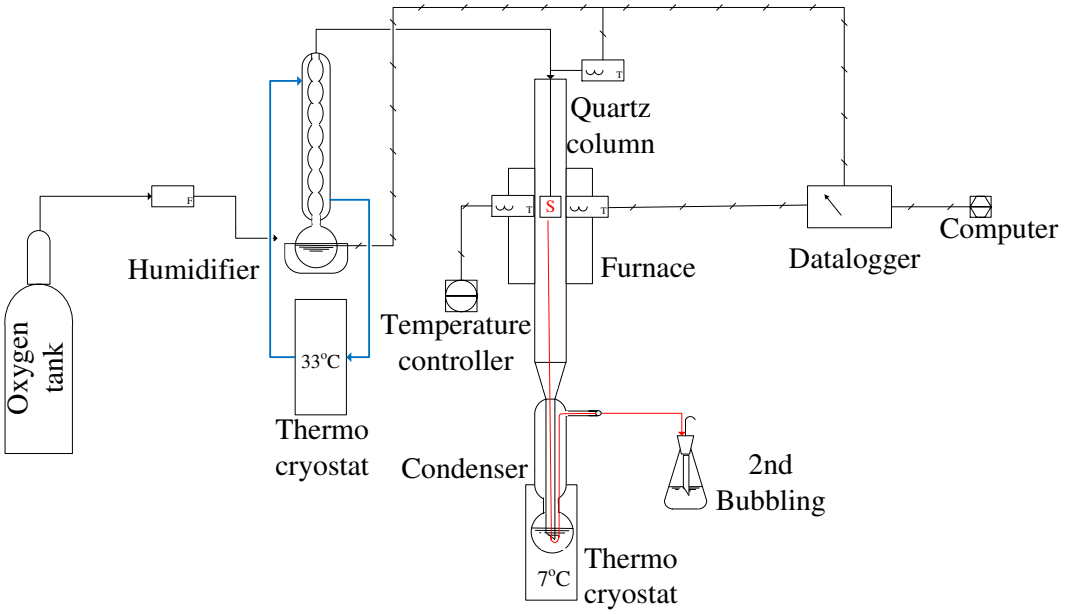

Figure 3.21 High temperature oxidation experimental setup for Cr volatilisation study.

In the case of Bare 441 oxidation, the effects of linear velocity of gas, oxidation time and surface roughness on Cr volatilisation were studied. For studying the effect of linear velocity of gas, the specimen was oxidised in 5% H_2O in O_2 at 800°C for 96 h. Linear velocity of gas at the heating zone inside the furnace was varied in the range of 1-10 cm/s. To investigate the effect of oxidation time, the specimen was oxidised in 2 cm/s of 5% H_2O in O_2 at 800°C. The oxidation time was varied in the range of 24-96 h. For surface roughness consideration, Cr species volatilisation of as-received AISI 441 (unpolished) was studied comparing with polished AISI 441 up to # 1200 grit SiC paper (Bare 441). The results of this part are reported in Chapter 4.

For protective 441 specimens that are coated 441 and preoxidised 441, only the effect of gas linear velocity on Cr species volatilisation was studied. The experimental conditions were the same as Bare 441 experiments (1-10 cm/s of 5% H_2O in O_2, 800°C, 96 h). Cr volatilisation results of these specimens are discussed in Chapter 6-8.

The preoxidised specimens, from now on, are abbreviated as P.(preoxidation atmosphere)-(preoxidation temperature) and the specimens after preoxidation and high temperature oxidation are abbreviated as P.(preoxidation atmosphere)-(preoxidation temperature)+ox.(linear velocity of wet O_2). For example, P.CO/CO_2-250+ox.4 stands for Bare 441 preoxidised in CO/CO_2 at 250°C for 3 h and oxidised in 4 cm/s of 5%H_2O in O_2 at 800°C for 96 h.

Before and after high temperature oxidation, the specimen surfaces were characterised SEM, EDX, XRD, XPS and Raman spectroscopy and cross sections were prepared with FIB, ensuring reliable observations of the few hundred of nanometres thick oxide scales.

References

[1] L. Antoni, J. Mougin, A. Galerie, and M. Dupeux, “Influence of Ti and Nb on the competition between oxidation kinetics and oxide adhesion on 18 % Cr stainless steels.”, Ugitech Internal Report, Ugine, France, 2001. [online]. Available: www.ugitech.com/fileadmin/user_upload/Ugitech/Documents/articlesCRU/C032-P142byLAntoni.pdf. [Accessed: 2-Apr-2015]

[2] J. R. Davis, Ed., ASM specialty handbook: Stainless steels, 1st ed. Ohio: ASM international, 1994.

[3] J. Hong, Y. Shin, and H. W. Lee, “Characterization of corrosion resistance in a ferritic stainless steel stabilized with Ti addition,” Int. J. Electrochem. Sci., vol. 9, pp. 7325–7334, 2014.

[4] L. X. Wang, C. J. Song, F. M. Sun, L. J. Li, and Q. J. Zhai, “Microstructure and mechanical properties of 12 wt.% Cr ferritic stainless steel with Ti and Nb dual stabilization,” Mater. Des., vol. 30, no. 1, pp. 49–56, 2009.

[5] M. P. Sello, “The Laves phase embrittment of ferritic stainless steel type AISI 441,” University of Pretoria, Republic of South Africa, Ph.D. Thesis. 2009.

[6] Z. Yang, G.-G. Xia, C.-M. Wang, Z. Nie, J. Templeton, J. W. Stevenson, and P. Singh, "Investigation of iron–chromium–niobium–titanium ferritic stainless steel for solid oxide fuel cell interconnect applications," J. Power Sources, vol. 183, no. 2, pp. 660–667, Sep. 2008.

[7] H. S. Seo, D. W. Yun, and K. Y. Kim, "Oxidation behavior of ferritic stainless steel containing Nb, Nb-Si and Nb-Ti for SOFC interconnect," Int. J. Hydrogen Energy, vol. 38, no. 5, pp. 2432–2442, 2013.

[8] G. B. Hunter and T. W. Eager, "Ductility of Stabilized Ferritic Stainless Steel Welds," Metall. Trans. A, vol. 11A, pp. 1–6, 1980.

[9] J. F. Shackelford and W. Alexander, Materials science and engineering handbook, 3rd ed. CRC Press LLC, 2001.

[10] H. Ali-Löytty, P. Jussila, T. Juuti, L. P. Karjalainen, A. A. Zakharov, and M. Valden, "Influence of precipitation on initial high-temperature oxidation of Ti-Nb stabilized ferritic stainless steel SOFC interconnect alloy," Int. J. Hydrogen Energy, vol. 37, pp. 14528–14535, 2012.

[11] ASM handbook: Materials characterization. ASM international, 1998.

[12] X. Hou and B. T. Jones, "Inductively Coupled Plasma/Optical Emission Spectrometry," Analytical Chemistry. John Wiley & Sons Ltd., pp. 9468–9485, 2000.

[13] C. B. Boss and K. J. Fredeen, Concepts, Instrumentation and Techniques in Inductively Coupled Plasma Optical Emission Spectrometry, 2nd ed. Perkin Elmer, 1997.

[14] C. Stadtländer, "Scanning electron microscopy and transmission electron microscopy of mollicutes: Challenges and opportunities," Mod. Res. Educ. Top. Microsc., pp. 122–131, 2007.

[15] P. J. Goodhew, J. Humphreys, and R. Beanland, Electron microscopy and analysis, 3rd ed. Taylor & Francis, 2001.

[16] B. Voutou and E. Stefanaki, "Electron microscopy : The Basics," 2008.

[17] "What are secondary electrons, how are they formed, and what can they tell us about the sample?," McSwiggen & Associates, 2005. [Online]. Available: http://www.mcswiggen.com/FAQs/FAQ_EF-2.htm. [Accessed: 21-Apr-2015].

[18] A. W. B. Skilbred and H. Fjeld, "Scanning electron microscope (SEM)." 2009. [Online]. Available: http://www.uio.no/studier/emner/matnat/fys/MENA3100/v09/lecture_notes/24february09.ppt. [Accessed: 17-Apr-2015].

[19] "Analytical methods for materials: Scanning electron microscopy and X-ray spectroscopy." University of Alabama, 2011. [Online]. Available: http://bama.ua.edu/~mweaver/courses/MTE481/2_MTE481-Principles_OM.pdf. [Accessed: 12-Mar-2015].

[20] G. Berthomé, “Surface analysis: An introduction to XPS,” Grenoble, France. Master lectures.

[21] J. Laun, M. Chen, and W. Hu, “Synthesis, characterization and photocatalytic activity of new photocatalyst $ZnBiSbO_4$ under visible light irridiation,” Int. Journal Mol. Sci., vol. 15, no. 6, pp. 9459–9480, 2014.

[22] “Basics of X-ray Diffraction,” Thermo ARL-CH Publ., 1999.

[23] K. Daikarn, “X-ray diffraction (XRD),” 2012. [Online]. Available: http://www.mfu.ac.th/center/stic/index.php/x-ray-analysis-instrument-menu/item. [Accessed: 16-Apr-2015].

[24] T. Thompson, “Fundamentals of Raman spectroscopy,” 2000. [Online]. Available: http://faculty.kfupm.edu.sa/PHYS/zhyamani/teaching/Coupled_Oscillations/lectures/lecture_8/Raman%20study%20material/fundamentals-of-raman-spectroscopy.whitepaperpdf.render.pdf. [Accessed: 12-Mar-2015].

[25] C. Hess, “Raman spectroscopy : Basic principles and applications.” 2006. [Online]. Available: http://www.fhi-berlin.mpg.de/acnew/department/pages/teaching/pages/teaching__wintersemester__2006_2007/hess_raman_spectroscopy_101106.pdf. [Accessed: 12-Mar-2015].

[26] H. H. Lou and Y. Huang, “Electroplating,” Encyclopedia of chemical processing. 2006. [Online]. Available: http://chem1.eng.wayne.edu/~yhuang/Papers/Book_Plating_ECHP.pdf. [Accessed: 13-Oct-2011].

[27] K. Osborne, “Electroplating,” Metal Protection Ltd., Auckland. [Online]. Available: http://nzic.org.nz/ChemProcesses/metals/8G.pdf. [Accessed: 13-Oct-2011].

[28] J. Wu, C. D. Johnson, R. S. Gemmen, and X. Liu, “The performance of solid oxide fuel cells with Mn-Co electroplated interconnect as cathode current collector,” J. Power Sources, vol. 189, pp. 1106–1113, 2009.

[29] J. Wu, Y. Jiang, C. Johnson, and X. Liu, “DC electrodeposition of Mn-Co alloys on stainless steels for SOFC interconnect application,” J. Power Sources, vol. 177, pp. 376–385, 2008.

[30] H. H. Lou and Y. Huang, “Electroplating,” Encyclopedia of chemical processing. 2006. [Online]. Available: http://chem1.eng.wayne.edu/~yhuang/Papers/Book_Plating_ECHP.pdf. [Accessed: 13-Oct-2011].

[31] W. Wongpromrat, “Chromium evaporation from stainless steel interconnect in solid oxide feul cells and its protection,” King Mongkut’s Institute of Technology Ladkrabang, 2012.

[32] W. Wongpromrat, H. Thaikan, W. Chandra-ambhorn, and S. Chandra-ambhorn, “Chromium vaporisation from AISI 441 stainless steel oxidised in humidified oxygen,” Oxid. Met., vol. 79, no. 5–6, pp. 529–540, Feb. 2013.

[33] D. J. Young, High temperature oxidation and corrosion of metals, 1st ed. Elsevier, Oxford UK/Amsterdam NL, 2008.

Chapter 4

Cr volatilisation from AISI 441

4.1 Specimen characterisations

4.1.1 Characterisations of the passive oxide scale before high temperature oxidation by XPS

Before high temperature oxidation, Bare 441 was analysed by XPS. The specimen surfaces were perpendicularly penetrated by X-ray. The penetration depth for this angle was around 10 nm. The results of this observation are shown in Figure 4.1. Si, Nb, O, Cr and Fe were observed at binding energy of 102, 207, 531, 576, and 712 eV respectively while Mn and Ti photoelectron lines were not detected. Figure 4.2 shows the peaks of Fe. These peaks implied that 2 different states of Fe could be observed that were Fe bound with O and metallic Fe from the substrate. This confirmed that the oxide layer formed on Bare 441 was thinner than 10 nm.

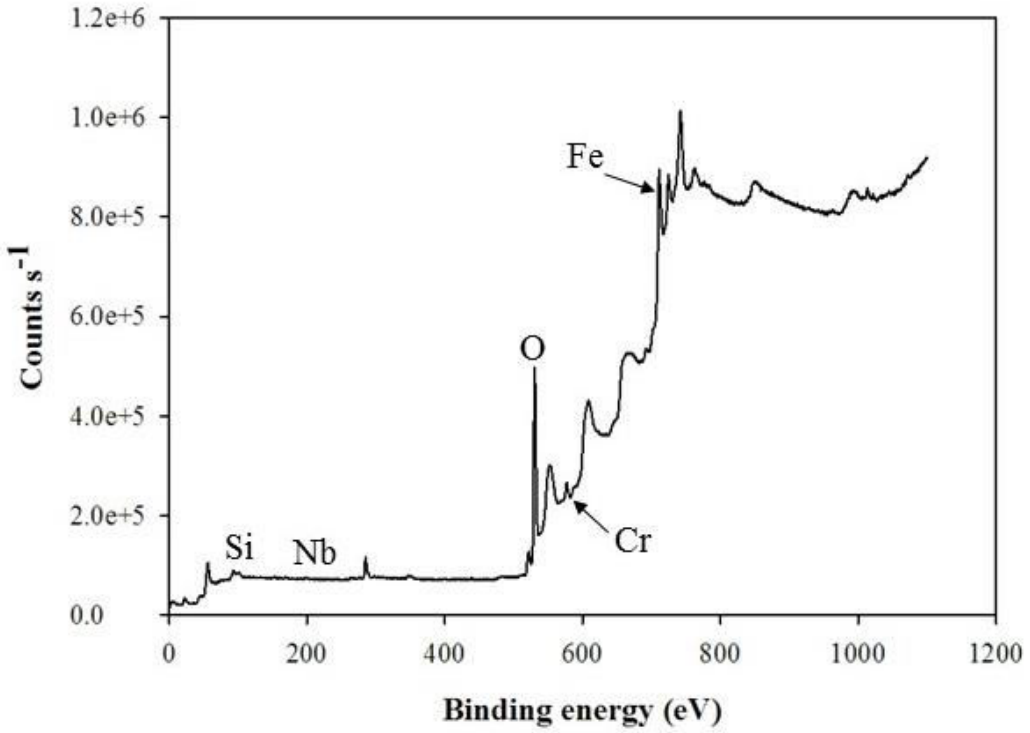

Figure 4.1 XPS results of Bare 441 before high temperature oxidation.

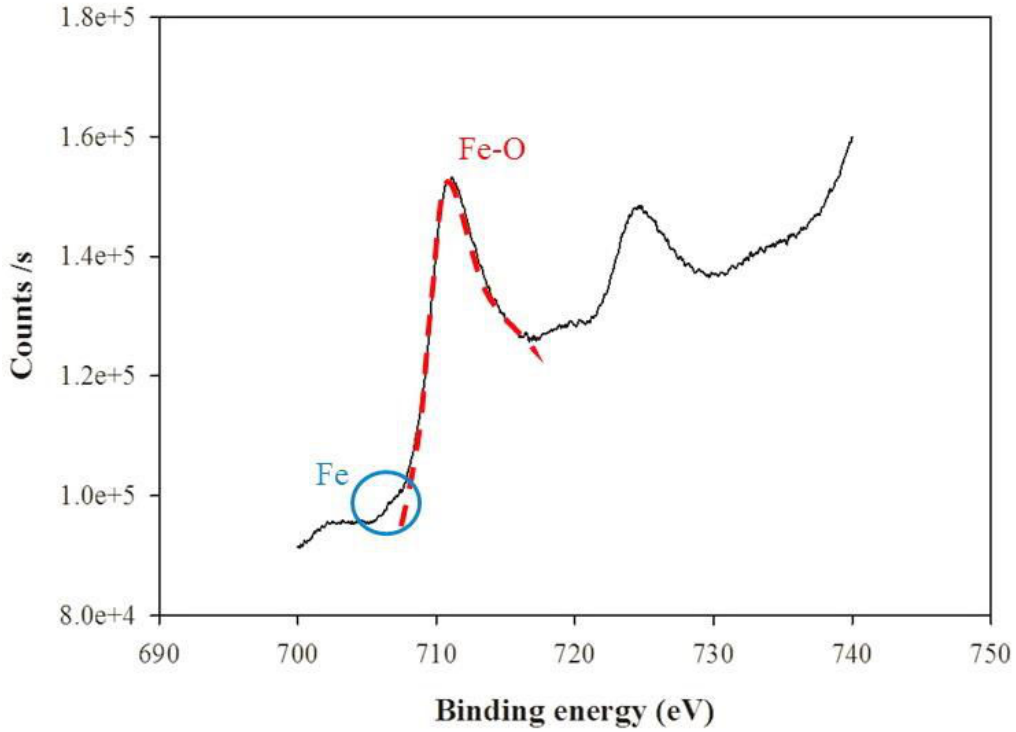

Figure 4.2 XPS peaks of Fe2p line observed on Bare 441 before high temperature oxidation.

4.1.2 Characterisations of the oxide scale after high temperature oxidation

Figures 4.3 show low magnification SEM images whereas EDX spectra are displayed on Figure 4.4. It can be observed that the specimen surface was not smooth. Overall qualitative analysis by EDX at 20 keV revealed that matrix surface was mainly composed of Fe, O and Cr and also contained Si, Nb, Ti and Mn. However, with a 20 keV primary electron beam, the interaction volume emitting X-Ray is much deeper than the thickness of the oxide layer (few µm vs few 100 nm), so Fe can still be detected with a very high intensity.

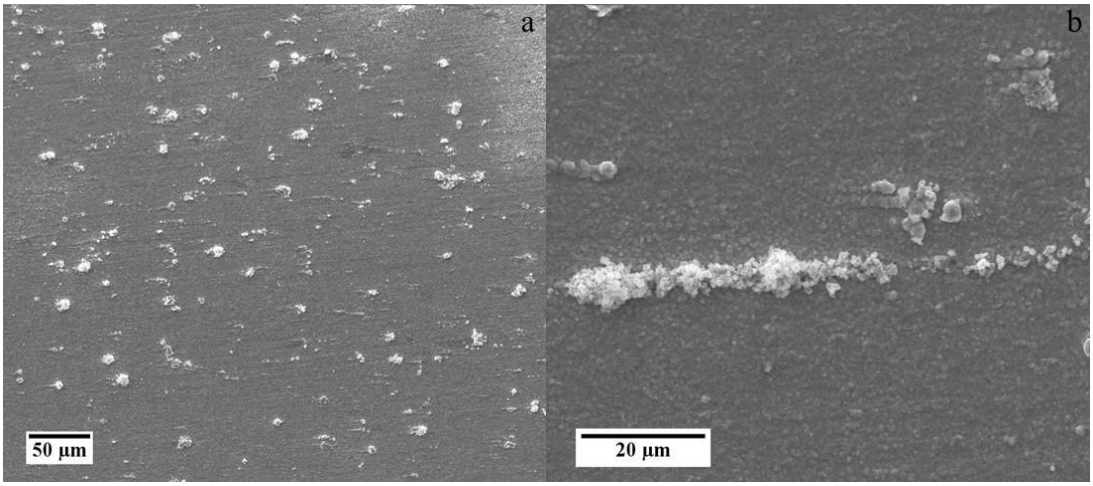

Figure 4.3 SEM images in SE mode of Bare 441 after high temperature oxidation (2 cm/s, 5%H_2O in O_2, 800°C, 96 h) when the magnifications of the images are a) 200x and b) 1000x.

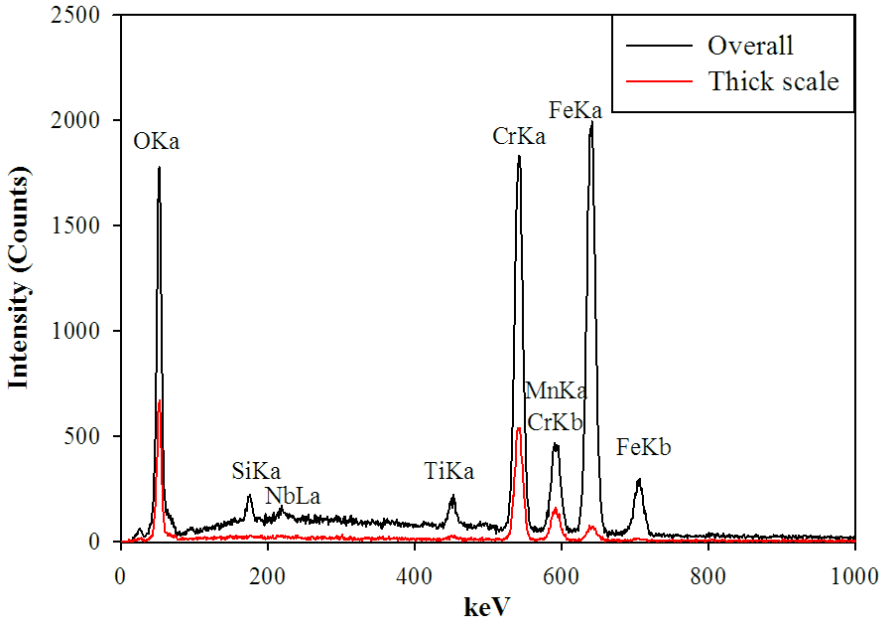

Figure 4.4 EDX results of Bare 441 after high temperature oxidation (2 cm/s, 5%H_2O in O_2, 800°C, 96 h).

Meanwhile, in SEM images (SE mode), the bright and thick phase can be observed. After increasing the magnification, it is clear that the bright thick phase was at the scratch position occurred in the polishing step. Therefore, it can be summarised that, at the scratch position, oxidation reaction can be occurred with higher rate than at the matrix that means the surface roughness affected oxidation process [1]. Since standard SEM observations are not suitable for studying such thin oxide scales, cross sections were prepared with FIB which will ensure reliable observations.

Surface and FIB cross sectional views of oxide scales grown on AISI 441 at 800°C in wet atmosphere (5% H_2O in O_2) for 4, 14 and 24 h are displayed in Figure 4.5. EDX map from

FIB cross section of oxide scale grown on AISI 441 at 800°C in wet atmosphere (5% H_2O in O_2, 2 cm/s) for 24 h is shown in Figure 4.6. EDX map includes thick and thin oxide scale as highlighted in Figure 4.6. According to surface views, the oxide exhibits a classical micro-crystallised scale which covers the entire surface. Grain growth can be observed with increasing oxidation time. The classical duplex structure consisting of a Mn-Cr spinel top layer and a Cr_2O_3-rich inner layer is clearly observed on cross sections and EDX map.

After 4 h of oxidation, the inner scale is continuous while the outer spinel is not. Some cavities can be observed at the metal oxide interface as well as TiN, NbC or intermetallic Laves phase Fe_2Nb [2]–[6]. Internal oxidation of Ti and Nb can also be noticed as well as the formation of a discontinuous silica layer. After 24 h of oxidation, the outer scale is continuous, characterised by large micro-crystallized grains inducing variations in scale thickness.

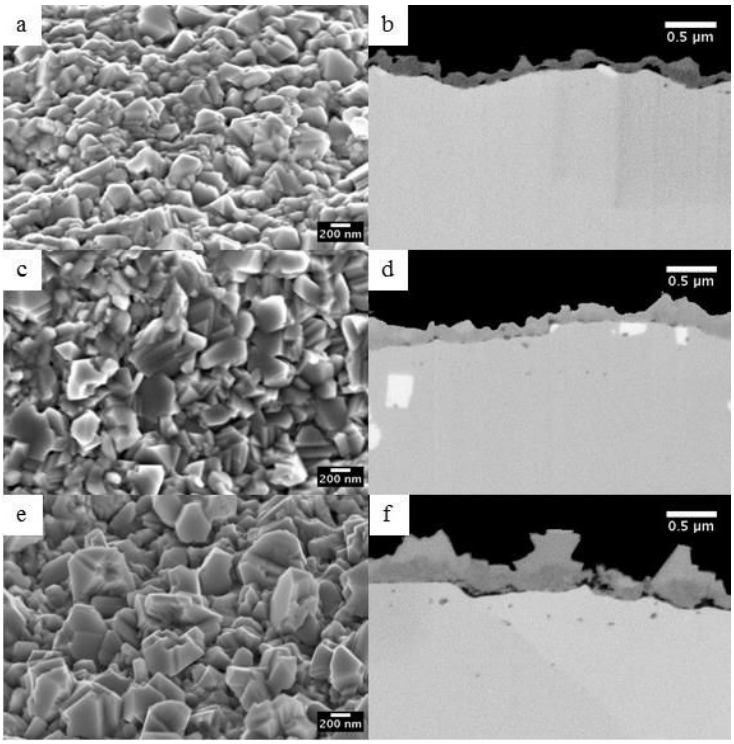

Figure 4.5 Surfaces and FIB cross sections of oxide scales grown on AISI 441 at 800°C in wet atmosphere (5% H_2O in O_2, 2 cm/s) for 4 h (a and b), 14 h (c and d) and 24 h (e and f).

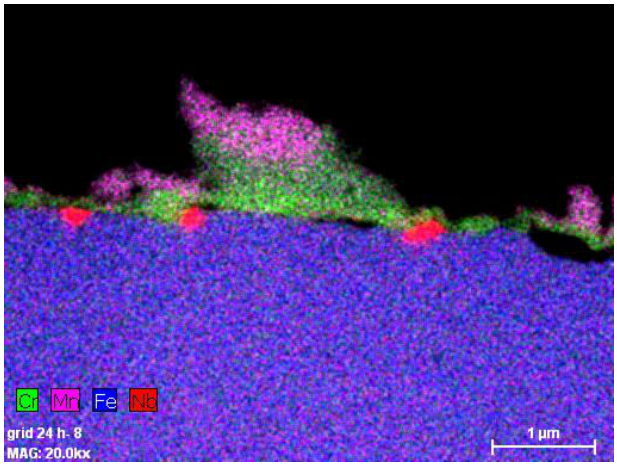

Figure 4.6 EDX map from FIB cross sections of oxide scales grown on AISI 441 at 800°C in wet atmosphere (5% H_2O in O_2, 2 cm/s, 24 h).

This results are in good agreement with the general morphology of Ti-Nb added steels after high temperature oxidation [7]–[10] shown in Figure 4.7.

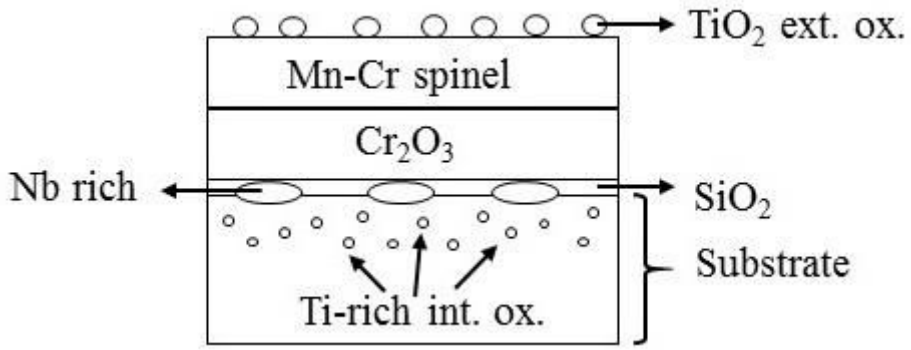

Figure 4.7 Schematic of general morphology of Ti-Nb added ferritic steel after high temperature oxidation.

4.2 Cr volatilisation results

4.2.1 Effect of linear velocity of gas on Cr species volatilisation

Figure 4.8 shows the specific Cr released of Bare 441 against linear velocity of gas after high temperature oxidation in 5% H_2O in O_2 at 800°C for 96 h. The repeatability of experiments was around ± 15%. From the figure, the tendency of the graph could be divided into 2 zones. The first zone was occupied at the linear velocity below 3 cm/s. In this zone, Cr volatilisation was increased with increasing linear velocity of gas. It implies that Cr volatilisation in this zone was limited by the diffusion of Cr volatile species from the specimen in the gas. Above 3 cm/s of gas linear velocity, Cr volatilisation was independent with gas linear velocity. Thus, this zone was limited by kinetics of reaction [11], [12].

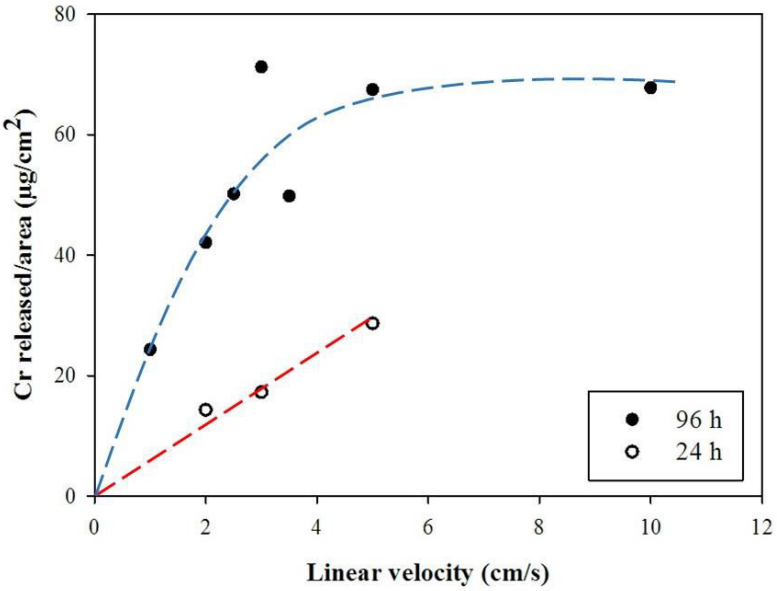

Figure 4.8 Specific Cr released of bare AISI 441 after high temperature oxidation (5%H_2O in O_2, 800°C, 24 and 96 h).

As mentioned in Chapter 2, Cr species volatilisation includes 2 steps that are reaction and diffusion steps. These steps occur in series. First, the reaction step is the reaction of Cr_2O_3 with O_2 (and possibly H_2O) to form Cr volatile species as shown in Eqs. 2.4-2.6. The diffusion step is the diffusion of Cr volatile species in the gas. The diffusion rate depends on the gas linear velocity while the reaction rate does not.

In our experiments, the diffusion limit was found at the gas linear velocity lower than 3 cm/s. It means that, in this range, the boundary layer thickness was thick, so the diffusion rate of Cr volatile species was lower than the reaction rate. When the gas linear velocity was increased, the boundary layer thickness decreased affecting faster diffusion of Cr volatile species through boundary layer. At least 3 cm/s of gas linear velocity, the boundary layer thickness of this zone was very thin, so Cr could diffuse through the boundary layer with the diffusion rate less than reaction rate. Therefore, the phenomenon of Cr species volatilisation became kinetics limit.

Many Cr species volatilisation is reported in the literatures. However, it is often difficult to compare with our results because of the dissimilarity of experimental conditions and unspecified data such as tube diameter, specimen surface area, temperature of the flow rate (ambient, standard or furnace). Figure 4.9 shows the transition linear velocity from diffusion to kinetics of our experiments comparing with that of Gindorf et al. [11] and Kurokawa et al. [13]. Gindorf et al. studied Cr volatilisation from chromia powder in 10%H_2O in air. Assuming a 3 cm in diameter tube which is the same range as the present work, Cr volatilisation phenomenon transformed from diffusion to kinetics limit at gas linear velocity around 1 cm/s. Kurokawa et al. studied Cr volatilisation from chromia pellets at 900°C in the same atmosphere as Gindorf et al. They found that the transition occurred at a gas linear velocity of 1.6 cm/s in the furnace (0.4 cm/s at STP).

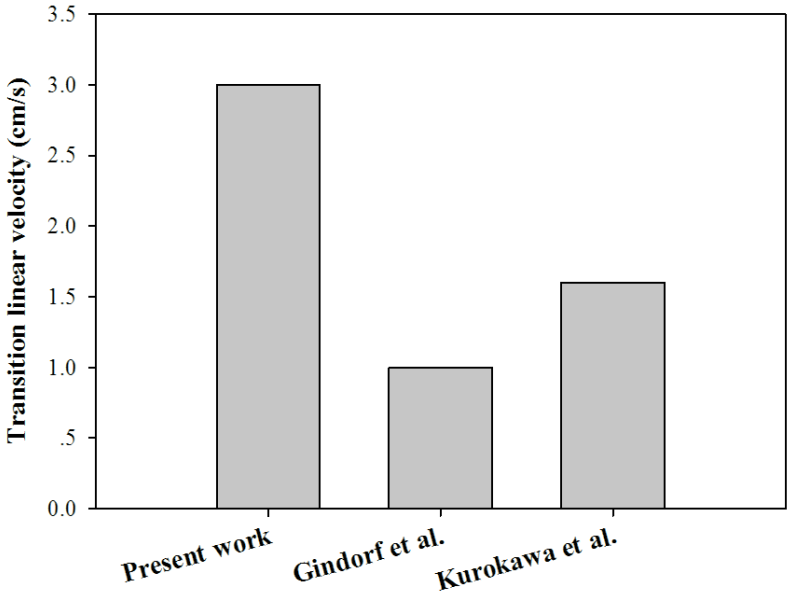

Figure 4.9 Linear velocity that Cr volatilisation transforms from diffusion to reaction limit comparing with that of Gindorf et al. [11] and Kurokawa et al.[13].

For Cr volatilisation rate consideration, 2 types of specimens that are chromia, Cr_2O_3 pellets or powder, and alloys were used to determine Cr volatilisation. Cr volatilisation from chromia and alloys comparing with our experiments are shown in Figures 4.10-4.11 respectively.

In Figure 4.10, our results are compared with the results of Kurokawa et al. [13], Galerie et al. [14] and Stanislowski et al. [12]. These results were obtained in the kinetic regimes. As described above, Kurokawa et al. [13] observed Cr volatilisation from chromia in 10%H_2O in air at 900°C. In the kinetic regime, Cr depletion rate was 2×10^{-10} g/cm^{2}s. Chandra-ambhorn also investigated Cr species volatilisation results in SIMaP laboratory. The conditions studied was the same as this experiment that were 5%H_2O in O_2 at 800°C. Cr volatilisation rate was 1.33×10^{-11} g/cm^{2}s. Stanislowski et al. [12] demonstrated Cr species volatilisation from Ducrolloy which is Cr-based alloy and behave like pure chromia because its oxide scale grown on these alloys is not polluted by Fe and Mn. Their experiments were launched in 1.88% H_2O in air at 800°C. Cr volatilisation rate reported in this literature was 7×10^{-11} g/cm^{2}s.

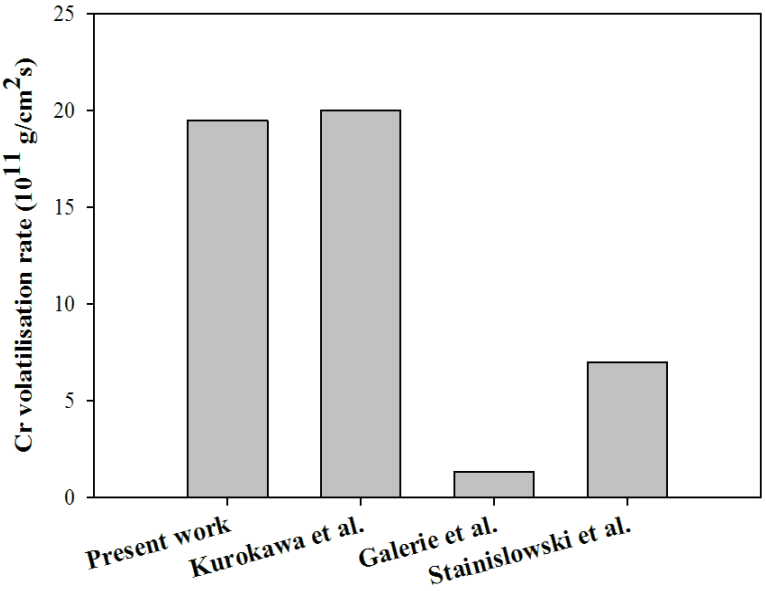

Figure 4.10 Cr volatilisation rate from Bare 441, our experiments, comparing with Cr volatilisation from chromia reported in the literatures [12]–[14].

Cr species volatilisation from Cr-containing alloys are generally lower than chromia due to the duplex oxide scale containing external $(Mn,Cr)_3O_4$ protecting the pure chromia subscale. AISI 441 presented in Figure 4.11 is our result. Stainislowski et al. [12] found that Cr species volatilisation from Crofer 22 APU in 1.88% H_2O in air at 800°C was 2.5×10^{-11} g/cm^{2}s. Collins et al. [15] vaporised Cr from AISI 430 in 3% H_2O in air at 800°C. Vaporisation rate of Cr was 4×10^{-12} g/cm^{2}s. Holcomb [16] found 1.1×10^{-10} g/cm^{2}s of Cr volatilisation rate from Haynes 230 in 37%H_2O in air at 760°C.

In summary, it appears that the present works using AISI 441 ferritic stainless steel lie in the broad cloud of experimental values.

Taking into account 24 h oxidation of Bare 441 in the linear velocity range of 2-5 cm/s, Cr species volatilisation was increased with increasing linear velocity which means that it was limited by diffusion of Cr volatile species in the gas. Comparing 24 h with 96 h oxidation times in the same experimental condition, Cr depleted from specimens oxidised for 24 h was lower than that of 96 h oxidation time for more than 2 times. However, Cr volatilisation rates of both experimental conditions (24 and 96 h) were not significantly different as shown in Figure 4.12. Therefore, in order to have a clear explanation, the effect of oxidation time on Cr volatilisation rate was determined.

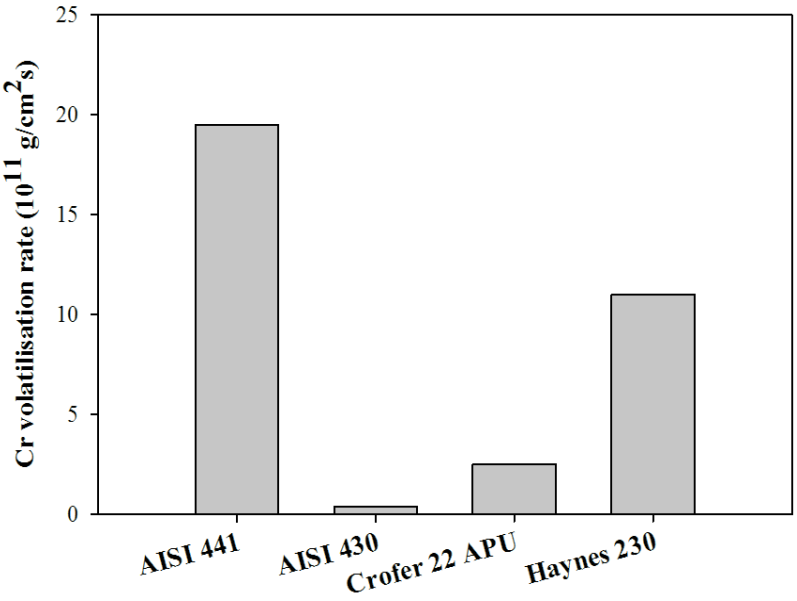

Figure 4.11 Cr volatilisation from Bare 441, our experiment, comparing with other alloys reported in the literatures [12], [15], [16].

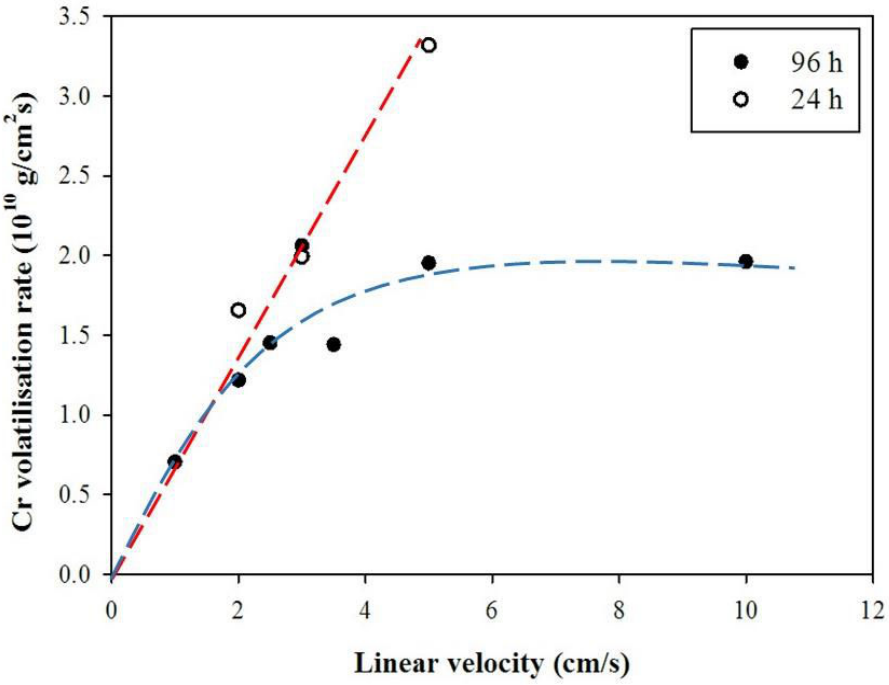

Figure 4.12 Cr volatilisation rate of Bare 441 after high temperature oxidation (5%H_2O in O_2, 800°C, 24 and 96 h).

4.2.2 Effect of oxidation time on Cr volatilisation

In this section, the effect of oxidation time on Cr species volatilisation was studied. Bare 441 was oxidised in the same experimental conditions as the last section (5%H_2O in O_2

at 800°C). Linear velocity of gas was set to be constant at 2 cm/s while oxidation duration was varied in the range of 24-96 h. The results are shown in Figure 4.13. The tendency of Cr species volatilisation in this experimental range seemed to be constant. This revealed that Cr species volatilisation was independent on oxidation time.

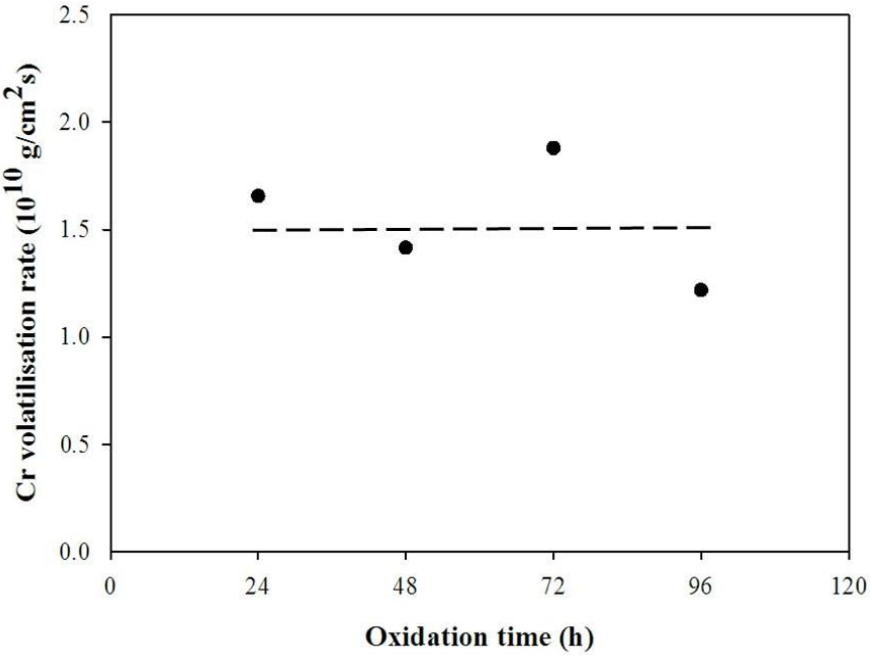

Figure 4.13 Effect of oxidation time on Cr volatilisation rate (2 cm/s, 5%H_2O in O_2, 800°C).

4.2.3 Effect of surface roughness on Cr volatilisation

Although, it is clear that high surface roughness leads to high oxidation rate, but the effect of surface roughness on Cr volatilisation remains unclear. Thus, in this part, this effect was studied by using 2 different specimens that were Bare 441 and as-received 441. As received 441 is the specimen obtained from the supplier. After 2B finishing (cold rolled, annealed, pickled and skin passed), its surface roughness was around 300-500 nm while the surface roughness of Bare 441, #1200 SiC polished, was 20.2 nm [17]. Thus, as-received 441 was rougher than Bare 441 around 15-25 times. Before high temperature oxidation experiment, both specimens were cleaned by EtOH in an ultrasonic bath for 5 min. As-received specimens were oxidised in 2 cm/s of 5%H_2O in O_2 at 800°C for 24 and 96 h. The results are shown in Figure 4.14.

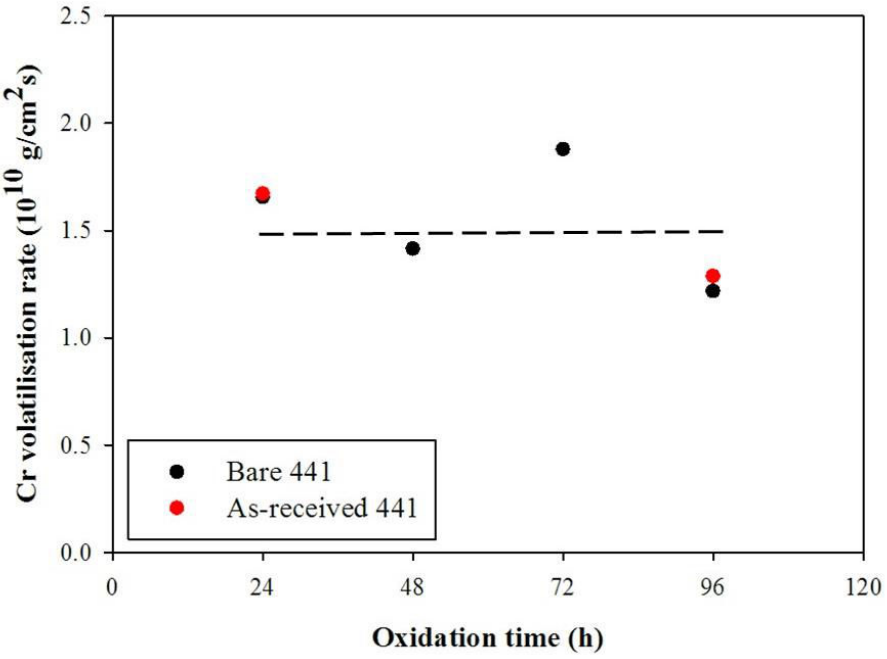

Figure 4.14 Effect of surface roughness on Cr volatilisation rate (2 cm/s, 5%H_2O in O_2, 800°C).

At the same experimental conditions, Cr volatilisation from Bare 441 and as-received 441 were similar. Thus, it can be summarised that Cr volatilisation rate did not depend on surface roughness of specimen. However, surface observation of both specimens by SEM shows the different surface topographies. For Bare 441, its surface was the same as the surface shown in Figure 4.3 while the surface of as-received 441 is shown in Figure 4.15.

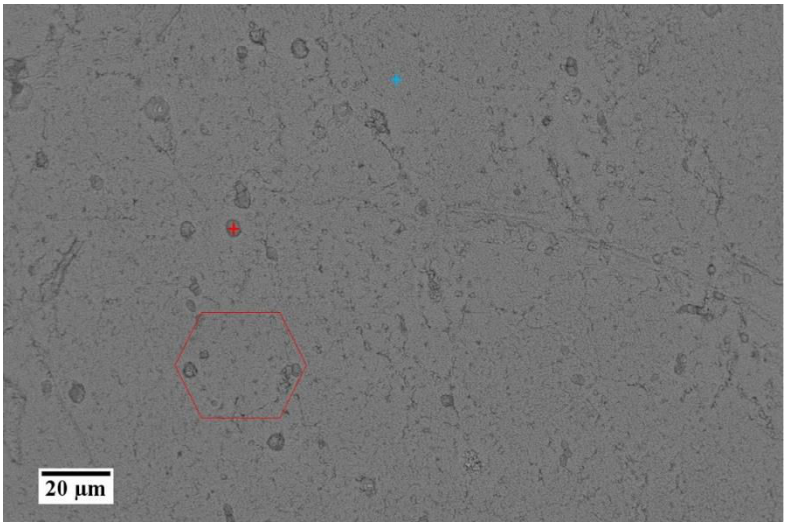

Figure 4.15 SEM images of as-received 441 after high temperature oxidation (2 cm/s, 5%H_2O in O_2, 800°C, 96 h).

The surface of as-received 441 was not smooth. The hexagons that are the shape of metallic grain boundaries can be observed. Also, the egg-shape nodules can be seen on the surface especially above the metallic grain boundaries. Normally, the formation of the Fe-rich nodules is a sign of catastrophic oxidation (breakaway oxidation) [18], [19]. Nevertheless, EDX showed that the major elements of nodules were Ti and/or Nb while the main components of the matrix scale were Cr, Mn, Fe and O. Therefore, these nodules were probably the new type which did not lead to breakaway oxidation. This hypothesis would be proved in the next chapter (Chapter 5). Also, the morphologies and other information of these nodules would be described.

4.2.6 Relation between Cr volatilisation and Net Mass Change

In this section, a study linking net mass changes and Cr weight losses is proposed. In order to compare net mass changes and Cr weight losses measured by ICP, experimental values are divided by the total duration of the high temperature experiment. Data related to net mass change correspond to a mean weight change rate due to O uptake for the formation of Cr_2O_3 and to Cr species volatilisation due to the formation of Cr(VI) volatile species. Data related to Cr weight loss correspond to a mean Cr volatilisation rate due to the formation of Cr(VI) volatile species. Results obtained for AISI 441 oxidised for 24 h, 48 h, 72 h and 96 h in wet atmosphere (5% H_2O in O_2) at 800°C for linear velocities varying from 1 cm/s to 10 cm/s are presented in Figure 4.16.

According to Figure 4.16, a linear relation between mass change mean rate and Cr weight loss mean rate can be made. The intercept of the linear fit is not zero although for no weight gain one might assume no Cr species volatilisation. The measured net mass changes are not only related to weight gain due to O uptake for the formation of Cr_2O_3 but also to Cr loss due to the formation of Cr(VI) volatile species. The weight gain rate due to O uptake is underestimated which results in shifting the data set. Experimental errors may also arise: despite the calibration procedure, systematic errors in ICP measurements can be argued. Since Cr collection yield is not equal to 1, weight loss due to Cr species volatilisation is also underestimated.

It is interesting to note that whatever the gas linear velocity and the oxidation time, high Cr volatilisation mean rate is related to high mass change mean rate. As seen on Figure 4.13, highest mean rates are higher for 24 h than for 96 h experiments. For a given time of oxidation, the highest linear velocities correspond to the highest Cr weight loss and net mass change mean rates.

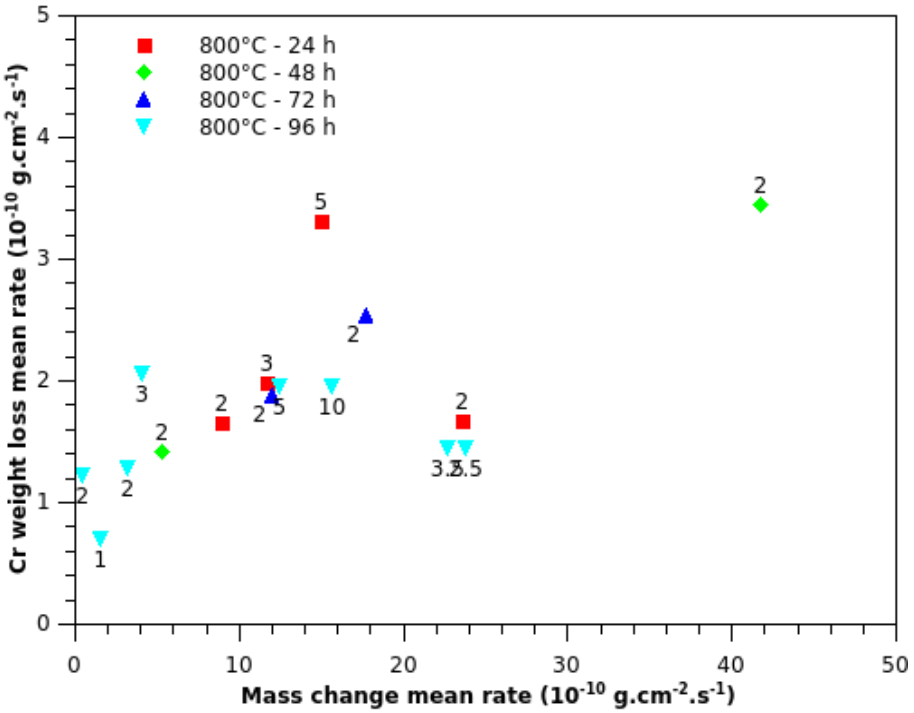

Figure 4.16 Evolution of Cr volatilisation mean rate according net mass change rate of AISI 441 oxidised for 24 h, 48 h, 72 h and 96 h in wet atmosphere (5% H_2O in O_2) at 800°C, for linear velocities varying from 1-10 cm/s.

Since for a majority of samples, Cr volatilisation rate values are far lower from mass change rate values, one can neglect the Cr loss due to volatilisation and match the mass change rate to a mass gain link only to O uptake for the formation of Cr_2O_3. This assumption can be discussed for the lowest mass change rates; however it allows linking the mass change rate to the growth rate of the Cr_2O_3 scale. Weight gain rate due to O uptake is then convert in an equivalent mass rate of oxidised Cr according to equations Eq. 4.2.

$$2Cr + 3O \rightarrow Cr_2O_3 \qquad \text{(Eq. 4.1)}$$

$$m_{Cr} = \frac{3}{2}\frac{M_{Cr}}{M_O} m_O \qquad \text{(Eq. 4.2)}$$

where m_i and M_i represent mass and molar mass of species i respectively.

According to this assumption, the ratio between volatilised and oxidised Cr can be considered and compared to the mass rate of oxidised Cr. Results are displayed in Figure 4.17. The set of data - 800 °C, 96 h, 2 cm/s - does not satisfied the assumption assuming that the Cr volatilisation rate values are far lower than mass change rate values and will not considered in the following.

According to Figure 4.17, the lowest ratio between volatilised and oxidised Cr are associated with high Cr oxidation mean rates and correspond to 24 h experiments or experiments performed at high velocities. On the contrary for the highest ratio between volatilised and oxidised Cr, Cr oxidation mean rate is low and correspond to experiment performed for 96 h at low gas linear velocities. Cr oxidation rate can be link with Cr_2O_3 growth rate. For high Cr_2O_3 growth rate, Cr volatilisation rate is low and conversely.

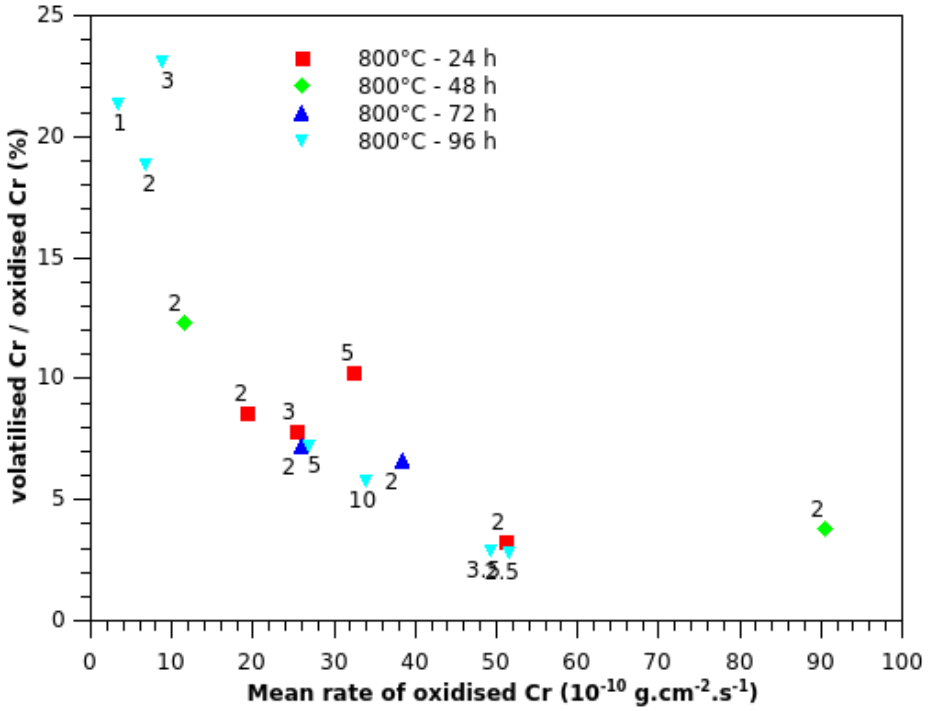

Figure 4.17 Evolution of the ratio between volatilised Cr and oxidised Cr according rate of oxidised Cr for AISI 441 oxidised for 24 h, 48 h, 72 h and 96 h in wet atmosphere (5% H_2O in O_2) at 800°C for linear velocities varying from 1 cm/s to 10 cm/s.

4.3 Conclusions

In this chapter, Bare 441 was oxidised in the simulated cathodic condition of SOFC that was 5%H_2O in O_2 at 800°C for examining Cr species volatilisation. First oxide scales before and after high temperature oxidation were presented. After high temperature oxidation, Cr, Fe, Mn, Si, Nb and Ti were unsurprisingly found. A thicker oxide was formed at the scratch position occurring from the polishing step. This implies that the oxidation rate at the scratch position was higher than that of the smoother area. Then, the effect of gas linear velocity on Cr species volatilisation was studied. The gas linear velocity was varied in the range of 1-10 cm/s and the oxidation time was 96 h. From this experiment, it can be seen that Cr species volatilisation characteristic can be divided into 2 zones. In the range that gas linear velocity lower than 3 cm/s, Cr species volatilisation increased with increasing gas linear velocity that means it was limited by the diffusion of Cr volatile species in the gas. Above this gas linear velocity range, Cr species volatilisation was limited by kinetics of reaction. Although, the

surface roughness affected the oxidation process and the morphologies of the steel surface, it did not affect Cr volatilisation rate. This was similar to the oxidation time that also did not affect Cr species volatilisation. Finally a link between net mass changes and Cr weight losses is proposed. It has been shown that whatever the gas linear velocity and the oxidation time, high Cr evaporation mean rate is related to high mass change mean rate. The highest Cr evaporation and mass change mean rates are for the shorter time of oxidation and for the highest linear velocities.

In case of the morphology investigation, for as-received 441, the egg-shape nodules were observed especially at the metallic grain boundaries while they cannot be seen on Bare 441 surface. The appearance of these nodules seemed similar to the Fe-rich nodules which were the cause of breakaway oxidation, but the components were different. These nodules would be deeply studied in the next chapter.

References

[1] S. C. Kuiry, S. Seal, S. K. Bose, and S. K. Roy, “Effect of surtace preparation on the high-temperature oxidation behaviour of AISl 316 stainless steel,” ISIJ Int., vol. 34, no. 7, pp. 599–606, 1994.

[2] Y. Kato, M. Ito, Y. Kato, and O. Furukimi, “Effect of Si on Precipitation Behavior of Nb-Laves Phase and Amount of Nb in Solid Solution at Elevated Temperature in High Purity 17%Cr-0.5%Nb Steels,” Mater. Trans., vol. 51, no. 9, pp. 1531–1535, 2010.

[3] H. Ali-Löytty, P. Jussila, and M. Valden, “Optimization of the electrical properties of Ti-Nb stabilized ferritic stainless steel SOFC interconnect alloy upon high-temperature oxidation: The role of excess Nb on the interfacial oxidation at the oxide-metal interface,” Int. J. Hydrogen Energy, vol. 38, no. 2, pp. 1039–1051, 2013.

[4] B. Kuhn, M. Talik, L. Niewolak, J. Zurek, H. Hattendorf, P. J. Ennis, W. J. Quadakkers, T. Beck, and L. Singheiser, “Development of high chromium ferritic steels strengthened by intermetallic phases,” Mater. Sci. Eng. A, vol. 594, pp. 372–380, 2014.

[5] J. Froitzheim, G. H. Meier, L. Niewolak, P. J. Ennis, H. Hattendorf, L. Singheiser, and W. J. Quadakkers, “Development of high strength ferritic steel for interconnect application in SOFCs,” J. Power Sources, vol. 178, no. 1, pp. 163–173, 2008.

[6] P. D. Jablonski, C. J. Cowen, and J. S. Sears, “Exploration of alloy 441 chemistry for solid oxide fuel cell interconnect application,” J. Power Sources, vol. 195, no. 3, pp. 813–820, 2010.

[7] J. Froitzheim, S. Canovic, M. Nikumaa, R. Sachitanand, L. G. Johansson, and J. E. Svensson, “Long term study of Cr evaporation and high temperature corrosion behaviour of Co coated ferritic steel for solid oxide fuel cell interconnects,” J. Power Sources, vol. 220, pp. 217–227, Dec. 2012.

[8] J. G. Grolig, J. Froitzheim, and J.-E. Svensson, "Coated stainless steel 441 as interconnect material for solid oxide fuel cells: Oxidation performance and chromium evaporation," J. Power Sources, vol. 248, pp. 1007–1013, Feb. 2014.

[9] J. Rufner, P. Gannon, P. White, M. Deibert, S. Teintze, R. Smith, and H. Chen, "Oxidation behavior of stainless steel 430 and 441 at 800 °C in single (air/air) and dual atmosphere (air/hydrogen) exposures," Int. J. Hydrogen Energy, vol. 33, pp. 1392–1398, 2008.

[10] Z. Yang, G.-G. Xia, C.-M. Wang, Z. Nie, J. Templeton, J. W. Stevenson, and P. Singh, "Investigation of iron–chromium–niobium–titanium ferritic stainless steel for solid oxide fuel cell interconnect applications," J. Power Sources, vol. 183, no. 2, pp. 660–667, Sep. 2008.

[11] C. Gindorf, L. Singheiser, and K. Hilpert, "Vaporisation of chromia in humid air," vol. 66, pp. 384–387, 2005.

[12] M. Stanislowski, E. Wessel, K. Hilpert, T. Markus, and L. Singheiser, "Chromium vaporization from high-temperature alloys: I. Chromia-forming steels and the influence of outer oxide layers," J. Electrochem. Soc., vol. 154, no. 4, p. A295, 2007.

[13] H. Kurokawa, C. Jacobson, L. Dejonghe, and S. Visco, "Chromium vaporization of bare and of coated iron–chromium alloys at 1073 K," Solid State Ionics, vol. 178, no. 3–4, pp. 287–296, Feb. 2007.

[14] A. Galerie, M. R. Ardigo, P. Berthod, W. Chandra-Ambhorn, S. Chevalier, P. Y. Hou, and F. Rouillard, "Influence of water vapor on high-temperature oxidation of chromia-forming materials." French Activity on High Temperature Corrosion in Water Vapor. Materials Science Foundations Vol. 76 Trans Tech Publications.

[15] C. Collins, J. Lucas, T. L. Buchanan, M. Kopczyk, a. Kayani, P. E. Gannon, M. C. Deibert, R. J. Smith, D. S. Choi, and V. I. Gorokhovsky, "Chromium volatility of coated and uncoated steel interconnects for SOFCs," Surf. Coatings Technol., vol. 201, no. 7 SPEC. ISS., pp. 4467–4470, 2006.

[16] G. R. Holcomb, "Calculation of reactive-evaporation rates of chromia," Oxid. Met., vol. 69, no. 3–4, pp. 163–180, 2008.

[17] Y. Madi, E. Salhi, F. Charlot, A. Galerie, and Y. Wouters, "Influence of polishing-induced surface hardening on the adhesion of oxide scales grown on a ferritic stainless steel," Oxid. Met., vol. 75, no. 3–4, pp. 167–181, Dec. 2010.

[18] A. Galerie, S. Henry, Y. Wouters, M. Mermoux, J.-P. Petit, and L. Antoni, "Mechanisms of chromia scale failure during the course of 15-18Cr ferritic stainless steel oxidation in water vapour .pdf," Mater. High Temp., vol. 21, no. 4, pp. 105–112, 2005.

[19] S. Henry, “Influence de la vapeur d’eau sur l'oxydation a haute temparature du chrome et de quelques aciers inoxydables ferritiques stabilises,” Institute National Polytechnique de Grenoble, Ph.D. Thesis, 2000, in French.

Chapter 5

Nodule development on as-received 441 during high temperature oxidation

Nodule development on an as-received specimens was shown in Figure 4.15. It is interesting that the appearance of the nodules was similar to nodule developed during catastrophic oxidation [1], [2], so-called breakaway oxidation. Figure 5.1 shows nodule developed during catastrophic oxidation reported by Henry [2].

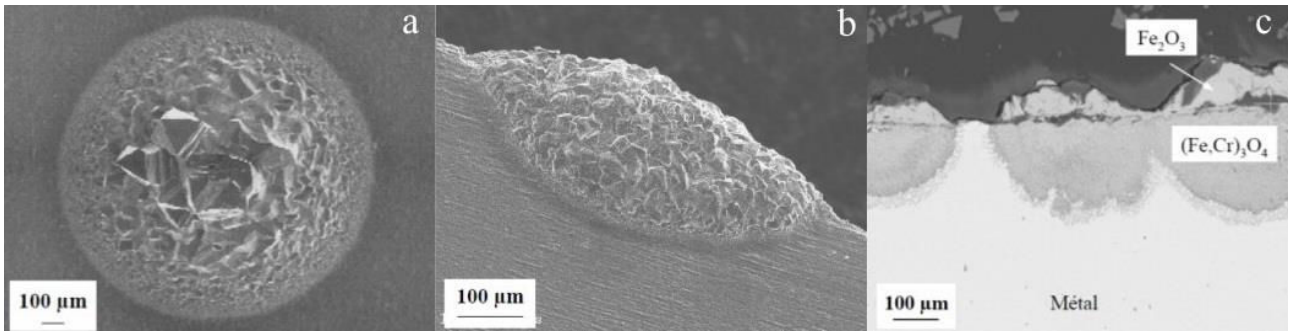

Figure 5.1 Nodule developed during catastrophic oxidation: a). top view b). side view and c). cross section of the nodule.

Galerie et al. [1] studied breakaway oxidation of Fe-18Cr ferritic stainless steel and found that the failure of protective chromia scale led to the formation of Fe-rich nodules as shown in Figure 5.1. The diameter of the nodule was around 900 µm. Figure 5.1c shows the cross sectional view of the nodule. It can be seen that the nodule can be divided into 2 parts that were the upper part located above oxide scale and the lower part located in the substrate. The upper part was composed of Fe_2O_3 while the lower part consisted of $(Fe,Cr)_3O_4$ spinel.

5.1 Kinetic studies

5.1.1 Short time study

Thickness measurements were performed of FIB cross sectional views of oxide scales grown on AISI 441 at 800°C in wet atmosphere (5% H_2O in O_2) for 4 h, 14 h and 24 h presented in Figure 4.6 (chapter 4). For each cross section, at least 20 measurements of thickness were performed using Fiji ImageJ software. Data plotted on "probability" axes are displayed in Figure 5.2. Probability plots, provides valuable information on the superposition of multiple oxidation mechanisms. Data fitting a Gaussian distribution appear as a straight line which slope is related to the standard deviation of the data set. Any deviation from a straight line is interpreted as the appearance of a second distribution in the measurement. Duplex distributions

of probabilities are clearly observed in Figure 5.2. These distributions are related to the simultaneous growth of the $(Mn,Cr)_3O_4$ spinel top layer and a Cr_2O_3-rich inner layer.

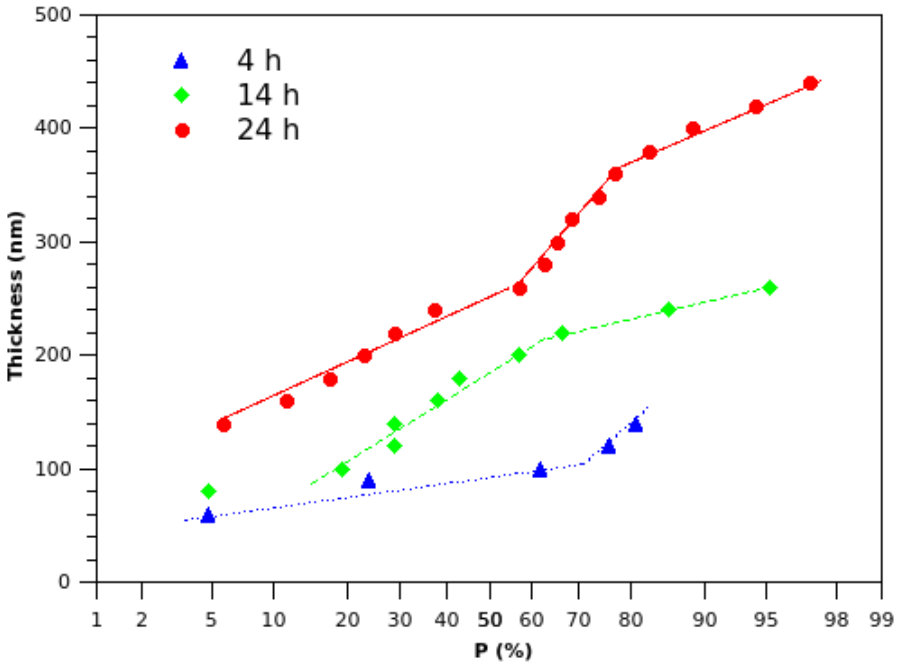

Figure 5.2 Probability plots of thickness measurements of oxide scales grown on AISI 441 at 800°C in wet atmosphere (5% H_2O in O_2, 2 cm/s) for 4 h (triangle), 14 h (diamond) and 24 h (circle).

Mean values of the thickness as well as the standard deviations of the measurements are reported in Table 5.1. Evolution of oxide scale thickness according oxidation time during high temperature oxidation of AISI 441 in wet atmosphere (5% H_2O in O_2, 2 cm/s) is reported in Figure 5.3.

Table 5.1 Mean values and standard deviations of oxide scale thickness according oxidation time for AISI 441 at 800°C in wet atmosphere (5% H_2O in O_2, 2 cm/s).

Oxidation time (h)	Oxide scale thickness (nm)	Standard deviation (nm)
4	100	31
14	178	64
24	274	89

Double logarithmic plot allows studying the oxidation behaviour. As long as protective oxide growth takes place, it can be described mathematically by Eq. 5.1.

$$e^n = k' t \qquad \text{(Eq. 5.1)}$$

where e = thickness
k' = oxidation rate constant
t = oxidation time

Experimental data were fitted to the particular case of the parabolic growth law described mathematically by Eq. 5.2.

$$e^2 = kt \qquad \text{(Eq. 5.2)}$$

where e = scale thickness
k = parabolic rate constant
t = oxidation time

The value of the obtained parabolic constant is 2750 ± 250 $nm^2.h^{-1}$. Fitted data are presented in Figure 5.3.

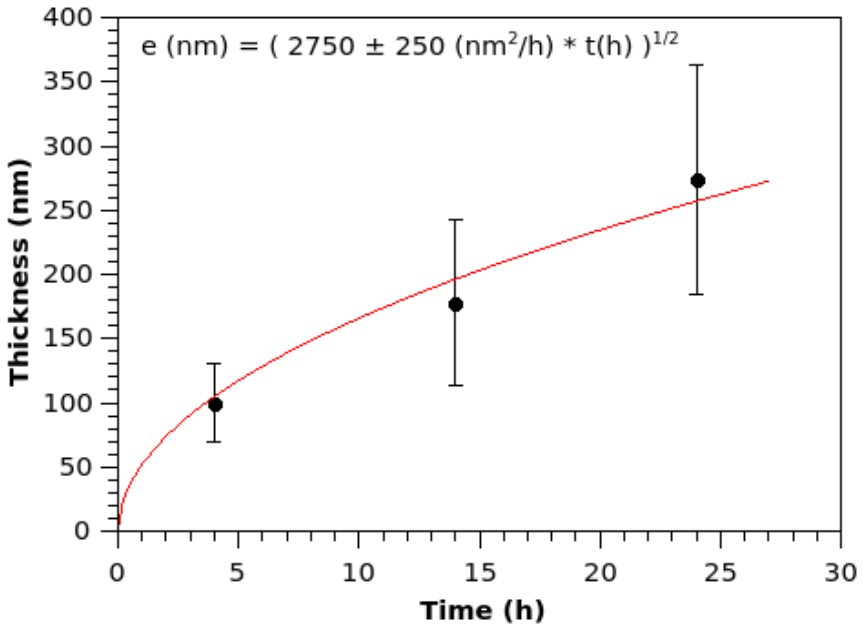

Figure 5.3 Evolution of oxide scale thickness according oxidation time of AISI 441 at 800°C in wet atmosphere (5% H_2O in O_2, 2 cm/s).

Since these experimental durations are probably too short to be in breakaway oxidation stage, the investigation of oxidation stage with longer experimental durations was still needed to confirm.

5.1.2 Long time study

Long time oxidations were performed on experimental setup shown in Figure 5.4. The general principle was similar to the experimental setup shown in Figure 3.20. The horizontal furnace was used instead of the vertical furnace in Figure 3.20 for less complexity. At the outlet of the column, 2 Erlenmeyer flasks were installed in order to condense remaining water in the gas stream and capture Cr volatile species before venting to the atmosphere.

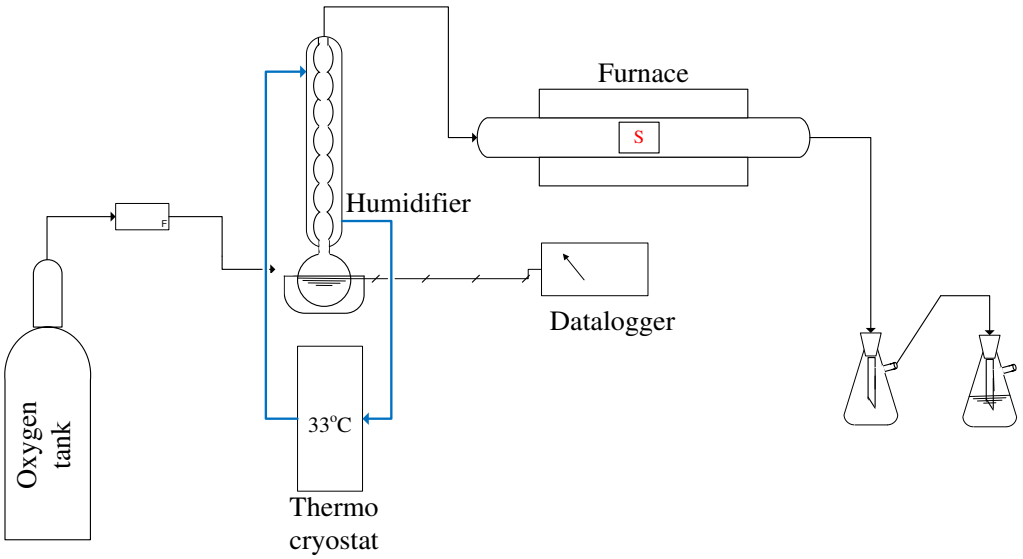

Figure 5.4 High temperature oxidation experimental setup: horizontal furnace.

This setup, Figure 5.4, was used for determining the weight change of the specimen after the oxidation duration up to 865 h. The weight change of the specimens for each oxidation time can imply the global oxidation kinetics. In this experiment, the specimens were oxidised in 2 cm/s of 5% H_2O in O_2 at 800°C.

After high temperature oxidation, the weight change of specimens was measured. Figure 5.5 shows the kinetics curve of Bare 441 during high temperature oxidation in 2 cm/s of 5%H_2O in O_2 at 800°C. The weight gain was plotted as a function of exposure time. The parabolic curve from this graph represents the protective stage of oxidation without the sign of any breakaway oxidation. Thus, it could be summarized that the nodule developed on the as-received 441 surface was not the nodules leading to breakaway oxidation.

Double logarithmic plot allows studying the oxidation behaviour. As long as protective oxide growth takes place, it can be described mathematically by Eq. 5.3.

$$m^n = k\,t \qquad \text{(Eq. 5.3)}$$

where m = weight gain per surface unit
k = oxidation rate constant
t = oxidation time

The best fit is for n = 3.5 ± 0.1 and k = $(2.7 \pm 0.5) \times 10^{-9}$ $(g \cdot cm^{-2} \cdot s^{-1})^{3.5}$. The growth rate is protective although it is not parabolic.

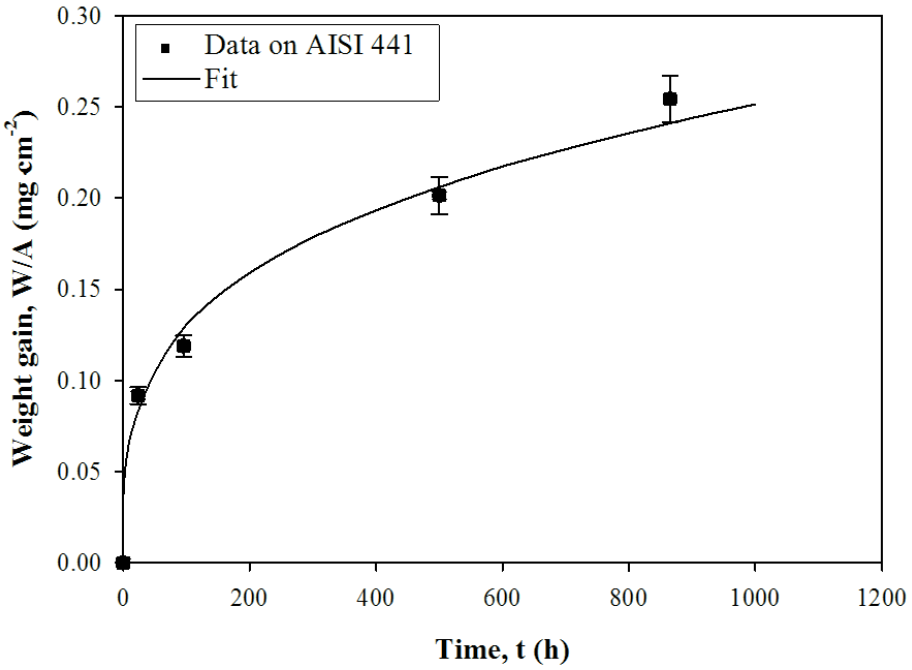

Figure 5.5 Kinetics curve of AISI 441 (2 cm/s, 5%H_2O in O_2, 800°C).

As mentioned above, the sign of breakaway oxidation was not appeared. However, nodules can be observed on as-received 441 after high temperature oxidation in 5%H_2O in O_2 for 96 h. In Figure 4.16, it can be seen the diameter of the nodule was around 5 µm which was much less than the one developed during breakaway oxidation. In this chapter, the nodule development before breakaway oxidation was studied.

Figures 5.6a and b show the SEM images of as-received 441 after high temperature oxidation in 5%H_2O in O_2 at 800°C for 24 and 96 h respectively. On both surfaces, the nodules and the metallic grain boundaries can be observed. However, when the oxide layer was thicker, the less clear view of the metallic grain boundaries was observed. Therefore, in order to have a better vision to study the development of nodules on the as-received 441 specimen during high temperature oxidation, experimental duration shorter than the last chapter, 24 h, was performed.

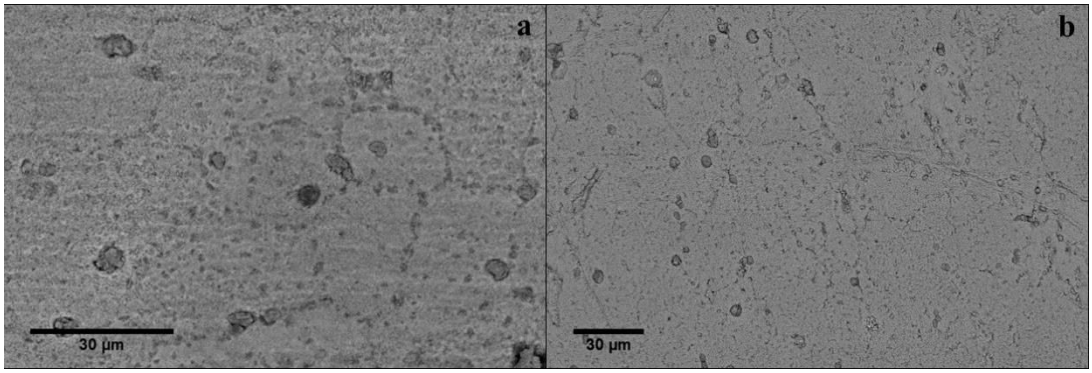

Figure 5.6 SEM images of as-received AISI 441 after high temperature oxidation for a). 24 h and b). 96 h (2 cm/s, 5%H_2O in O_2, 800°C).

5.2 Experiments

5.2.1 Sample preparation

Before high temperature oxidation, the precise size of as-received 441 was measured. Then, this specimen was cleaned by EtOH in an ultrasonic bath for 5 min. After that, it was weighed and, then, the high temperature oxidation experiment could be launched.

5.2.2 Experimental setup and conditions

The experiment setup used in this part is shown in Figure 5.4. The high temperature oxidation experiment was also performed in simulated cathodic condition of SOFCs. The specimen was oxidised in 5%H_2O in O_2. Linear velocity of gas in the furnace was maintained at 2 cm/s. The operating temperature was 800°C and the oxidation duration was 24 h.

5.2.3 Characterisations and additional programs

5.2.3.1 Surface and cross section observations

After high temperature oxidation in 2 cm/s of 5%H_2O in O_2 at 800°C for 24 h, surface observation was achieved by SEM. Raman spectroscopy was used to analyse the composition of the nodules and the matrix surface. Furthermore, cross sectional views of nodules were observed by FIB-SEM that was composed of FIB column and SEM. The nodules were cut, technically called milled, by Ga^+ beam in FIB column, then, the images were taken by SEM. However, the specimen surface could be destroyed during the milling process. Thus, before milling, the surface area needed to be protected by C-deposition.

5.2.3.2 Thin lamella preparation and analysis

Due to the large volume analysis of EDX in semi-infinite samples, the result of the specific area was inexact. Therefore, it was necessary to reduce the volume analysis in order to avoid the discrepant results. Thin lamellas with a thickness of 100-150 nm were prepared for analysing more precisely composition of the nodules.

Figure 5.7 shows the thin lamella preparation procedure. First, as shown in Figure 5.7a, C must be deposited on the surface in order to protect the surface from the milling step. After that, the FIB-boxes were made at both sides of the lamella: Figure 5.7b. The right side, beneath and the left side of the lamella were cut (the red dash lines refer to the cutting lines) while the small connection bridge at the left side was still remained in order to maintain the lamella as shown in Figures 5.7c and d. After that, the lamella was connected with a pin by C-deposition, then, the small bridge can be cut. The lamella was moved to the Cu grid. The lamella and Cu grid were connected together and, then, the pin was disconnected. Finally, the lamella was slenderised to 100-150 nm thick and analysed by EDX.

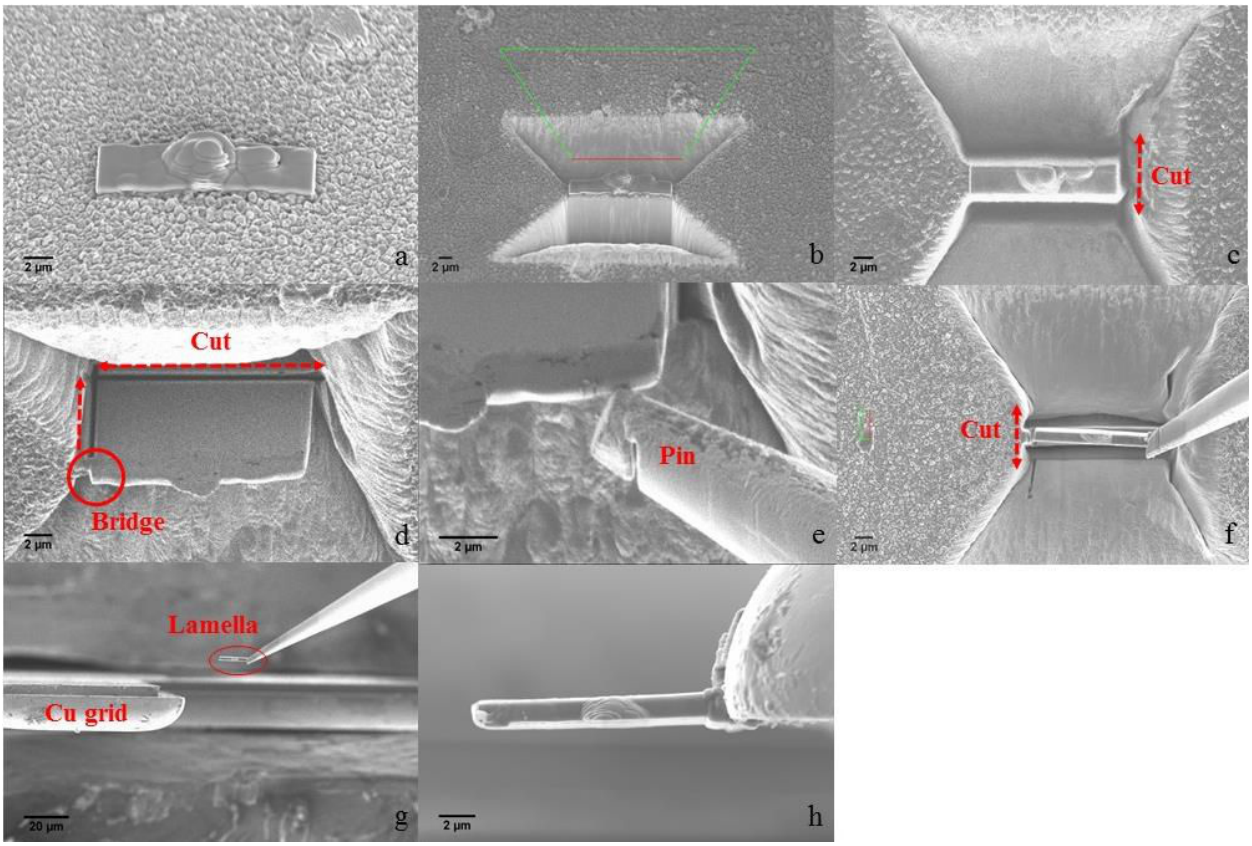

Figure 5.7 Thin lamella preparation: a)-h) represent the preparing steps 1-8 respectively.

5.2.3.3 3D reconstruction of the nodule and quantitative analysis

In order to reconstruct the 3D view of the nodule, FIB-SEM was an important tool in this part. First, the surface of the interesting areas, nodule and oxide, were protected by C-deposition. The FIB-box was made at one side of the deposited area as shown in Figure 5.8. After that, the nodule was eroded every 20 nm. The images of each slice were taken by SEM. Until the end of nodule, 300-400 images were obtained. All images were combined by Fiji ImageJ program and the evolution of the nodule could be determined. After that, the threshold of the stack images was adjusted to be consistent with Nb, Si and oxide phases. Finally, 3D reconstruction of the nodule and the quantitative analysis of Nb were obtained.

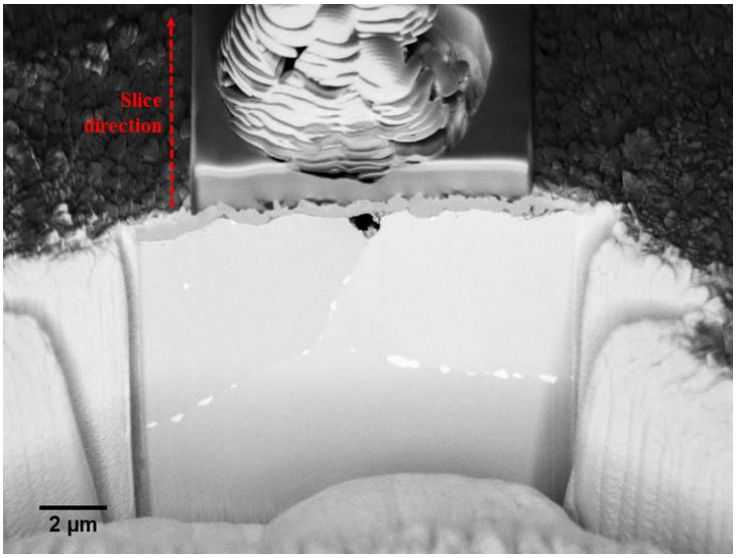

Figure 5.8 FIB-box.

5.3 Surface observations

5.3.1 SEM

Figure 5.9 shows surface observation of as-received 441 after high temperature oxidation taken by SEM in black scattering electron (BSE) mode. The hexagon metallic grain boundaries could be observed with a diameter around 15 µm. The nodules were observed at the position of metallic grain boundaries (GB-nodule) as well as in the grain (in-grain, IG-nodule). The nodules were black in BSE mode which means they were composed of light element(s), possibly Ti. Therefore, it could be concluded that these nodules, developed during high temperature oxidation before catastrophic oxidation, were not nodules leading to breakaway oxidation. On the contrary, these were a new type of nodule that has not been reported before.

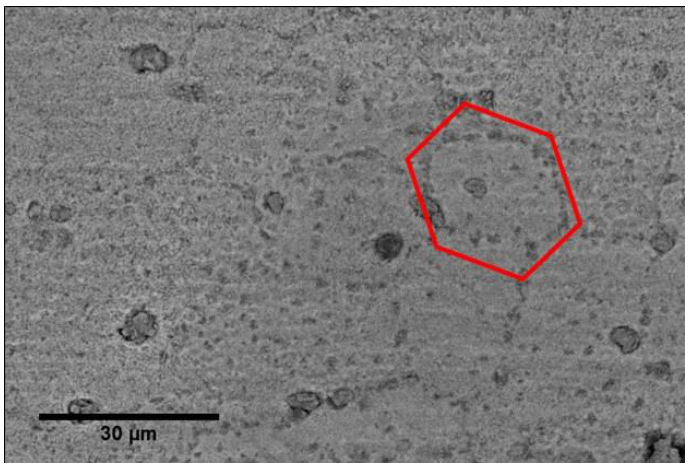

Figure 5.9 Surface observation of as-received 441 after high temperature oxidation (2 cm/s, 5%H_2O in O_2, 800°C, 24 h).

5.3.2 Raman spectroscopy

Raman spectroscopy was used to analyse the phases at the matrix and nodule positions. The analysis penetration depth was around 1 µm. The results are shown in Figure 5.10. At the matrix positions, it is clear that Cr_2O_3 (peak at ~ 560 cm^{-1}) [4]–[10] and spinel (peak at ~ 680 cm^{-1}) was formed but it was difficult to indicate the phase of spinel without the subpeaks. The possible phase could be Mn-Cr spinel [6], [7], [9], [11], [12] or Fe-Cr spinel [6], [7], [9], [10], [13]–[15] . At the position of the nodules, spinel and TiO_2 [9] were observed, so this confirmed the hypothesis in Section 5.3.1 indicating that the nodule was mainly Ti.

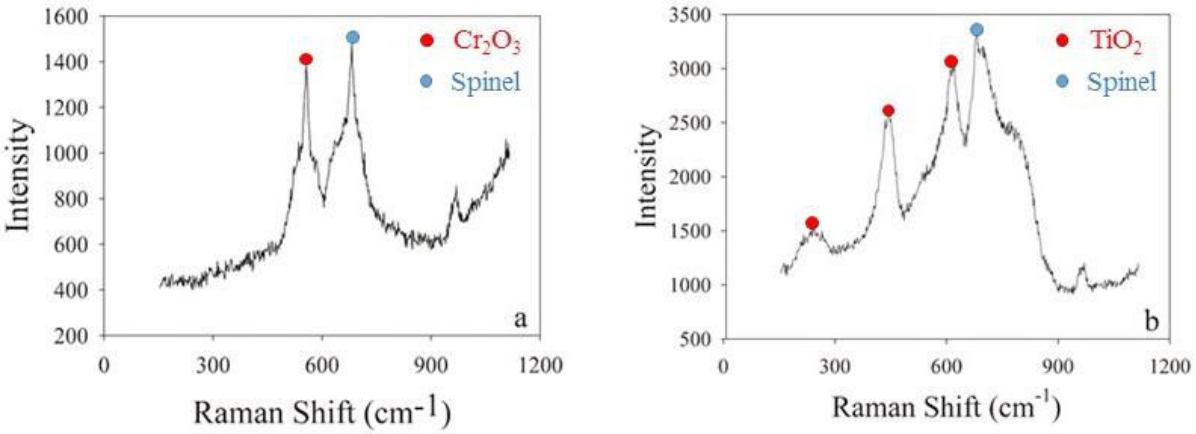

Figure 5.10 Raman spectra obtained on the oxidised surface after 24 h oxidation (2 cm/s, 5%H_2O in O_2, 800°C, 24 h). a) laser focused on the matrix, b) laser focused on the nodules.

As mentioned above, there were 2 types of nodules: GB-nodule and IG-nodule. Therefore, the following results and discussion would be separated into 2 parts corresponding to both types of nodule.

5.4 Cross sectional observation

Figure 5.11 shows SEM images in BSE mode of the cross sectional observation of both nodules, GB-nodule and IG-nodule. In this figure, C-deposition can be seen above the nodule and the oxide layer. Due to the dissimilarity of the orientation of each metallic grain, the levels of grey of each grain were different. In the substrate, white precipitates can be observed. These precipitates were mainly located along the metallic grain boundaries while some precipitates were also located in the grain. These precipitates were brighter than the substrate in SEM-BSE mode. Thus, the precipitates were mainly composed of a heavy metal that should be Nb.

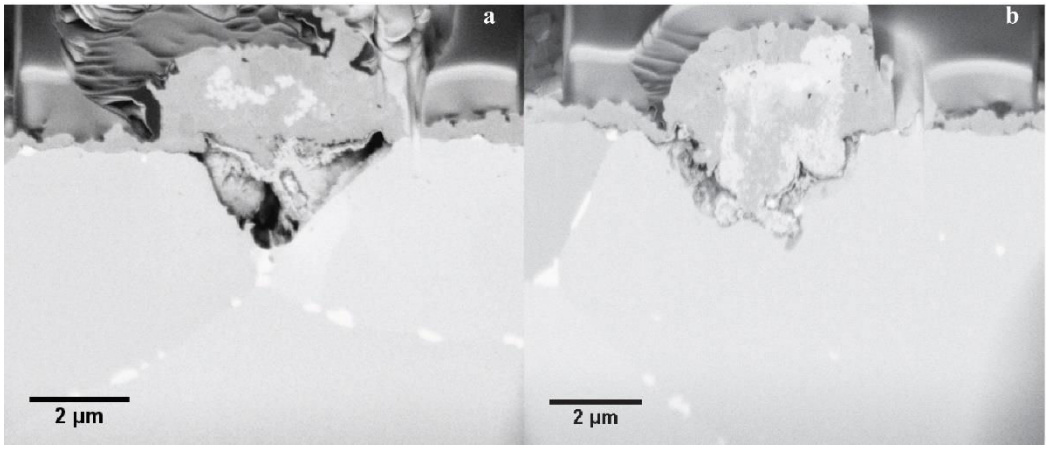

Figure 5.11 SEM images in BSE mode of cross sectional observation of the nodules a). located at the metallic grain boundaries b). located in the grains.

Both nodules shown in Figures 5.11a and b, can be divided into 2 parts that were the upper part located above the substrate and the lower part occupied in the substrate. Many levels of grey can be observed in the nodule that means there were many phases in the nodule. The white phase in the nodule seems to be the same level of grey with the precipitates located along the metallic grain boundaries in the substrate, so it should be Nb compound(s). The phase darker than the substrate in SEM-BSE mode represents the light elements. Therefore, this probably confirmed the results of Raman spectroscopy that the nodules consisted of TiO_2.

5.5 Thin lamella analysis

In this section, 2 cartographies obtained from EDX would be presented as shown in Figures 5.13 and 5.16. Each figure contains the first biggest image and other small ones. The small images represent the map of each element; Fe, Cr, Mn, Ti, O, C, Si and Nb. The biggest images show the combination of many elements. Some elements, i.e. O in Figure 5.13, which was everywhere were neglected in order to avoid the confusion and colour-mixed that can lead to the misunderstanding.

Figure 5.12 shows the cursory drawing of both nodules. It was sketched from cartographies of the nodules shown in Figures 5.13 and 5.16. In the nodules, there are 2 layers; Layers 1 and 2 in Figure 5.12. Layers 1 and 2 were located at the upper and lower parts of the nodule respectively. For Layer 3, it is located at the lower edge of the nodule. Thus, for a clear explanation, the layer in the upper part, lower part and lower edge of the nodule are defined as Layers 1, 2 and 3 respectively.

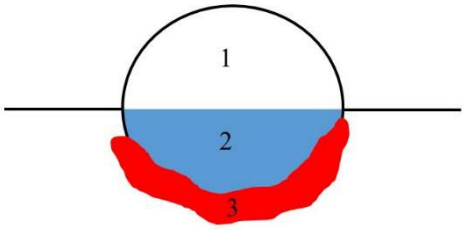

Figure 5.12 Schematics of a nodule.

5.5.1 GB-nodule

Figure 5.13 shows the cartography obtained from thin lamella of the GB-nodule. Beneath C deposited layer, thin layer of Cr and/or Mn in Layer 1 that should be Cr_2O_3 and Mn-Cr spinel was observed in the middle of the nodule. This layer connected with the passive scale outside the nodule. In Layer 2, the appearance of this layer is like v-shape. Cr, Mn and O were observed in Layer 2 while Ti was a main component in Layer 1. Pores can be observed inside TiO_2. Nb, Si, C and O were also scattered in the nodule while Fe was not detected. Thus, it can be confirmed that the nodule developed during initial stage of high temperature oxidation was not a nodule leading to catastrophic oxidation (Fe-rich nodule). At the lower edge of the nodule (Layer 3), dense Nb and Ti were detected. Si layer were clearly seen at this position. In the substrate, precipitates located along the metallic grain boundaries were observed. The precipitates consisted of Nb and Si. EDX of the precipitates shown in Figure 5.14 presents that the precipitates were composed of Fe, Nb and Si. These were possible to be Fe_2Nb with Si contamination. This is in good agreement with the studies of Yang [16] and Yan [17], [18] indicating that Fe_2Nb could capture Si preventing the growth of SiO_2 continuous layer. This results in lowering electrical resistance of the materials [19].

Comparing with the results obtained by Raman spectroscopy, they are in good agreement. With a penetration depth around 1 μm of Raman spectroscopy, only Layer 1 comprising TiO_2 and spinel located in the middle of the nodule could be observed. On the contrary, Layer 2 could not be detected. The schematic of Raman analysis is shown in Figure 5.15. Considering the thin spinel layer in Layer 1, it was composed of Cr, Mn and O. Thus, spinel detected by Raman spectroscopy should be Mn-Cr spinel.

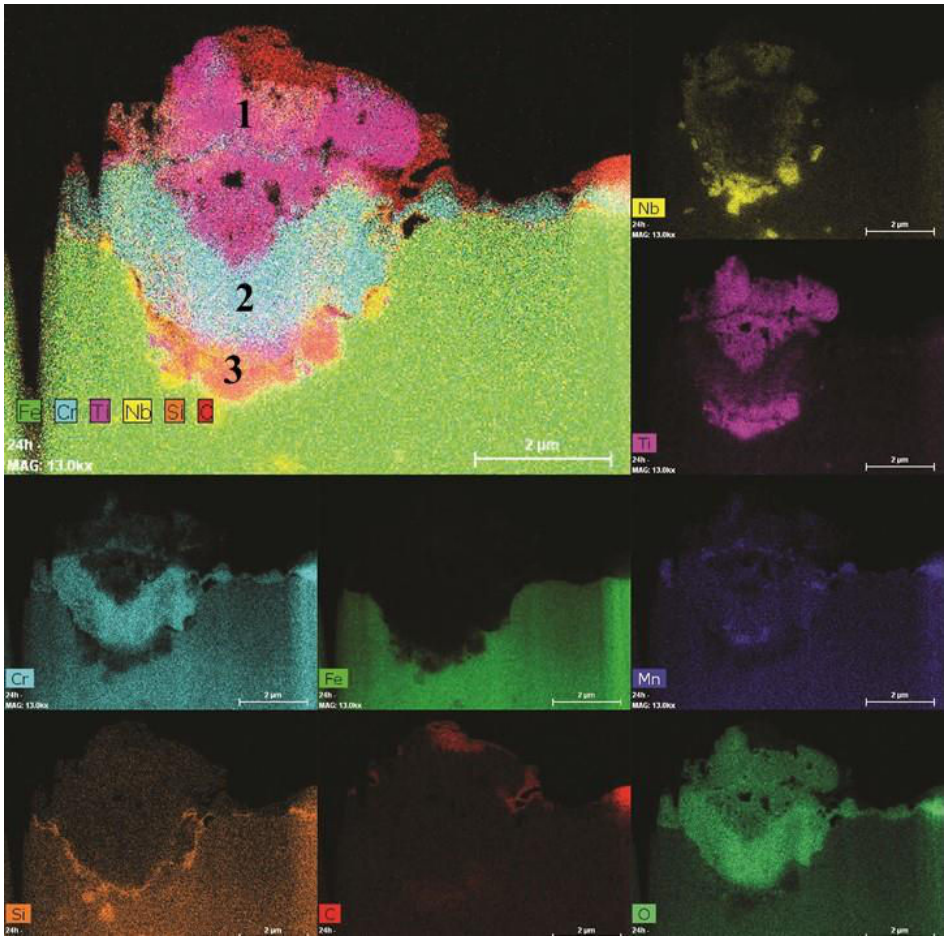

Figure 5.13 Cartography of GB-nodule (2 cm/s, 5%H_2O in O_2, 800 °C, 24 h).

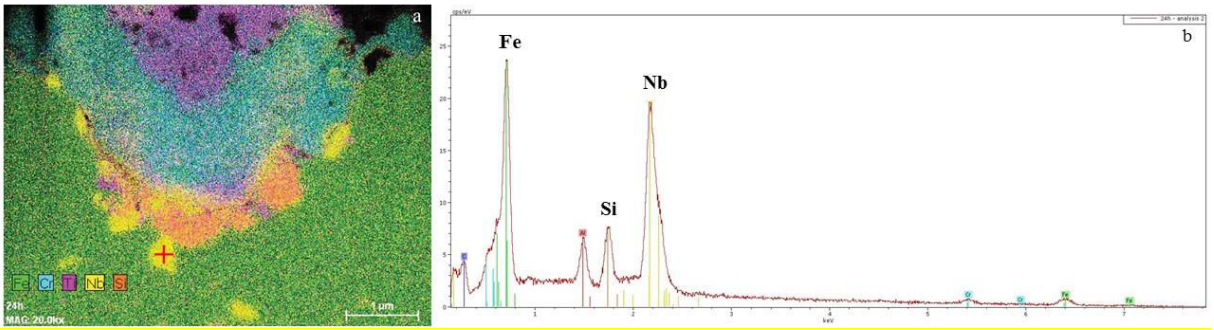

Figure 5.14 a) cartography of GB-nodule and b) EDX of precipitate located long the metallic grain boundaries. The green, blue violet, yellow and orange refer to Fe, Cr, Ti, Nb and Si respectively.

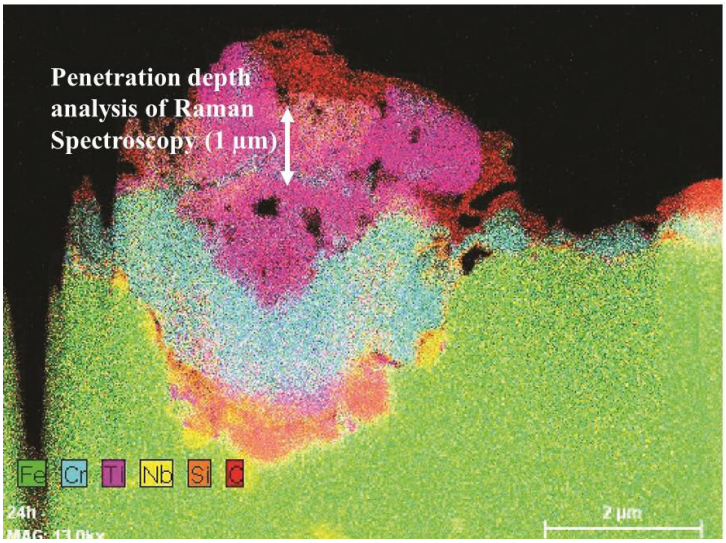

Figure 5.15 Schematic of Raman spectroscopy analysis focusing on the nodule.

5.5.2 IG-nodule

The cartography of the IG-nodule is shown in Figure 5.16. Generally, it was similar to the nodule located at the metallic grain boundaries especially for the configuration point of view. In Layer 2, Cr and Mn were occupied while Ti was the main element in Layer 1. Pores in TiO_2 were also observed in this nodule. In Layer 3, Nb, C and Si were also observed. Si was detected intensely where Nb was found. Nevertheless, there were some differences between both nodules. The appearance of Layer 2 of IG-nodule was flat while that of GB-nodule was v-shape. For the IG-nodule, TiO_2 in Layer 1 was surrounded by Mn and Cr. Moreover, Ti was also observed in Layer 3 of the IG-nodule but it was not intensely detected like the GB-nodule. Little amount of Fe was found in the IG-nodule while it was absent in the GB-nodule.

In summary, the configurations of both nodules were similar. Thin layer of chromia and Mn-Cr spinel was observed in the middle of the nodule and connected to the passive scale outside the nodules. Nb seemed to accompany Ti at the same locations while Si was captured by Nb precipitates especially along the metallic grain boundaries. The upper part of the nodule (Layer 1) mainly consisted of TiO_2 while the lower part (Layer 2) was occupied by the oxide layer of Cr_2O_3 and Mn-Cr spinel. Separation of external and internal TiO_2 can be observed as a result of outward diffusion of Ti^{4+} and inward diffusion of O^{2-} respectively. The divergence of ionic fluxes driven by chemical potential gradient led to void formation in the oxide layer [20], [21]. Additionally, little amount of Fe can be detected in the IG-nodule while it was absent in GB-nodule. Normally, during high temperature oxidation, Fe, Cr, Mn and also Ti and Nb upwardly diffused. Diffusivities of these elements were greater via metallic grain boundaries where the activation energy was lower than that in the bulk [22]. However, Nb was mainly precipitated along the metallic grain boundaries in terms of Laves phase (Fe_2Nb) leading to the decrease of diffusivities of the elements such as Fe to the top surface [23]. Therefore, the amount of Fe in the GB-nodule was less than that of the IG-nodule.

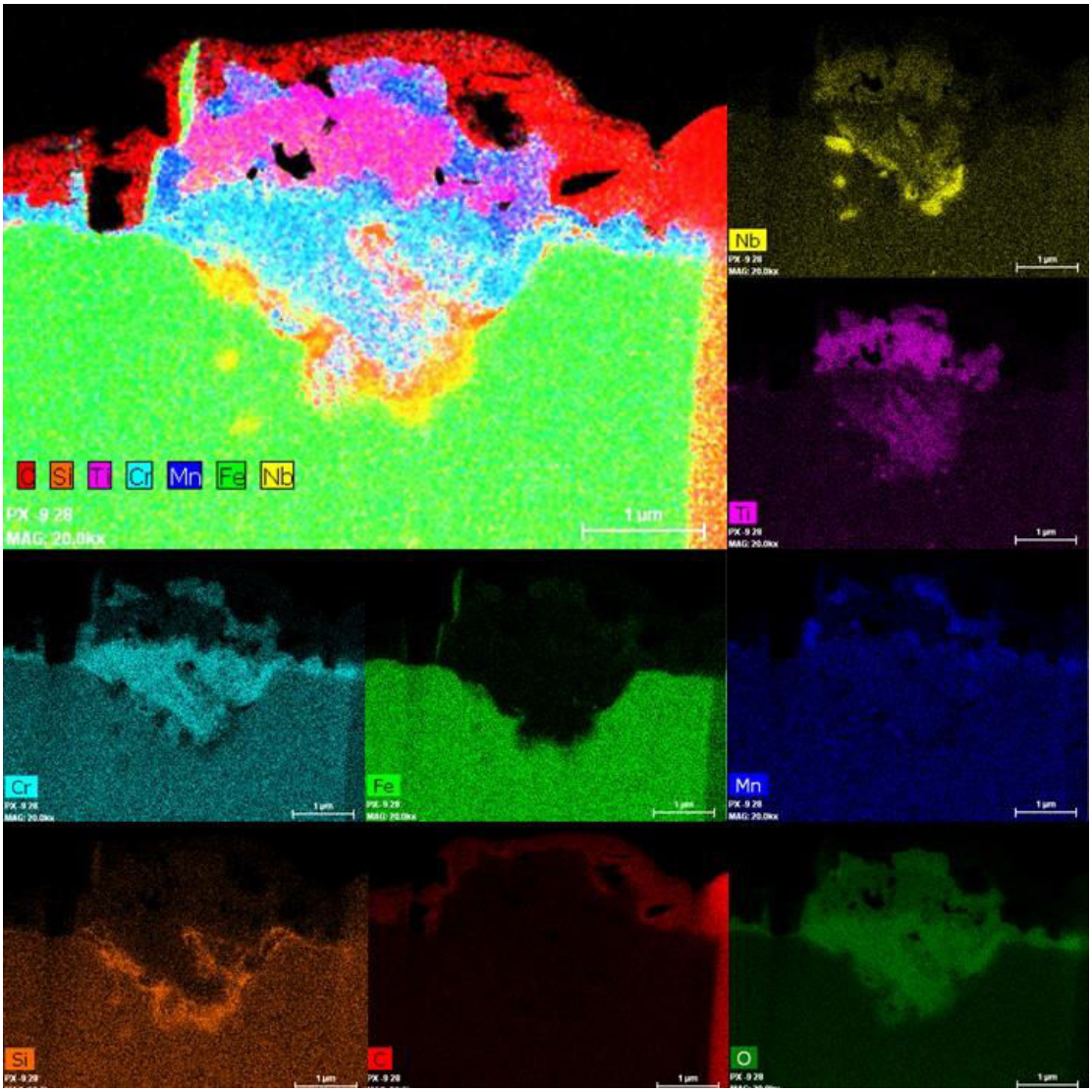

Figure 5.16 Cartography of the IG-nodule (2 cm/s, 5%H_2O in O_2, 800°C, 24 h).

5.6 3D reconstruction of the nodules

After eroding the nodules and taking the images of each slice, the stack of images was built by combining all images using Fiji ImageJ. After that, binarisation (black and white images) was performed by adjusting threshold for focusing on the observed elements. The examples of the images after binarisation are shown in Figures 5.17-5.19. The lower and upper threshold values were set to be consistent with Nb phases, silicon and voids, and oxide phases. The threshold values are shown in Table 5.2.

Figure 5.17 Binarisation of oxide phases (white phase) observed from the IG-nodule.

Figure 5.18 Binarisation of Si and voids (white phase) observed from the IG-nodule.

Figure 5.19 Binarisation of Nb phases (white phase) observed from the IG-nodule.

Table 5.2 Lower and upper threshold values of Nb phases, Si + voids and oxide phases.

Phases	Lower threshold value	Upper threshold value
Nb phases	0	242
Si + voids	0	218
Oxide phases	184	215

Figures 5.20a and b show 3D reconstruction of the GB-nodule and IG-nodule respectively. Red, blue and yellow represent oxide phases, Si and Nb respectively. Nb phases consisted of Nb intermetallic (Fe_2Nb), NbC and/or (Ti,Nb)(C,N). White phase in Figure 5.20a represents a big porosity in the nodule. This was clearly seen that both nodules were surrounded by continuous oxide layer. Si was observed at metal/oxide interface. Inside the nodule, it is difficult to attribute and classify all phases. However, according to the EDX results, it can be

explained that both nodules were Ti-Nb nodules mainly containing Ti, Nb, Cr and Mn. The most interesting thing in these 3D images was the configuration of Nb (yellow phase). Nb was formed along the metallic grain boundaries as well as in the grain. The appearances of Nb precipitates can be classified into 2 shapes that are the rod-shape and round shape depending on the phases. Fe_2Nb was a rod-shape while NbC and/or (Ti,Nb)(C,N) were spherical [17]. Obviously, Fe_2Nb was only precipitated along the metallic grain boundaries [23] while others were precipitated everywhere. This can be described by the equilibrium diagram [18] shown in Figure 5.21. Fe_2Nb formed during cooling at temperature lower than 800 °C, so nucleation phenomena are slow and need special catalytic sites, i.e. grain boundaries [17], [18]. On the contrary, Nb(C,N) and TiN precipitate at much higher temperature and can appear within grains. These are in good agreement with the research of Yan [18] describing that Laves phase of Nb (Fe_2Nb) was mainly precipitated along the metallic grain boundaries while niobium carbide (NbC) and /or titanium-niobium carbonitride, (Ti,Nb)(C,N), were precipitated anywhere.

The configurations of Nb inside the nodules are shown in Figure 5.22. For the GB-nodule, Nb was densely around the nodule like a cup-shape while it was disappeared in the middle of the nodule. In the case of IG-nodule, Nb was randomly distributed.

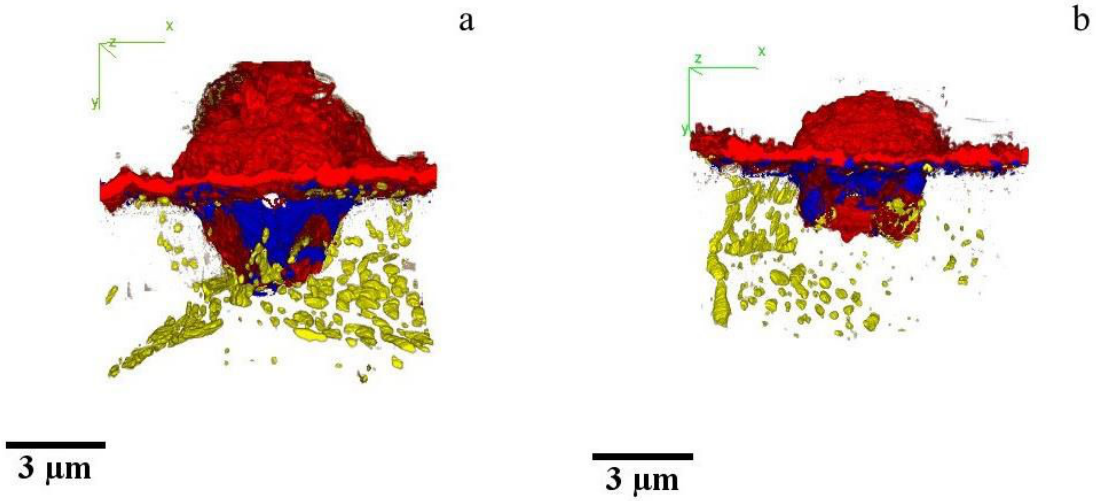

Figure 5.20 3D reconstruction of a) GB-nodule b) IG-nodule.

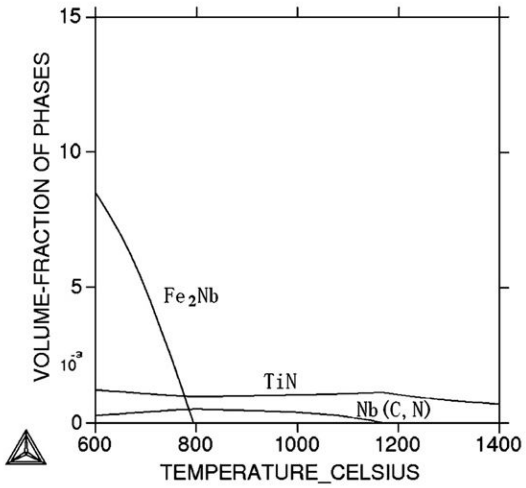

Figure 5.21 Equilibrium precipitation diagram of Nb [18].

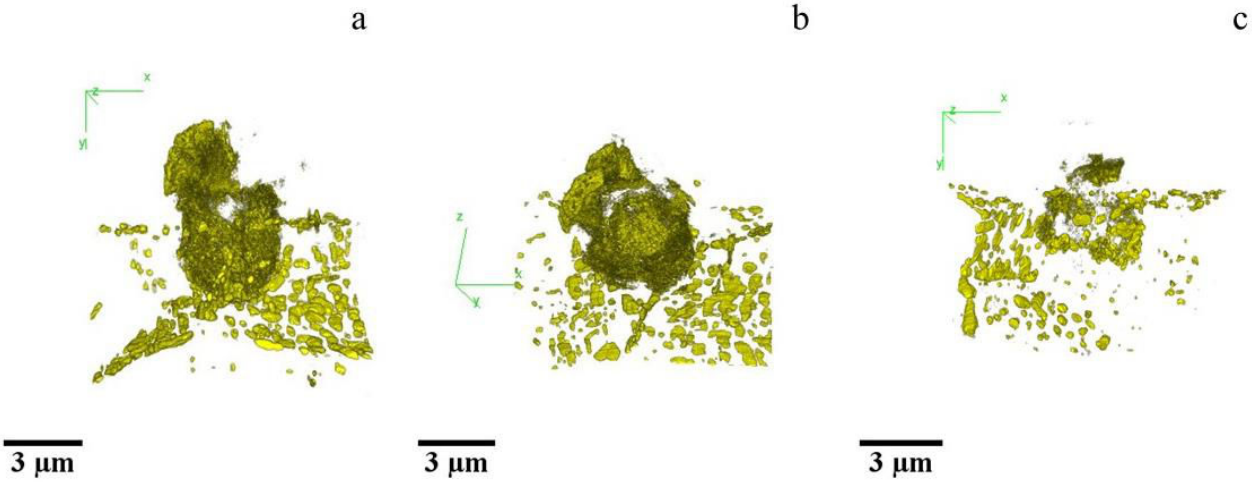

Figure 5.22 3D reconstruction of Nb of a), b) GB-nodule and c) IG-nodule.

5.7 Quantitative analysis of Nb

The quantitative analysis of Nb was achieved by adjusting threshold of the images as mentioned above. After binarisation of the stack images, the area fraction of white precipitates was calculated by Fiji ImageJ. Area fraction of each image was plotted against the penetration depth as shown in Figure 5.23. Blue and red lines represent the percentages of Nb area in the substrates and inside the nodules respectively while the black ones represent the total area fraction of Nb in the images (blue + red). Comparing both nodules, it can be seen that the total amount of Nb presented in Figure 5.23a (GB-nodule) was higher than that of Figure 5.23b (IG-nodule) for around 3 times. This ensured that the diffusivity of Nb along the metallic grain boundaries was higher than its diffusivity in the bulk (in the grain). The shapes of curves were bell-shapes. The variation of Nb percentage depended on the volume of the nodule while the amount of Nb in the substrate seemed to be constant. The maximum percentages of Nb in both nodules were around 5 times higher than that in the substrates. In the GB-nodule, 2 sub-bell-

curves were presented as a result of the cup-shape distribution of Nb as shown in Figure 5.22. For IG-nodule, the sub-curve could not be observed because of the random distribution of Nb in the nodule. Thus, comparing Nb distribution in both nodules, it could be concluded that the distribution of Nb in GB-nodule was not homogeneous while Nb in IG-nodule was more uniformly distributed.

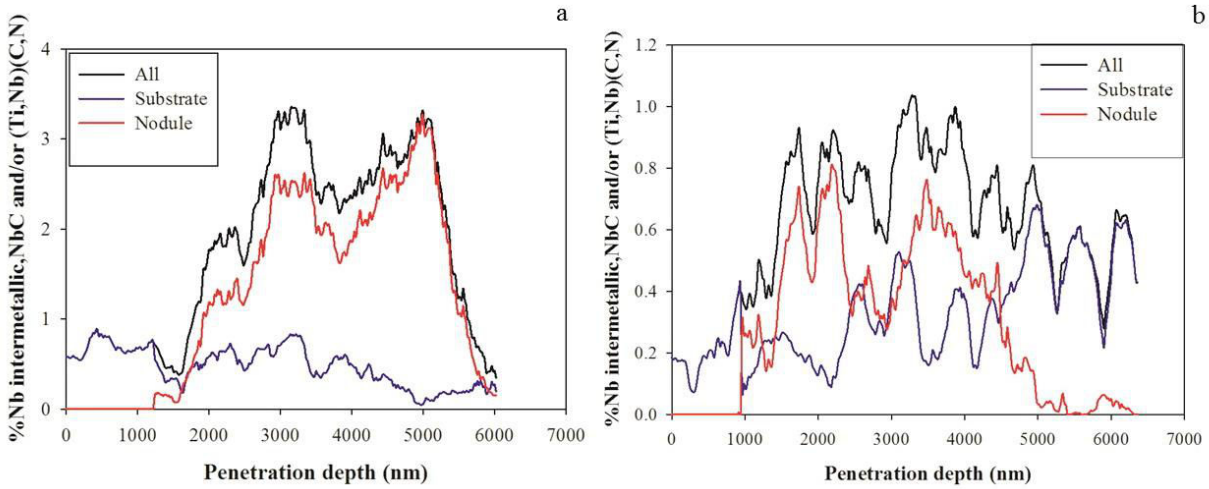

Figure 5.23 Quantitative analysis of Nb intermetallic (Fe_2Nb), NbC and/or (Ti,Nb)(C,N) of a) GB-nodule b) IG-Nodule.

5.8 Conclusions

During high temperature oxidation of as-received 441 for short time, Ti-Nb nodules were developed. The appearance of the nodules were similar to the nodules developed during catastrophic oxidation reported by Henry et al. However, the kinetics study confirmed that this experiment was performed before catastrophic oxidation. It is possible that the formation of the pre-breakaway nodules might be the result of Nb and Ti being as isolated domains in the metals (on the contrary, Mn is dissolved in the steel and forms a quasi-continuous layer of spinel oxide). With their high oxidation state, low ionic radius and high positive charge, they are possible to diffuse through chromia scale and form as nodules on the surface.

These nodules were exposed above the metallic grain boundaries as well as in the grains. The nodules can be divided into 2 parts that are the upper part located above the substrate and the lower part occupied in the substrate. The volumes of upper and lower parts were approximately equivalent. The configurations of both nodules were similar. According to EDX and Raman spectroscopy results, TiO_2 was plenty in the upper parts of the nodules while the lower parts of the nodules were occupied by Cr_2O_3 and Mn-Cr spinel. The separation of external and internal TiO_2 was obviously seen as a result of outward diffusion of Ti^{4+} and inward diffusion of O^{2-}. Nb seemed to accompany Ti at the same locations while Si was captured by Nb precipitates especially at the metallic grain boundaries.

The amount of Fe in GB-nodule was less than that in IG-nodule because Fe_2Nb formed along the metallic grain boundaries obstructed outward diffusion of Fe, while, beneath the IG-

nodule, there was no obstacle preventing diffusion of Fe leading to higher Fe in the nodule. However, the amount of Fe found in the nodule was very little (Fe could not be visible in GB-nodule), so the nodules formed on this specimen during high temperature oxidation for short time was not a nodule developed at breakaway oxidation.

3D reconstructions of the nodules ensured that the rod-shapes Fe_2Nb were located at the metallic grain boundaries while the round ones representing NbC and/or (Ti,Nb)(C,N) were exposed everywhere in the substrate. In the GB-nodule, Nb distributed like a cup-shape while it was randomly scattered in IG-nodule. Comparing Nb quantitative analysis of both nodules, the amount of total Nb (nodule + substrate) of GB-nodule was higher than that of IG-nodule for about 3 times that means Nb diffusivity along the metallic grain boundaries was higher than in the bulk. In the substrate, Nb amount seemed constant along the penetration depth while Nb in the nodules was dependent on the volume of the nodules. The maximum Nb amounts of both nodules were about 5 times higher than Nb amount in the substrate.

References

[1] A. Galerie, S. Henry, Y. Wouters, M. Mermoux, J.-P. Petit, and L. Antoni, "Mechanisms of chromia scale failure during the course of 15-18Cr ferritic stainless steel oxidation in water vapour," Mater. High Temp., vol. 21, no. 4, pp. 105–112, 2005.

[2] S. Henry, "Influence de la vapeur d'eau sur l'oxydation a haute temparature du chrome et de quelques aciers inoxydables ferritiques stabilises," Institute National Polytechnique de Grenoble, 2000.in french.

[3] I. Antepara, I. Villarreal, L. M. Rodríguez-Martínez, N. Lecanda, U. Castro, and a. Laresgoiti, "Evaluation of ferritic steels for use as interconnects and porous metal supports in IT-SOFCs," J. Power Sources, vol. 151, no. 1–2, pp. 103–107, 2005.

[4] J. Mougin, T. Le Bihan, and G. Lucazeau, "High-pressure study of Cr_2O_3 obtained by high-temperature oxidation by X-ray diffraction and Raman spectroscopy," J. Phys. Chem. Solids, vol. 62, pp. 553–563, 2001.

[5] P. Y. Hou, J. Ager, J. Mougin, and A.Galerie, "Limitations and advantages of Raman spectroscopy for the determination of oxidation stresses," Oxid. Met., vol. 75, pp. 229–245, 2011.

[6] B. D. Hosterman, "Raman spectroscopic study of solid solution spinel oxides," University of Nevada, 2011.

[7] R. L. Farrow, P. L. Mattern, S. N. Laboratories, and S. Diego, "Characterization of surface oxides by raman spectroscopy," Appl. Phys. Lett., vol. 73, pp. 353–358, 1980.

[8] J. Birnie, C. Craggs, D. J. Gardiner, and P. R. Graves, "Ex-situ and in-situ determination of stress distribution in chromium oxide films by Raman spectroscopy," Corros. Sci., vol. 33, no. 1, pp. 1–12, 1992.

[9] J. Mougin, “Tenue mécanique de couches d’oxyde thermiques générées sur le chrome et sur quelques aciers inoxydables ferritiques: Étude des contraintes et de d'adhérence,” Institut National Polytechnique de Grenoble, 2001, in french.

[10] D. Renusch, B. Veal, K. Natesan, and M. Grimsditch, “Transient oxidation in Fe-Cr-Ni alloys : a Raman-scattering study,” Oxid. Met., vol. 46, no. 5–6, pp. 365–381, 1996.

[11] R. J. Anderson, “Oxidation mechanisms of Fe-18Cr-3Mo: a Raman study,” J. Vac. Sci. Technol. A Vac. Surf. Film, vol. 3, no. 3, p. 1296, 1985.

[12] Y. Matsuda, S. Hinotani, and K. Yamanaka, “Characterization of oxide layers on SUS410Ti stainless steel grown in low oxygen pressures by Raman spectroscopy,” Tetsu to Hagane, vol. 82, no. 3, pp. 32–37, 1996.

[13] K. Veena, V. K. Vaidyan, and P. Koshy, “Characterization of ferrochromium thin films,” J. Mater. Sci. Lett., vol. 8, pp. 80–82, 1989.

[14] J. C. Hamilton and R. J. Anderson, “Oxidation of Fe-18Cr-3Mo : an in-situ Raman study,” High Temp. Sci., vol. 19, pp. 307–321, 1985.

[15] D. J. Gardiner, C. J. Littleton, K. M. Thomas, and K. N. Strafford, “Distribution and characterization of high temperature air corrosion products on iron-chromium alloys by Raman microscopy,” Oxid. Met., vol. 27, no. 1–2, pp. 57–72, 1987.

[16] Z. Yang, G.-G. Xia, C.-M. Wang, Z. Nie, J. Templeton, J. W. Stevenson, and P. Singh, “Investigation of iron–chromium–niobium–titanium ferritic stainless steel for solid oxide fuel cell interconnect applications,” J. Power Sources, vol. 183, no. 2, pp. 660–667, Sep. 2008.

[17] H. Yan, H. Bi, X. Li, and Z. Xu, “Microstructure and texture of Nb + Ti stabilized ferritic stainless steel,” Mater. Charact., vol. 59, no. 12, pp. 1741–1746, 2008.

[18] H. Yan, H. Bi, X. Li, and Z. Xu, “Precipitation and mechanical properties of Nb-modified ferritic stainless steel during isothermal aging,” Mater. Charact., vol. 60, no. 3, pp. 204–209, 2009.

[19] H. Ali-Löytty, P. Jussila, T. Juuti, L. P. Karjalainen, a. a. Zakharov, and M. Valden, “Influence of precipitation on initial high-temperature oxidation of Ti-Nb stabilized ferritic stainless steel SOFC interconnect alloy,” Int. J. Hydrogen Energy, vol. 37, pp. 14528–14535, 2012.

[20] K. Akiba, M. Ueda, K. Kawamura, and T. Maruyama, “Quantitative Prediction of Voids Formation in a Growing Cobaltous Oxide Scale at 1373 K,” Mater. Trans., vol. 48, no. 11, pp. 2997–3006, 2007.

[21] K. Akiba, M. Ueda, K. Kawamura, and T. Maruyama, “Quantitative Prediction of Voids Formation in a Growing Nickel Oxide Scale at 1373 K,” Mater. Trans., vol. 48, no. 10, pp. 2753–2761, 2007.

[22] P. Sarrazin, A. Galerie, and J. Fouletier, Mechanisms of high temperature corrosion: A kinetic approch. 2008. Trans Tech Publ., Stafa-Zürich, Switzerland.

[23] T. Horita, H. Kishimoto, K. Yamaji, Y. Xiong, N. Sakai, M. E. Brito, and H. Yokokawa, “Evaluation of Laves-phase forming Fe-Cr alloy for SOFC interconnects in reducing atmosphere,” J. Power Sources, vol. 176, pp. 54–61, 2008.

Chapter 6

Cr volatilisation from AISI 441 coated with Mn-Co spinel by an electroplating method

After determining Cr species volatilisation of Bare 441 as presented in Chapter 4, then, Cr species volatilisation from the specimen had been tried to be suppressed. The protecting procedure commonly used is the coating method. Various coating materials and methods have been applied for an interconnect application. However, no appropriate materials and methods could suppress Cr species volatilisation while maintaining other properties of interconnect particularly electrical conductivity.

As described in Chapter 2, Mn-Co spinel, $(Mn,Cr)_3O_4$, is one of the most attractive coatings used for depositing on the metallic interconnect surface. It could reduce Cr_2O_3 formation and Cr species volatilisation from the alloy surface while maintaining high electrical conductivity and thermal expansion match with other cell parts [1]–[3]. Thus, this research used Mn-Co spinel as a coating material of interconnect in SOFCs. For the coating method, electrodeposition, so-called electroplating method was chosen because it is a simple method, easy to set up in the laboratory, not expensive and safe.

6.1 Cr volatilisation results

Figure 6.1 shows specific Cr released from Bare 441 and Coated 441 after high temperature oxidation for 24 and 96 h according to linear velocity of gas. It can be seen that, at the same exposure condition, Cr species volatilisation from Bare 441 and Coated 441 were similar. However, their phenomena seemed different. For Bare 441, as mentioned in Chapter 4, its phenomenon can be separated into 2 zones; diffusion control at linear velocity lower than 3 cm/s and reaction control at linear velocity of 3 cm/s and above. For Coated 441, only reaction limit could be observed in the linear velocity range of 2-5 cm/s. Furthermore, considering Cr volatilisation rate of both specimens in Figure 6.2, it was clearly seen that, at the same gas linear velocity, Cr volatilisation rates were similar and they were not dependent on oxidation time. Therefore, it can be summarised that this coating, Mn-Co spinel by the electroplating method, was not effective for protecting Cr species volatilisation from the specimen.

These results seem to be controversial with the previous publications presented in Chapter 2 [4]-[14] that Mn-Co spinel was an effective inhibitor of Cr diffusion leading to lowering oxidation and Cr volatilisation rates. Thus, SEM and EDX were used to analyse Coated 441 specimens before and after high temperature oxidation in order to find the reason why our coated specimen could not suppress Cr species volatilisation like other literatures.

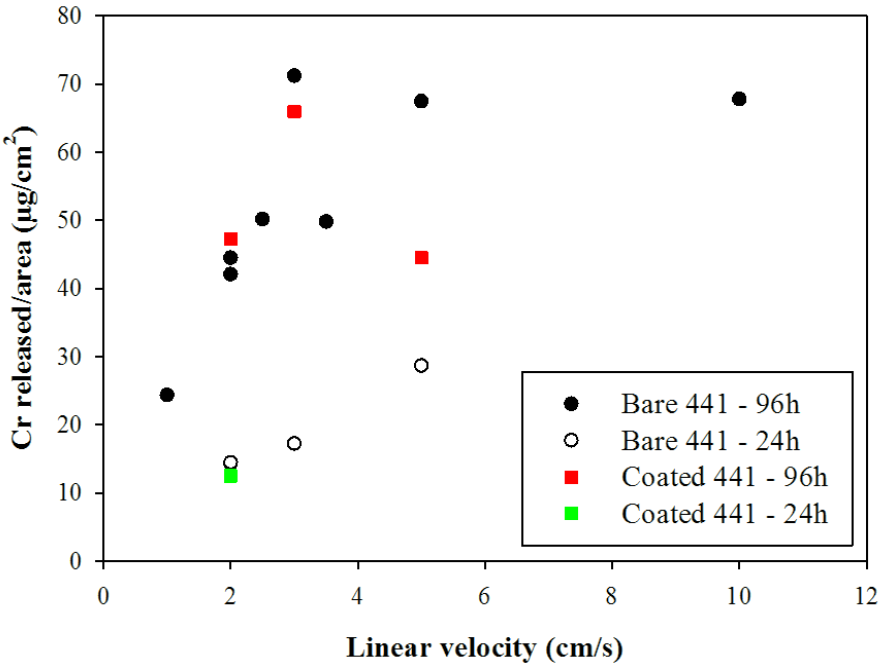

Figure 6.1 Cr species volatilisations of Bare 441 and Coated 441 (5%H_2O in O_2, 800°C, 24 and 96 h).

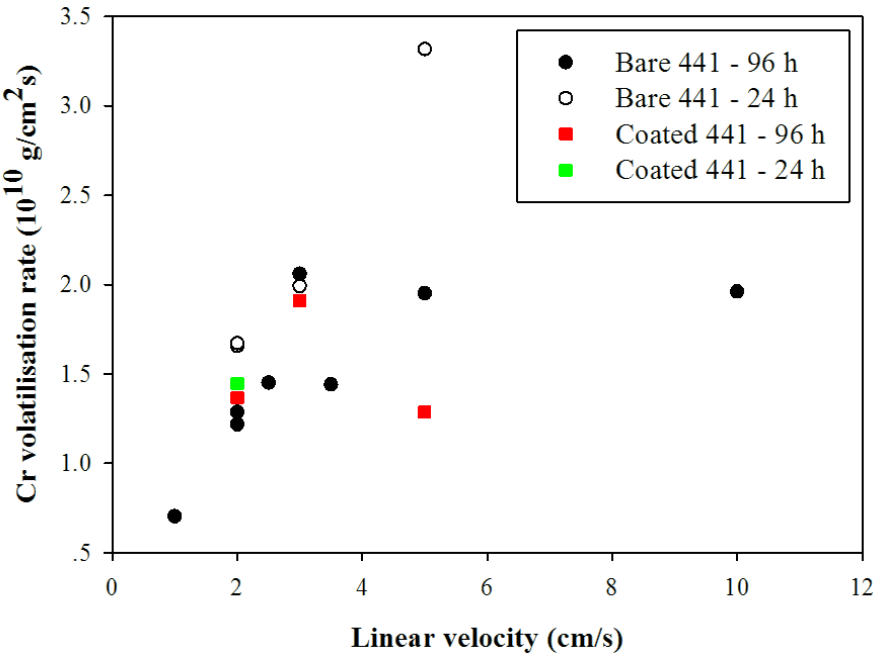

Figure 6.2 Effect of linear velocity on Cr volatilisation rate from Bare 441 and Coated 441 (5%H_2O in O_2, 800°C, 24 and 96 h).

6.2 Surface observation

6.2.1 Before high temperature oxidation

Figure 6.3 shows SEM images of Coated 441 before high temperature oxidation. The specimen surface was not smooth. Some cracks and holes can be observed. EDX results of these positions are shown in Figure 6.4. Red line in Figure 6.4b corresponding with the red plus symbol (+) in Figure 6.4a represents EDX analysis at the hole. The blue one represents EDX analysis of the matrix scale that was the same as overall observation. At the hole, Co that was the coating component cannot be observed. Meanwhile, at this position, Fe, Cr, Mn, O and Si can be observed. The observation at this position was similar to the analysis of Bare 441 after high temperature oxidation. That means this position was free-coating area and it can be concluded that the coating did not cover the entire specimen surface. Although the coating, Mn and Co, can be detected at the matrix scale, Cr and Fe can still be observed with the intensity higher than that of coating. This implies that the coating adhering on the specimen surface was very thin.

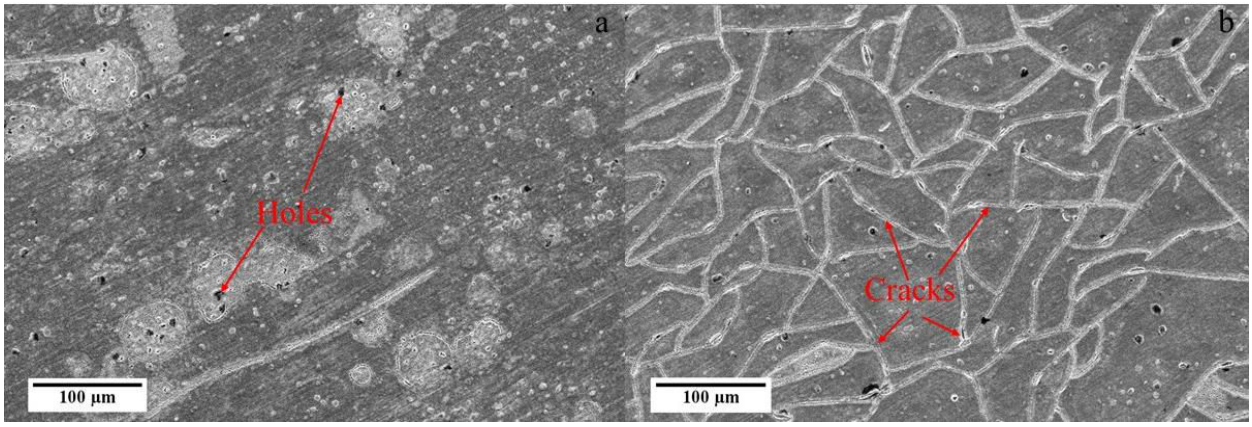

Figure 6.3 SEM images of Coated before high temperature oxidation. Figures a) and b) show the different locations on the same specimen.

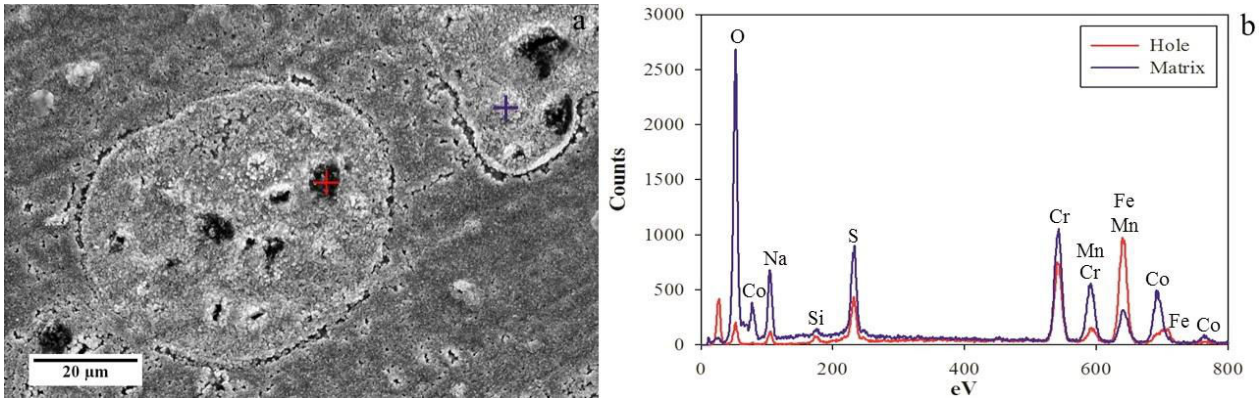

Figure 6.4 a) SEM image and b) EDX results focusing on the hole (red line) and the matrix scale (blue line).

6.2.2 After high temperature oxidation

Figure 6.5 shows SEM images of Coated 441 after high temperature oxidation in 2 cm/s of 5%H_2O in O_2 at 800°C for 96 h. From this figure, 2 crystallised zones that are the triangle and another one which seemed to be spherical can be observed. EDX revealed that the triangle one was mainly Cr and O that should be Cr_2O_3 while another crystalline zone, the spherical one, was composed of Cr with few amount of coating. Taking into account SEM images of the specimen surface before high temperature oxidation, Figure 6.5, the triangle crystalline could not be seen. That means this Cr_2O_3 did not developed during calcination process of oxide spinel, but it was exposed in high temperature oxidation process. This Cr_2O_3 can be observed not only at the cracks and/or spalled areas but also above the coating layer. Therefore, this coating was not able to prohibit the inward diffusion of O to the metal. Cr could still reacted with O on the top surface and formed Cr_2O_3. Cr species volatilisation can still proceed.

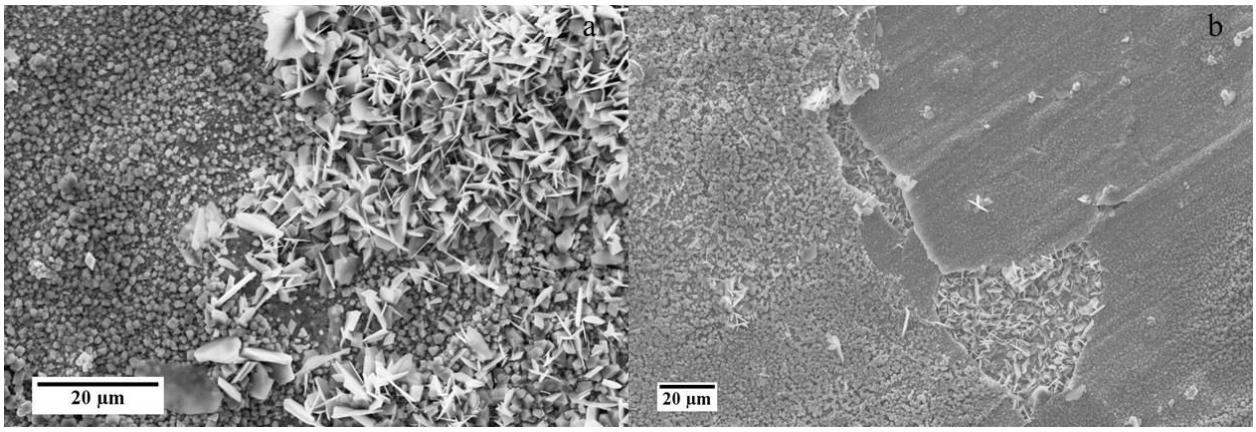

Figure 6.5 SEM images of Coated 441 after high temperature oxidation (2 cm/s, 5%H_2O in O_2, 800°C, 96 h). Figures a) and b) show the different locations on the same specimen.

6.3 Conclusions

Mn-Co spinel was tried to use as a coating on AISI 441 specimen by the electroplating method. After high temperature oxidation of these specimens, the results show that this coating, comparing with Bare 441, not only could not suppress Cr species volatilisation but also changed Cr volatilisation phenomenon. For Coated 441, Cr species volatilisation was limited by kinetics over all experimental range. On the contrary, diffusion and reaction limits can be observed from Bare 441. Furthermore, Cr volatilisation rate of both specimens were independent on oxidation time.

SEM and EDX were used to discuss the reason why this coating cannot suppress Cr species volatilisation. The results were clear that the coating was not smooth and covered the entire surface. Some cracks and holes which were free-coating areas can be obviously seen. Furthermore, this coating was very thin and it was not a diffusion barrier of Cr upward diffusion on the surface. There was no significant difference between coated and uncoated specimens, Coated 441 and Bare 441. Therefore, Cr_2O_3 could still form and volatile in high temperature

oxidation condition. This procedure could be improved by making the coating more compact and adherent, by adding for example a surfactant compound in the electrolysis bath.

References

[1] J. Wu, C. D. Johnson, R. S. Gemmen, and X. Liu, "The performance of solid oxide fuel cells with Mn-Co electroplated interconnect as cathode current collector," J. Power Sources, vol. 189, pp. 1106–1113, 2009.

[2] H. Kurokawa, C. Jacobson, L. Dejonghe, and S. Visco, "Chromium vaporization of bare and of coated iron–chromium alloys at 1073 K," Solid State Ionics, vol. 178, no. 3–4, pp. 287–296, Feb. 2007.

[3] X. Chen, P. Hou, C. Jacobson, S. Visco, and L. Dejonghe, "Protective coating on stainless steel interconnect for SOFCs: oxidation kinetics and electrical properties," Solid State Ionics, vol. 176, no. 5–6, pp. 425–433, Feb. 2005.

[4] K. Przybylski and T. Brylewski, "Interface Reactions between Conductive Ceramic Layers and Fe-Cr Steel Substrates in SOFC Operating Conditions," Materials Transactions, vol. 52, no. 3, pp. 345-351, 2011.

[5] V. Sauchuk, S. Megel, E. Girdauskaite, N. Trofimenko, M. Kusnezoff and A. Michaelis, "Influence of protective layers on SOFC operation," Russia Journal of Electrocheimistry, vol. 47, no. 5, pp. 522-530, 2011.

[6] Y. Fang, C. Wu , X. Duan, S. Wang and Y. Chen, "High-temperature oxidation process analysis of $MnCo_2O_4$ coating on Fe-21Cr alloy," Int. J. Hydrogen Energy, vol. 36, pp. 5611-5616, 2011.

[7] T. Uehara, N. Yasuda, M. Okamoto and Y. Baba, "Effect of Mn-Co spinel coating for Fe-Cr ferritic alloy ZMG232L and 232J3 for solid oxide fuel cell interconnects on oxidation behavior and Cr-evaporation," J. Power Sources., vol. 196, pp. 7251-7256, 2011.

[8] J. W. Stevenson, Z. G. Yang, G. G. Xia, Z. Nie and J. D. Templeton, "Long-term oxidation behavior of spinel-coated ferritic stainless steel for solid oxide fuel cell interconnect applications," J. Power Sources., vol. 231, pp. 256-263, 2013.

[9] L. Chen, E. Y. Sun, J. Yamanis and N. Magdefrau, "Oxidation kinetics of $Mn_{1.5}Co_{1.5}O_4$-coated Haynes 230 and Crofer 22 APU for solid oxide fuel cell intetconnects," J. Electrochem. Soc., vol. 157, no. 6, pp. B931-B942, 2010.

[10] W. Wei, W. Chen and D. G. Ivey, "Oxidation resistance and electrical properties of anodically electrodeposited Mn-Co oxide coatings for solid oxide fuel cell interconnect applications," J. Power Sources., vol. 186, pp. 428-434, 2009.

[11] M. R. Bateni, P. Wei, X. Deng and A. Petric, "Spinel coatings for UNS 430 stainless steel interconnects," Surf. Coat. Tech., vol. 201, pp. 4677-4684, 2007.

[12] M. R. Ardigo, I. Popa, S. Chevalier, V. Parry, A. Galerie, P. Girardon, F. Perry, R. Laucournet and A. Brevet, "Effect of coatings on a comercial stainless steel for SOFC interconnect application in anode atmosphere," ESC Trans., vol. 57, no. 1, pp. 4490-44952301-2311, 2013.

[13] A. Kruk, M. Stygar and T. Brylewski, "Mn-Co spinel protective-conductive coating on AL453 ferritic stainless steel for IT-SOFC interconnect applications," J. Solid State Electrochem, vol. 17, pp. 993-1003, 2013.

[14] K. Wang, Y. Liu and J. W. fergus, "Interaction between SOFC interconnect coating materials and chromia," J. Am. Ceram. Soc., vol. 94, no. 12, pp. 4490-4495, 2011.

Chapter 7

Cr volatilisation reduction by preoxidising AISI 441 in Ar

For many decades, researchers have been trying to solve Cr species volatilisation problem. Many coatings were developed and coated on the alloys [1]–[6]. However, no coating can improve the performance of interconnect and provide service work hours reaching up to 40,000 - 50,000 h. Similarly to the coating presented in Chapter 6, no one could suppress Cr volatilisation. Hence, in Chapters 7 and 8, a new method of surface heat treatment called preoxidation was used and the effect of preoxidation on Cr volatilisation was demonstrated.

In the present chapter, Bare 441 was preoxidised in Ar. In these conditions, Sabioni et al. [7] and Magdefrau et al. [8] reported that the oxides formed on the alloy surfaces after preoxidation at high temperatures (850-1050 °C) were Cr_2O_3, $MnCr_2O_4$ and TiO_2. These oxides are the same as the oxides formed on Bare 441 after high temperature oxidation, as described in Chapter 4. However, after preoxidising in Ar at high temperatures for short time, the grain size of alloy increased, leading to lower nucleation rate of Cr_2O_3 and $MnCr_2O_4$ and the increases in (i) the thickness of spinel layer, (ii) the proportional of this spinel layer in the oxide and (iii) the oxidation resistance. Hence, it can be seen that, after peroxidation in Ar, the steel was improved in oxidation resistance and was more suitable for applying as metallic interconnect of SOFC. Even though preoxidation of alloy in Ar at high temperatures could increase oxidation resistance, its effect on Cr volatilisation is unknown. Thus, in this chapter, the effect of preoxidation of Bare 441 in Ar on Cr volatilisation will be discussed.

7.1 Cr volatilisation results

Figure 7.1 shows Cr species volatilisation from P.Ar-250 and P.Ar-850 against linear velocity of gas comparing with that of Bare 441. For P.Ar-250, Cr species volatilisation seems to be reduced comparing with that of Bare 441. At linear velocity of gas in the range of 1-3 cm/s, Cr species volatilisation from P.Ar-250 was lower than that of Bare 441 for about 2 times. However, at 10 cm/s of gas linear velocity, Cr species volatilisation from P.Ar-250 was similar to that of Bare 441. On the contrary, Cr species volatilisation from P.Ar-850 cannot be suppressed. Moreover, its tendency seems to increase with increasing gas linear velocity. At 10 cm/s of gas linear velocity, Cr species volatilisation from P.Ar-850 was higher than that of Bare 441 for more than 2 times. In addition, it increased with increasing gas linear velocity revealing that it was controlled by diffusion of Cr volatile species in the gas. Therefore, some catalytic effect may occur and accelerate Cr species volatilisation reaction.

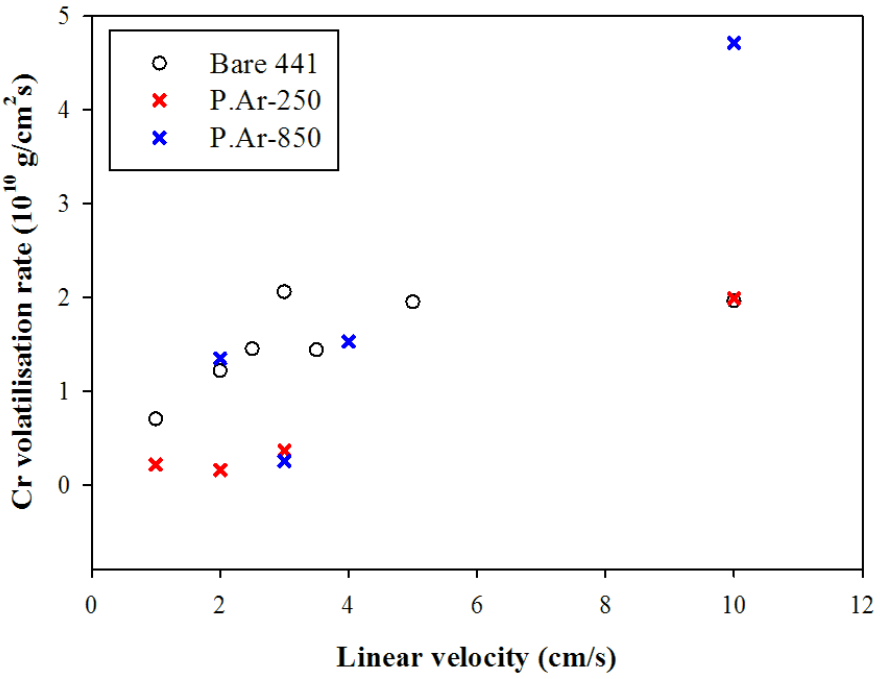

Figure 7.1 Cr volatilisation rate from Bare 441, P.Ar-250 and P.Ar-850 as a function of gas linear velocity (5%H_2O in O_2, 800°C, 96 h).

Even though Magdefrau et al. [8] reported that preoxidation in Ar at high temperatures, 850°C-1050°C, can improve the global oxidation kinetics and, hence, reduce parabolic rate constant of the alloy, it is proved by these results that this preoxidation condition could not certainly reduce Cr species volatilisation. Considering Cr species volatilisation point of view, the performance of P.Ar-850 was probably worse than that of Bare 441. Among these specimens; Bare 441, P.Ar-250 and P.Ar-850; the performance of P.Ar-250 was the best especially at low linear velocity of gas. Thus, it could be summarised that, during preoxidation in Ar at 250°C, the protective film was developed. This film may act as a diffusion barrier of Cr and/or O. However, this protection failed when operated at high linear velocity of gas. Spallation can be obviously visible as shown in Figure 7.2. This was possibly the reason why Cr species volatilisation from P.Ar-250 was similar to that of Bare 441 when the gas linear velocity was 10 cm/s [9], [10].

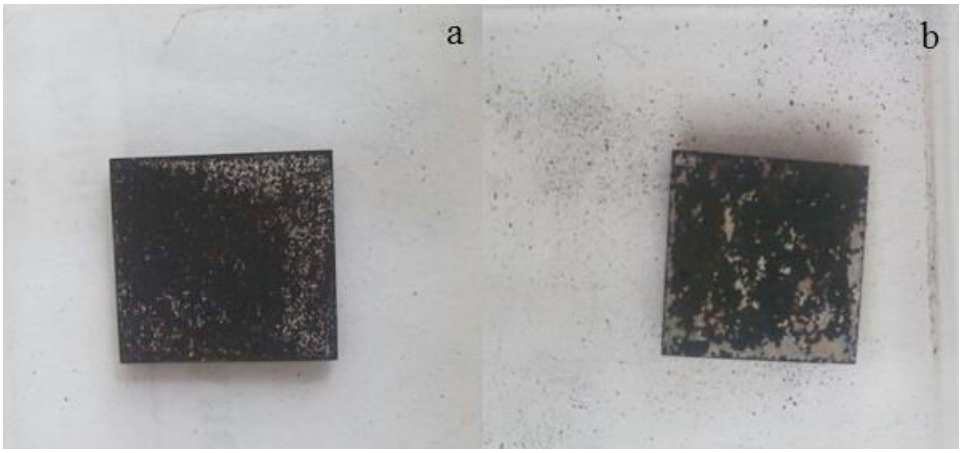

Figure 7.2 Surfaces of a). P.Ar-250+ox.10 and b). P.Ar-850+ox.10.

7.2 Surface observation

SEM, EDX, XRD, XPS and Raman spectroscopy were used for diagnosing the specimen surfaces. SEM was used to observe the topographies of the surfaces while others used for qualitative analysis (phases identification on/near the surfaces). Among these techniques, the penetration depth of XPS was the thinnest i.e. about 5 and 10 nm when the analysis angle were 30° and 90° respectively. The penetration depth of Raman spectroscopy was around 1 µm. XRD and EDX were used for identifying phases with a penetration depth deeper than 1 µm.

7.2.1 The specimen preoxidised in Ar at 250°C

7.2.1.1 Before high temperature oxidation

Figure 7.3 shows SEM image in SE mode of P.Ar-250. Due to very thin oxide layer, the scratches occurring from the polishing steps can be observed in this figure. As described in Chapter 3, the penetration depths of SEM and EDX were large, thus, EDX, SEM topographic image and XRD results can explain nothing. Therefore, only XPS and Raman results would be discussed in this section.

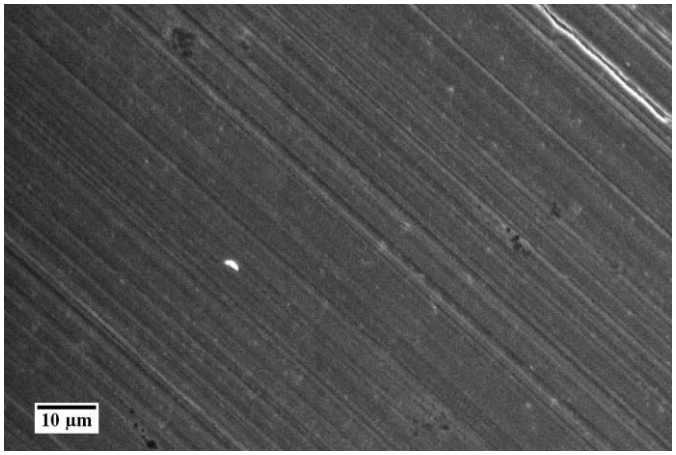

Figure 7.3 SEM image in SE mode of P.Ar-250.

Figure 7.4 shows Raman spectra of P.Ar-250. Two phases were exposed on this specimen surface that were the main component of Fe_2O_3 [11] and $FeCr_2O_4$ [11]–[13]. Fe_2O_3 formation exposed by the reaction of Fe_3O_4 forming by outwardly injecting of Fe vacancies [14] and O_2 [15]. Meanwhile, $FeCr_2O_4$ internally formed [14]. On the other hand, XPS, Figure 7.5, can detect the peaks of Fe and a trace of Si, so Fe_2O_3 should be the external layer (Cr was not detected). When the main peak of Fe was enlarged in the binding energy range of 700-740 eV, Figure 7.6, only Fe-O peak could be observed. No metallic Fe from the substrate can be detected like in Figure 4.2. That means the thickness of Fe_2O_3 was not less than 10 nm. Quantitative analysis by XPS was achieved by calculating the curve area of the main peaks of each element. Then, the curve area of each element was divided by their own sensibility factors [16]. The ratio of element can be calculated by Eq. 7.1. Fe/(Fe+Cr) ratios of Bare 441 before high temperature oxidation and P.Ar-250 are shown in Figure 7.7.

$$\text{Ratio of } \frac{A}{B} = \frac{\dfrac{\text{The curve area of A}}{\text{Sensibility factor of A}}}{\dfrac{\text{The curve area of B}}{\text{Sensibility factor of B}}} \qquad \text{(Eq. 7.1)}$$

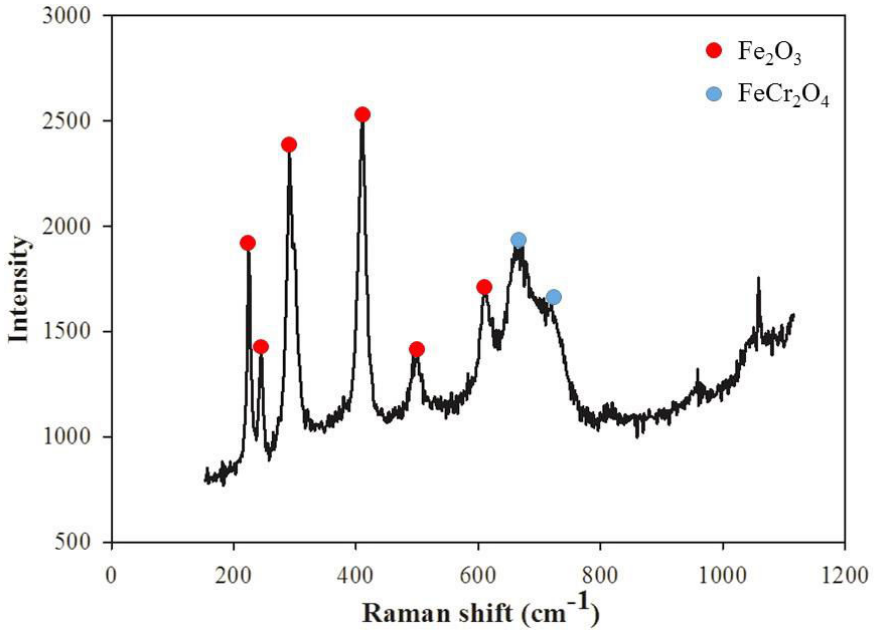

Figure 7.4 Raman spectra of P.Ar-250.

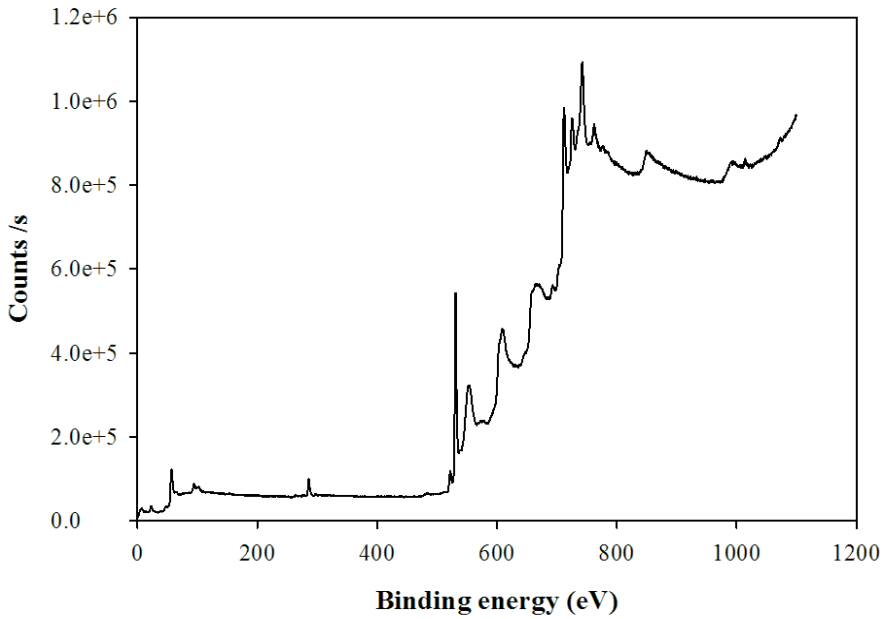

Figure 7.5 XPS spectrum of P.Ar-250 when the incident angle was 90°.

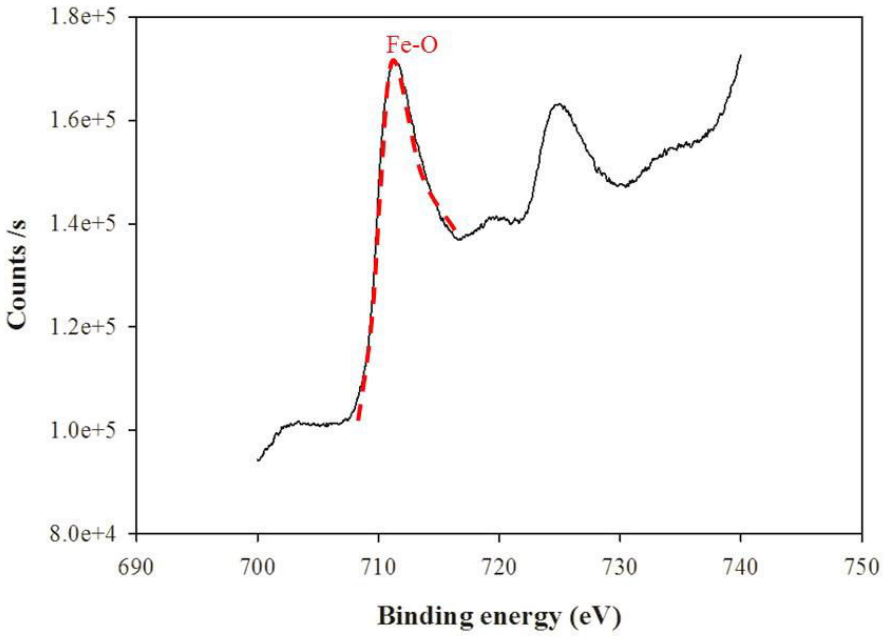

Figure 7.6 Fe spectrum observed on P.Ar-250 detected by XPS.

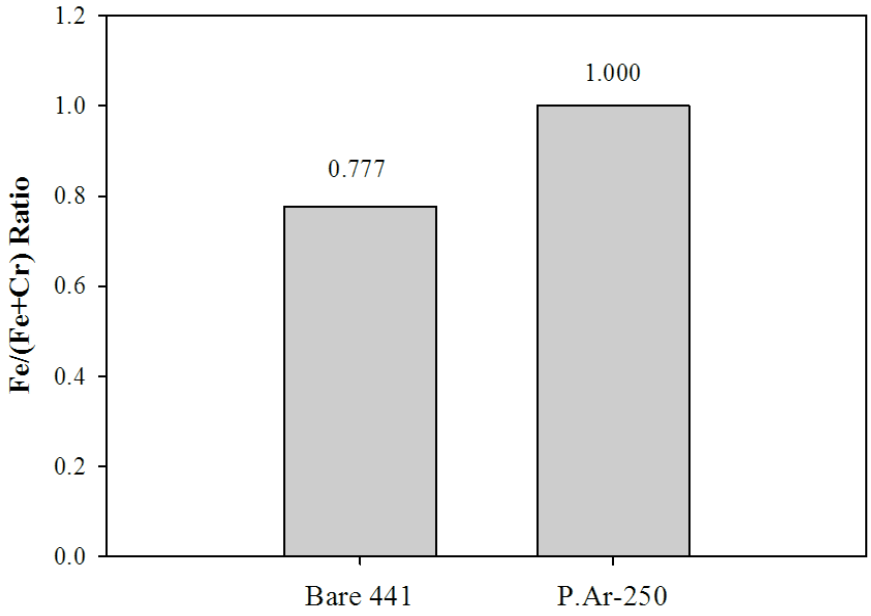

Figure 7.7 Fe/(Fe+Cr) ratios of Bare 441 and P.Ar-250 obtained by XPS.

From Figure 7.7, it can be seen that Fe/(Fe+Cr) ratio of P.Ar-250 equals 1 (no Cr on the top surface) while the Fe/(Fe+Cr) ratio of Bare 441 which was 0.777 (Cr was existed). That means, during preoxidation in Ar at 250°C for 3 h, only Fe was promoted on the top surface [17].

The formation of Fe_2O_3 was also confirmed by Ellingham/Richardson diagram [9] shown in Figure 7.8. This diagram presents the temperature dependence on the stabilities of

the compounds. In Figure 7.8, it is the Ellingham/Richardson diagram of the metal oxides. In this preoxidising condition, $P_{O_2} = 2\times10^{-6}$ bar (as mentioned in Section 7.1.1) and T = 250°C, it can be seen that Fe_2O_3 can be formed in this condition. Cr_2O_3 is also stable in these conditions, but does not form due to the very low temperature making Cr-diffusion in the alloy infinitely slow.

As described in Section 7.1, Cr species volatilisation from P.Ar-250 was less than that of Bare 441. Hence, it is possible that Fe_2O_3 formed on this specimen surface acts as a diffusion barrier for Cr and/or O between the alloy and the gas, resulting in the reduction of Cr species volatilisation. This is consistent with the research of Froitzheim et al. [3] explaining that Cr species volatilisation could be significantly reduced if Cr was not exposed on the top surface.

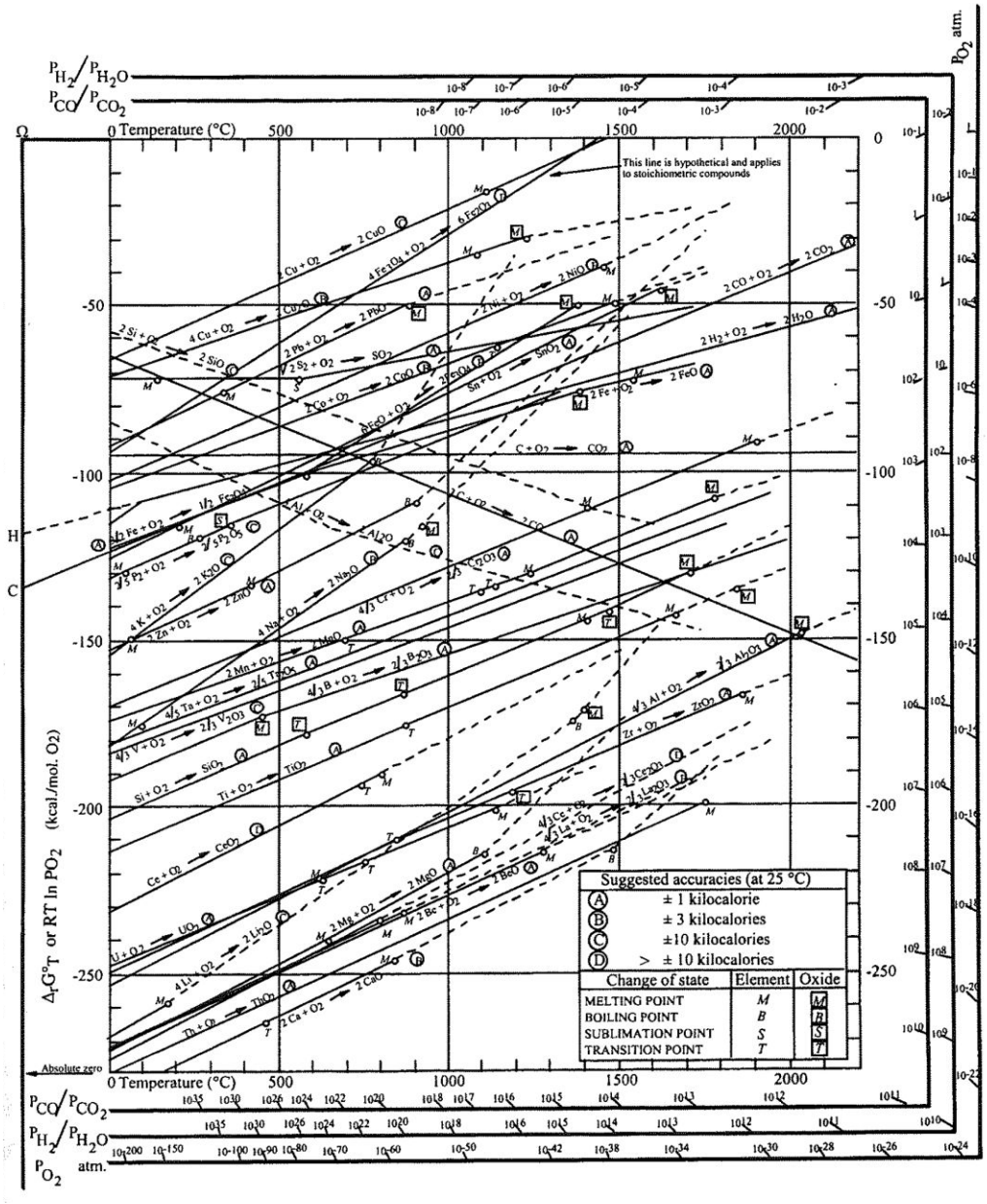

Figure 7.8 Ellingham/Richardson diagram for oxides of the metals [9].

7.2.1.2 After high temperature oxidation

Figure 7.9 shows SEM images of P.Ar-250+ox.4 in SE and BSE modes. In Figure 7.9a, SE mode image, the oxide observed could be classified into 2 areas that are the darker matrix scale and the brighter swell areas located on the matrix. However, after observing by BSE mode of SEM which the levels of grey depend on atomic number of the elements, the levels of grey of the matrix and swell areas are similar. This implies that the composition(s) of these areas is the same. The apparent contrast results from the cavities in the swell regions appearing in black on the images. EDX presented that the elements of the matrix are Cr, Fe, Mn, Ti, Si, Nb, O and C (reminding that the interaction volume was high, making all the steel elements appear) while the swell area mainly comprised Cr. Raman spectroscopy ensured the EDX results by analysing 10 points on P.Ar-250+ox.4. The 10 spectra obtained from Raman analysis exactly show the same results that only Cr_2O_3 [11]–[13], [18]–[21] and spinel were formed. The example of these spectra is shown in Figure 7.10. As usual, the exact spinel phase could not be identified by Raman, Mn-Cr, Cr-Fe or Mn-Fe spinel [11], [12], [22]–[25].

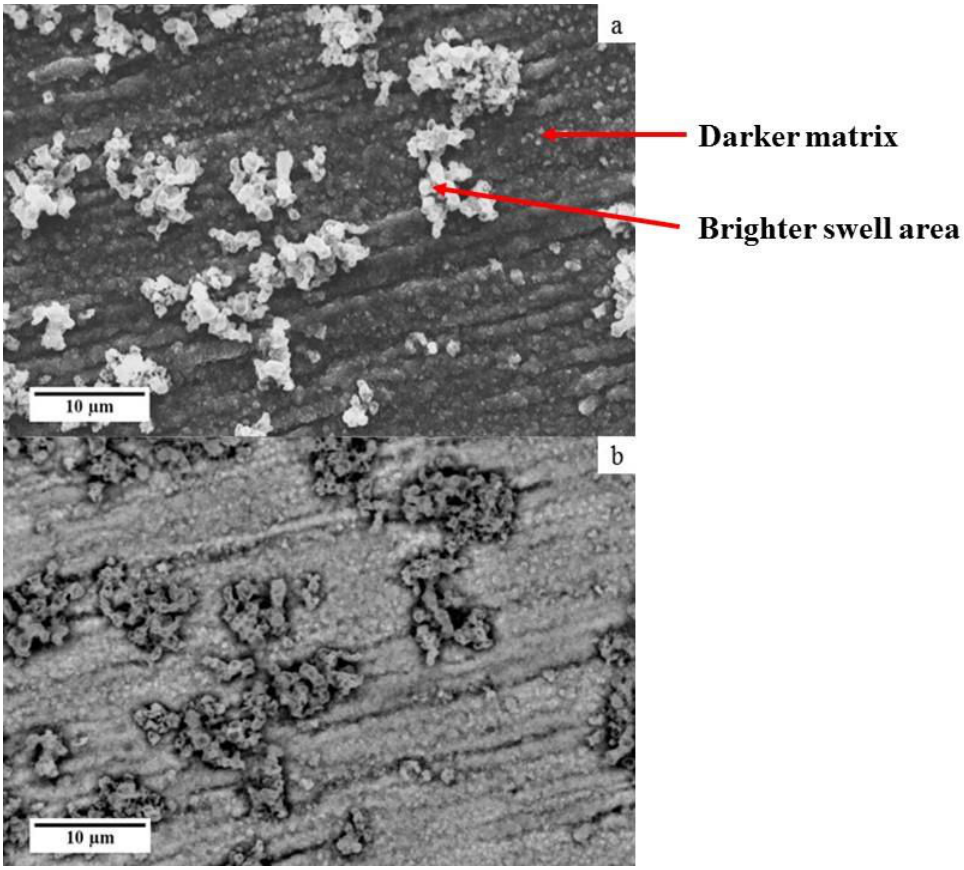

Figure 7.9 SEM images of P.Ar-250+ox.4 in a). SE mode and b). BSE mode.

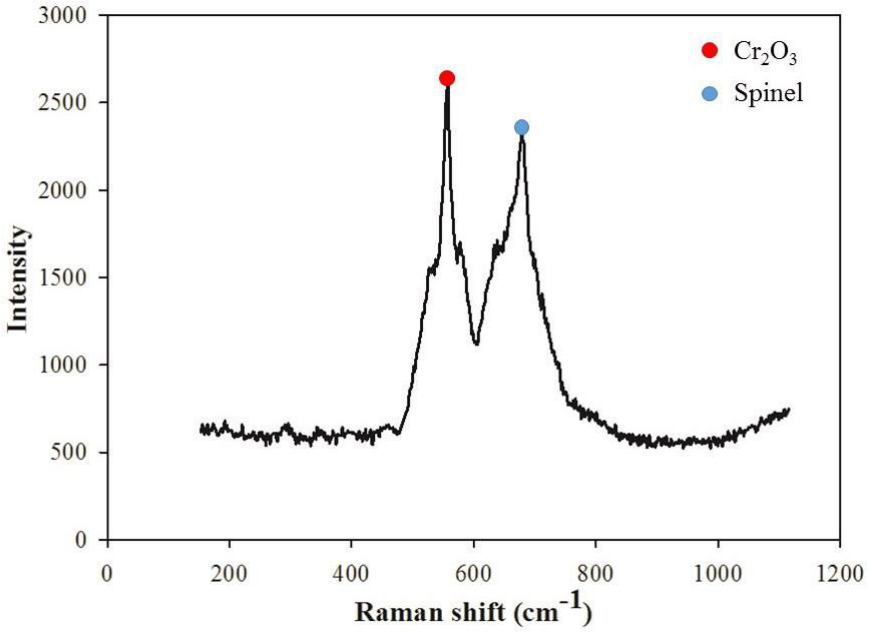

Figure 7.10 Raman spectrum of P.Ar-250+ox.4.

Figure 7.11 shows XRD pattern of P.Ar-250+ox.4. With a high penetration depth of XRD, ferrite peaks were seen as a major phase while other 2 phases could also be observed that were Mn-Cr spinel and Fe-doped Cr_2O_3. Fe-doped Cr_2O_3, has the Cr_2O_3 structure with substitution of Cr^{3+} by Fe^{3+} (solid solution). When this phase is observed by Raman, all peaks slightly shift from the positions of pure Cr_2O_3 [11]. The possible range of Fe-doped Cr_2O_3 was in the range between Raman spectra of Cr_2O_3 and Fe_2O_3. In the present case, only the main peak of Cr_2O_3 was observed by Raman. No sub-peaks could be detected. Thus, it was not possible to conclude that there was some element inserted in Cr_2O_3 structure by using only Raman spectroscopy. Another spinel phase can be observed, like Raman result, which was Mn-Cr spinel. Thus, the spinel phase detected by Raman was Mn-Cr spinel.

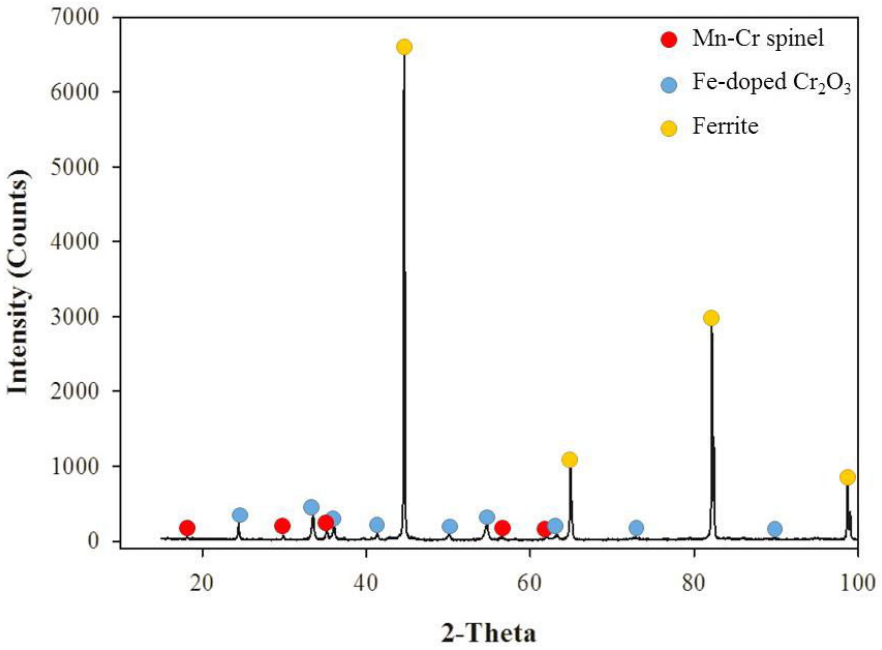

Figure 7.11 XRD pattern of P.Ar-250+ox.4.

7.2.2 The specimen preoxidised in Ar at 850°C

7.2.2.1 Before high temperature oxidation

Figure 7.12 shows Cr/Fe, Mn/Cr, Ti/(Mn+Cr) and Fe/(Fe+Cr) XPS ratios of P.Ar-850 comparing with that of P.Ar-250 and Bare 441. This figure was also obtained by calculating the element ratios from Eq. 7.1 like Figure 7.7. As mentioned above, preoxidation in Ar at 250°C promoted the outward diffusion of Fe to the top surface, so only Fe/(Fe+Cr) ratio can be measured and it equalled 1. For Bare 441 before high temperature oxidation, Mn and Ti were not detected while Cr and Fe were observed. Fe was a major element since the Cr/Fe ratio was much less than 1. Considering the ratios of P.Ar-850, it can be seen that Cr/Fe was very high as about 3 while Fe/(Fe+Cr) was less than 1. That means Cr was promoted on the top surface during preoxidation in Ar at 850°C [17]. Mn and Ti were also exposed on the top surface because their diffusion mobilities were normally higher than that of Cr at high temperatures [26], [27]. The incident angle of XPS was adjusted to 30° in order to observe the top 5 nm. Mn/Cr ratios at 30° and 90° of P.Ar-850 were plotted in Figure 7.13. It can be seen that Mn/Cr ratio when analysed with 30° of X-ray incident angle (5 nm depth) was higher than that with 90° of X-ray incident angle (10 nm depth). That means almost Mn diffused and located at the top surface of specimen.

In summary, the top surface of P.Ar-850 and P.Ar-250 were very different. Preoxidation temperature was a strong influence affecting the diffusion of the elements to the top surface [17]. P.Ar-250 promoted only Fe while P.Ar-850 mainly promoted Cr on the top surface. As mentioned above, Froitzheim et al. [3] found that Cr species volatilisation would be significantly reduced if there was no Cr on the top surface. Thus, this probably the reason why P.Ar-850 cannot suppress Cr species volatilisation while P.Ar-250 can. However, there was controversial with the research of Stanislowski et al. [28] proving that Mn-Cr spinel was a protective layer even though it contained Cr at the top surface. The present work is consistent

with the work of Stanislowski et al., probably implying that the oxide formed on P.Ar-850 should not be a protective Mn-Cr spinel. Therefore, other characterisation techniques were necessary to identify the phases of this oxide.

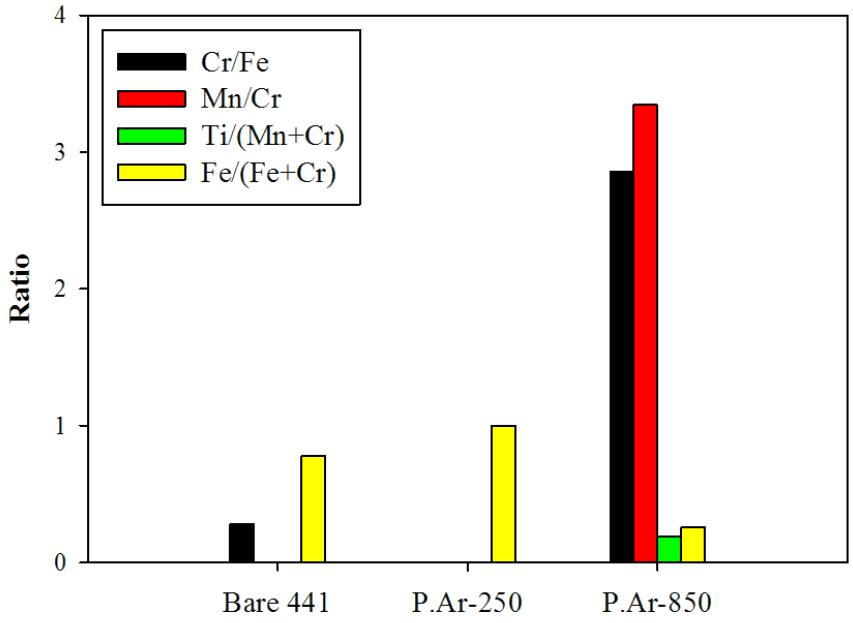

Figure 7.12 The element ratios of Bare 441, P.Ar-250 and P.Ar-850 obtained by quantitative analysis of XPS.

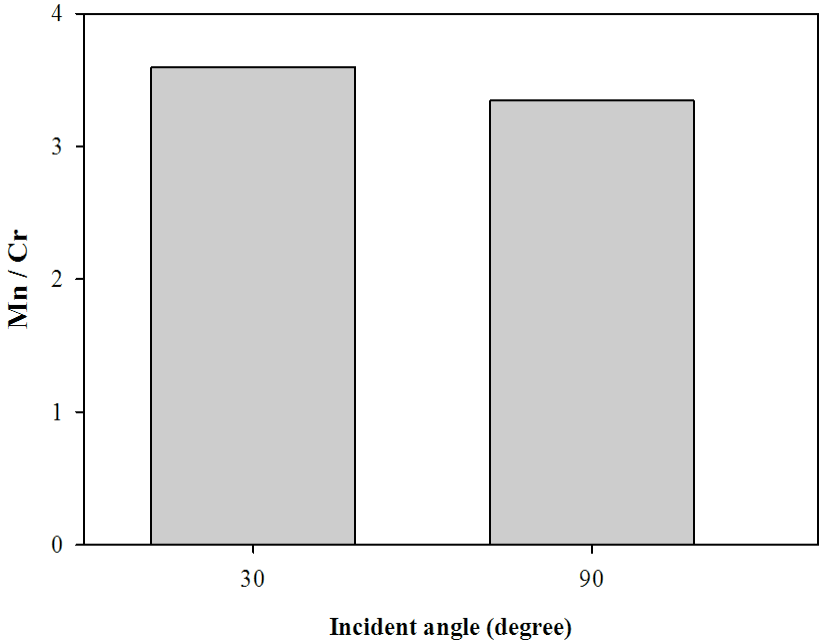

Figure 7.13 Mn/Cr ratio of P.Ar-850 when the incident angles were 30° and 90°.

SEM images of P.Ar-850 are shown in Figure 7.14. The scratches occurring from the polishing steps were also observed like on P.Ar-250, but they were less intense than on P.Ar-250, due to thicker oxide. The crystalline steel structure can be seen on the surface. Small nodules like observed on as-received 441 after high temperature oxidation in 5%H_2O in O_2 at 800°C for 24 h in Chapter 5 can be seen. Their diameters were around 6 µm. They seem locating above the metallic grain boundaries and also in the grain which was consistent with the results in Chapter 5. Normally, the metallic grain boundaries could be observed from the oxidation of as-received specimen and the specimen polished with very fine tools such as electropolishing [29]. In this work, before preoxidation, specimen was polished by SiC up to #1200 grit. Its surface should be similar to Bare 441 even thinner oxide layer was formed on the surface. Thus, it was possible that the preoxidation atmosphere affected the presence of metallic grain boundaries as well as the nodules. However, the metallic grain size in Figure 7.14a was around 100 µm which was 5 times bigger than the metallic grain size observed on as-received 441 after high temperature oxidation. This was in good agreement with the work of Magdefrau et al. [8] reporting that preoxidation in Ar led to the increase of metallic grain size. Even though they reported that kinetics rate constant could be reduced by preoxidation in Ar at high temperature, in the present work, Cr species volatilisation from P.Ar-850 was not suppressed. EDX was used to analyse the compositions of the matrix and nodule. It was found that the matrix consisted of Fe, Cr, Mn, Ti, Si, Nb and O that were similar to the composition of Bare 441. The nodule was composed of Cr, Ti and Nb which were similar to the composition of the nodule reported in Chapter 5.

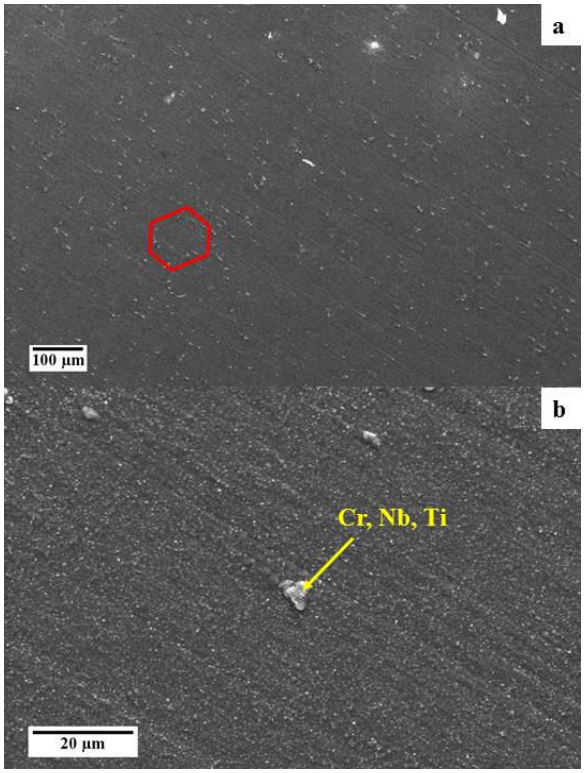

Figure 7.14 SEM images in SE mode of P.Ar-850 when the magnification of the images were a). 100x and b). 1000x.

Figure 7.15 shows Raman spectrum of P.Ar-850. With a penetration depth around 1 µm, 3 phases were found: chromia, spinel and trace of Nb_2O_5 [30]. The precise composition of spinel was identified by XRD in Figure 7.16. In this figure, high intensities of ferrite peaks were observed as a major component due to the high interaction volume. The other 2 phases detected by XRD were Fe-doped Cr_2O_3 and Mn-Fe spinel. Thus, spinel detected by Raman was Mn-Fe spinel. Mn-Fe spinel formation was ensured by the work of Ding et al. [31]. However, the protective ability of Mn-Fe spinel has still been unclear. This spinel was possibly not a protective spinel, so Cr species volatilisation from P.Ar-850 was not reduced comparing with that of Bare 441. On the other hand, if Mn-Fe spinel was also a protective spinel, its thickness was probably too thin to decelerate the diffusion of Cr and/or O.

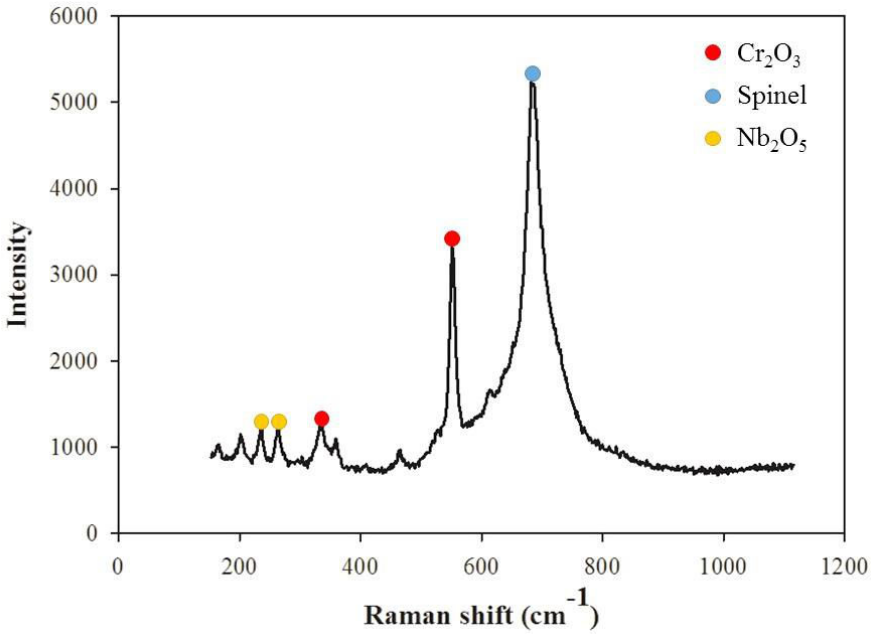

Figure 7.15 Raman spectrum of P.Ar-850.

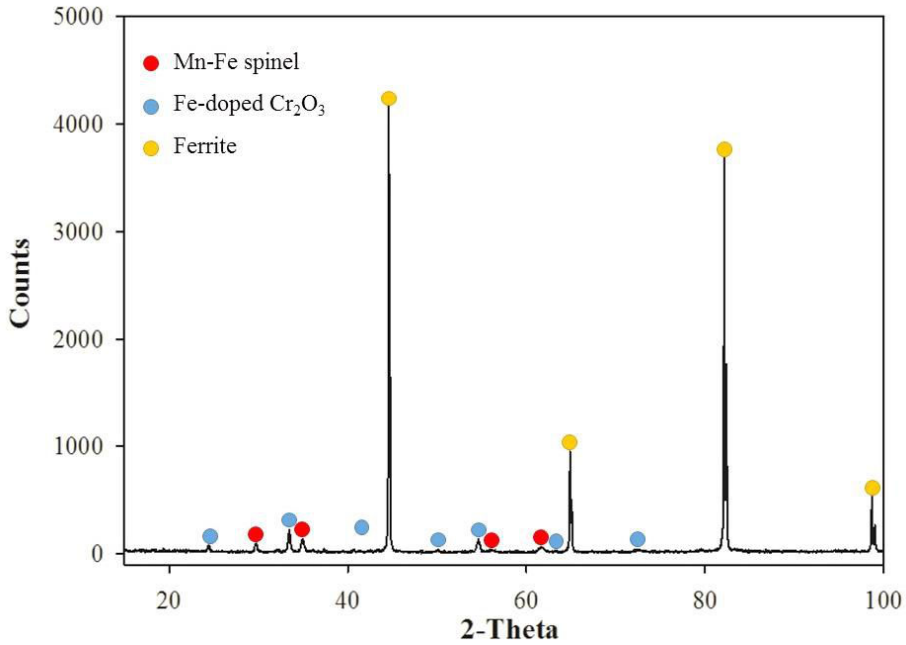

Figure 7.16 XRD pattern of P.Ar-850.

7.2.2.2 After high temperature oxidation

Figure 7.17 shows the SEM images of P.Ar-850+ox.4 in SE mode. In Figure 7.17a, it can be seen that the nodules were developed above the metallic grain boundaries as well as in the grain. Comparing with the SEM image of P.Ar-850, Figure 7.14a, the metallic grain boundaries were less visible than that of Figure 7.17a, due to thick oxide formation. When increasing the magnification of the image, Figure 7.17b, the crystalline structure formed on P.Ar-850+ox.4 was finer than that of P.Ar-250+ox.4. Similar to the matrix of P.Ar-250+ox.4, the matrix of P.Ar-850+ox.4 was composed of Fe, Cr, Mn, Ti, Nb, Si, O and C. Some nodules comprised Cr, Nb and Ti like the ones developed on P.Ar-850 and as-received 441 in Chapter 5 while some nodules contained only Cr which could be chromia.

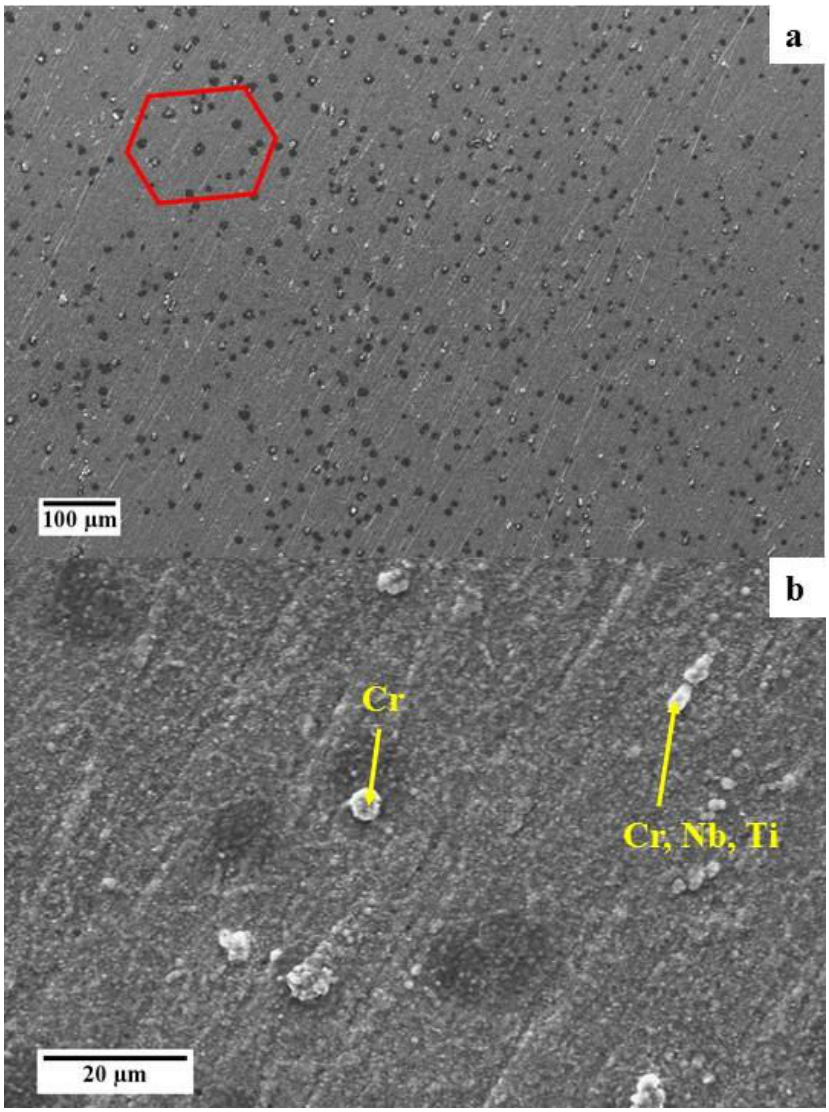

Figure 7.17 SEM images in SE mode of P.Ar-850+ox.4 when the magnifications were a). 100x and b). 1000x.

Raman spectra of P.Ar-850+ox.4 are shown in Figure 7.18. From 10 points of analysis, there are 2 types of spectra observed that were (i) the characteristic of chromia and spinel and (ii) the characteristic of TiO_2 [12] and spinel. These ensured the results obtained by SEM that there were the nodule like in Chapter 5 developed on the oxides of chromia and spinel during high temperature oxidation of P.Ar-850. However, the spinel phase cannot still be specified. Therefore, XRD was used to identify the exact phases of spinel and other oxide(s) formed on P.Ar-850+ox.4 in case that there were some elements interrupting in the oxide structures. The result is shown in Figure 7.19.

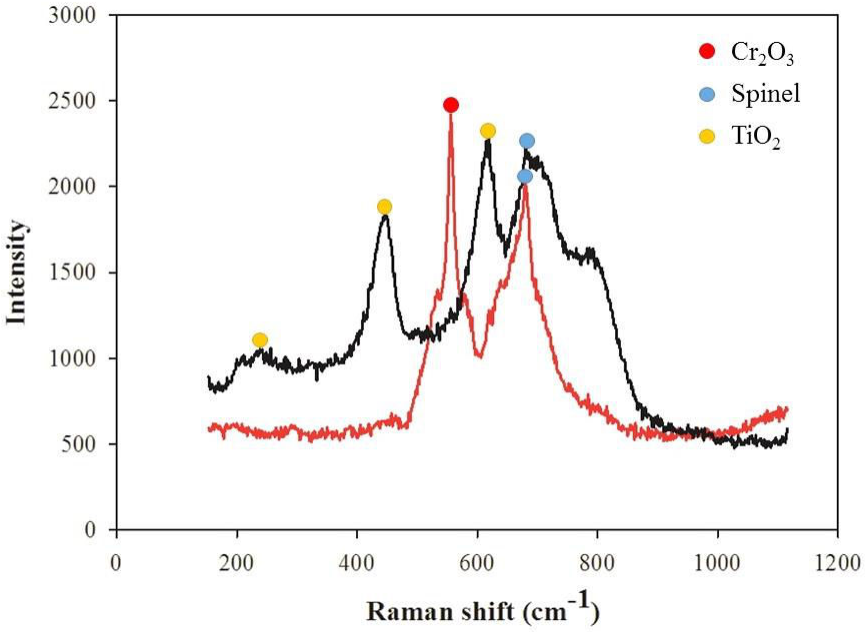

Figure 7.18 Raman spectra of P.Ar-850+ox.4.

In Figure 7.19, XRD detected 3 phases: ferrite, Mn-Cr spinel and chromia with Fe-insertion (Fe-doped Cr_2O_3). Thus, the spinel detected by Raman spectroscopy was Mn-Cr spinel. TiO_2 could not be observed by XRD like Raman. This probably because of high interaction volume of XRD. TiO_2 normally appears as an external phase and as internal precipitates, so the amount of TiO_2 was relatively very low. Hence, its intensity was probably too low to distinguish it from the base line.

In summary, the surface of P.Ar-850+ox.4 was similar to P.Ar-250+ox.4. After high temperature oxidation, chromia and Mn-Cr spinel were intensely formed on both surfaces. Dissimilarly, the Ti-Nb nodules were observed on P.Ar-850 and P.Ar-850+ox.4 while cannot be seen on P.Ar-250 and P.Ar-250+ox.4.

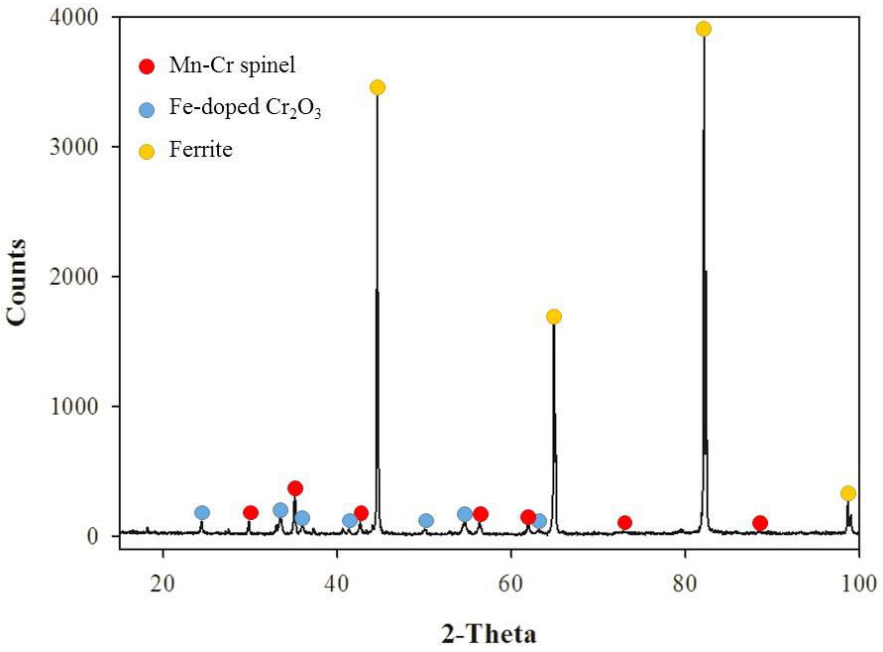

Figure 7.19 XRD spectrum of P.Ar-850+ox.4.

7.3 Conclusions

In this chapter, Bare 441 was preoxidised in Ar before high temperature oxidation in order to improve Cr species volatilisation resistance. P_{O_2} in Ar tank was 2×10^{-6} bar. The preoxidation temperatures were 250°C and 850°C and the preoxidation duration was 3 h. The results show that preoxidation temperature was a strong influence affecting upward diffusion of elements. For P.Ar-250, Fe was promoted on the top surface while Cr upwardly diffused to the top of P.Ar-850. Fe_2O_3 was observed on the top of P.Ar-250 while chromia and Mn-Fe spinel were detected on P.Ar-850. Cr volatilisation results show that P.Ar-250 can suppress Cr species volatilisation while P.Ar-850 cannot. This was possibly because the phases formed on both specimens were different. Fe_2O_3 may be a diffusion barrier of Cr and/or O, so the oxidation reaction was decelerated leading to reduction of Cr volatilisation reaction. For P.Ar-850, Mn-Fe spinel was probably not a protective oxide reducing the chemical potential of Cr on the top surface like Mn-Cr spinel. Moreover, Mn-Fe spinel formed on P.Ar-850 was possibly a catalytic phase promoting Cr species volatilisation reaction. Thus, it was not able to suppress Cr species volatilisation. In addition, the metallic grain size of P.Ar-850 was around 5 times bigger than that of as-received 441. Therefore, it can be concluded that, even the increase of grain size improved the oxidation resistance as reported by Magdefrau et al., it did not affect Cr volatilisation reaction.

After high temperature oxidation, the oxides formed on both specimens, P.Ar-250+ox.4 and P.Ar-850+ox.4, were similar. Even though the phases after preoxidation on both specimens were different, chromia and Mn-Cr spinel were exposed during high temperature oxidation. The surface of P.Ar-250+ox.4 was similar to that of Bare 441 after high temperature oxidation. There were swell chromia areas on the matrix scale. On the contrary, the surface of P.Ar-850+ox.4 was similar to that of as-received 441 after high temperature oxidation. The

Ti-Nb nodules located above the metallic grain boundaries as well as in the grain were observed. Furthermore, after high temperature oxidation in high linear velocity of wet O_2, the spallation occurred on both specimens leading to higher Cr volatilisation rate than specimen oxidised in lower velocity.

References

[1] S. Canovic, J. Froitzheim, R. Sachitanand, M. Nikumaa, M. Halvarsson, L.-G. Johansson, and J.-E. Svensson, "Oxidation of Co- and Ce-nanocoated FeCr steels: A microstructural investigation," Surf. Coat. Technol., vol. 215, pp. 62–74, Jan. 2013.

[2] C. Collins, J. Lucas, T. L. Buchanan, M. Kopczyk, a. Kayani, P. E. Gannon, M. C. Deibert, R. J. Smith, D. S. Choi, and V. I. Gorokhovsky, "Chromium volatility of coated and uncoated steel interconnects for SOFCs," Surf. Coat. Technol., vol. 201, no. 7 SPEC. ISS., pp. 4467–4470, 2006.

[3] J. Froitzheim, S. Canovic, M. Nikumaa, R. Sachitanand, L. G. Johansson, and J. E. Svensson, "Long term study of Cr evaporation and high temperature corrosion behaviour of Co coated ferritic steel for solid oxide fuel cell interconnects," J. Power Sources, vol. 220, pp. 217–227, Dec. 2012.

[4] J. G. Grolig, J. Froitzheim, and J.-E. Svensson, "Coated stainless steel 441 as interconnect material for solid oxide fuel cells: Oxidation performance and chromium evaporation," J. Power Sources, vol. 248, pp. 1007–1013, Feb. 2014.

[5] H. Kurokawa, C. Jacobson, L. Dejonghe, and S. Visco, "Chromium vaporization of bare and of coated iron–chromium alloys at 1073 K," Solid State Ionics, vol. 178, no. 3–4, pp. 287–296, Feb. 2007.

[6] T. Uehara, N. Yasuda, M. Okamoto, and Y. Baba, "Effect of Mn–Co spinel coating for Fe–Cr ferritic alloys ZMG232L and 232J3 for solid oxide fuel cell interconnects on oxidation behavior and Cr-evaporation," J. Power Sources, vol. 196, no. 17, pp. 7251–7256, Sep. 2011.

[7] A. C. Sabioni, A-M. Huntz, E. Conceição, M. Mantel, and C. Haut, "Comparative study of high temperature oxidation behaviour in AISI 304 and AISI 439 stainless steels," Mater. Res., vol. 6, no. 2, pp. 179–185, 2003.

[8] N. J. Magdefrau, L. Chen, E. Y. Sun, and M. Aindow, "Effects of alloy heat treatment on oxidation kinetics and scale morphology for Crofer 22 APU," J. Power Sources, vol. 241, pp. 756–767, 2013.

[9] P. Sarrazin, A. Galerie, and J. Fouletier, Mechanisms of high temperature corrosion: A kinetic approach. 2008.

[10] C. A. Barrett and C. E. Lowell, "Comparison of isothermal and cyclic oxidation behavior of twenty-five commercial sheet alloys at 1150 °C," Oxid. Met., vol. 9, no. 4, pp. 307–355, 1975.

[11] B. D. Hosterman, “Raman spectroscopic study of solid solution spinel oxides,” University of Nevada, Thesis 2011.

[12] J. Mougin, “Tenue mécanique de couches d’oxyde thermiques générées sur le chrome et sur quelques aciers inoxydables ferritiques: Étude des contraintes et de d'adhérence,” Institut National Polytechnique de Grenoble, Thesis 2001.

[13] D. Renusch, B. Veal, K. Natesan, and M. Grimsditch, “Transient oxidation in Fe-Cr-Ni alloys : a Raman-scattering study,” Oxid. Met., vol. 46, no. 5–6, pp. 365–381, 1996.

[14] F. Rouillard, G. Moine, L. Martinelli, and J. C. Ruiz, “Corrosion of 9Cr steel in CO_2 at intermediate temperature I: Mechanism of void-induced duplex oxide formation,” Oxid. Met., vol. 77, no. 1–2, pp. 27–55, 2012.

[15] N. A. Shariff, A. Jalar, M. I. Sahri, and N. K. Othman, “Effect of high temperature corrosion on austenitic stainless steel grade 304 in CO_2 gas at 700^{o}C,” Sains Malaysiana, vol. 43, no. 7, pp. 1069–1075, 2014.

[16] G. Berthomé, “Surface analysis: An introduction to XPS,” Grenoble.

[17] G. Bertomé, “Réactivité physico-chimique des surfaces : Optimisation des propriétés d’usage,” Grenoble, 2014.

[18] J. Birnie, C. Craggs, D. J. Gardiner, and P. R. Graves, “Ex-situ and in-situ determination of stress distribution in chromium oxide films by Raman spectroscopy,” Corros. Sci., vol. 33, no. 1, pp. 1–12, 1992.

[19] P. Y. Hou, J. Ager, J. Mougin, and A. Galerie, “Limitations and advantages of Raman spectroscopy for the determination of oxidation stresses,” Oxid. Met., vol. 75, no. 5–6, pp. 229–245, Jan. 2011.

[20] R. L. Farrow, P. L. Mattern, S. N. Laboratories, and S. Diego, “Characterization of surface oxides by raman spectroscopy,” Appl. Phys. Lett., vol. 73, pp. 353–358, 1980.

[21] J. Mougin, T. Le Bihan, and G. Lucazeau, “High-pressure study of Cr_2O_3 obtained by high-temperature oxidation by X-ray diffraction and Raman spectroscopy,” J. Phys. Chem. Solids, vol. 62, pp. 553–563, 2001.

[22] J. C. Hamilton and R. J. Anderson, “Oxidation of Fe-18Cr-3Mo : an in-situ Raman study,” High Temp. Sci., vol. 19, pp. 307–321, 1985.

[23] D. J. Gardiner, C. J. Littleton, K. M. Thomas, and K. N. Strafford, “Distribution and characterization of high temperature air corrosion products on ironchromium alloys by Raman microscopy,” Oxid. Met., vol. 27, no. 1–2, pp. 57–72, 1987.

[24] R. L. Farrow, R. E. Benner, A. S. Nagelberg, and P. L. Mattern, “Characterization of surface oxides by Raman spectroscopy,” Thin Solid Films, vol. 73, pp. 353–358, 1980.

[25] K. Veena, V. K. Vaidyan, and P. Koshy, “Characterization of ferrochromium thin films,” J. Mater. Sci. Lett., vol. 8, pp. 80–82, 1989.

[26] D. H. Speidel and A. Muan, “The system manganes oxides-Cr_2O_3 in air,” J. Am. Ceram. Soc., vol. 46, pp. 577–578, 1963.

[27] X. Chen, P. Hou, C. Jacobson, S. Visco, and L. Dejonghe, "Protective coating on stainless steel interconnect for SOFCs: oxidation kinetics and electrical properties," Solid State Ionics, vol. 176, no. 5–6, pp. 425–433, Feb. 2005.

[28] M. Stanislowski, E. Wessel, K. Hilpert, T. Markus, and L. Singheiser, "Chromium vaporization from high-temperature alloys," J. Electrochem. Soc., vol. 154, no. 4, p. A295, 2007.

[29] Y. Madi, E. Salhi, F. Charlot, A. Galerie, and Y. Wouters, "Influence of polishing-induced surface hardening on the adhesion of oxide scales grown on a ferritic stainless steel," Oxid. Met., vol. 75, no. 3–4, pp. 167–181, Dec. 2010.

[30] B. X. Huang, K. Wang, J. S. Church, and Y.-S. Li, "Characterization of oxides on niobium by raman and infrared spectroscopy," Electrochim. Acta, vol. 44, no. 15, pp. 2571–2577, 1999.

[31] J. Ding, P. G. McCormick, and R. Street, "Formation of spinel Mn-ferrite during mechanical alloying," J. Magn. Magn. Mater., vol. 171, no. 3, pp. 309–314, 1997.

Chapter 8

Cr volatilisation reduction by preoxidising AISI 441 in CO/CO_2

The objective of this chapter is the same as in Chapter 7 that is to suppress Cr species volatilisation from AISI 441 specimen. Bare 441 specimen was also preoxidised in the similar preoxidising temperatures and period as in the previous chapter, but the atmosphere was different. In this section, Bare 441 was preoxidised in mixed-CO/CO_2 atmosphere, to study the effect of the low oxygen potential which is known to change the chromia semiconducting properties. But also, in C-containing atmospheres, carburisation usually occurs during process. Metal carbides are formed in the inner oxide layer at the metal surface [1]–[3]. According to the morphology transformation, it possibly affects Cr species volatilisation. Hence, the effect of chemistry and morphology change of Bare 441 by preoxidising in CO/CO_2 atmosphere on Cr species volatilisation was studied and compared with Cr species volatilisation of Bare 441, P.Ar-250 and P.Ar-850.

8.1 Cr volatilisation results

Figure 8.1 shows Cr species volatilisation from Bare 441, P.CO/CO_2-250 and P.CO/CO_2-850 as a function of the gas linear velocity. It can be seen that Cr volatilisation rates from specimens preoxidised in CO/CO_2 at both temperatures were lower than that of Bare 441 in this experimental range. At low linear velocity, in the range of 1-4 cm/s, Cr species volatilsations in this linear velocity range in both conditions seem constant at about 2.5×10^{-11} g/cm^2s which was lower than Cr species volatilisation from Bare 441 for about 6-8 times. At 10 cm/s linear velocity of gas, Cr volatilisation rates from P.CO/CO_2-250 and P.CO/CO_2-850 increased. Comparing with Cr depletion rates which were vaporised in lower gas linear velocities, Cr species volatilisations from P.CO/CO_2-250 and P. CO/CO_2-850 were higher for about 3 and 6 times respectively. However, Cr volatilisation rates of P.CO/CO_2-250 and P.CO/CO_2-850 at 10 cm/s were still lower than that of Bare 441 for around 1.3 and 2.7 times respectively. Furthermore, the oxides formed on the P.CO/CO_2-250 and P.CO/CO_2-850 surfaces were well adherent. No spallation was observed as shown in Figure 8.2.

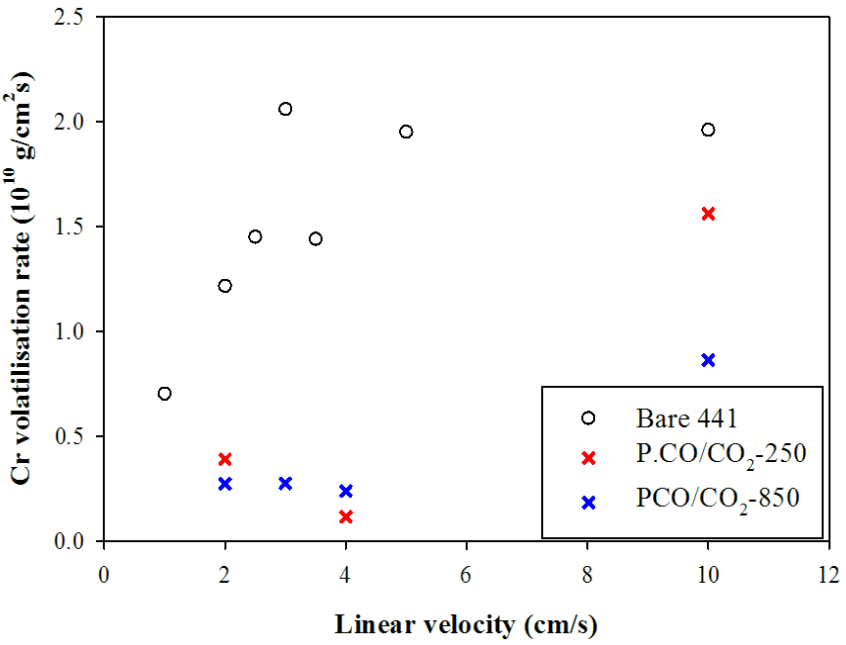

Figure 8.1 Cr volatilisation rates from Bare 441, P.CO/CO_2-250 and P.CO/CO_2-850 as a function of gas linear velocity (5%H_2O in O_2, 800°C, 96 h).

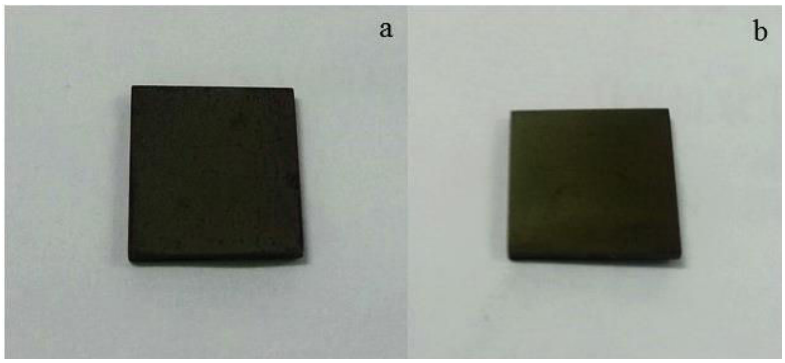

Figure 8.2 a). P.CO/CO_2-250+ox.10 and b). P.CO/CO_2-850+ox.10.

Considering Cr volatilisation rates from all specimens in Figure 8.3, it was clear that P.Ar-850 was the worst specimen which was not able to suppress Cr species volatilisation. For other preoxidised specimens, Cr species volatilisations from these specimens in the gas linear velocity range of 1-4 cm/s seem to be constant and were well reduced by about 6-8 times. At 10 cm/s of gas linear velocity, Cr volatilisation rates from preoxidised specimens increased, but Cr species volatilisation from the ones preoxidised in CO/CO_2 were still lower than that of Bare 441. The difference between specimens preoxidised in Ar and CO/CO_2 after vaporising in 10 cm/s of 5%H_2O in O_2 was the spallation of oxides on P.Ar-250+ox.10 and P.Ar-850+ox.10 while the oxides formed on P.CO/CO_2-250+ox.10 and P.CO/CO_2-850+ox.10 did not spall. This probably implies that the failure of Cr species volatilisation reduction from P.Ar-250+ox.10 and P.Ar-850+ox.10 was probably caused by the spallation of oxide layer leading to the reduction of protective performance of specimens [2]–[5]. On the contrary, the

oxides formed on P.CO/CO_2-250+ox.10 and P.CO/CO_2-850+ox.10 did not spall. Thus, the protective layers on these specimens were an obstruction decelerating volatilisation reaction.

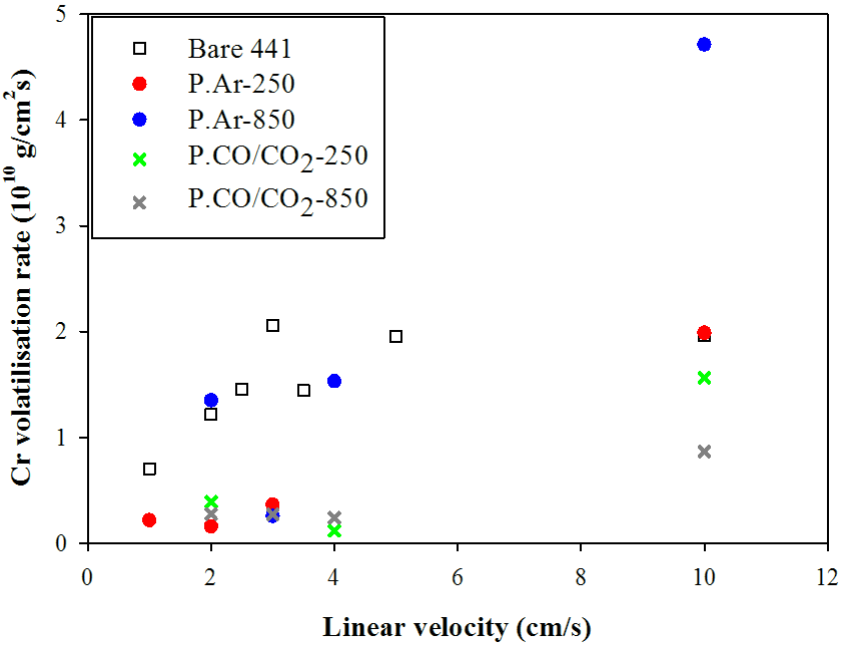

Figure 8.3 Cr volatilisation rates from all specimens (Bare 441, P.Ar-250, P.Ar-850, P.CO/CO_2-250 and P. CO/CO_2-850) as a function of gas linear velocity (5%H_2O in O_2, 800°C, 96 h).

8.2 Surface observation

8.2.1 The specimen preoxidised in CO/CO_2 at 250°C

8.2.1.1 Before high temperature oxidation

Figure 8.4 shows SEM image of P.CO/CO_2-250. Alike P.Ar-250, the oxide formed on P.CO/CO_2-250 during preoxidation was very thin. Thus, with a large interaction volume of SEM, the surrounding extremely disturbed the oxide analysis. No crystalline structure could be observed in this image. Only scratches resulting from the polishing steps can be seen. In order to find the phases formed on this surface without any disturbance, only XPS and Raman spectroscopy were used.

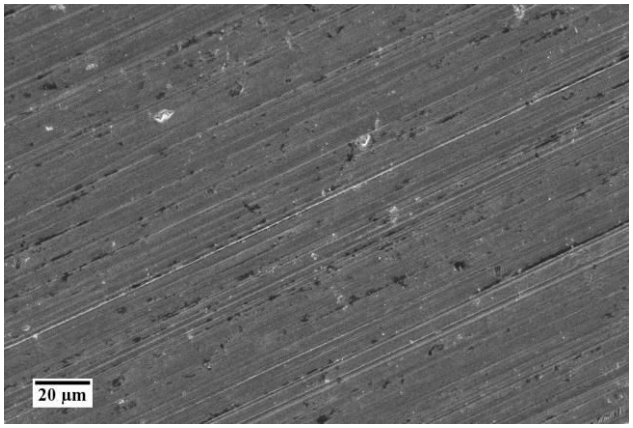

Figure 8.4 SEM image in SE mode of P.CO/CO_2-250.

Figure 8.5 shows XPS spectrum of P.CO/CO_2-250. From this spectrum, it was demonstrated that only Fe and trace of Si were observed. After expanding the binding energy in the range of 700-740 eV, it can be seen that Fe detected by XPS at the top 10 nm was the oxide of Fe. No Fe from the substrate can be observed as seen in Figure 8.6. This result was the similar to XPS results of P.Ar-250 which only oxide of Fe and trace of Si can be detected and the thickness of oxides formed on both specimens were not thinner than 10 nm. Our XPS results ensured the work of Berthomé [6] that preoxidation at low temperature around 250°C promoted Fe oxidation as Cr and minor elements of the steel were not able to diffuse to the top surface due to too low temperature. The preoxidation atmospheres seem to have no effect on the element diffusion. This hypothesis would be proved again in the part of XPS characterisation of P.CO/CO_2-850.

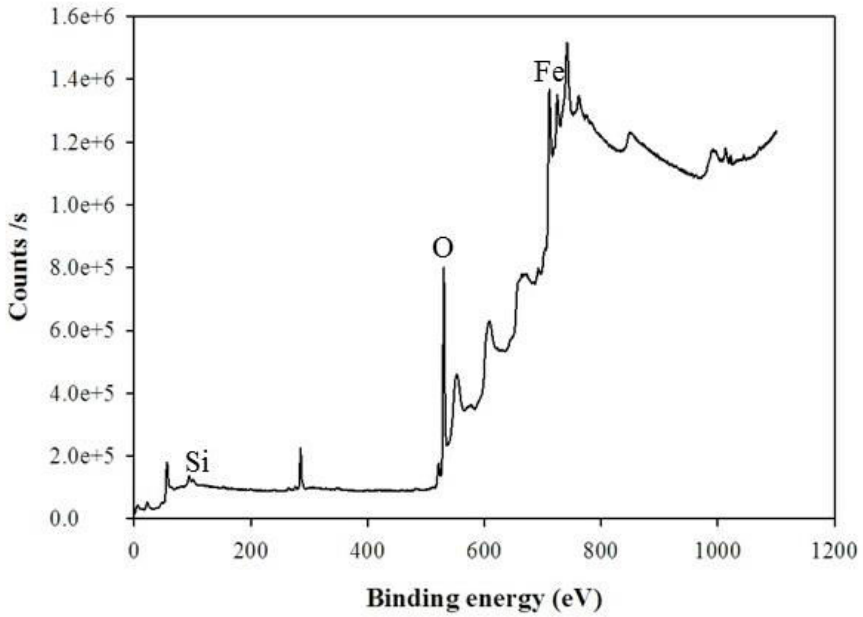

Figure 8.5 XPS spectrum of P.CO/CO_2-250.

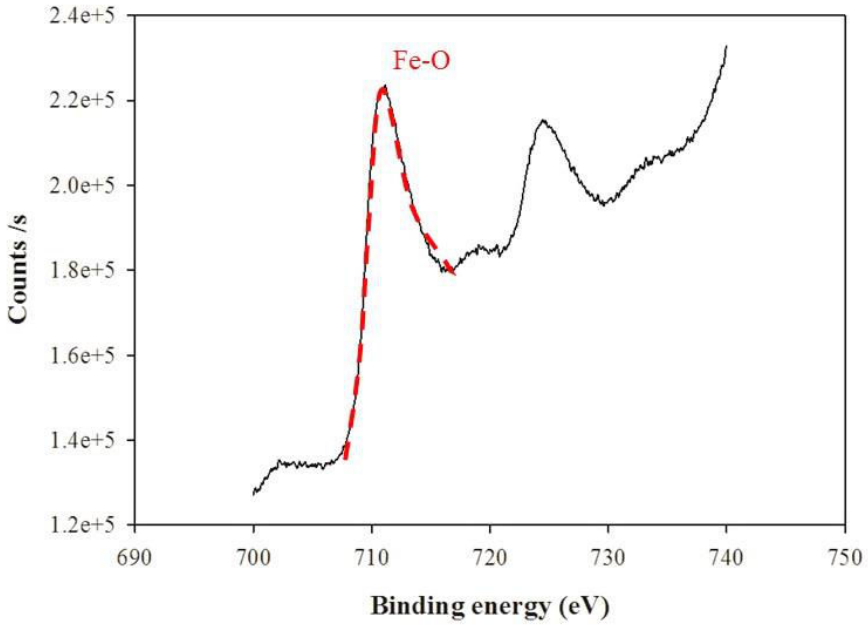

Figure 8.6 Fe spectrum observed on P.CO/CO_2-250 by XPS.

Phase identification of P.CO/CO_2-250 was achieved by using Raman spectroscopy as shown in Figure 8.7. In this figure, it was obviously seen that all bands in this graph well matched with the presence of Fe_3O_4 [7]. This was different with the phase formed on P.Ar-250 which was Fe_2O_3. However, these phases on both specimens were in good agreement with the results specified from Ellingham/Richardson diagram in Figure 7.8. In the conditions containing P_{O_2} of 2×10^{-6} bar (P.Ar-250) and 4.56×10^{-48} bar (P.CO/CO_2-250), the stable phases formed on both specimens were Fe_2O_3 and Fe_3O_4 respectively. Kofstad [3] and Shariff et al. [8] explained that, at the beginning, metallic Fe of the top surface first reacted with adsorbed O on the surface. FeO formed due to the reducing character of the metal and was further oxidised by O_2, giving Fe_3O_4, the stable product in contact with the gas. In case of higher P_{O_2}, Fe_3O_4 would be continuously oxidised and would form Fe_2O_3. The reactions are shown in Eqs. 8.1-8.3 [8]. In our case, P_{O_2} in CO/CO_2 at 250°C was too low to oxidise Fe_3O_4 while P_{O_2} in Ar at 250°C was enough to form Fe_2O_3, so the oxide phases of Fe formed on both specimens were different. Nevertheless, different Fe oxide phases did not affect Cr species volatilisation especially at low linear velocity of wet O_2. Cr species volatilisations from P.CO/CO_2-250 and P.Ar-250 were very similar when the gas velocity was not above 4 cm/s. That means Fe_xO_y could be a diffusion barrier of Cr and/or O preventing Cr species volatilisation. However, the global oxidation kinetics should be further studied because Sabioni et al. [9] reported that the presence of Fe-O external layer led to the increasing of oxidation rate. Furthermore, spallation of oxide scale occurred on P.Ar-250 at gas linear velocity of 10 cm/s leading to poorer protective performance of the specimen. On the contrary, at 10 cm/s of gas linear velocity, no spallation was observed on P.CO/CO_2-250. Shariff et al. [8] confirmed that the scale formed on specimen after oxidation in CO_2 was dense. Thus, the protective scale

may still remain. On the contrary, the oxides formed on P.Ar-250 and P.Ar-850 were not well compact leading to oxide spallation after high temperature oxidation in high gas velocity. This was the possible reason why P.CO/CO_2-250 had a better performance than P.Ar-250 at 10 cm/s of gas linear velocity.

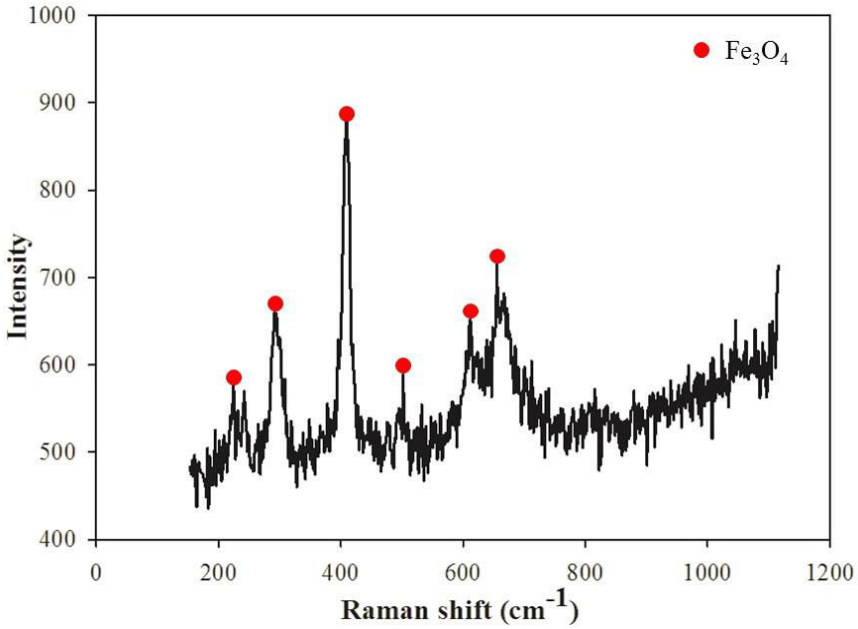

Figure 8.7 Raman spectrum of P.CO/CO_2-250.

$$2Fe + O_2 \rightarrow 2FeO \quad \text{(Eq. 8.1)}$$

$$6FeO + O_2 \rightarrow 2Fe_3O_4 \quad \text{(Eq. 8.2)}$$

$$4Fe_3O_4 + O_2 \rightarrow 6Fe_2O \quad \text{(Eq. 8.3)}$$

8.2.1.2 After high temperature oxidation

Figure 8.8 shows SEM images of P.CO/CO_2-250+ox.4 in SE mode. The Ti and Ti-Nb nodules as well as thick chromia areas were observed on the surface like P.Ar-850 and P.Ar-850+ox.4. Dissimilarly, the metallic grain boundaries cannot be seen on P.CO/CO_2-250+ox.4 surface. Furthermore, the crystalline structure observed on this specimen surface was rougher than that of P.Ar-850+ox.4. The scratches occurring from the polishing steps were obviously seen. It possibly means that the oxide was very thin and may not well cover on the specimen surface due to low oxidation rate. The matrix of this specimen was the same as other specimens after high temperature oxidation. It consisted of Cr, Fe, Mn, Ti, Nb, Si, O and C.

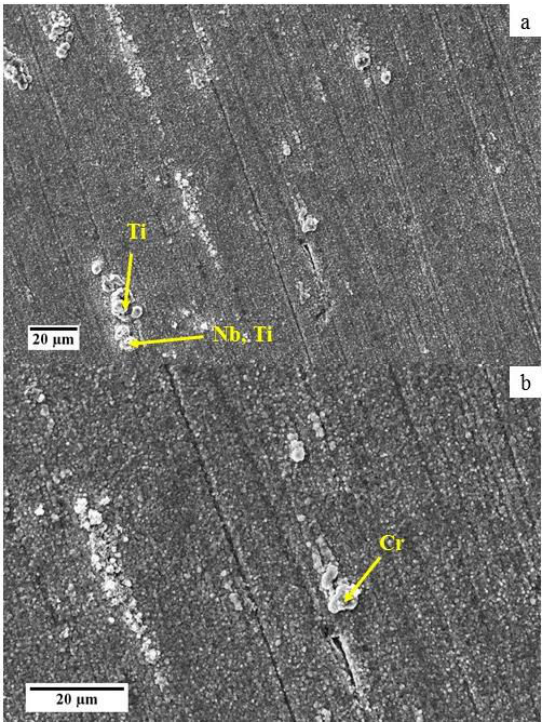

Figure 8.8 SEM images in SE mode of P.CO/CO_2-250+ox.4. a). and b). show the different locations and their magnifications were 500x and 1000x respectively.

Raman spectroscopy was also used to characterise the top surface with a penetration depth less than that of SEM. Raman spectrum of P.CO/CO_2-250+ox.4 is shown in Figure 8.9. It can be seen that chromia [7], [10]–[15] and unspecifiable type of spinel can be found. Since Raman is a randomly point analysis tool, there is a possibility that the specific point like nodule would not be detected. Like in this case, no Ti and Ti-Nb nodules were detected by Raman meanwhile SEM can observe them. Reminding again that the interaction volume of SEM is large, so Ti and Nb detected by SEM were probably located in the substrate in terms of Ti-internal oxidation and Laves phase (Fe_2Nb). Therefore, in order to ensure the nodule phase(s) and identify spinel composition, XRD was used.

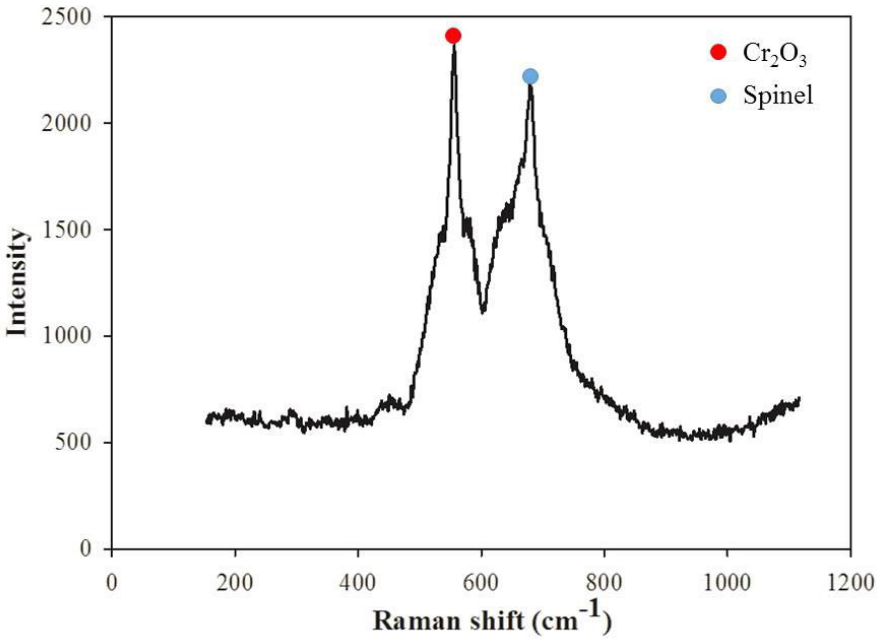

Figure 8.9 Raman spectrum of P.CO/CO_2-250+ox.4.

The results of XRD characterised on P.CO/CO_2-250+ox.4 is shown in Figure 8.10. Ferrite phase was still the main component on this specimen due to large interaction volume. The spinel phase detected by Raman was confirmed and identified as Mn-Cr spinel. Chromia was also detected with an insertion of Fe which was the same as the specimens oxidised and/or preoxidised at high temperature. TiO_2 and Ti-Nb presented at the position of the nodules shown in SEM images could not be found by XRD. It is possible that the intensity of TiO_2 and Ti-Nb structure was very low, so it cannot be distinguished from the XRD base line.

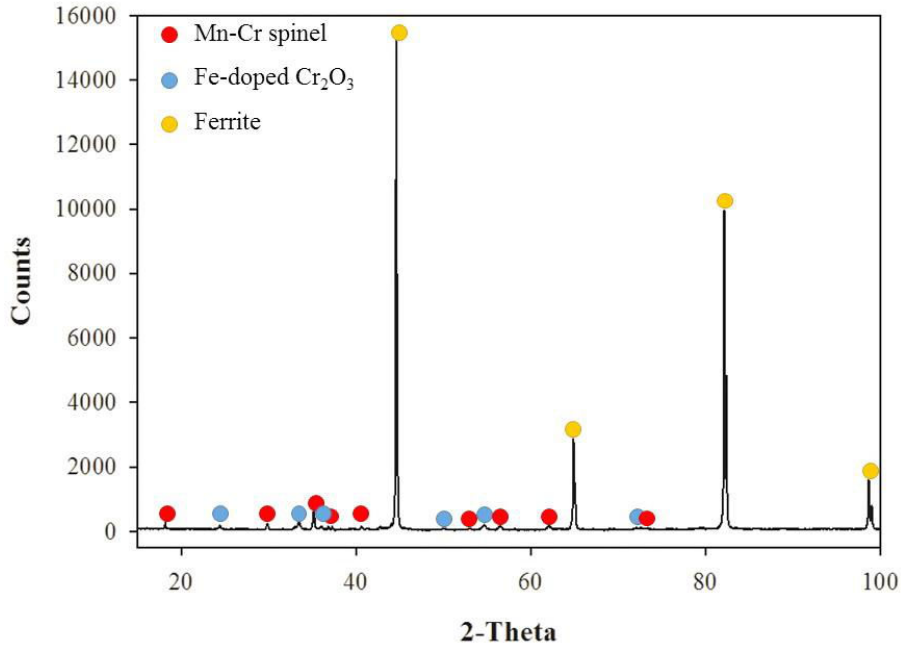

Figure 8.10 XRD pattern of P.CO/CO_2-250+ox.4.

8.2.2 The specimen preoxidised in CO/CO_2 at 850°C

8.2.2.1 Before high temperature oxidation

Figure 8.11 shows Cr/Fe, Mn/Cr, Ti/(Mn+Cr) and Fe/(Fe+Cr) ratios of Bare 441, P.Ar-250, P.Ar-850, P.CO/CO_2-250 and P.CO/CO_2-850 obtained by XPS. From this graph, it confirmed our hypothesis in the previous section that preoxidation temperatures affected the element diffusion while preoxidation atmospheres did not affect. At 250°C, only Fe was present on the top surface while Cr was exposed on the top at 850°C.

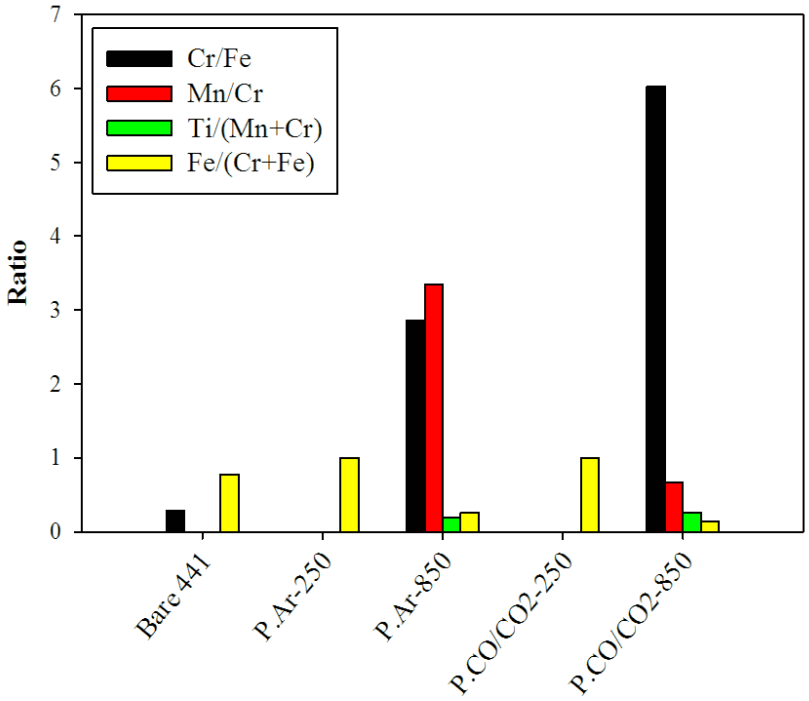

Figure 8.11 Element ratios of all specimens (Bare 441, P.Ar-250, P.Ar-850, P.CO/CO_2-250 and P.CO/CO_2-850) obtained by XPS.

SEM image of P.CO/CO_2-850 is shown in Figure 8.12. The metallic grain boundaries were not observed on this specimen. The scratches resulting from the polishing steps can be observed like the other preoxidised specimens before high temperature oxidation. The matrix scale and nodules were observed. These nodules were composed of Ti and Nb while the matrix scale consisted of Fe, Cr, Mn, Ti, Nb, Si and O.

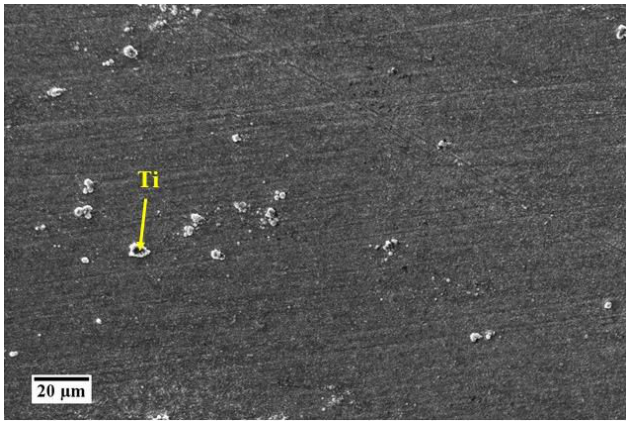

Figure 8.12 SEM image in SE mode of P.CO/CO_2-850.

Raman spectroscopy was used to analyse phases on the surface and the results are shown in Figure 8.13. Three phases were found: Cr_2O_3 [7], [10]–[15], TiO_2 [7] and unspecifiable spinel. It can be seen that the phases formed on P.CO/CO_2-850 (Cr_2O_3, TiO_2 and spinel) and P.Ar-850 (Cr_2O_3, Nb_2O_5 and Mn-Fe spinel) were similar. However, their performances suppressing Cr species volatilisation were extremely different. Considering Cr species volatilisation from all specimens, P.CO/CO_2-850 was the best one which was able to reduce Cr volatilisation even in high gas velocity condition, on the contrary, P.Ar-850 was the worst which was not only cannot certainly suppress Cr species volatilisation in all experimental conditions but also promoted Cr species volatilisation in high gas velocity. TiO_2 and Nb_2O_5 did probably not participate in the Cr species volatilisation reaction. The traces of them existing in terms of the nodules could not reduce an activity of Cr on the surface like Mn-Cr spinel. Thus, the difference of Cr species volatilisation suppression ability of both specimens should be caused by the spinel. Before discussing in details, XRD was used to identify the phase of spinel formed on P.CO/CO_2-850. The result is shown in Figure 8.14.

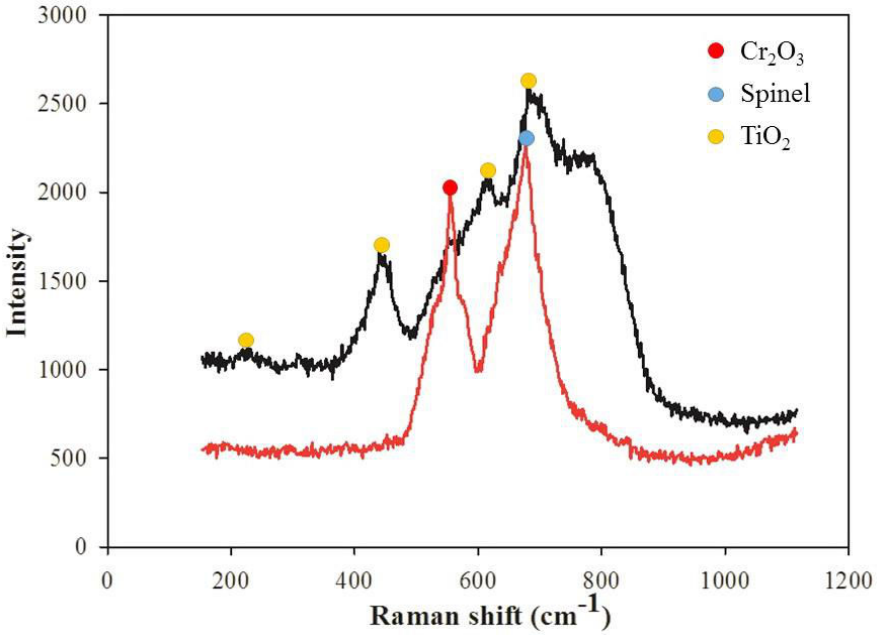

Figure 8.13 Raman spectra of P.CO/CO_2-850 when the laser focused on the matrix scale (red line) and the nodule (black line).

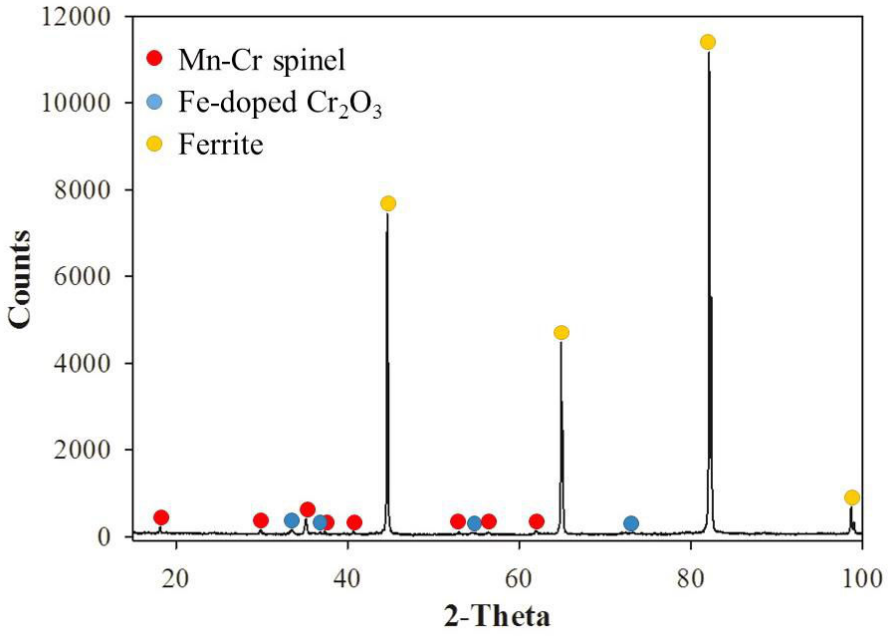

Figure 8.14 XRD pattern of P.CO/CO_2-850.

XRD confirmed the results of Raman that chromia and spinel were formed on the specimen. Chromia formed on this specimen also contained Fe in the structure while the spinel detected by Raman was Mn-Cr. These formations of chromia and spinel are corresponding with the works of Fujii et al. [16] and Giggins et al. [17]. Furthermore, Promdirek et al. [18] studied oxidation of AISI 441 in pure CO_2 at high temperature which was very close to the present work. Their results are also in good agreement with ours. They found the formation of chromia, Mn-Cr spinel and dispersion of TiO_2. It is very well known that Mn-Cr spinel was a potential spinel which is able to suppress Cr species volatilisation by reducing Cr activity on the surface [19]. However, Mn-Cr spinel was also formed on Bare 441, but the formation of Mn-Cr spinel on P.CO/CO_2-850 led to lower Cr volatilisation rate. It was possible that this spinel formed on P.CO/CO_2-850 was much thicker than Bare 441, so Cr and/or O must diffused in longer path comparing with that of the diffusion path on Bare 441 resulting in the decelerations of diffusion and Cr volatilisation rate from P.CO/CO_2-850.

Continuing discussion about P.Ar-850 compared with P.CO/CO_2-850, as mentioned above, the Cr species volatilisation suppression abilities of these specimens were possibly affected by the spinel. It was very clear that Mn-Cr spinel protected Cr depletion from P.CO/CO_2-850. For P.Ar-850, there was no Mn-Cr spinel shield like P.CO/CO_2-850. On the contrary, Mn-Fe spinel covering on P.Ar-850 surface may not be a protective layer. It was possible that Mn-Fe spinel formed on P.Ar-850 did not well cover the surface and/or was probably too thin to obstruct the diffusion of Cr and/or O. Hence, P.Ar-850 was not a good candidate used as metallic interconnect of SOFC.

8.2.2.2 After high temperature

Figure 8.15 shows SEM images of P.CO/CO_2-850+ox.4 in SE mode. It can be seen that the crystalline features on the matrix surface were finer than for the scale grown on P.CO/CO_2-250+ox.4 and Bare 441 after high temperature oxidation [20]. However, it was already proved in Chapter 4 that the surface roughness did not affect Cr species volatilisation. Thus, the difference of Cr species volatilisations from both specimens was more possibly caused by their oxide nature and morphology. The nodules were randomly distributed on the surface. Some of them were composed of Ti while others contained Ti and Nb. Cr, Mn and Fe were everywhere even in the nodule that may be due to the large interaction volume of SEM. Another interesting thing obtained by SEM was white lines on the surface. Their appearances were similar to the hexagonal shape of metallic grain boundaries as shown in a red hexagon in Figure 8.15b. They were different from the metallic grain boundaries observed on P.Ar-850 and P.Ar-850+ox.4 where the metallic grain boundaries can be seen as locations of the nodules (the nodules usually located above the metallic grain boundaries). In the case of P.CO/CO_2-850+ox.4, the metallic grain boundaries were observed as white extrusion lines (possibly due to charging effects). In order to analyse the component of these lines, the analysis mode must be switched from SE to BSE mode. The SEM images of the same location as in Figure 8.15a in SE and BSE mode are shown in Figure 8.16a and 8.16b respectively. In BSE mode which the levels of grey are influent by the atomic number of the elements, the metallic grain boundaries lines can hardly be observed. This was the obstacle to know the component(s) of these extrusions. However, their levels of grey were similar to that of the matrix scale, so it was possible to be composed of chromia and spinel like in the matrix. Nevertheless, there was still an unclear question about the high temperature oxidation mechanisms. It can be seen that, after preoxidation, the oxides growth aligned along the polishing lines. After that, during high temperature oxidation, the oxide growth was completely changed. It became growing along the metallic grain boundaries. Thus, the factor(s) changing the behaviour of oxide growth should be investigated in further work.

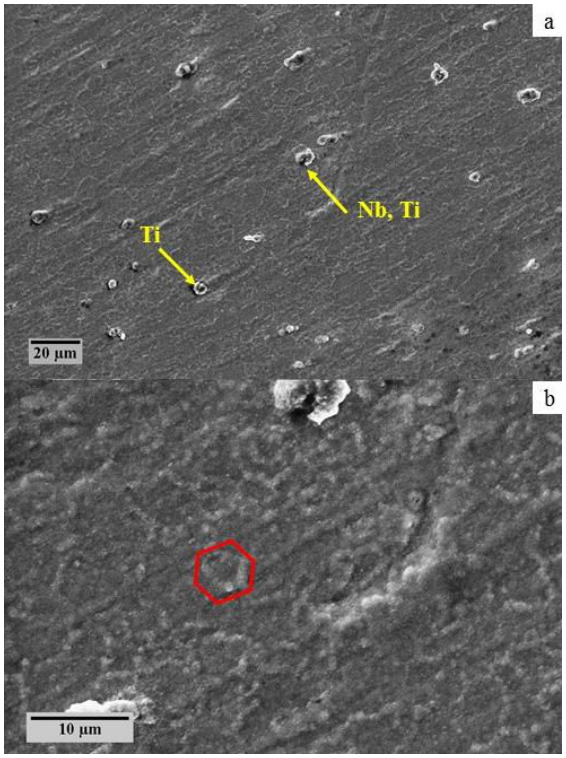

Figure 8.15 SEM images in SE mode of P.CO/CO_2-850+ox.4 when the magnifications were a). 500x and b). 2000x.

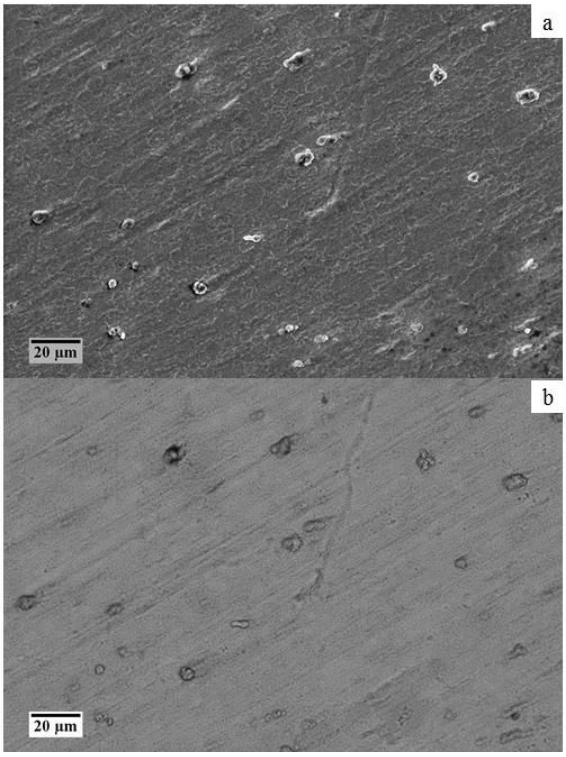

Figure 8.16 SEM images of P.CO/CO_2-850+ox.4 at the same location in a). SE and b). BSE modes.

Raman spectroscopy was used to randomly analyse 10 points on P.CO/CO_2-850+ox.4 surface. The result is shown in Figure 8.17. All spectra detected only the existence of chromia and unspecifiable spinel phase. The nodules were also not detected like in the case of P.CO/CO_2-250+ox.4. However, one more characterisation tool was used to observe the overall surface that was XRD. The XRD result of P.CO/CO_2-850+ox.4 is shown in Figure 8.18.

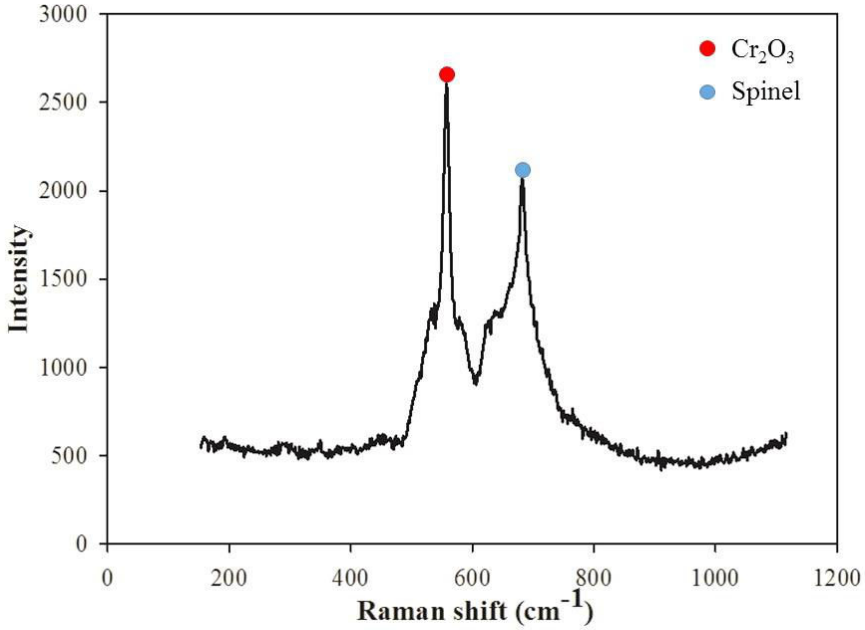

Figure 8.17 Raman spectrum of P.CO/CO_2-850+ox.4.

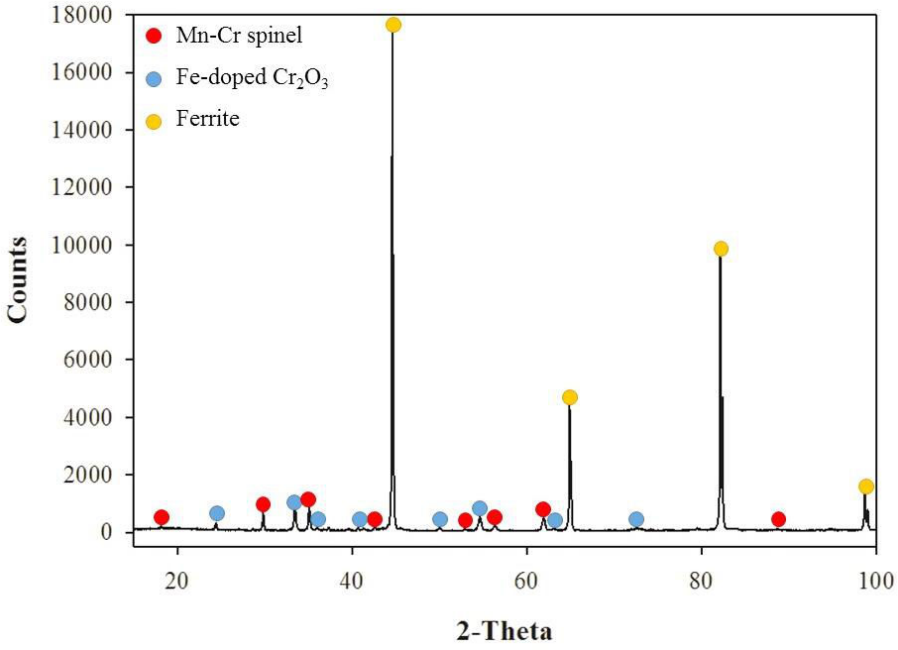

Figure 8.18 XRD pattern of P.CO/CO_2-850+ox.4.

XRD result in Figure 8.18 presents 3 phases detected: ferrite, Mn-Cr spinel and Fe-doped Cr_2O_3. Comparing with the XRD results of P.CO/CO_2-850, it can be seen that the phases on both specimens were exactly the same. There was no phase transformation or change during high temperature oxidation.

Taking into account the phases formed on all specimens after high temperature oxidation, it can be demonstrated that they were the same. Even though the oxides formed during each preoxidation condition were different, the major oxides after high temperature oxidation were the same that were composed of Fe-doped chromia and Mn-Cr spinel. This implies that the Cr species volatilisation mechanism was not change even the reaction was promoted on the different surfaces. That means these oxides or some change attained from preoxidation process did not participate in the Cr species volatilisation reaction. They just decelerated the diffusion of Cr/O resulting in lowering Cr volatilisation rate.

8.3 Discussion and conclusions

In this chapter also, Cr species volatilisation from the AISI 441 specimen was tried to be suppressed by smart preoxidation before high temperature oxidation. The difference with chapter 7 was the use of the equimolar CO/CO_2 mixture instead of Ar as preoxidising gas. The preoxidising conditions were the same: 250°C or 850°C for 3 h. The results show that the specimens preoxidised in CO/CO_2 at both temperatures were able to suppress Cr species volatilisation even in high linear velocity of gas, which was not the case when using argon. No spallation was observed. XPS confirmed that preoxidising temperatures affected the diffusion of elements. Fe and Cr were promoted on the top surface at 250°C and 850°C, respectively, in both atmospheres.

For specimens preoxidised at 250°C, a very low temperature, iron oxide only was formed according to the prevalence of surface reaction kinetics against chemical thermodynamics which needs high temperatures to reach equilibrium. This layer acts as a diffusion barrier between the Cr-containing steel and the oxidising atmosphere, leading to strong reduction of Cr species volatilisation reaction.

For P.CO/CO_2-850, which presents the best results in terms of Cr species volatilisation reduction, the formed products are chromia and Mn-Cr spinel, a situation which is not chemically different from that observed during normal oxidation procedures. Therefore, understanding the reason of the volatilisation reduction must envisage a new idea: the influence of the defect structure of chromia on the oxido-reduction reactions producing Cr(VI) volatile species (for this discussion, the presence of Mn-Cr spinel is not taken into account). In the equimolar CO/CO_2 atmosphere at 850°C, the oxygen pressure lies near 10^{-10} atm, inducing a change in the chromia conduction type, from a n-p double layer in pure oxygen, with Cr interstitials and vacancies [21] to an only n single layer with Cr interstitials. As mentioned above, Promdirek et al. [18] clearly showed by photoelectrochemistry pure n-type conduction of CO_2-grown chromia, whereas chromia grown in oxygen or air exhibits insulator-type photoelectrochemical curves, with both p and n contributions [22]. The electronic properties of the oxide surface in contact with the gas therefore changes from n to p when CO/CO_2 is used

as preoxidising agent. The influence of this modification is now discussed in terms of kinetic mechanisms.

When Cr_2O_3 is n-type semiconductor, the possible point defects are Cr interstitials and O vacancies. The literature does not afford any evidence for the predominance of one or the other of these species, but it is indisputable that such chromia contains oxygen vacancies (major or minor point defect) whereas p-type chromia do not. Such O vacancies are well known to be possible sites for OH^-, due to small charge and size of these ions [23].

Considering the two possible equations for chromia volatilisation:

$$Cr_2O_3 + 3/2\ (O_2) \rightarrow 2\ CrO_3$$

$$Cr_2O_3 + 3/2\ (O_2) + 2\ H_2O \rightarrow 2\ CrO_2(OH)_2$$

It is observed thermodynamically that the largely predominant gaseous species at 800°C in O_2-5% H_2O atmosphere is Cr oxyhydroxide, $CrO_2(OH)_2$. So, any modification of chromia changing the surface concentration of H_2O or adsorbed OH species will influence the kinetics of volatilisation. This change is depicted in Figure 8.19, where it is shown that OH groups adsorbed on the surface of p-type chromia are used for the synthesis of $CrO_2(OH)_2$ only. On the contrary, OH groups adsorbed on n-type chromia are partly consumed by dissolution into the oxide, diffusion to the metal-oxide interface and internal formation of chromia. Their surface concentration is low and Cr species volatilisation is therefore slower compared to a p-type surface.

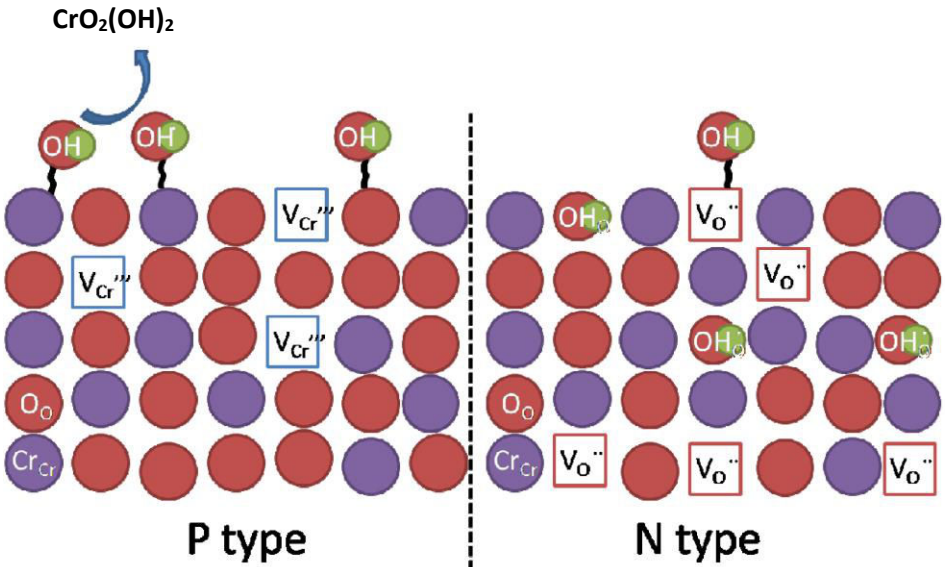

Figure 8.19 Effect of chromia semiconducting properties on the volatilisation kinetics of chromium oxyhydroxide, $CrO_2(OH)_2$.

References

[1] X. G. Zheng and D. J. Young, "High-temperature corrosion of Cr_2O_3-forming alloys in CO-CO2-N2 atmospheres," Oxid. Met., vol. 42, no. 3–4, pp. 163–190, 1994.

[2] D. J. Young, High temperature oxidation and corrosion of metals, 1st ed. Elsevier, Oxford UK/Amsterdam NL, 2008.

[3] P. Kofstad, High temperature corrosion. Elsevier Applied Science, London/New York, 1988.

[4] P. Sarrazin, A. Galerie, and J. Fouletier, Mechanisms of high temperature corrosion: A kinetic approch. 2008.

[5] C. A. Barrett and C. E. Lowell, "Comparison of isothermal and cyclic oxidation behavior of twenty-five commercial sheet alloys at 1150 °C," Oxid. Met., vol. 9, no. 4, pp. 307–355, 1975.

[6] G. Bertomé, "Réactivité physico-chimique des surfaces : Optimisation des propriétés d'usage," Master lecture, Grenoble, 2014.

[7] J. Mougin, "Tenue mécanique de couches d'oxyde thermiques générées sur le chrome et sur quelques aciers inoxydables ferritiques: Étude des contraintes et de d'adhérence," Institue National Polytechnique de Grenoble, Ph.D. Thesis, 2001, in French.

[8] N. A. Shariff, A. Jalar, M. I. Sahri, and N. K. Othman, "Effect of High Temperature Corrosion on Austenitic Stainless Steel Grade 304 in CO_2 Gas at 700ºC," Sains Malaysiana, vol. 43, no. 7, pp. 1069–1075, 2014.

[9] A. C. S. Sabioni, A. Huntz, E. Conceição da Luz, M. Mantel, and C. Haut, "Comparative study of high temperature oxidation behaviour in AISI 304 and AISI 439 stainless steels," Mater. Res., vol. 6, no. 2, pp. 179–185, 2003.

[10] J. Birnie, C. Craggs, D. J. Gardiner, and P. R. Graves, "Ex-situ and in-situ determination of stress distribution in chromium oxide films by Raman spectroscopy," Corros. Sci., vol. 33, no. 1, pp. 1–12, 1992.

[11] B. D. Hosterman, "Raman spectroscopic study of solid solution spinel oxides," University of Nevada, Ph.D. Thesis, 2011.

[12] P. Y. Hou, J. Ager, J. Mougin, and A. Galerie, "Limitations and advantages of Raman spectroscopy for the determination of oxidation stresses," Oxid. Met., vol. 75, pp. 229–245, 2011.

[13] R. L. Farrow, R. E. Benner, A. S. Nagelberg, and P. L. Mattern, "Characterization of surface oxides by raman spectroscopy," Appl. Phys. Lett., vol. 73, pp. 353–358, 1980.

[14] J. Mougin, T. Le Bihan, and G. Lucazeau, "High-pressure study of Cr2O3 obtained by high-temperature oxidation by X-ray diffraction and Raman spectroscopy," J. Phys. Chem. Solids, vol. 62, pp. 553–563, 2001.

[15] D. Renusch, B. Veal, K. Natesan, and M. Grimsditch, “Transient oxidation in Fe-Cr-Ni alloys : a Raman-scattering study,” Oxid. Met., vol. 46, no. 5–6, pp. 365–381, 1996.

[16] C. T. Fujii and R. A. Meussner, “Carburization of Fe-Cr alloys during oxidation in dry carbon dioxide,” J. Electrochem. Soc., vol. 114, no. 5, pp. 435–442, 1967.

[17] C. S. Giggins and F. S. Pettit, “Corrosion of metals and alloys in mixed gas environments at elevated temperatures,” Oxid. Met., vol. 14, no. 5, pp. 363–413, 1980.

[18] P. Promdirek, G. Lothongkum, S. Chandra-Ambhorn, Y. Wouters, and A. Galerie, “Oxidation kinetics of AISI 441 ferritic stainless steel at high temperatures in CO2 atmosphere,” Oxid. Met., vol. 81, no. 3–4, pp. 315–329, 2014.

[19] M. Stanislowski, E. Wessel, K. Hilpert, T. Markus, and L. Singheiser, “Chromium vaporization from high-temperature alloys: I. Chromia-forming steels and the influence of outer oxide layers,” J. Electrochem. Soc., vol. 154, no. 4, p. A295, 2007.

[20] D. J. Young, T. D. Nguyen, and J. Zhang, “Corrosion of chromia formers by hot CO2 gas: A review,” Conference Proceeding, International Symposium on High-Temperature Oxidation and Corrosion, 2014.

[21] S. Henry, J. Mougin, Y. Wouters, J.-P. Petit, and A. Galerie, “Characterization of chromia scales grown on pure chromium in different oxidizing atmospheres”, Mater. High Temp., vol. 17m no. 2, pp. 231-234, 2000.

[22] A. Galerie, J.-P. Petit, Y. Wouters, J. Mougin, A. Srisrual, and P.Y. Hou, “Water Vapour Effects on the Oxidation of Chromia-Forming Alloys”, Mater. Sci. Forum, vol. 6962011, pp. 200-205, 2011.

[23] A. Galerie, Y. Wouters, and M. Caillet, “The kinetic behaviour of metals in water vapour: can general rules be proposed?”, Mater. Sci. Forum, vol. 369-372, pp. 231-238, 2001.

Chapter 9

General conclusions and perspectives

9.1 General conclusions

According to all results reported in the preceding chapters, the conclusions can be divided into 4 parts.

9.1.1 Cr volatilisation from Bare 441

In the condition of 5%H_2O in O_2 at 800°C, the phenomena of Cr species volatilisation can be categorised into 2 sections against the gas linear velocity. In the linear velocity range of 1-3 cm/s, Cr species volatilisation depended on the gas linear velocity while it was independent when the gas linear velocity was in the range of 3-10 cm/s. This can be explained by the boundary layer thickness of the gas surrounding the specimen. The boundary layer thickness is reverse proportional with the gas linear velocity. When the gas linear velocity increased, the boundary layer thickness decreased leading to faster diffusion of Cr volatile species from the specimen surface. The minimum gas velocity that the diffusion rate was higher than reaction rate was about 3 cm/s. For higher velocities, volatilisation was limited by surface reaction. The global kinetics was also demonstrated. The kinetic rate constant was measured to be $(2.7 \pm 0.5) \times 10^{-9}$ $(g \cdot cm^{-2} \cdot s^{-1})^{3.5}$ (n = 3.5) which was much higher than the expected value suitable for using as metallic interconnect of SOFC. Thus, specimen must be improved before using in that application.

The oxides formed on this specimen were chromia and Mn-Cr spinel. They were developed along the polishing lines. At the scratch positions, chromia was exposed in higher rate than that in the matrix because of the lower activation energy of nucleation at these positions.

For as-received specimen, although the surface roughness affects oxidation reaction in terms of oxide growth, it did not affect Cr species volatilisation reaction. However, the morphologies of as-received and polished 441 after high temperature oxidation were different. Ti-Nb nodules were observed on the surface of as-received 441 above the metallic grain boundaries as well as in the grain. More explanation would be described in the next section of conclusions.

9.1.2 Characterisation of nodule developed on as-received 441 surface

The nodules were classified into 2 types: GB-nodule located at the metallic grain boundaries and IG-nodule located in the metallic grain. The cross sectional images of both nodules presented complex structures. Several levels of grey were observed implying that the nodules were composed of many elements and phases. The compositions and configuration of both GB and IG nodules were very similar. They mainly contain Ti and Cr in the upper and

lower parts respectively. The lower part of the nodules connected with the oxide in the matrix scale. Ti was also at the lower edges of the nodules. Nb seemed accompany Ti. Trace of Fe was observed in IG-nodule while it was absent in GB-nodule due to the existence of Nb intermetallic and NbC along the metallic grain boundaries. These phases obstructed the diffusion of Fe to the top surface while Nb and Ti diffusions were faster than that in the grain.

Nb distributions in both nodules were achieved by 3D reconstruction using FIB-SEM and Fiji ImageJ. Nb was randomly scattered in IG nodule while its distribution was a cup-shape in GB-nodule. Also, Nb was precipitated in the substrate in form of Laves phase (Fe_2Nb), NbC and/or (Ti, Nb)(C,N). According to the thermodynamics, Laves phase can precipitate only along the metallic grain boundaries while other phases appear everywhere. Near the surface, Laves phase captured Si preventing the formation of SiO_2 continuous layer resulting in lowering the electrical resistance of the specimen.

9.1.3 Cr volatilisation from coated specimen

Cr species volatilisation from Coated 441 with Mn-Co spinel deposited by the electroplating method was tested comparing with that of Bare 441. The results show that this coating cannot suppress Cr species volatilisation from Bare 441 specimen because the coating was not a diffusion barrier, so it cannot reduce the contact between O_2 and Cr. Moreover, the coverage of the coating on 441 specimen was poor. The cracks, spallation and free-coating areas can be obviously seen on the specimen surface. These are the reasons why this coated specimen cannot applied as an interconnect of SOFC.

9.1.4 Cr volatilisation from preoxidised specimens

Before high temperature oxidation, Bare 441 was preoxidised in either Ar or CO/CO_2 at 250°C or 850°C for 3 h. Comparing with Bare 441, the surface improvement by preoxidation reaction can reduce Cr species volatilisation except the one which was preoxidised in Ar at 850°C. After preoxidising at 250°C, Fe_2O_3 and Fe_3O_4 were developed on P.Ar-250 and P.CO/CO_2-250 respectively. These Fe oxides were a diffusion barrier of Cr and/or O decelerating oxidation reaction. For P.CO/CO_2-850, protective Mn-Cr spinel was exposed and reduced the activity of Cr on the surface. Meanwhile, the diffusion rate of Cr and/or O was decelerated due to the thicker spinel formed on P.CO/CO_2-850 than Bare 441.

P.Ar-850 was the only one specimen which cannot absolutely suppress Cr volatilisation. From its surface observation, Mn-Fe spinel was observed. This spinel was probably not only be a non-protective layer preventing the oxidation reaction but also be a catalytic phase promoting higher Cr volatilisation reaction rate than that of Bare 441. In addition, Cr volatilisation rate of P.Ar-850 was higher than the diffusion rate of Cr volatile species in the gas although the oxidation was proceeded at high linear velocity of gas.

In the regard of semiconducting properties of oxides, it is known that Cr_2O_3 behaves as p-type semiconductor characterised by cation vacancies. Comparing with n-type semiconductor specified by anion vacancies, it can be seen that OH^- cannot integrate into the structure of p-type semiconductor leading to the exposure of Cr volatilisation at the surface

while it can enter to n-type semiconductor structure. Therefore, Cr volatilisation from p-type semiconductor is higher than n-type semiconductor. In the present work, it was possible that, during preoxidation, oxides formed on P.Ar-250, P.CO/CO_2-250 and P.CO/CO_2-850 were n-type semiconductor. Hence, Cr volatilisation from these specimens was lower than that of Bare 441 for which p-type semiconductor of Cr_2O_3 was promoted during oxidation. It is also possible that the surface volatilisation reaction could be slower for n-type chromia surface due to the high energy difference between the redox potential of the oxidising gas and the bottom of the conduction band.

After high temperature oxidation of all specimens, the composition of oxides formed on the surfaces were similar. Chromia and Mn-Cr spinel were developed which were the same as Bare 441. This implies that the phase and morphology changes resulting from preoxidation did not affect Cr species volatilisation mechanism. These changes just decelerated the diffusion, oxidation and Cr volatilisation rates.

9.2 Perspectives

The suggestions for further study are as the following.

1). The global kinetics of all specimens should be investigated in order to estimate their performances. This information can help to select the metallic interconnect candidate.

2). In the part of nodule development observation, longer experimental durations should be done for observing the evolution of the nodules and find the connection between the nodule developed during short time thermal oxidation and catastrophic oxidation.

3). Longer Cr volatilisation experiments should be performed. In SOFC application, the cell must work at least 40,000 h. Thus, the behaviour of metallic interconnect is important. Furthermore, other properties should be investigated i.e. mechanical properties, electrical properties and the adhesion of the oxide scale.

4). Cr volatilisation kinetics studied and properties of specimen preoxidised in other atmospheres are also interesting to demonstrate. Perhaps, the appropriate metallic interconnect may be attained.

5). Investigation of the chromia grown on AISI 441 specimen preoxidised in CO/CO_2 at 850°C for 3 h by photoelectrochemistry should be done in order to ensure the semiconducting type of oxide.

6). Cr volatilisation reaction kinetics determination should be solved by varying oxidation temperature. Compare the results with the global oxidation kinetics.

Appendices

Appendix A

Experimental conditions

Appendix A-1: Flow calculation

Appendix A-2: Humidity in O_2

Appendix A-1: Flow calculation

The schematic of the pipe in the experimental setup, Figure 4.1, is shown in Figure A-1.1.

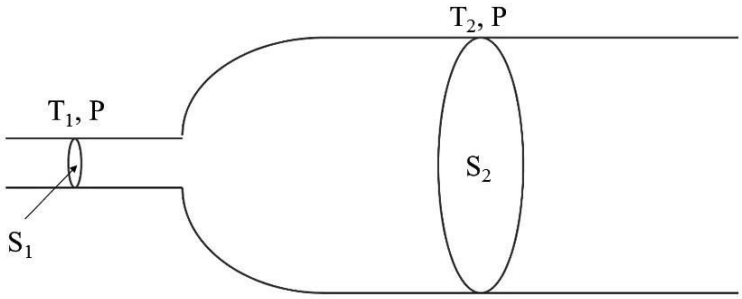

Figure A-1.1 The schematic of the pipe in the experimental setup.

where S_1 is the surface area of the position 1 where is at the location which the gas was flowed before entering to the column.

S_2 is the surface area of the column.

P is pressure that is equivalent to the atmospheric pressure.

T_1 and T_2 are the temperatures at the positions 1 and 2 respectively.

Assume ideal gas: $PV = nRT$ (Eq. A-1.1)

$PV_m = RT$ (Eq. A-1.2)

Where V and V_m are volumetric flow rate and molar volumetric flow rate of gas and R is gas constant.

At position 1, $T_1 = 20°C$:

$$V_{m_1} = \frac{RT_1}{P} = 24.4 \text{ L/mol}$$

At position 2, $T_2 = 800°C$:

$$V_{m_2} = \frac{RT_2}{P} = 89.3 \text{ L/mol}$$

From, $V_m = Sv\ dt$ (Eq. A-1.3)

So, $V_{m_1} = S_1 V_1 dt$ (Eq. A-1.4)

$V_{m_2} = S_2 V_2 dt$ (Eq. A-1.5)

Divided Eq. A-1.4 by Eq. A-1.5,

$$\frac{V_{m_1}}{V_{m_2}} = \frac{S_1 V_1}{S_2 V_2} = \frac{D_1}{S_2 V_2}$$

$\therefore$ $$\boxed{D_1 = \frac{V_{m_1}}{V_{m_2}} S_2 V_2}$$ (Eq. A-1.6)

where $S_2 = \pi r^2$ (r = the radius of tube = 1.49 cm).

Appendix A-2: Humidity in O_2

Expected water vapor percentage = 5%
Pressure (P) = 1 atm = 101.325 kPa
∴ water vapor pressure $= 0.05 \times 101.325$
$= 5.066$ kPa

From Antoine equation [1]:

$$\ln P\,(\text{kPa}) = A - \frac{B}{C + T(^{o}C)} \qquad \text{(Eq. A-1.7)}$$

For water: A = 16.3872, B = 3885.70 and C = 230.170

$$\ln(5.066) = 16.3872 - \frac{3885.70}{230.170 + T(^{o}C)}$$

$$T = 33.00\ ^{o}C$$

∴ Temperature set at humidifier is 33 °C.

Appendix B

XPS information

Appendix B-1: XPS line positions from Mg X-rays of some elements

Appendix B-2: Atomic sensibility factor (ASF) of elements

Appendix B-1: XPS line positions from Mg X-rays of some elements

Table B-1.1 XPS line positions from Mg X-rays of some elements [2].

Element	Atomic No.	Range, eV	Photoelectron lines											Range, eV	Auger lines							
			1s	2s	$2p_1$	$2p_3$	3s	$3p_1$	$3p_3$	$3d_3$	$3d_5$	4s	$4p_1$	$4p_3$		KL_1L_1	KL_1L_{23}	$KL_{23}L_{23}$	$L_3M_{23}M_{23}$	$L_2M_{23}M_{23}$	$L_3M_{23}M_{45}$ ^1P	$L_3M_{23}M_{45}$ ^3P	$L_2M_{23}M_{45}$ ^1P	$L_3M_{45}M_{45}$	$L_2M_{45}M_{45}$
Li	3		56																						
Be	4	4	113															1082							
B	5	8	191															993							
C	6	12	287															875							
N	7	9	402											12				743							
O	8	4	531	23										10	779	764		599							
F	9	6	686	30										8	645	626		435							
Ne	10	0	863	41	14									0	491	468		264							
Na	11	2	1072	64	31									4	332	303									
Mg	12	2		90	51																				
Al	13	4		119	74																				
Si	14	6		153	103	102																			
P	15	8		191	134	133	14																		
S	16	8		229	166	165	17												1103						
Cl	17	11		270	201	199	17												1071						
Ar	18	0		319	243	241	22													1035					
K	19	1		378	296	293	33		17										1037	1003					
Ca	20	2		439	350	347	44		25										1005	961					
Sc	21	6		501	407	402	53		31										964						
Ti	22	8		565	464	458	62		37											920					
V	23	6		630	523	515	69		40											873	892				
Cr	24	6		698	586	577	77	46	45											822	839				
Mn	25	4		770	652	641	83	49	48											767	784				
Fe	26	8		847	723	710	93	56	55											715	729				
Co	27	6		927	796	781	103	63	61											659	670			620	
Ni	28	6		1009	873	855	112	69	67												608			553	
Cu	29	4		1098	954	934	124	79	77										604	597	546	541		483	468
Zn	30	2		1196	1045	1022	140	92	89		10								548	542	482	476		410	393
Ga	31	2			1144	1117	160	108	105		20								486	479	416	408	396	337	317
Ge	32	4					184	128	124	32	31								429	422	352	343	329	265	242
As	33	7					207	148	143	45	44								368	361	284	275	257	189	162
Se	34	8					232	169	163	58	57								305	297	215	205	184	113	82
Br	35	7					256	189	182	70	69														
Kr	36	0					287	216	208	89	88	22													
Rb	37	1					322	247	238	111	110	29		14											
Sr	38						358	280	269	135	133	37		20											
Y	39						395	313	301	160	158	45		25											
Zr	40	6					431	345	331	183	181	51		29											
Nb	41	8					470	379	364	209	206	59	35			$M_{45}N_{23}V$	$M_5N_{45}N_{45}$	$M_4N_{45}N_{45}$							
																1008	1056								

Note: The circled values are the main bands

Appendix B-2: Atomic sensibility factor (ASF) of elements.

Table B-2.1 Atomic sensibility factor (ASF) of elements [2]**.**

Atomic number	Element	Line	ASF (Area)
3	Li	1s	0.012
4	Be	1s	0.039
5	B	1s	0.088
6	C	1s	0.205
7	N	1s	0.38
8	O	1s	0.63
9	F	1s	1.00
10	Ne	1s	1.54
11	Na	1s	2.51
		1s	(2.27)
12	Mg	1s	(3.65)
		2p	0.07
13	Al	2p	0.11
14	Si	2p	0.17
15	P	2p	0.25
16	S	2p	0.35
17	Cl	2p	0.48
18	Ar	$2p_{3/2}$	0.42
19	K	$2p_{3/2}$	0.55
20	Ca	$2p_{3/2}$	0.71
21	Sc	$2p_{3/2}$	0.90
22	Ti	$2p_{3/2}$	1.1
23	V	$2p_{3/2}$	1.4
24	Cr	$2p_{3/2}$	1.7
25	Mn	$2p_{3/2}$	2.1
26	Fe	2p[a)]	3.8
27	Co	2p[a)]	4.5
28	Ni	2p[a)]	5.4
29	Cu	$2p_{3/2}$	4.3
30	Zn	$2p_{3/2}$	5.3
31	Ga	$2p_{3/2}$	6.9
		$2p_{3/2}$	(5.8)
32	Ge	$2p_{3/2}$	9.2
		$2p_{3/2}$	(7.2)
		3d	0.30

[a)] Variable and complex pattern makes it usually desirable to measure areas of entire doublet region.

Atomic number	Element	Line	ASF (Area)
33	As	$2p_{3/2}$	(9.1)
		3d	0.38
34	Se	3d	0.48
35	Br	3d	0.59
36	Kr	3d	0.72
37	Rb	3d	0.88
38	Sr	3d	1.05
39	Y	3d	1.25
40	Zr	$3d_{5/2}$	0.87
41	Nb	$3d_{5/2}$	1.00
42	Mo	$3d_{5/2}$	1.2
43	Tc	$3d_{5/2}$	1.35
44	Ru	$3d_{5/2}$	1.55
45	Rh	$3d_{5/2}$	1.75
46	Pd	$3d_{5/2}$	2.0
47	Ag	$3d_{5/2}$	2.25
48	Cd	$3d_{5/2}$	2.55
49	In	$3d_{5/2}$	2.85
50	Sn	$3d_{5/2}$	3.2
51	Sb	$3d_{5/2}$	3.55
52	Te	$3d_{5/2}$	4.0
53	I	$3d_{5/2}$	4.4
54	Xe	$3d_{5/2}$	4.9
55	Cs	$3d_{5/2}$	5.5
56	Ba	$3d_{5/2}$	6.1
57	La	$3d_{5/2}$	6.7
		4d[a)]	1.22
58	Ce[a)]	3d	12.5
		4d	1.29
59	Pr[a)]	3d	14.0
		4d	1.38
60	Nd[a)]	3d	15.7
		4d	1.48
61	Pm[a)]	3d	17.6
		4d	1.57
62	Sm[a)]	3d	20.3
		4d	1.66
63	Eu	3d	23.8

[a)] Variable and complex pattern makes it usually desirable to measure areas of entire doublet region.

Atomic number	Element	Line	ASF (Area)
63	Eu	3d	23.8
		3d	(20.2)
		4d	1.76
64	Gd[a)]	3d	29.4
		3d	(22.6)
		4d	1.84
65	Tb[a)]	3d	(26.7)
		4d	1.93
66	Dy[a)]	3d	(30.0)
66	Dy[a)]	4d	2.03
67	Ho[a)]	4d	2.12
68	Er[a)]	4d	2.19
69	Tm[a)]	4d	2.28
70	Yb[a)]	4d	2.36
71	Lu[a)]	4d	2.45
72	Hf	4f	1.55
73	Ta	4f	1.75
74	W	4f	2.0
75	Re	$4f_{7/2}$	1.25
76	Os	$4f_{7/2}$	1.4
77	Ir	$4f_{7/2}$	1.55
78	Pt	$4f_{7/2}$	1.75
79	Au	$4f_{7/2}$	1.9
80	Hg	$4f_{7/2}$	2.1
81	Tl	$4f_{7/2}$	2.3
82	Pb	$4f_{7/2}$	2.55
83	Bl	$4f_{7/2}$	2.8
90	Th	$4f_{7/2}$	4.8
92	U	$4f_{7/2}$	5.6

[a)] Variable and complex pattern makes it usually desirable to measure areas of entire doublet region.

Appendix C
Raman spectra of compounds

Table C-1.1 Raman spectra of compounds

Oxide phase	**Raman shift (cm^{-1})**								**Reference**
Cr_2O_3	307	350		524	**551**		610	1398	[3]
	310	351		531	**552**		609		[4]
	307	350		524	**551**		610		[5]
	304	345	380	530	**550**	580			[6]
	290	352		528	**547**		617		[7]
	306	352			**557**		617		[8]
	305	340			**554**	570	600		[9]
	304	353		529	**553**		616	1398	[10]
	296	350		528	**554**		615		[11]
$(Fe,Cr)_2O_3$	298-310	380-420			500-550	616-650	**664-685**	1319-1381	[10]
Fe_2O_3	**226**	245	292	299	411	499	613		[4]
	227	246	292	299	411	497	612		[12]
	236	253		298	413	502	616	1319	[10]
	225	250		300	410	500	610		[6]
	227			298	414	501	612	665	[13]
	227	245	293	298	414	501	612		[14]
Fe_3O_4		295			531		**667**		[4]
		300	410		550		**660**		[6]
		302		513	533		**663**		[12]
			425			612	**667**		[13]
						616	**663**		[14]
					542		**671**		[10]
	193	306			538		**668**		[15]
	188	307	434		544		**670**		[16]
$(Fe,Cr)_3O_4$				540-560		636	**670-680**		[10]
$FeCr_2O_4$		531		635	**678**				[4]
		522		639	**684**				[17]
		500	595	631	**677**				[18]
	283	400	445		**680**	730			[19]
					686		1265	1357	[10]

Note: The bold values are the main peaks

Oxide phase	Raman shift (cm^{-1})								Reference
$(Fe,Ti)_3O_4$ (Ti = 0.02-0.10)	190-193	300-302	348-419	496-528	**634-663**				[16]
$(Fe,Mn)_3O_4$ (Ti = 0.01-0.50)	38-69	190-192	296-307	408-430	496-540	**642-668**			[20]
$MnCr_2O_4$	500-580	**660**							[21]–[23]
	500-580	**680**							[24]
Mn_3O_4	298	305	390	477	**660**				[25]
Mn_5O_8	171	264	431	477	533	577	617	**648**	[25]
TiO_2 anatase	145	218	323	399		521	**642**		[26]
				395		515	**640**		[27]
	142			395	450	512	655		[28]
	145	198		399		516	640		[29]
	140	194		394		513	636		[3]
	144	198		394	443	514	610	634	[30]
TiO_2 rutile	236	442	**612**						[3]
	240	443	**610**						[30]
Ti_2O_3	**228**	269	302	347	452	530	564		[24]
SiO_2	**400-500**	600	820						[31]
NbO_2		392	476	**704**					[32]
	240			698	980				[33]
Nb_2O_5	**240**	308	350	472	552	632	664	996	[32]
	240					600-690	698	980	[33]

Note: The bold values are the main peaks

Appendix references

[1] J. M. Smith, Introduction to chemical engineering thermodynamics, 7th ed. McGraw-Hill, 2005.

[2] D. Briggs and M. P. Seah, Eds., Practical surface analysis by Auger and X-ray photoelectron spectroscopy. John Wiley & Sons, 1983.

[3] J. Mougin, “Tenue mécanique de couches d’oxyde thermiques générées sur le chrome et sur quelques aciers inoxydables ferritiques: Étude des contraintes et de d'adhérence,” Institut National Polytechnique de Grenoble, 2001.

[4] B. D. Hosterman, “Raman spectroscopic study of solid solution spinel oxides,” 2011.

[5] J. Mougin, T. Le Bihan, and G. Lucazeau, “High-pressure study of Cr_2O_3 obtained by high-temperature oxidation by X-ray diffraction and Raman spectroscopy,” vol. 62, pp. 553–563, 2001.

[6] D. Renusch, B. Veal, K. Natesan, and M. Grimsditch, “Transient oxidation in Fe-Cr-Ni alloys : a Raman-scattering study,” Oxid. Met., vol. 46, no. 5–6, pp. 365–381, 1996.

[7] J. Birnie, C. Craggs, D. J. Gardiner, and P. R. Graves, “Ex-situ and in-situ determination of stress distribution in chromium oxide films by Raman spectroscopy,” Corros. Sci., vol. 33, no. 1, pp. 1–12, 1992.

[8] D. J. Gardiner, C. J. Littleton, K. M. Thomas, and K. N. Strafford, “Distribution and characterization of high temperature air corrosion products on ironchromium alloys by Raman microscopy,” Oxid. Met., vol. 27, no. 1–2, pp. 57–72, 1987.

[9] G. Calvarin, A. M. Huntz, A. Hugot-Le-Goff, S. Joiret, and M. C. Bernard, “Oxide scale stress determination by Raman spectroscopy application to the NiCr/Cr_2O_3 system and influence of yttrium,” Scr. Mater, vol. 38, no. 11, pp. 1649–1658, 1998.

[10] K. F. McCarty and D. R. Boehme, “A Raman study of the system $Fe_{3-x}Cr_xO_4$ and $Fe_{2-x}Cr_xO_3$,” J. Solid State Chem., vol. 79, pp. 19–27, 1989.

[11] J. Mougin, T. Le Bihan, and G. Lucazeau, “High-pressure study of Cr_2O_3 obtained by high-temperature oxidation by x-ray diffraction and Raman spectroscopy,” J. Phys. Chem. Solids, vol. 62, pp. 553–563, 2001.

[12] D. L. A. de Faria, S. Venâncio SIlva, and M. T. de Oliveira, “Raman microspectroscopy of some iron oxides and oxyhydroxides,” J. Raman Spectrosc., vol. 28, pp. 873–878, 1997.

[13] S. C. Tjong, “Laser Raman spectroscopic studies of the surface oxides formed on iron chromium alloys at elevated temperatures,” Mater. Res. Bull., vol. 18, pp. 157–165, 1983.

[14] R. J. Thibeau, C. W. Brown, and R. H. Heidersbach, “Raman spectra of possible corrosion products of iron,” J. Appl. Spectrosc., vol. 32, no. 6, pp. 532–535, 1978.

[15] O. N. Shebanova and P. Lazor, “Raman spectroscopy study of magnetite ($FeFe_2O_4$): A new assignment for the vibration spectrum,” J. Solid State Chem., vol. 174, pp. 424–430, 2003.

[16] D. Varshney and A. Yogi, “Structural, transport and spectroscopic properties of Ti^{4+} substituted magnetite: $Fe_{3-x}Ti_xO_4$,” Materials Chemistry and Physics, vol. 133, no. 1. pp. 103–109, 2012.

[17] A. Wang, K. E. Kuebler, B. L. Jolliff, and L. A. Haskin, “Raman spectroscopy of Fe-Ti-Cr oxides, case study: Martian meteorite EETA79001,” Am. Mineral., vol. 89, pp. 665–680, 2004.

[18] M. Chen, J. Shu, X. Xie, and H. Mao, “Natural $CaTi_2O_4$- structured $FeCr_2O_4$ polymorph in the Suizhou meteorite and its significance in mantle mineralogy,” Geochim. Cosmochim. Acta, vol. 67, no. 20, pp. 3937–3942, 2003.

[19] K. Veena, V. K. Vaidyan, and P. Koshy, “Characterization of ferrochromium thin films,” J. Mater. Sci. Lett., vol. 8, pp. 80–82, 1989.

[20] D. Varshney and A. Yogi, “Structural and transport properties of stoichiometric Mn^{2+}-doped magnetite: $Fe_{3-x}Mn_xO_4$,” Mater. Chem. Phys., vol. 128, no. 3, pp. 489–494, 2011.

[21] J. C. Hamilton and R. J. Anderson, “Oxidation of Fe-18Cr-3Mo : an in-situ Raman study,” High Temp. Sci., vol. 19, pp. 307–321, 1985.

[22] R. L. Farrow, R. E. Benner, A. S. Nagelberg, and P. L. Mattern, “Characterization of surface oxides by Raman spectroscopy,” Thin Solid Films, vol. 73, pp. 353–358, 1980.

[23] R. L. Farrow and A. S. Nagelberg, “Raman spectroscopy of surface oxides at elevated temperautres,” Appl. Phys. Lett., vol. 36, no. 12, pp. 945–947, 1980.

[24] Y. Matsuda, S. Hinotani, and K. Yamanaka, “Characterization of oxide layers on SUS410Ti stainless steel grown in low oxygen pressures by Raman spectroscopy,” Tetsu to Hagane, vol. 82, no. 3, pp. 32–37, 1996.

[25] C. B. Azzoni, M. C. Mozzati, P. Galinetto, a. Paleari, V. Massarotti, D. Capsoni, and M. Bini, "Thermal stability and structural transition of metastable Mn_5O_8: in situ micro-Raman study," Solid State Commun., vol. 112, no. 7, pp. 375–378, 1999.

[26] R. López and R. Gómez, "Photocatalytic degradation of 4-nitrophenol on well characterized sol-gel molybdenum doped titania semiconductors," Top. Catal., vol. 54, no. 8–9, pp. 504–511, 2011.

[27] H. Y. Chuang and D. H. Chen, "Catalyst-free low temperature synthesis of discrete anatase titanium dioxide nanocrystals with highly thermal stability and UVC-cut capability," J. Nanoparticle Res., vol. 10, pp. 233–241, 2008.

[28] F. Milella, J. M. Gallardo-Amores, M. Baldi, and G. Busca, "A study of Mn–Ti oxide powders and their behaviour in propane oxidation catalysis," J. Mater. Chem., vol. 8, no. 11, pp. 2525–2531, 1998.

[29] Z. Lin, "$BaTiO_3$ Nanocrystals," The Lin Research Group, School of Materials Science and Engineering, Georgia Institute of Technology, 2011. [Online]. Available: http://www.nanofm.mse.gatech.edu/Progress.html. [Accessed: 21-Feb-2014].

[30] F. Hardcastle, "Raman Spectroscopy of Titania (TiO_2) Nanotubular Water-Splitting Catalysts," J. Ark. Acad. Sci., vol. 65, pp. 43–48, 2011.

[31] K. Yuda and H. Tanabe, "Silicon oxide film, method of forming the silicon oxide film, and apparatus for depositing the silicon oxide film," US 6,444,327 B1, 2002.

[32] B. X. Huang, K. Wang, J. S. Church, and Y.-S. Li, "Characterization of oxides on niobium by raman and infrared spectroscopy," Electrochim. Acta, vol. 44, no. 15, pp. 2571–2577, 1999.

[33] C. Cao, D. Ford, S. Bishnoi, T. Proslier, B. Albee, E. Hommerding, a. Korczakowski, L. Cooley, G. Ciovati, and J. F. Zasadzinski, "Detection of surface carbon and hydrocarbons in hot spot regions of niobium superconducting rf cavities by Raman spectroscopy," Phys. Rev. Spec. Top. - Accel. Beams, vol. 16, no. 6, pp. 1–9, 2013.

Résumé français étendu

Préambule

Les aciers inoxydables ferritiques sont actuellement les meilleurs candidats pour répondre au cahier des charges des matériaux destinés aux interconnexions de piles à combustibles à oxyde solide (SOFC acronyme anglo-saxon pour Solid Oxide Fuel Cell). Ces systèmes de production d'énergie peuvent présenter plusieurs géométries dont la plus courante est de type planaire comme cela est présenté en Figure 1. Les problématiques que soulève la durabilité en service de ces piles sont multiples.

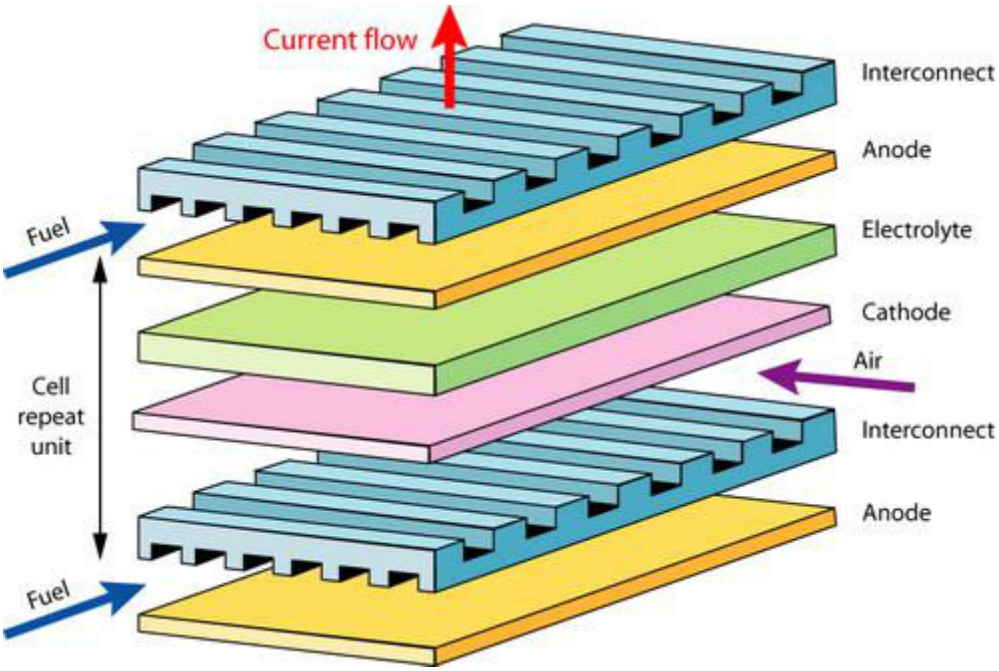

Figure 1 : Pile à combustible de type SOFC de géométrie planaire.

Concernant la thématique de l'oxydation à haute température, les matériaux métalliques d'interconnexion qui assurent notamment la rigidité de l'ensemble de l'empilement présenté en Figure 1 sont soumis à des conditions agressives (température et atmosphères oxydantes) susceptibles de générer la formation d'un film d'oxydation. Bien souvent l'oxydation à haute température peut se révéler catastrophique, avec par exemple l'établissement d'un régime d'oxydation accéléré intervenant après un certain temps repris sous le terme de "breakaway time" dans la littérature (voir Figure 2).

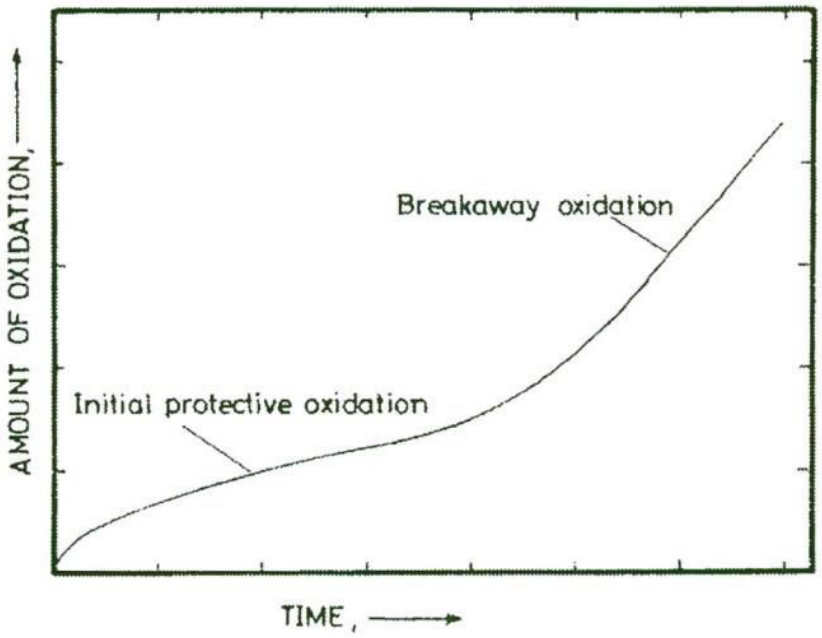

Figure 2 : Exemple d'un matériau présentant une cinétique d'oxydation de type catastrophique.

On recherche, bien entendu à minimiser ce phénomène qui entraîne à coup sûr la dégradation des propriétés mécaniques de l'empilement. L'établissement d'un film d'oxydation protecteur (oxyde de faible épaisseur, imperméable, couvrant et adhérent) est donc nécessaire mais génère un autre problème. Un tel film risque de réduire drastiquement la conductibilité électronique de la pile, ce qui n'est évidemment pas recherché. De plus, le compartiment cathodique de ces piles, où l'on peut rencontrer de la vapeur d'eau, génère un phénomène de sublimation du chrome à haute température qui conduit également à des dégradations importantes, réduisant ainsi la durée de vie en service des SOFC et qui vient donc encore complexifier la thématique. C'est sur cet aspect particulier que s'initie ce travail de thèse de doctorat qui porte l'ambition de la mesure du phénomène de sublimation du chrome (réputée difficile), sa meilleure compréhension et le développement de procédés susceptibles de conduire à la réduction du phénomène de sublimation en conditions réelles de service.

Les objectifs de ce travail de thèse sont donc d'étudier le phénomène de sublimation du chrome sur un acier inoxydable ferritique et de rechercher un ou plusieurs moyens susceptibles d'atténuer cette même sublimation. Le matériau d'étude s'est naturellement porté vers une nuance d'acier ferritique AISI 441 très étudiée au cours de la dernière décennie et qui semble être à ce jour un des meilleurs candidats pour les matériaux d'interconnexion.

Dispositif expérimental

Le dispositif expérimental mis en œuvre dans ce travail pour la mesure de la cinétique de sublimation du chrome à haute température est présenté en Figure 3. Il est composé d'un four à géométrie tubulaire régulé en température dans lequel sera inséré un tube en quartz lui même contenant l'échantillon. Un gaz vecteur chargé en vapeur d'eau à pression de vapeur saturante, elle même contrôlée par l'imposition d'une température fixée dans une colonne à reflux, sera orientée vers le four par son entrée supérieure.

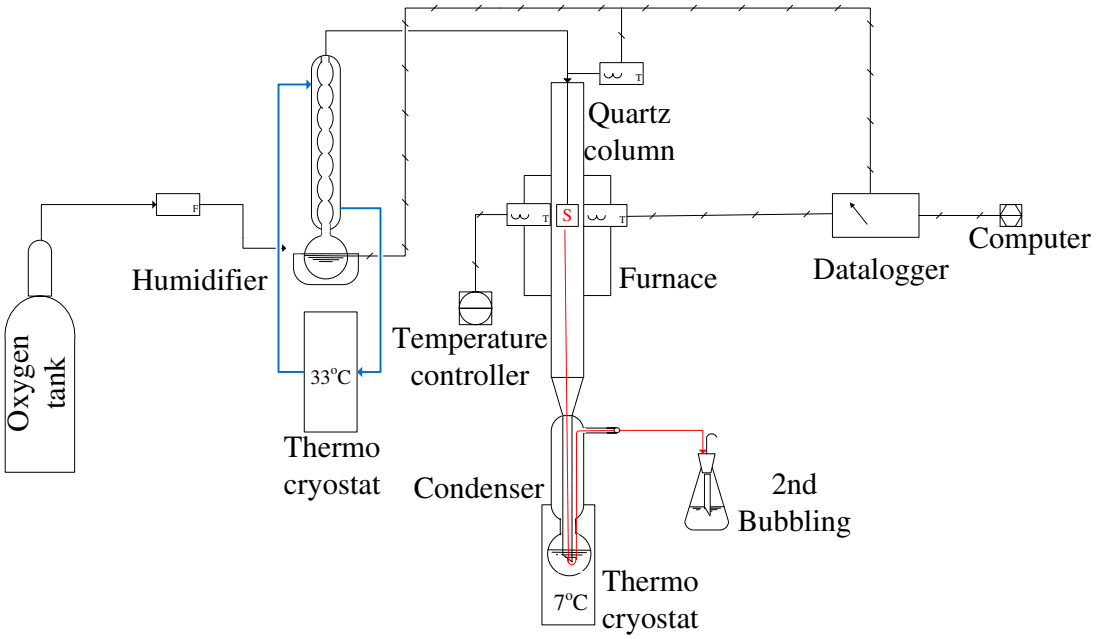

Figure 3 : Dispositif expérimental mis en œuvre dans ce travail pour la mesure de cinétique de sublimation du chrome.

Au cours de l'oxydation thermique, les vapeurs d'espèces chromées seront entraînées puis condensées sur un point froid régulé et positionné en aval du four. Une fois l'expérience terminée, le condensat solide est resolubilisée en milieu acide pour être mesurée par analyse ICP (Inductive Coupled Plasma) avec une résolution analytique de l'ordre de la partie par million. Les autres techniques de caractérisation utilisées dans ce travail sont plus classiques et ne seront pas décrites dans ce résumé.

Caractérisation des films d'oxydation

La caractérisation des échantillons avant oxydation thermique et notamment par l'analyse d'extrême surface par XPS révèle la présence d'un film passif d'oxydation classique de quelques nanomètres d'épaisseur de type duplex avec une partie interne plutôt riche en chrome et une partie externe davantage riche en nickel. Après oxydation à haute température (typiquement, vitesse des gaz : 2 cm/s, atmosphère composée de 5%H_2O dans O_2 à 800 °C pendant 96 h), là encore, nous observons un film d'oxydation tout à fait classique et par ailleurs bien documentée dans la littérature [1-5]. La Figure 4 présente schématiquement cette couche d'oxydation composée d'une partie interne riche en chrome et d'une partie externe riche en manganèse. On observe également la présence de silice et de niobium à l'interface métal/oxyde. Le titane est pour sa part susceptible de présenter une oxydation dite interne mais également de diffuser très rapidement vers l'extérieur pour former des ilots de dioxyde de titane.

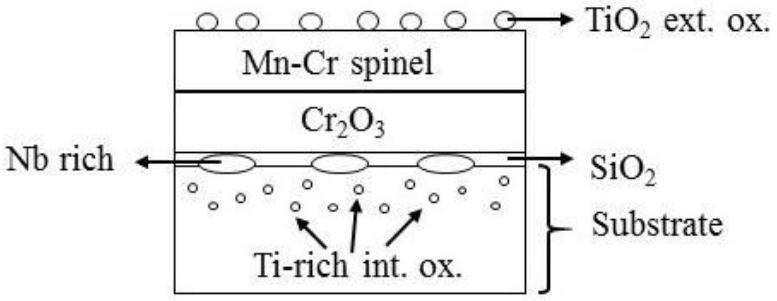

Figure 4 : Vue schématique d'un film d'oxydation thermique formé sur un alliage 441.

De nombreuses analyses ont été conduites sur ces films pour confirmer l'état de l'art. Nous présentons ici deux exemples de résultats obtenus par spectrométrie EDX et en microscopie électronique à haute résolution sur des vues de surfaces et sur des coupes obtenues par abrasion ionique (FIB) en Figures 5 et 6.

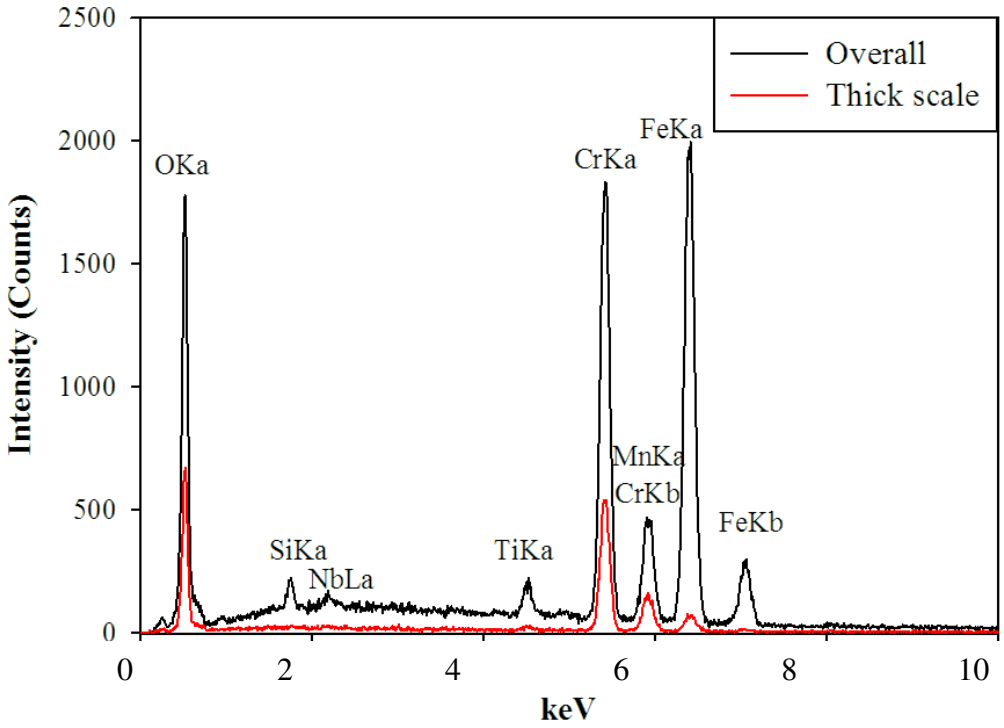

Figure 5 : Analyse EDX d'un film d'oxydation thermique formé sur un alliage 441 (2 cm/s, 5%H_2O dans O_2, 800 °C, 96 h).

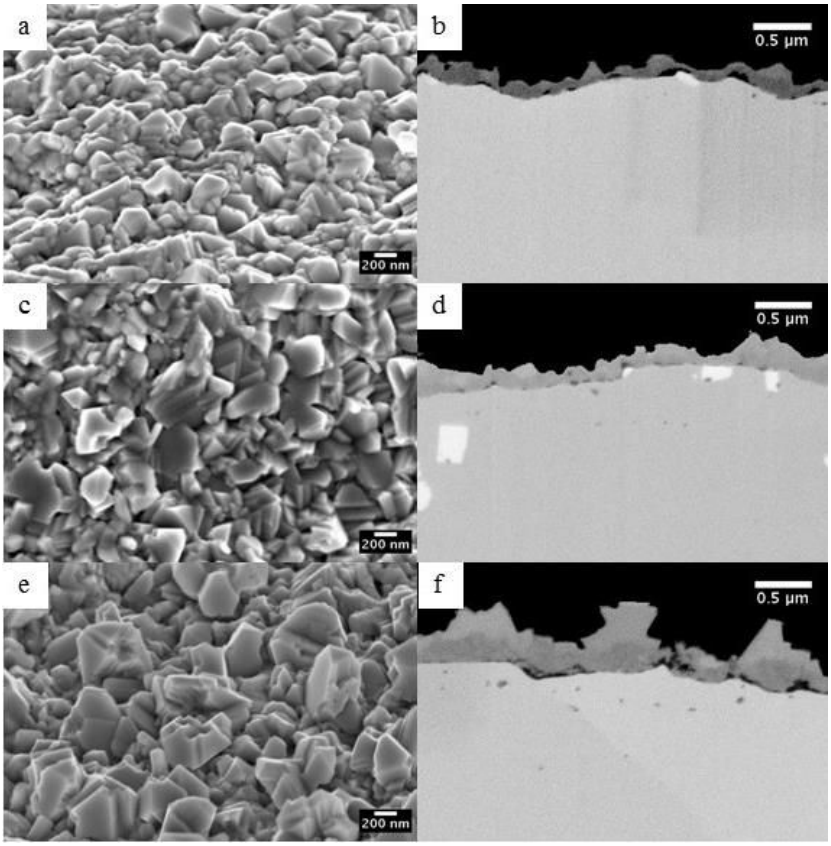

Figure 6 : Analyse par microscopie électronique (vues de surface et transversales) d'un film d'oxydation thermique formé sur un alliage 441 (2 cm/s, 5%H_2O in O_2, 800 °C), durée d'oxydation de 4 h (a et b), 14 h (c et d) et 24 h (e et f).

Mesure de la sublimation du chrome

Pour la mesure des quantités de chrome sublimées, 2 temps d'oxydation ont été choisis; 24 et 96 h. Pour chacun d'entre eux, une étude a été conduite en faisant varier la vitesse des gaz dans le réacteur d'oxydation. La Figure 7 présente l'évolution de la quantité de chrome sublimée rapportée à l'aire de l'échantillon (et donc l'aire réactionnelle) en fonction de la vitesse des gaz.

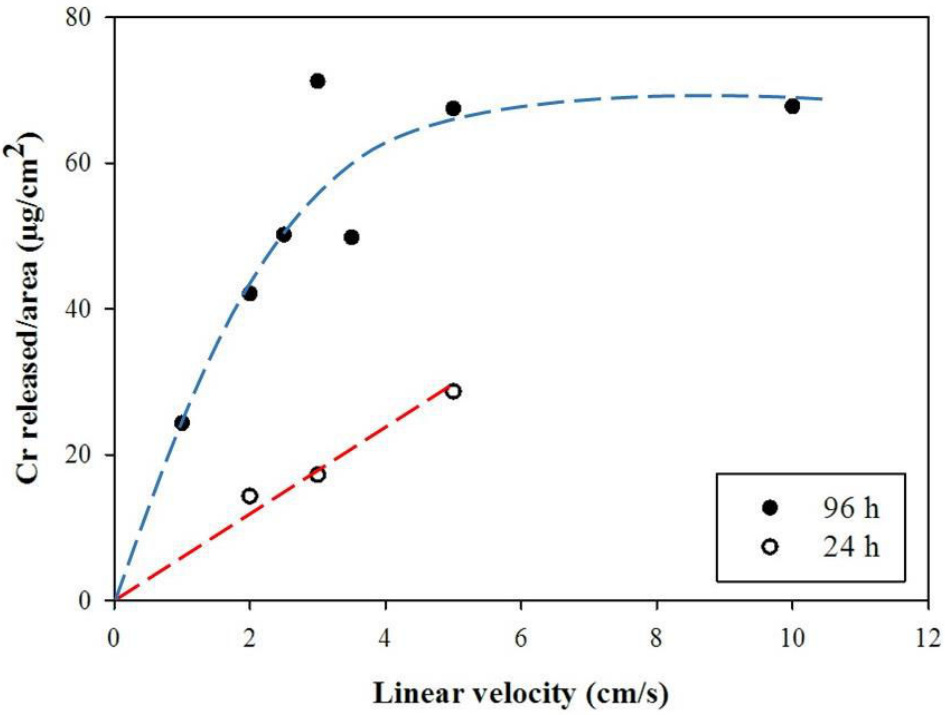

Figure 7 : Évolution de la quantité de chrome sublimée (rapportée à l'aire réactionnelle) en fonction de la vitesse du gaz imposée dans le réacteur après une oxydation thermique de 24 ou 96 heures (5%H_2O dans O_2, 800 °C).

Cette quantité s'exprime donc en unité de masse par unité d'aire, en l'occurrence des micro grammes par centimètre carré. Concernant le temps court (24 h), une dépendance d'allure linéaire est observée. Notons cependant que la mesure à 10 cm/s n'a pu être effectuée pour des raisons techniques. Cette dépendance est confirmée au temps long de 96 h mais avec une décélération à 10 cm/s de la quantité de chrome relâchée et la présence d'un plateau. Ce résultat a été interprété dans ce travail comme la manifestation classique d'un processus de diffusion en milieu gazeux limitant la sublimation du chrome à faible vitesse de gaz dans le réacteur d'oxydation. On peut ici tout simplement évoquer la diffusion d'espèces chromée depuis l'interface libre de l'échantillon vers le cœur du réacteur (i.e. le tube de quartz positionné dans le four tubulaire). A plus forte vélocité, un régime laminaire impose d'une part l'établissement d'une couche de diffusion de plus faible épaisseur en milieu gazeux et d'autre part la stabilisation du régime laminaire. La diffusion en milieu gazeux n'est plus limitante (car intrinsèquement désormais très rapide). Un nouveau processus limitant est alors révélé, très certainement localisé à l'interface externe (interface oxyde/gaz). Nous appelons de façon générique cette vitesse, vitesse de réaction. En deuxième lieu, il apparaît utile de présenter l'évolution de la vitesse (moyenne) de sublimation du chrome en fonction de la vitesse des gaz introduits dans le four. Cette évolution est présentée en Figure 8 et révèle que les 2 courbes sont superposables (temps court et temps long) aux faibles vitesses de gaz mais qu'en revanche cela n'est plus vrai aux vitesses de gaz élevées. Cette observation peut traduire que la vitesse

moyenne de sublimation du chrome (nommée plus haut dans le texte vitesse de réaction) est plus élevée pendant les premières 24 première heures d'oxydation.

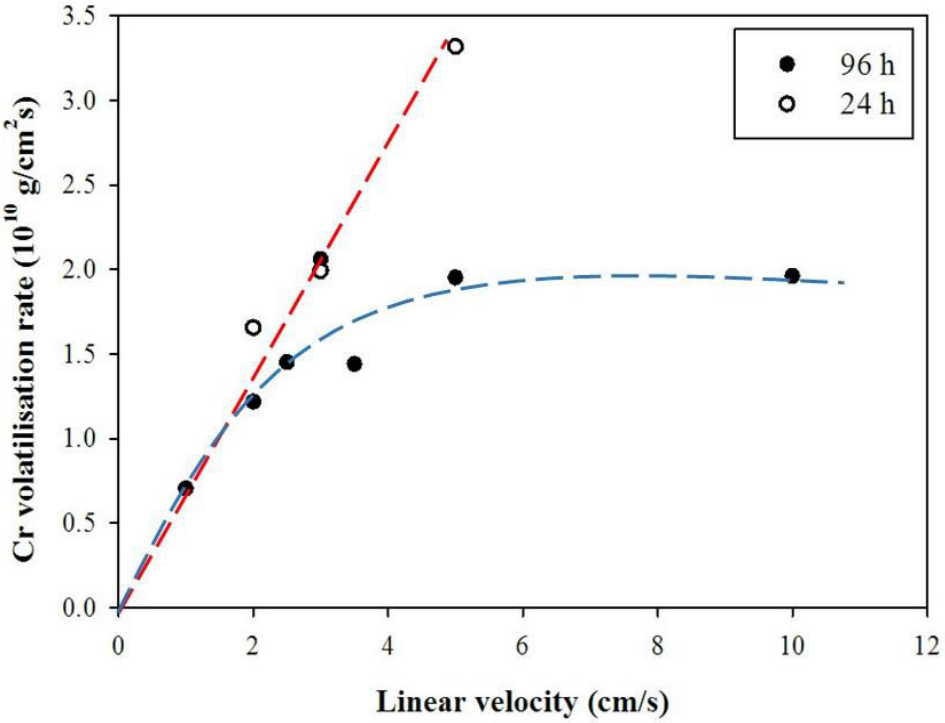

Figure 8 : Évolution de la vitesse moyenne de sublimation du chrome en fonction de la vitesse du gaz imposée dans le réacteur au cours d'une oxydation thermique de 24 ou 96 heures (5%H_2O dans O_2, 800 °C).

Il a donc été montré ici qu'il était possible de s'affranchir des effets de limitation de la vitesse par la diffusion des espèces chromées dans le gaz et de mesurer une vitesse purement réactionnelle. Nous nommerons dans la suite du texte cette vitesse purement réactionnelle "vitesse réactionnelle de sublimation". Nous souhaitons donc nous concentrer sur la vitesse réactionnelle de sublimation du chrome. La valeur numérique de 0,2 nano grammes par cm carré par seconde a pu être ainsi extraite de la Figure 8. Cette valeur a pu être comparée à celles relevées dans la littérature sur plusieurs nuances de matériaux [6-10], les résultats apparaissent en Figure 9.

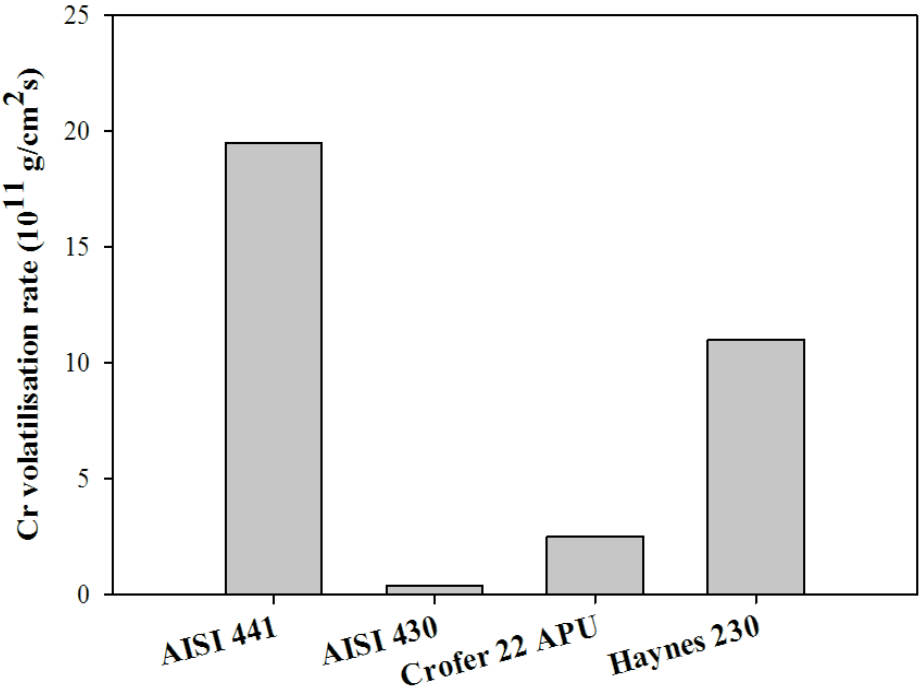

Figure 9 : Vitesse réactionnelle de sublimation expérimentale obtenues sur l'acier 441 dans cette étude et comparaison de cette valeur à celles relevées dans la littérature sur plusieurs nuances de matériaux [6-10].

Ainsi, l'acier 441 ne semble pas constituer le meilleur choix si l'on s'intéresse à la problématique de la sublimation. Il n'en reste pas moins un excellent candidat pour les piles à combustible au regard de l'ensemble pré requis industriels. Il semble donc nécessaire de développer un procédé susceptible d'abaisser de façon considérable la vitesse réactionnelle de sublimation.

Effet de la rugosité de surface

L'évolution de la vitesse réactionnelle de sublimation à été étudiée sur deux préparations de surface considérées comme référentes en milieu industrielles (voir résultats présentés en Figure 10).

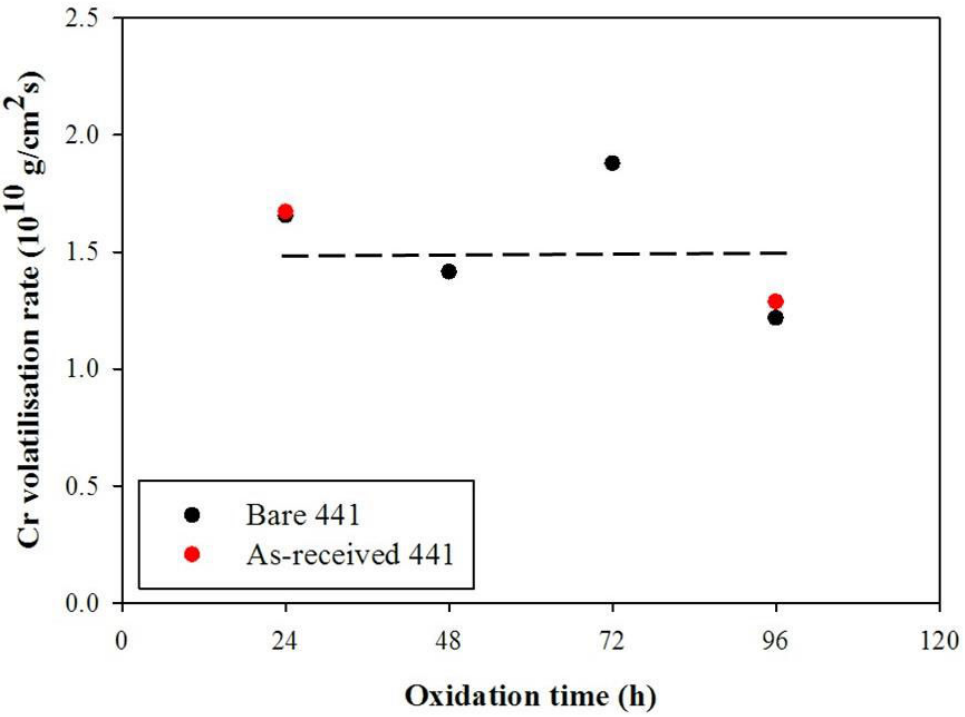

Figure 10 : Évolution de la vitesse réactionnelle de sublimation en fonction de la préparation de surface de l'acier (2 cm/s, 5%H_2O dans O_2, 800 °C).

En premier la finition de type 2B présentant une rugosité de surface d'environ 300 nm (As-received sur la Figure 10) et en deuxième lieu une préparation de surface laboratoire consistant en un polissage au carbure de silicium jusqu'au grade 1200. La Figure 10 montre clairement qu'aucun effet de la rugosité de surface ne peut être observé dans notre étude. Au cours de la caractérisation des films d'oxydation, nous avons relevé la présence de nodules de structure remarquable. En particulier sur les surfaces de plus forte rugosité (surfaces industrielles), nous avons noté le développement de nodules que nous avons classé en deux types, ceux croissants à l'aplomb de joints de grains et ceux localisés en cœur de grain du métal sous-jacent. Ces nodules ont pu être caractérisés par tomographie reconstructive. Cette technique, récemment développée au laboratoire, consiste en l'observation d'objet en microscopie à haute résolution (canon à effet de champs) sur une série de coupes transversales obtenues au fur et à mesure d'une abrasion ionique (par un canon à ion gallium). La résolution en profondeur de cette technique étant pour le moment d'une vingtaine de nanomètres. L'observation d'un objet de la taille d'un micromètre exige donc l'obtention d'une cinquantaine de clichés. La Figure 11 présente un exemple de résultat obtenu sur ces nodules. Les fausses couleurs utilisées en Figure 11 correspondent à différentes phases repérées par leur niveaux de gris respectif (images codées 8 bits et comprenant donc 256 niveaux de gris). Le détecteur utilisé, d'électrons rétro-diffusés, a permis l'identification de différentes phases par contraste de phase en liaison avec d'autres techniques complémentaires, en particulier la spectrométrie à perte d'énergie (EDX) sur lames minces (environ 100 nm d'épaisseur) qui ont pu être obtenues selon le protocole détaillée en Figure 12. Sur la Figure 11, trois codes couleurs ont été utilisés. La couleur rouge correspond

aux oxydes riches en fer, la couleur bleu à la silice et la couleur jaune, aux phases de lave de type Fe_2Nb qui ont pu être notamment observées le long des joints de grain métalliques.

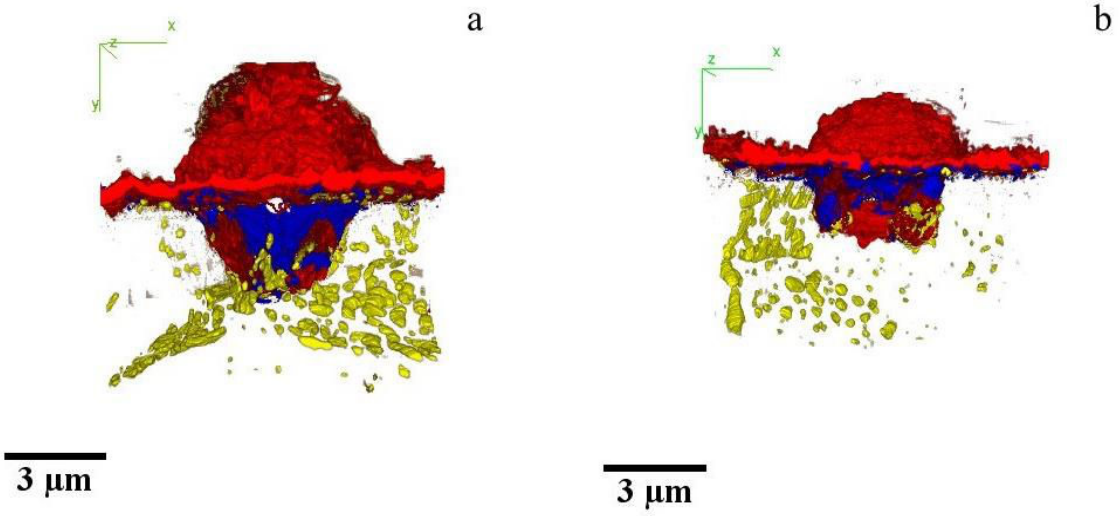

Figure 11 : Tomographies reconstructives obtenues sur des nodules ayant cru à l'aplomb d'un joint de grain (a) ou localisés en cœur de grain du métal sous-jacent (b).

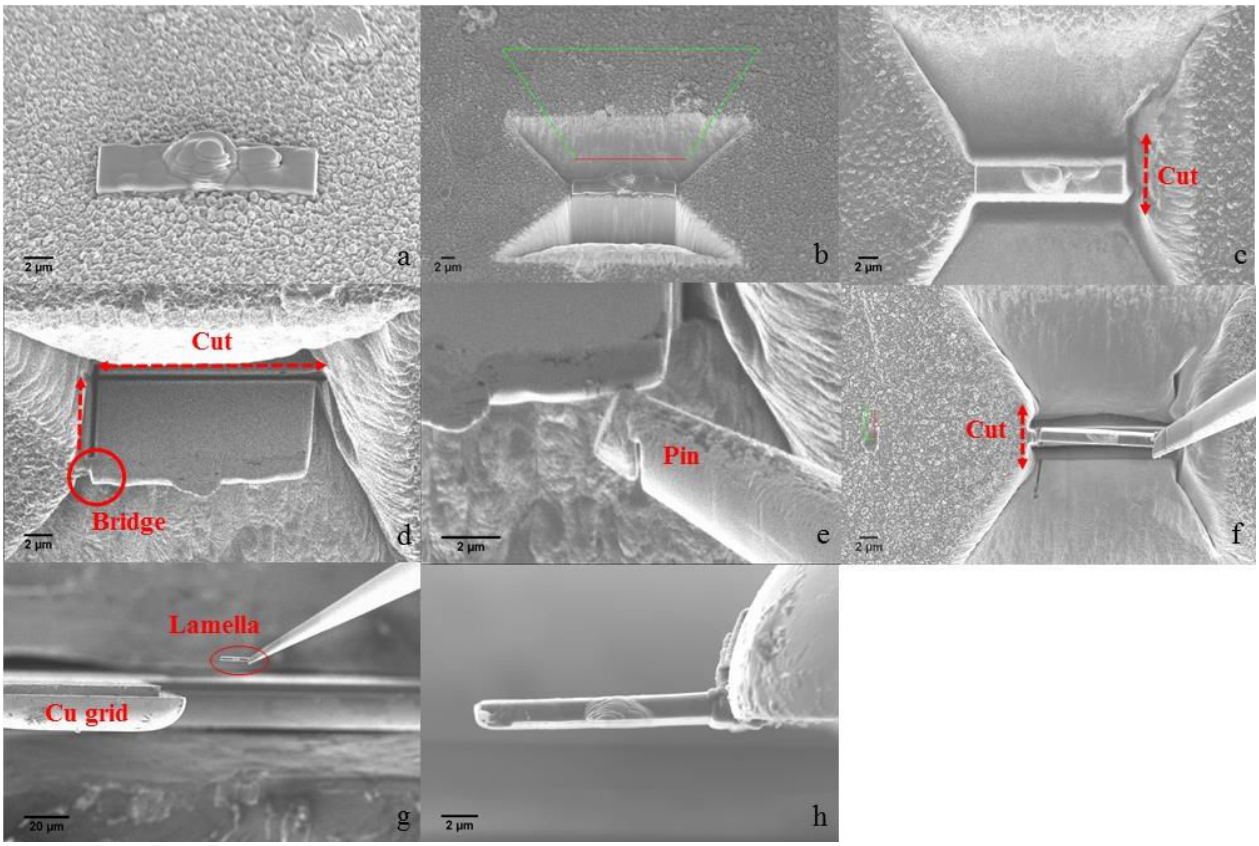

Figure 12 : Méthode de préparation d'une lame mince d'environ 100 nm d'épaisseur pour son observation en microscopie électronique à transmission et EDX haute résolution. La méthode comprend huit étapes.

Protection des aciers par traitement de surface.

Au cours de ce travail de thèse, une première voie de protection de l'alliage 441 a consisté à protéger le substrat par un traitement de surface, ce dernier consistant au dépôt d'un spinelle manganèse cobalt (réputé être protecteur) par une technique de dépôt électrochimique cathodique. La Figure 13 présente le dispositif utilisé dans ce travail.

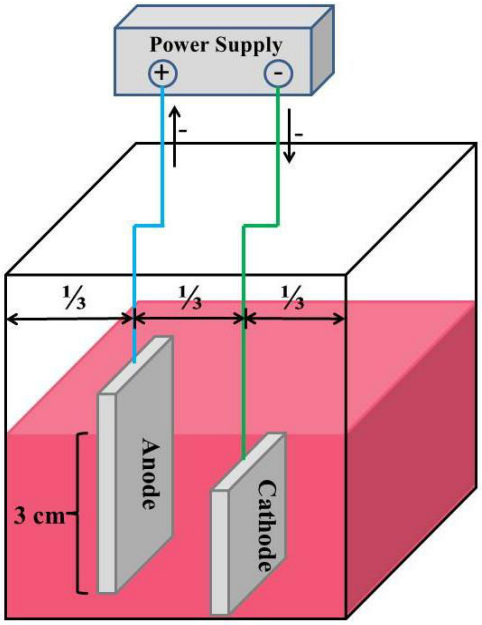

Figure 13 : Schéma du dispositif électrochimique utilisé pour l'obtention de spinelle Mn-Co de surface (0,2 A, 6 min).

Des échantillons ont donc étés protégés par cette méthode puis rapidement exposés aux conditions d'oxydation. Leur vitesse réactionnelle de sublimation a pu alors être mesurée à haute température dans des conditions analogues à celle présentées dans les parties précédentes de ce résumé. La Figure 14 présente les résultats obtenus. Il est clair que le traitement de surface ne conduit à aucune réduction de la vitesse réactionnelle de sublimation.

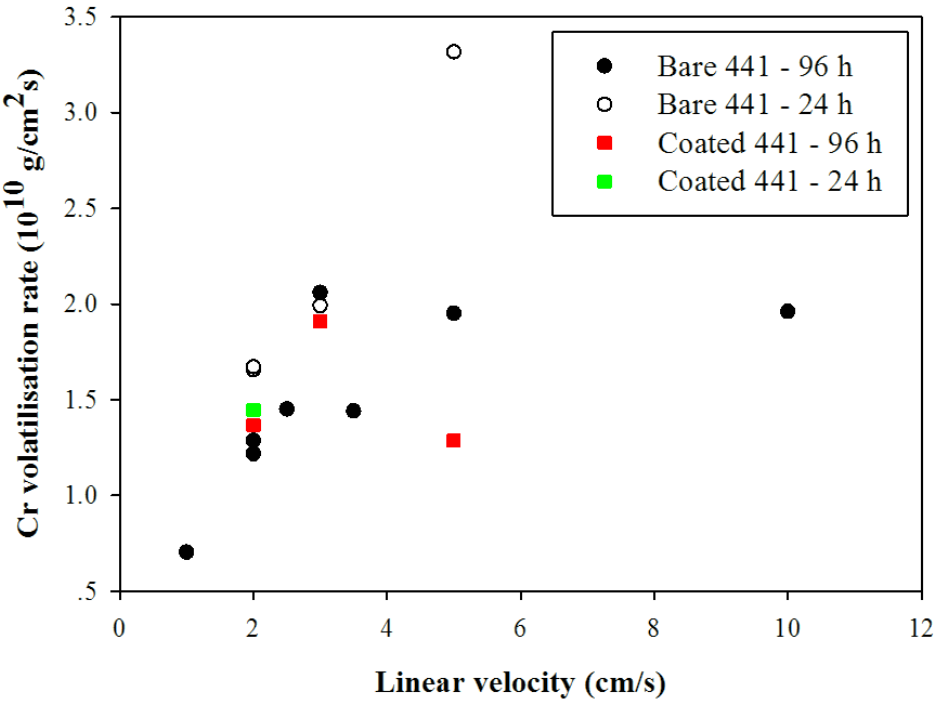

Figure 14 : Mesure de la vitesse réactionnelle de sublimation du chrome sur des substrats 441 protégés par traitement de surface (carrés colorés). Comparaison avec les échantillons de référence (cercles blancs et noirs) (5%H_2O dans O_2, 800 °C, 24 et 96 h).

Des analyses complémentaires, que nous ne présenterons pas ici, par microscopie électronique et analyse EDX ont montré que les couches de spinelles déposées par voie électrochimiques n'étaient pas couvrantes et/ou adhérentes aux substrats 441. En particulier la présence de nombreuses fractures parallèles ou transversales aux interfaces ont pu être régulièrement observées. A ce stade du travail de thèse, il eut été légitime de tenter d'optimiser les paramètres de dépôt des spinelles Mn-Co mais des raisons techniques nous ont conduit à ne pas poursuivre dans cette voie.

Protection des aciers par préoxydation en milieu contrôlé.

Dans un deuxième temps, la voie de protection de l'alliage 441 par une étape de préoxydation a pu être testée. Deux atmosphères contrôlées de type argon impur ou mélanges gazeux équimolaires CO / CO_2 ont étés choisies ainsi que deux températures ; 250 °C et 850 °C, la durée de préoxydation étant fixée à 3 h. Les résultats présentés en Figure 15 et montrent que la préoxydation conduit dans 3 cas sur quatre à une réduction considérable (jusqu'à un facteur 10) de la vitesse de sublimation du chrome mesurée dans les conditions de références, c'est-à-dire 5%H_2O dans O_2 à 800 °C durant 96 h. Seul le cas de la préoxydation dans l'argon à 850 °C semble conduire à l'absence de protection. Concernant les expériences de préoxydation menées à basse température (250 °C), la formation d'un film riche en fer peut expliquer cette réduction par l'établissement d'une barrière de diffusion. La Figure 16 illustre cet aspect avec la présence d'un pic caractéristique de la liaison fer oxygène (aux alentours de 710 eV) sur un spectre XPS obtenu sur un acier 441 préoxydé en milieu CO/CO_2 à 250 °C. De la même façon, l'analyse par spectroscopie Raman sur ce même échantillon (voir Figure 17) révèle clairement la présence d'oxyde de fer et en particulier la présence de la magnétite lorsque la préoxydation intervient en milieu CO/CO_2 à basse température (250 °C).

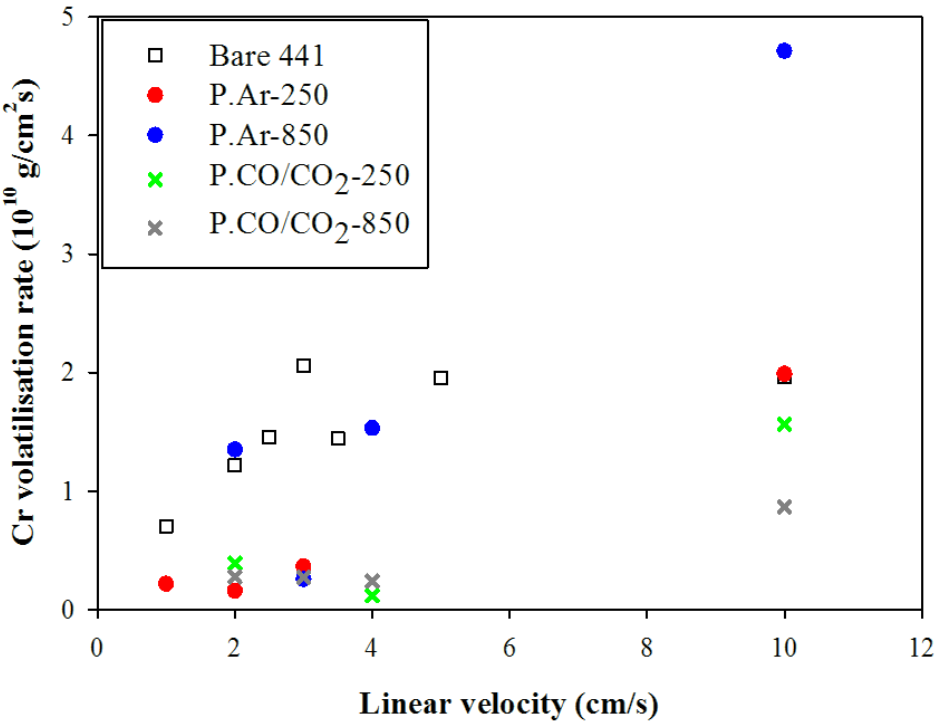

Figure 15 : Mesure de la vitesse réactionnelle de sublimation du chrome sur des substrats 441 (5%H_2O dans O_2, 800 °C, 96 h). Comparaison de substrats préoxydés pendant 3 h (P.Ar-250, P.Ar-850, P.CO/CO_2-250 et P.CO/CO_2-850) avec les échantillons de référence (carrés blancs). Ces vitesses sont présentées en fonction de la vitesse linéaire du gaz dans le réacteur.

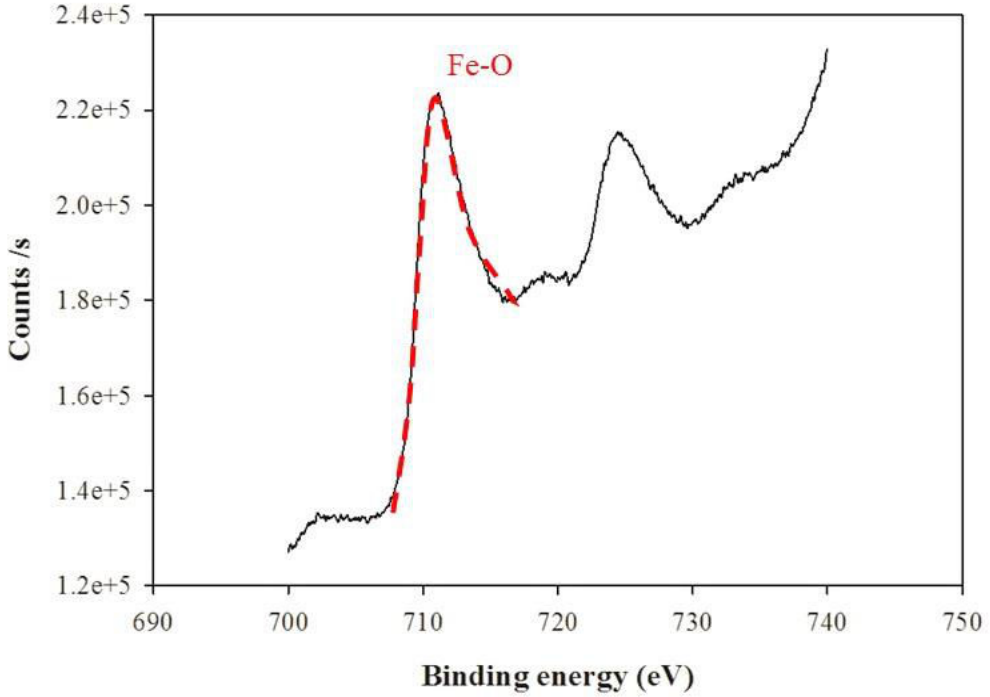

Figure 16 : Spectre XPS obtenu sur un acier 441 préoxydé en milieu CO/CO_2 à 250 °C.

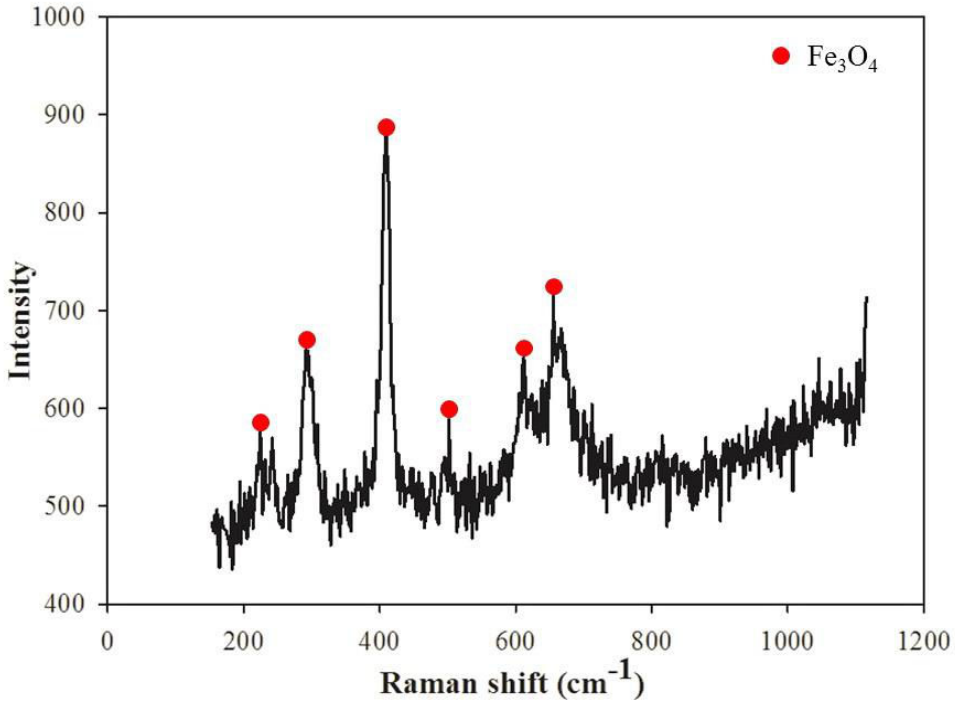

Figure 17 : Spectre Raman obtenu sur un acier 441 préoxydé en milieu CO/CO_2 à 250 °C.

Lorsque l'on observe les mêmes analyses conduites sur un acier 441 préoxydé en milieu Ar à 250 °C, les résultats sont sensiblement analogues (voir Figures 18 et 19). L'analyse XPS révèle toujours la présence d'un pic caractéristique de la liaison fer oxygène (aux alentours de 710 eV). De son coté, l'analyse par spectroscopie Raman confirme la présence d'oxyde de fer et en particulier celle de l'hématite et d'un spinel fer chrome oxygène.

Il apparaît donc clairement qu'une étape de préoxydation à la température de 250 °C semble conduire au développement d'oxyde de fer, et ce, quelle que soit l'atmosphère utilisée. Ce résultat n'est pas surprenant et correspond à ce qui est connu dans la littérature.

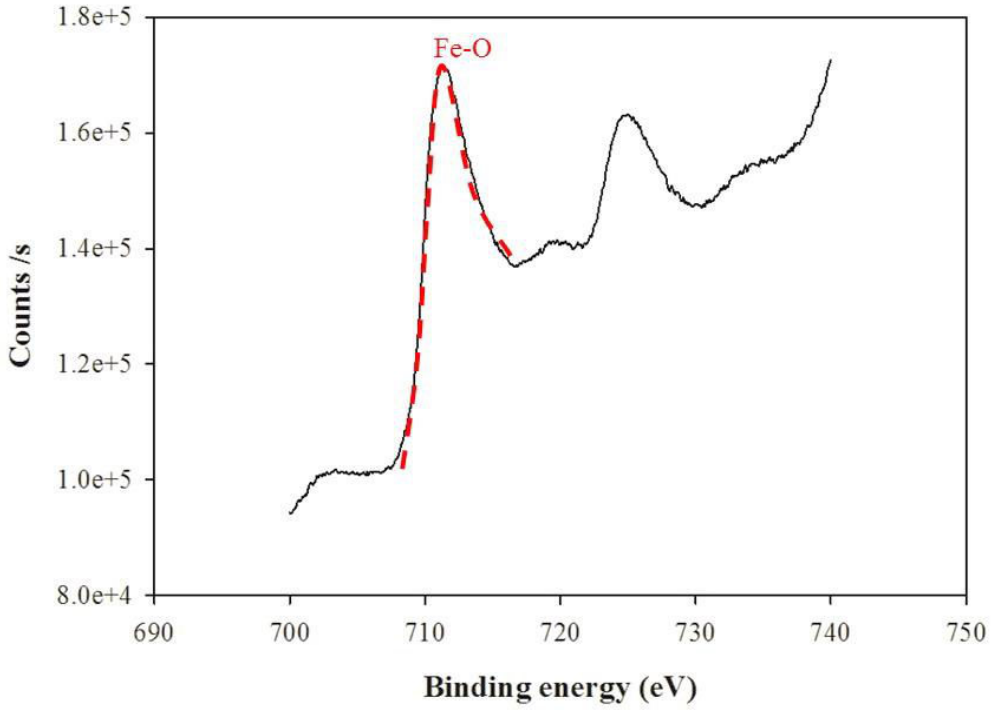

Figure 18 : Spectre XPS obtenu sur un acier 441 préoxydé en milieu Ar à 250 °C.

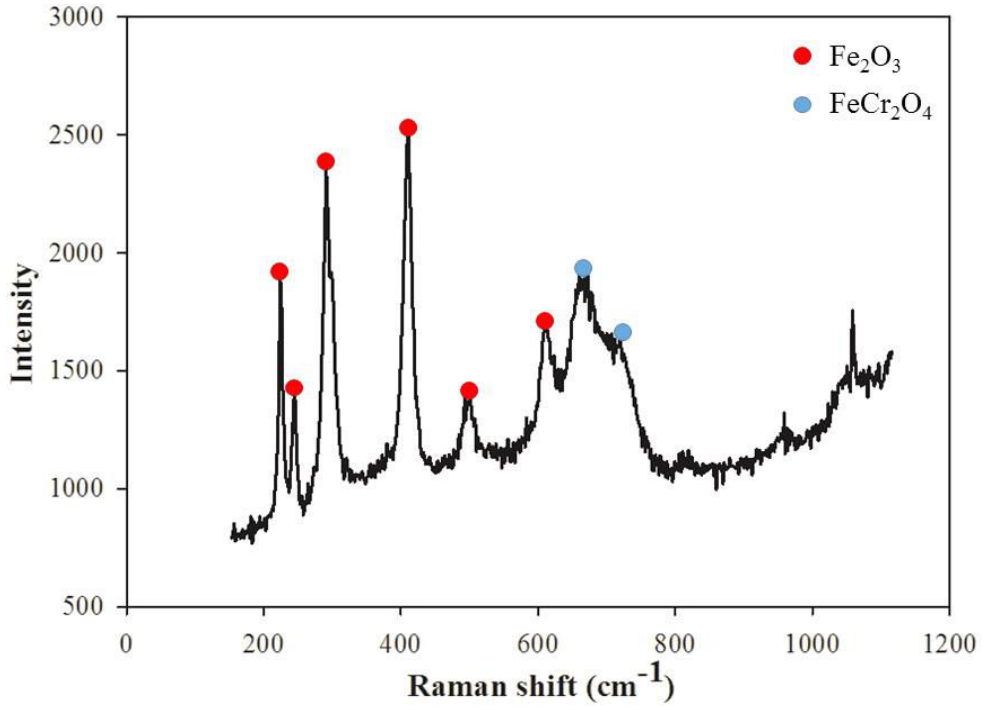

Figure 19 : Spectre Raman obtenu sur un acier 441 préoxydé en milieu Ar à 250 °C.

Concernant l'essai de préoxydation dans l'argon à 850 °C qui ne conduit pas à une réduction de la vitesse de sublimation du chrome mesurée dans les conditions de références, les analyses par spectroscopie Raman et diffraction des RX présentées en Figure 20 et 21 montrent que la couche d'oxydation formée au cours de l'étape de préoxydation est de type standard, c'est-à-dire majoritairement formée de chromine surmontée d'un spinel fer chrome comprenant du manganèse. Il n'est en conséquence pas surprenant que cette étape de préoxydation n'est pas conduit à la réduction de la vitesse de sublimation du chrome.

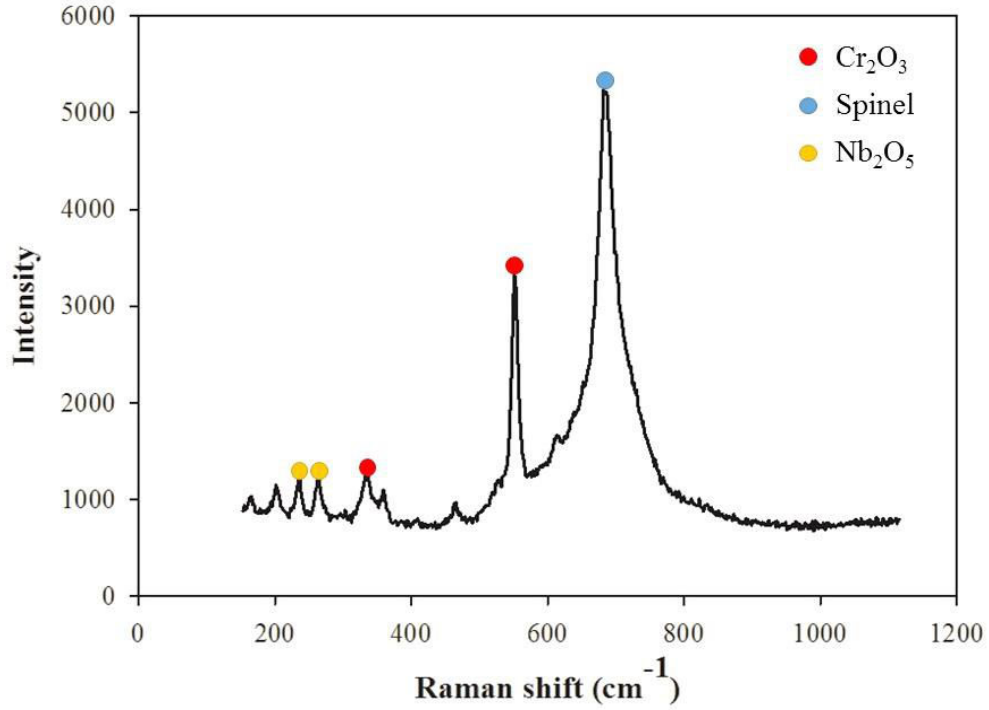

Figure 20 : Spectre Raman obtenu sur un acier 441 préoxydé en milieu Ar à 850 °C.

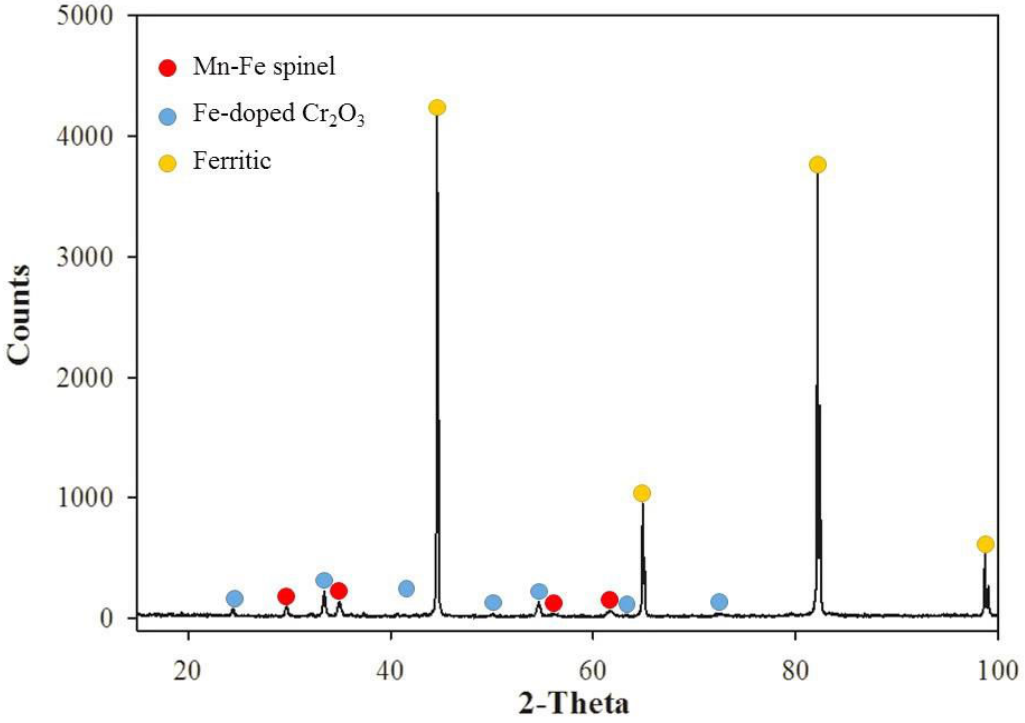

Figure 21 : Spectre de diffraction des RX obtenu sur un acier 441 préoxydé en milieu Ar à 850 °C.

En revanche, la réduction de la vitesse de sublimation du chrome est surprenante s'agissant des films formés par préoxydation à 850 °C dans CO / CO_2. En effet, les analyses montrent que ces films sont riches en chrome et ne semblent différer en rien de ceux, non protecteurs, obtenus à la même température dans de l'argon impur. Ces observations découlant notamment des analyses obtenues par spectroscopie Raman et diffraction des RX qui sont présentées en Figure 22 et 23.

Une vue d'ensemble de la composition des films formées au cours des étapes de préoxydation apparaît en Figure 24 avec la synthèse des résultats obtenus par spectroscopie XPS sur les échantillons d'alliages 441 préoxydés dans les quatre conditions expérimentales décrites plus haut. Ces résultats apparaissent sous forme de ratio des éléments chimiques chrome, fer manganèse et titane.

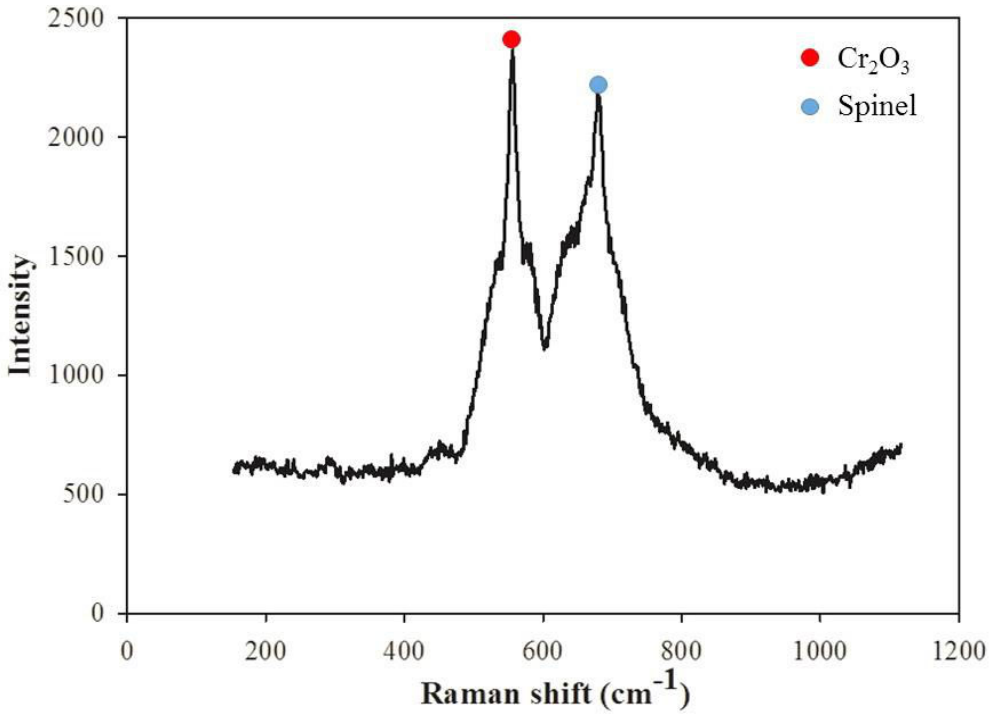

Figure 22 : spectre Raman obtenu sur un acier 441 préoxydé en milieu CO/CO_2 à 850 °C.

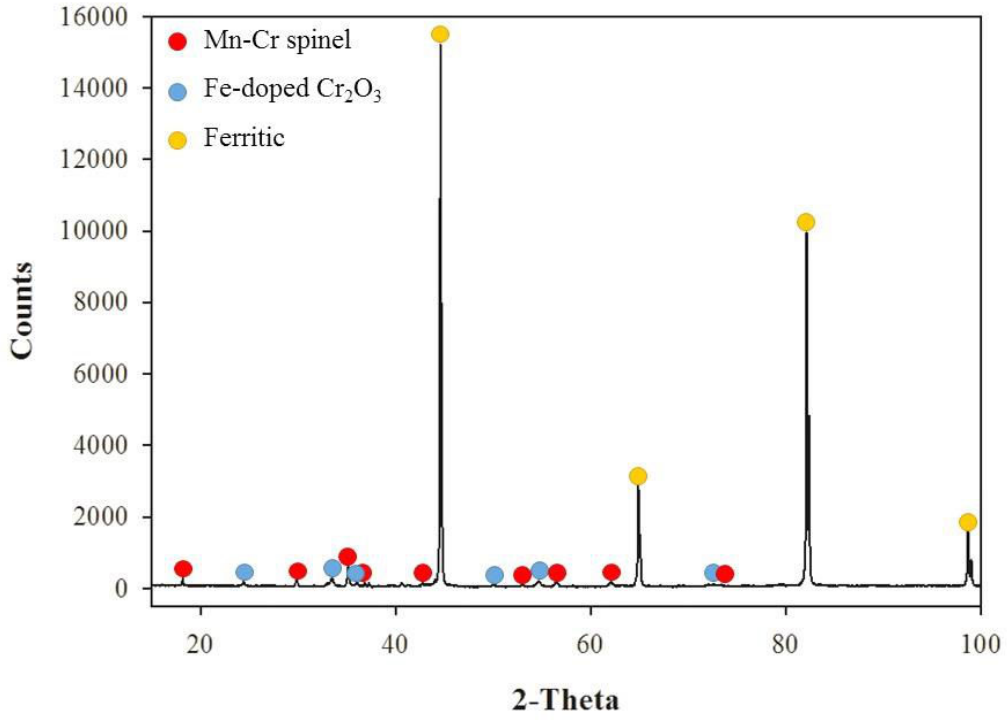

Figure 23 : Spectre de diffraction des RX obtenu sur un acier 441 préoxydé en milieu CO/CO_2 à 850 °C.

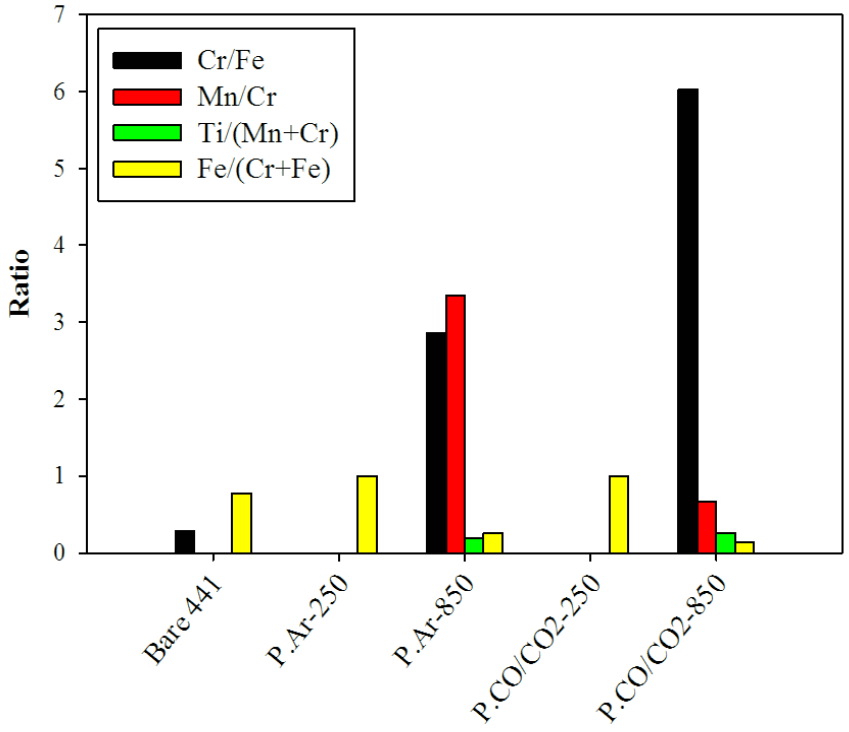

Figure 24 : Synthèse des résultats obtenus par spectroscopie XPS sur les échantillons d'alliages 441 préoxydés dans différentes conditions : "Bare 441" (référence non préoxydée), P.Ar-250, P.Ar-850, P.CO/CO_2-250 et P.CO/CO_2-850. Ces résultats apparaissent sous forme de ratio des éléments chimiques chrome, fer manganèse et titane.

Nous proposons dans ce travail une interprétation originale basée sur les différences de nature semi-conductrice des films de chromine formées à haute pression d'oxygène (proche de l'atmosphère) et identifiés comme étant de type p par rapport à ceux obtenus à basse pression (dans CO/CO_2) qui sont connu pour être de type n.
Lors de la chimisorption dissociative de la molécule d'eau, des groupements hydroxydes de type OH viennent s'adsorber sur des sites appropriés et saturer la surface de l'oxyde. Si cette réaction n'est pas à l'équilibre thermodynamique, le type de semi conductivité de l'oxyde formé (n ou p) pourrait influer sur la concentration de surface de groupements hydroxydes.

Dans le cas d'un type p (resp. type n), la nature du défaut ponctuel susceptible d'assurer le transport de matière peut correspondre à une lacune de chrome (resp. lacune d'oxygène) dans le sous réseau cationique (resp. anionique) de l'oxyde. Dans ces conditions, la concentration de surface de groupements hydroxydes pourrait varier. Par exemple, en présence de lacune d'oxygène, la vitesse de consommation des groupements hydroxydes pourrait être augmentée comme cela est illustré en Figure 25.
La variation de la concentration de surface de groupements hydroxydes peut alors entrainer la variation de la vitesse de sublimation du chrome. Ainsi en présence de lacunes d'oxygène dans le sous réseau de l'oxyde (semi conduction de type n obtenue à basse pression d'oxygène), l'abaissement de la concentration de surface de groupements hydroxydes pourrait conduire à l'abaissement de la vitesse de sublimation du chrome.
Dès lors, les résultats expérimentaux obtenus dans cette étude pourraient trouver ici une interprétation logique.

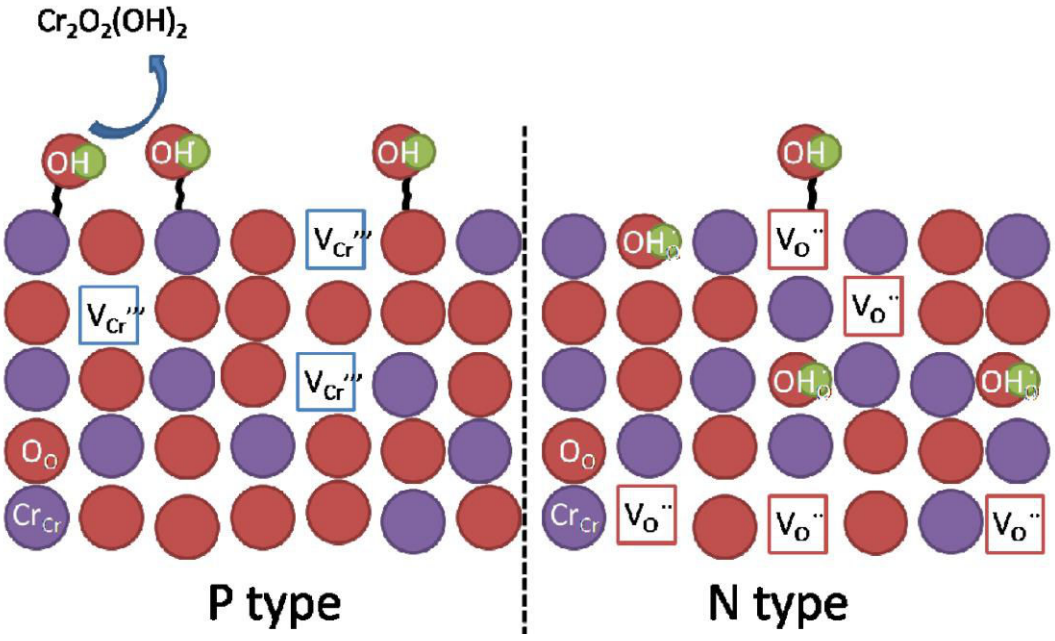

Figure 25 : Proposition de mécanisme de sublimation du chrome à partir d'une chromine de type p ou de type n.

Conclusion

Au terme de ce travail de thèse, il peut être conclu que la pré-oxydation de l'alliage 441 à basse température (250 °C) dans l'argon ou le mélange CO/CO_2 ou encore à plus haute température (850 °C) dans le mélange CO/CO_2 sont des traitements qui conduisent à l'abaissement de la vitesse de sublimation du chrome et par voie de conséquence à l'amélioration de la tenue de cet alliage en condition d'oxydation dans le compartiment cathodique des SOFC.

Références

[1] L. Antoni, J. Mougin, A. Galerie, and M. Dupeux, "Influence of Ti and Nb on the competition between oxidation kinetics and oxide adhesion on 18 % Cr stainless steels.", Ugitech Internal Report, Ugine, France, 2001. [online]. Available: www.ugitech.com/fileadmin/user_upload/Ugitech/Documents/articlesCRU/C032-P142byLAntoni.pdf. [Accessed: 2-Apr-2015]

[2] J. Froitzheim, S. Canovic, M. Nikumaa, R. Sachitanand, L. G. Johansson, and J. E. Svensson, "Long term study of Cr evaporation and high temperature corrosion behaviour of Co coated ferritic steel for solid oxide fuel cell interconnects," J. Power Sources, vol. 220, pp. 217–227, Dec. 2012.

[3] J. G. Grolig, J. Froitzheim, and J.-E. Svensson, "Coated stainless steel 441 as interconnect material for solid oxide fuel cells: Oxidation performance and chromium evaporation," J. Power Sources, vol. 248, pp. 1007–1013, Feb. 2014.

[4] J. Rufner, P. Gannon, P. White, M. Deibert, S. Teintze, R. Smith, and H. Chen, "Oxidation behavior of stainless steel 430 and 441 at 800 °C in single (air/air) and dual atmosphere (air/hydrogen) exposures," Int. J. Hydrogen Energy, vol. 33, pp. 1392–1398, 2008.

[5] Z. Yang, G.-G. Xia, C.-M. Wang, Z. Nie, J. Templeton, J. W. Stevenson, and P. Singh, "Investigation of iron–chromium–niobium–titanium ferritic stainless steel for solid oxide fuel cell interconnect applications," J. Power Sources, vol. 183, no. 2, pp. 660–667, Sep. 2008.

[6] M. Stanislowski, E. Wessel, K. Hilpert, T. Markus, and L. Singheiser, "Chromium vaporization from high-temperature alloys: I. Chromia-forming steels and the influence of outer oxide layers," J. Electrochem. Soc., vol. 154, no. 4, p. A295, 2007.

[7] H. Kurokawa, C. Jacobson, L. Dejonghe, and S. Visco, "Chromium vaporization of bare and of coated iron–chromium alloys at 1073 K," Solid State Ionics, vol. 178, no. 3–4, pp. 287–296, Feb. 2007.

[8] A. Galerie, M. R. Ardigo, P. Berthod, W. Chandra-Ambhorn, S. Chevalier, P. Y. Hou, and F. Rouillard, “Influence of water vapor on high-temperature oxidation of chromia-forming materials.” French Activity on High Temperature Corrosion in Water Vapor. Materials Science Foundations Vol. 76 Trans Tech Publications.

[9] C. Collins, J. Lucas, T. L. Buchanan, M. Kopczyk, a. Kayani, P. E. Gannon, M. C. Deibert, R. J. Smith, D. S. Choi, and V. I. Gorokhovsky, “Chromium volatility of coated and uncoated steel interconnects for SOFCs,” Surf. Coatings Technol., vol. 201, no. 7 SPEC. ISS., pp. 4467–4470, 2006.

[10] G. R. Holcomb, “Calculation of reactive-evaporation rates of chromia,” Oxid. Met., vol. 69, no. 3–4, pp. 163–180, 2008.

Étude de la sublimation du chrome lors de l'oxydation haute température de l'alliage AISI 441 et recherche de solutions de protection

Les aciers inoxydables ferritiques sont actuellement les meilleurs candidats pour répondre au cahier des charges des matériaux destinés aux interconnexions de piles à combustibles à oxyde solide (SOFC acronyme anglo-saxon pour Solid Oxide Fuel Cell). Cependant, du coté du compartiment cathodique de ces piles, le phénomène de sublimation du chrome à haute température conduit à des dégradations importantes, réduisant ainsi la durée de vie en service des SOFC. Les objectifs de ce travail de thèse sont (i) d'étudier le phénomène de sublimation du chrome sur l'acier inoxydable ferritique AISI 441 et (ii) de rechercher le ou les moyen(s) d'atténuer cette même sublimation. Sur le deuxième point, des méthodes de protection ont été mises en oeuvre, en particulier avec le dépôt de films minces de spinelle Mn-Co obtenues via un procédé de galvanoplastie ou bien encore en procédant à des pré-oxydations des alliages dans des atmosphères contrôlées de type argon impur ou mélanges gazeux équimolaires CO/CO_2 (250°C ou 850°C, pour une durée totale de 3 h). Concernant l'étude de la sublimation du chrome, des essais d'oxydation simulant les conditions de service ont été conduites dans des mélanges gazeux : 5% de H_2O dans O_2 à 800°C pendant 96 h. Au terme de ce travail de thèse, il peut être conclu que la pré-oxydation de l'alliage 441 à basse température (250°C) dans l'argon ou le mélange CO/CO_2 ou encore à plus haute température (850°C) dans le mélange CO/CO_2 sont des traitements qui conduisent à l'abaissement de la vitesse de sublimation du chrome et par voie de conséquence à l'amélioration de la tenue de cet alliage en condition d'oxydation dans le compartiment cathodique des SOFC.

Mots-clés: Acier ferritique, Evaporation du chrome, Oxydation haute température, Vapeur d'eau, Analyse chimique, Analyse microstructurale

High temperature oxidation and volatilisation of chromium from AISI 441 ferritic steel in humidified atmosphere and its protection

Ferritic stainless steels are the most attractive materials that are able to fulfil SOFC (Solid Oxide Fuel Cell) interconnect properties. However, in cathodic SOFC condition, Cr volatilisation from ferritic steels leads to degradations of interconnect and cathode materials and shorter service lifetime of SOFC. The objectives of this work are (i) to study Cr volatilisation from AISI 441 ferritic stainless steel and (ii) to find the way out to suppress Cr volatilisation. The Cr volatilisation protective methods used in this work were coating with Mn-Co spinel by an electroplating method and preoxidation in the condition of Ar or CO/CO_2 at either 250°C or 850°C, for 3 h. Cr volatilisation experiments were performed in 5%H_2O in O_2 at 800°C for 96 h. According to the results, it can be concluded that the preoxidation of the AISI 441 in Ar or CO/CO_2 at low temperature (250°C) or in the CO/CO_2 at a higher temperature (850°C) are treatments that lead to lowering the sublimation rate of the Cr and improvement in the oxidation resistance of this alloy in the cathodic compartment of the SOFC.

Keywords: Ferritic stainless steel, Chromium evaporation, High temperature oxidation, Water vapour, Chemical analysis, Microstructural analysis